Millifluidic Process Development for the Magnetophoretic Fractionation of Heterogeneous Yeast Cell Cultures by Age

Leonie Elisabeth Wittmann

Science doesn't always go forward. It's a bit like doing a Rubik's cube. You sometimes have to make more of a mess with a Rubik's cube before you can get it to go right. – Jocelyn Bell Burnell

Acknowledgements

First and foremost, I would like to express my sincere thanks to my supervisor, Assoc. Prof. Dr. Sebastian Schwaminger. Despite our physical meetings being limited to two months at our chair, your invaluable support, whether from MIT in Boston or the Medical University of Graz, was really valuable. Your readiness to listen to my data and plenty of ideas to advance the project, all while granting me the autonomy to follow my own research, has been truly remarkable. Additionally, I appreciate your support in all my collaborations and conferences. Thank you very much, Basti; I learned so much from you.

I am equally grateful to my second supervisor, Prof. Dr. Sonja Berensmeier, for the opportunity to work in your group, the freedom in my research, and your consistent support in all my collaborations and conferences. My thanks also extend to my cooperation partners at the Chair of Brewing and Beverage Technology, Dr. Marco Eigenfeld and Roland Kerpes. It was a pleasure to successfully finalize the project together. Special thanks to Emily Krucker-Velasquez and Professor Dr. Martin Bazant's group at MIT for their valuable collaboration in integrating experiments and simulations and to Dr. Olivier Sandre from Université de Bordeaux for his cooperation in magnetic aggregation and assistance in constructing the Halbach array.

I am profoundly thankful to my colleagues and friends, particularly Chiara and Eva, my office partners. I loved our office mood, working together and always having an open ear for each other as colleagues and friends. Thanks a lot for proofreading my thesis. Special mention goes to Lea, my role model throughout my PhD journey. We started together as I was writing my Master's thesis with you, and now we are friends. Together with you and Michi, we went for so many morning and evening runs at the Isar (btw, we should definitely cross the Isar at some point). Michi, we always had an open ear for each other during our walks to Garching. Forgetting a long working day got really easy when we started dancing, first with you Michi, and then with Patrick, Chiara and Robin. Robin, I am so happy that we got to know each other, that you always stand behind me, and that you share my passion for kite surfing. My appreciation also goes to Lucía, Stefan, Tatjana, Yasmin, Gregor, Alexander, Ines, Dennis, Marko, Tobi, Julian, Rike, Paula, Lisa, Alejandra, Sabrina, Stefan, and Jonas for the memorable times at the chair, both in the lab and during leisure.

Abstract

The age-based fractionation of yeast cells is essential for analyzing age-related phenomena in yeast physiology and using this knowledge to optimize industrial processes. This work established a novel approach for sorting individual yeast cells based on age using magnetophoretic fractionation in a 3D-printed, millifluidic chip. Therefore, the bud scars of *S. pastorianus ssp. carlsbergensis* cells were labeled using a bifunctional linker-protein and functionalized magnetic nanoparticles (MNPs).

The MNPs had to meet specific criteria to ensure consistent magnetic response relative to the number of bud scars. Steric and electrostatic stabilization also ensured time-stable agglomerate homogeneity to prevent undesirable agglomeration in magnetic fields. In contrast to bare iron oxide nanoparticles, ethylenediaminetetraacetic acid functionalized silica-coated iron oxide nanoparticles (ION@Si@EDTA) exhibited controlled agglomeration, enhanced colloidal stability, and specificity in the bud scar labeling process of the yeast cells.

A millifluidic chip facilitated high-throughput fractionation, overcoming the limitations of microfluidic alternatives, such as label-free sorting based on size-age correlation. Process enhancements, including sample dispersion methods and chip design optimization, ensured efficient cell sorting while maintaining viability. The colloidal stability of the used ION@Si@EDTA avoided magnetic aggregation successfully; however, because of the centimeter scale of the flow channels, magnetically induced convection was unavoidable in reasonable process conditions. This was evaluated by a model system consisting of non-magneto-responsive and magneto-responsive nanoparticles. As a result, the non-magnetically young daughter cells would always comigrate along with the hydrodynamically generated motion of the magnetically labeled mother cells. That is why a multi-step approach was developed. The process consisted of a static batch separation, separating the non-magnetically labeled daughter cells from the magnetically labeled mother cells. These were then introduced for further age-based sorting in the millifluidic flow channel. A rectangular, a trapezoidal, and a pinch-shaped channel were tested, and the pinch-shaped channel geometry, relying on the magnetophoretic and the size-based sorting principle, achieved precise age-based sorting with reproducibility and high throughput of $1.18 \times 10^6 \pm 1.54 \times 10^5$ cells mL^{-1}. Four age fractions were derived, with a minimum bud scar number of 2.33 ± 0.82 and a maximum bud scar

number of 6.27 ± 0.45, indicating an effective enrichment of older cells. Metabolomic and genomic analysis of the sorted cells unveiled age-related variations in metabolic pathways and gene expression profiles, offering insights into cellular aging mechanisms. The results gained by analyzing the age-sorted yeast cells could help increase product yields and optimize processes in the beverage and pharmaceutical industries, with the potential for upscale and adaptation to diverse yeast strains.

Kurzzusammenfassung

Die altersbasierte Fraktionierung von Hefezellen ist unerlässlich, um altersbedingte Phänomene in der Hefephysiologie zu analysieren und dieses Wissen zur Optimierung industrieller Prozesse zu nutzen. In dieser Arbeit wurde ein neuartiger Ansatz für die Sortierung einzelner Hefezellen auf der Grundlage des Alters durch magnetophoretische Fraktionierung in einem 3D-gedruckten, millifluidischen Chip entwickelt. Dazu wurden die Sprossnarben von *S. pastorianus ssp. carlsbergensis* Zellen mit einem bifunktionalen Linkerprotein und funktionalisierten magnetischen Nanopartikeln (MNPs) markiert.

Die MNPs mussten bestimmte Kriterien erfüllen, um eine konsistente magnetische Reaktion im Verhältnis zur Anzahl der Sprossnarben zu gewährleisten. Sterische und elektrostatische Stabilisierung gewährleisteten außerdem eine zeitstabile Homogenität der Agglomerate, um unerwünschte Agglomerationen in Magnetfeldern zu verhindern. Im Gegensatz zu reinen Eisenoxid-Nanopartikeln zeigte ION@Si@EDTA eine kontrollierte Agglomeration, erhöhte kolloidale Stabilität und Spezifität im Sprossnarbenmarkierungsprozess der Hefezellen.

Ein Millifluidik-Chip erleichterte die Hochdurchsatzfraktionierung und überwand die Einschränkungen mikrofluidischer Alternativen, wie die markierungsfreie Sortierung auf der Grundlage der Größen-Alters-Korrelation. Prozessverbesserungen, einschließlich Probendispersionsmethoden und Optimierung des Chipdesigns, gewährleisteten eine effiziente Zellsortierung unter Beibehaltung der Lebensfähigkeit. Die kolloidale Stabilität des verwendeten ION@Si@EDTA verhinderte erfolgreich die magnetische Aggregation; aufgrund der Centimeterskala der Fließkanäle war jedoch eine magnetisch induzierte Konvektion unter angemessenen Prozessbedingungen unvermeidbar. Dies wurde anhand eines Modellsystems aus nicht-magnetisch reagierenden und magnetisch reagierenden Nanopartikeln bewertet. Woraus resultierte, dass die nicht-magnetisch jungen Tochterzellen immer mit der hydrodynamisch erzeugten Bewegung der magnetisch markierten Mutterzellen mitwandern würden. Aus diesem Grund wurde ein mehrstufiger Ansatz entwickelt. Der Prozess bestand aus einer statischen Batch-Separation, bei der die nicht magnetisch markierten Tochterzellen von den magnetisch markierten Mutterzellen getrennt wurden. Diese wurden dann zur weiteren altersabhängigen Sortierung in den Millifluidik-Flusskanal eingeführt. Es wurden ein rechteckiger, ein trapezförmiger und ein pinchförmiger Kanal getestet. Die pinchförmige

Kanalgeometrie, die sich auf das magnetophoretische und das größenbasierte Sortierprinzip stützt, erzielte eine präzise altersbasierte Sortierung mit Reproduzierbarkeit und einem hohen Durchsatz von $1,18 \times 10^6 \pm 1,54 \times 10^5$ Zellen mL^{-1}. Es wurden vier Altersfraktionen mit einer minimalen Sprossnarbenzahl von $2,33 \pm 0,82$ und einer maximalen Sprossnarbenzahl von $6,27 \pm 0,45$ erzielt, was auf eine effektive Anreicherung älterer Zellen hinweist. Metabolom- und Genomanalysen der sortierten Zellen enthüllten altersbedingte Variationen in Stoffwechselwegen und Genexpressionsprofilen, die Einblicke in zelluläre Alterungsmechanismen bieten. Die durch die Analyse der alterssortierten Hefezellen gewonnenen Erkenntnisse könnten dazu beitragen, die Produktausbeute zu erhöhen und die Prozesse in der Getränke- und Pharmaindustrie zu optimieren, wobei das Potenzial für ein Upscaling und die Anpassung an verschiedene Hefestämme besteht.

Table of Contents

Abbreviations

ADP	adenosine diphosphate
APTES	(3-aminopropyl)triethoxysilane
ATP	adenosine triphosphate
BION	bare iron oxide nanoparticles
ChBD	chitin binding domain
DLS	dynamic light scattering
DLVO	Derjaguin, Landau, Verwey and Overbeek
EDTA	ethylenediaminetetraacetic acid
FACS	fluoresence-activated cell sorting
FT-IR	Fourier-transform infrared spectroscopy
his	histidine
ION@Si@EDTA	ethylenediaminetetraacetic acid functionalized silica-coated iron oxide nanoparticles
KPP	potassium phosphate
LED	light-emitting diode

MACS	magnetic-activated cell sorting
MAD	miniature-chemostat aging device
MES	2-(N-morpholino)ethane sulfonic acid
MNP	magnetic nanoparticle
MNP@Si@NH$_2$	silica-coated magnetic nanoparticles
MOPS	3-(N-morpholino)propane sulfonic acid
NAD$^+$	nicotinamide adenine dinucleotide
PBS	phosphare buffered saline
PC	phosphate citrate
PDMS	polydimethylsiloxane
PMMA	polymethylmethacrylate
RS	Ringers solution
SME	micro, small, and medium-sized
SQUID	superconducting quantum interference device
TEM	transmission electron microscopy
TEOS	tetraethyl orthosilicate
TRIS	tris(hydrocymethyl)aminomethane
XRD	X-ray diffraction

Symbolslist

Sign	Description	Unit
B	Magnetic flux density	T
D	Hydrodynamic dispersion	$\mathrm{m^2\ s^{-1}}$
D_h	Hydraulic diameter	m
F_b	Buoyancy force	N
F_d	Drag force	N
F_g	Gravitational force	N
F_l	Lift force	N
F_m	Magnetic force	N
F_{sl}	Shear-induced lift force	N
F_{wl}	Wall-induced lift force	N
Gr_m	Grashof number	-
H	Magnetic field strength	$\mathrm{A\ m^{-1}}$
K_{eff}	Boltzmann constant	$\mathrm{J\ m^{-3}}$
L	Characteristic length	m
M	Magnetization	$\mathrm{emu\ g^{-1}}$
M_s	Saturation magnetization	$\mathrm{emu\ g^{-1}}$
N^*	Aggregation parameter	-
Pe	Péclet number	-
R	Radius of curvature	m
Re	Reynolds number	-
Re_c	Reynolds number	-
T	Temperature	K
$U_{i,j}$	Lennard-Jones Potential	J
V	Volume	$\mathrm{m^{-3}}$

Sign	Description	Unit
$c_{i,j}$	Interaction coefficient	-
$d_{i,j}$	Interaction coefficient	-
f	Any external force	N
k_B	Boltzmann constant	$\text{m}^2 \text{ kg s}^{-2} \text{ K}^{-1}$
m	Mass	m
r	Radius	m
u	Velocity	m s^{-1}
u_D	Dean velocity	m s^{-1}
u_{max}	Maximum velocity	m s^{-1}
v_{mag}	Magnetophoretic sedimentation velocity	m s^{-1}
Γ	Magnetic coupling parameter	-
χ	Zeta potential	mV
χ	Magnetic susceptiblity	-
ϵ	Characteristic energy	Joule
η	Viscosity	$\text{kg m}^{-1} \text{ s}^{-1}$
μ_{max}	Maximum growth rate	h^{-1}
μ	Magnetic permeability	$\text{V s A}^{-1} \text{ m}^{-1}$
π	Geometrical value	-
ρ	Density	kg m^{-3}

1 Introduction

Brewing is one of the earliest applications of biotechnology, as the first production of fermented beverages is dated back to 7000 B.C. in ancient China [1]. However, it was only with the invention of the microscope in 1680 by Antoine van Leeuwenhoek that yeast could be identified as a "spherical structure" in the fermentation substrate [2]. In 1883, Emil Hansen of the Carlsberg brewery was the first who used a pure yeast cell culture of *S. pastorianus ssp. carlsbergensis* to commercially produce beer. Since then, the brewing process has been explored worldwide, leading to many beer styles differing in aroma, flavor, and strength [2]. Beyond its application in fermentation, yeast has also become a model organism in genetics, biochemistry, and biology because of its genetic simplicity and eukaryotic nature. Yeast has been used to analyze biological mechanisms, including cell cycle, gene expression regulation, signal transduction, apoptosis, and aging [1]. The aging phenotype in yeast is marked by diminished physiological functionality and reduced capacity to adapt to environmental shifts [3]. Until now, different approaches have been developed to separate a heterogeneous yeast cell culture into young and old cell fractions for age-based analysis [4]. However, there is still the need for a non-invasive, high-throughput method to fractionate yeast cells into distinct age groups. So, this project aims to develop such a process. In the following, the basics of a separation process are explained in more detail, as well as the cell fractionation techniques by magnetophoresis and size suitable for yeasts.

1.1 Separation Technology

In general, separation technology encompasses the methods and processes used to isolate desired components of a mixture based on differences in their physical, chemical, thermal, and biological properties. A separation process relies on differences in size, shape, density, phase, solubility, volatility, magnetic susceptibility, etc. (Figure 1.1). However, temperature changes can also be applied to separation. The resulting separation processes are chromatography, sieving, flotation, or extraction, among other things. In cases where a single separation criterion is insufficient, combining multiple operations often facilitates achieving the desired separation outcome. In natural and engineering science, the term *separation* typically refers

to the process of dividing a mixture into two components; a *fractionation*, on the other hand, involves dividing a mixture into a gradient of multiple subgroups of components with similar properties. *Yield* refers to the ratio of the separated component to the maximum theoretical amount of this component, whereas *purity* defines the proportion of pure product in the mixture after the separation process. Another key figure is the *selectivity* of a separation process, which indicates how close the separation process comes to an ideal separation. [5]
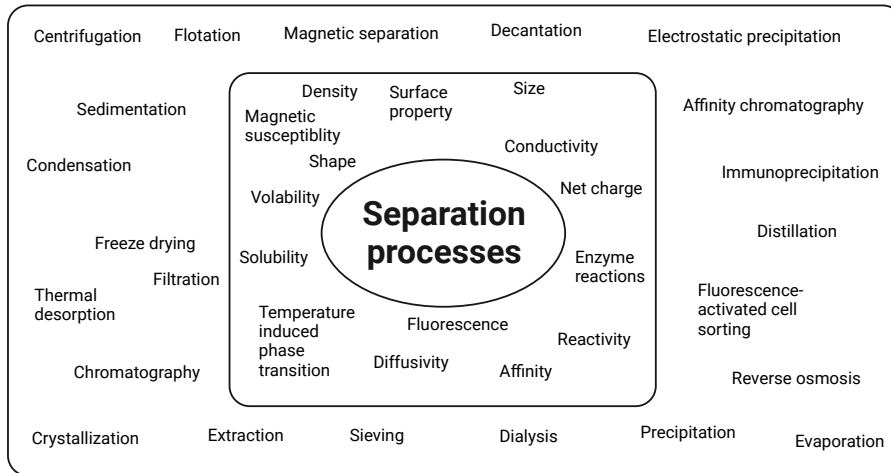
Figure 1.1: Classification of separation processes based on different principles, criteria, and examples. Adapted from [5].

Especially in medicine, biotechnology, and cellular biology, separation is employed to enrich or purify cell samples into well-defined populations to enhance efficiency in research and development applications, such as therapeutics and diagnostics cell separation. Here, cell separation from heterogeneous solutions containing a mixture of cell types or biomolecules represents a critical task, as the desired entity has to be separated selectively. [6]

According to Lee et al., traditional cell separation is realized by label-free and label-based techniques. For the latter, the selective binding of a monoclonal antibody to a specific cellular component provides high separation yield and purity in the process; however, the labeling processes are complex and may change cellular functions, such as signaling pathways or receptor functions. Additionally, commercially available antibodies are expensive and limited in targets or need specific markers. Three common cell sorting techniques are fluoresence-activated cell sorting (FACS), magnetic-activated cell sorting (MACS), and cell panning [7]. FACS, the first commercial cell sorter, based on fluorescent labeling of cells, was invented in the late 1960s and has evolved to become automated and robust these days, offering high specificity using multiple morphological and fluorescent cell signatures, such as cell surface labels, cell size, and granularity [8, 9]. MACS, another label-based cell separation technique,

operates on the principle of antibody-conjugated beads binding to cells, followed by the magnetic separation of these labeled cells. Introduced in 1989 by Miltenyi et al. [10], this batch-wise operation mode offers a high throughput of $10^6 - 10^7$ cells mL^{-1} [11], whereas the continuous mode of FACS is limited to 10^4 cells min^{-1} [7, 12]. In a direct comparison, MACS processes resulted in higher yields and efficiency compared to FACS due to its capability for parallel processing [13]. The third label-based technique, cell panning, relies on immobilizing antibodies to withhold cells with specific antigens on a surface. This method is advantageous, as high purities are reached, however, high cell loss occurs during the process. Despite yielding high purity, all three methods lack quantitative separation capability and offer only a binary separation without fractionation [7].

In contrast, label-free cell separation techniques are based on the physical properties of cells, such as size, density, deformability, electrical polarizability, adherence, and growth [7]. For example, cell separation by filtration employs uniform microscale meshes or pores to segregate cells based on size or deformability, often serving as a pre-enrichment step for further purification [14]. While being simple and inexpensive, significant cell loss and fouling are disadvantageous. Centrifugation [15, 16], or sedimentation [17] differentiates cells based on density or size, enabling processing of large volumes. However, in order to achieve a higher purity, several runs or the use of media with density gradients are often necessary [18]. The shear stress on the cells during centrifugation might impact cell viability [19, 20]. Cell adherence-based separation [21] utilizes a cell's adhesion properties or selective media to enrich specific cell types but may not yield high purity or retain the original cell characteristics. [7]

1.2 Micro- and Millifluidic Separation Technology

Within separation technology for cell analysis, the separation requirements have become more complex as research genomics and cell biology have improved. Therefore, a more refined fractionation into different subgroups has become necessary compared to binary separation. Microfluidics has emerged as a response to these requirements, as it not only offers a fast, precise, and gentle way of separation, but fractionation processes are also possible [7]. Shields et al. state that with microfluidics, the manipulation of fluids within sub-millimeter channels allows for the precise control of fluid flow and the application of cell sorting mechanisms that are impractical at larger scales, like velocity gradients for hydrodynamic sorting. The advantages of microfluidics for cell sorting are numerous: It offers high throughput by parallel processing, requires reduced sample volumes, operates at low cost, and has the potential for automation within lab-on-a-chip systems [22].

Hydrodynamics in Micro- and Millifluidics

The laminar flow within microfluidic channels minimizes the shear stress onto cells, preserving their integrity and viability, which is a significant advantage over traditionally employed cell separation methods that can cause cell damage [23].

Generally, in fluid dynamics, two primary theoretical models are employed to describe flow behavior: The molecular model and the continuum model [24]. The molecular model, which focuses on discrete intermolecular interactions, utilizes the Lennard-Jones Potential (Equation 1.1) to represent every molecule's behavior.

$$U_{i,j}(r) = 4\varepsilon \left[c_{i,j} \cdot \left(\frac{r}{\sigma}\right)^{-12} - d_{i,j} \cdot \left(\frac{r}{\sigma}\right)^{-6} \right] \tag{1.1}$$

Here, $U(r)$ represents the potential energy as a function of the distance r between two particles i and j. $c_{i,j}$ and $d_{i,j}$ are interaction coefficients, and the variable ε denotes the characteristic energy, reflecting the strength of the attraction between the particles having a distance r. The parameter σ is the finite distance at which the interparticle potential is zero, signifying the equilibrium point where the potential energy is minimized. The term with the power of -12 describes the repelling potential, and the second term with the power of -6 presents the attractive part due to van der Waals forces [25, 26]. The calculation of the molecular model delivers a detailed physical description but requires significant computational resources. [24]

In contrast, the continuum model considers fluid as a spatial continuum, where material properties such as viscosity and density are well-defined at every point. The Navier-Stokes equations (Equation 1.2) exemplify the continuum approach. [24]

$$\rho \left(\frac{\partial \vec{u}}{\partial t} + \vec{u} \cdot \nabla \vec{u} \right) = -\nabla p + \eta \nabla^2 \vec{u} + \vec{f} \tag{1.2}$$

In the Navier-Stokes equations for incompressible fluids, the variable ρ presents the density of the fluid, $\vec{u}$ the fluids' velocity, and t the time, while p indicates the pressure within the fluid. The fluid's dynamic viscosity is given by η, and $\vec{f}$ symbolizes external forces acting on the fluid, such as gravity. The pressure field gradient is expressed as ∇p, and the Laplacian of the velocity field, $\nabla^2 u$, accounts for the viscous effects in the fluid dynamics [27]. According to Ruffert et al., this model is effective for macroscopic scale analysis, where the effects of individual molecules are negligible. However, in microfluidic processes, where fluidic channels approach the scale of the mean free path of molecules, the continuum assumption breaks down, leading to non-continuum effects like slip flow and deviations from classical fluid dynamics. Thus, depending on the physical characteristics of the fluids in microfluidics, the applicability of the Navier-Stokes equation has to be evaluated. The growing influence of van der Waals

forces and electrostatic forces are the cause of the model deviations during a transition from a macro- to a microsystem. For example, the frictional force in a microsystem becomes dependent on the surface, and the pressure drop, which is neglected in the macrosystem, must be regarded as essential. [24].

The dimensionless Reynolds number can be used to characterize the flow in a microfluidic chip. It represents the ratio of inertia to viscous forces:

$$Re = \frac{\rho \cdot \vec{u} \cdot L}{\eta} \tag{1.3}$$

where the characteristic length L describes the channel length. At low Reynolds numbers ($Re < 10$ [28]), cells entrained in this flow are expected to follow fluidic streamlines unless deflected by an external force or by an obstacle; however, with increasing Reynolds numbers, inertial effects become significant, leading to the generation of secondary flows. For example, Dean flow develops in curved channels due to centrifugal forces [28].

If two homogeneous and mixable liquids flow together in a microfluidic channel, mixing will depend on the flow velocity, the channel length, and the hydrodynamic dispersion D, making dispersion control paramount for a separation process [29–31]. The Péclet number Pe specifies the advective to diffusive transport ratio as follows [32],

$$Pe = \frac{\vec{u} \cdot L}{D} \tag{1.4}$$

Micro- and Millifluidic Techniques

Microfluidic platforms can be classified according to their functional principles, displayed in Table 1.1, based on different separation criteria, such as size, deformability, shape, density, polarizability, net charge, and susceptibility [7]. As shown in Table 1.1, each separation technique has its advantages and disadvantages, necessitating careful selection for specific applications. Besides the described general advantages of microfluidic technology in the chapter beginning, there are also challenges independent of the separation technique. The fabrication of the devices often requires specialized equipment and expertise, and scaling up to increase the cell throughput remains difficult (further discussed in subsection 1.2.3).

Table 1.1: Overview of microfluidic cell separation techniques. Adapted from [7, 33].

Separation technique	Mode	Separation criteria	Advantage	Disadvantage	Example
Passive techniques					
Mechanical filter	Size exclusion	Size, deformability	Simple, label-free, high throughput	Clogging	[34, 35]
Hydrodynamic	Streamline manipulation	Size, shape	Simple, label-free	Low throughput	[36, 37]
Deterministic lateral displacement	Migration in micropost array	Size, shape	Label-free, combination with external forces	Low throughput, structural complexity	[38, 39]
Microstructure	Microstructure perturbation	Size, density, deformability	High sensitivity, high purity, label-free	Complex, sensitive	[40, 41]
Aqueous to phase systems	Differential affinity	Surface property, net charge	High selectivity, gentle	Dilution, usability	[42, 43]
Inertial	Lift force, secondary flow	Size, shape, deformability	High throughput, label-free, simple	Sample dilution, no quantitative design rules	[44, 45]
Active techniques					
Electric	Dielectrophoresis	Polarizability, size	Easy to integrate, label-free	Low/ medium throughput, affected cell properties	[46, 47]
Magnetic	Magnetic mobility	Magnetic susceptibility	High purity, neg. magn. is label-free	Magnetic properties needed	[48, 49]
Acoustic	Acoustic radiation force	Size, density, compressibility	Label-free, gentle	Temperature increase, same sign contrast factors	[50, 51]
Optical	Optical lattice	Refraction index, size	High resolution, low contamination	High cost, complex, low throughput	[52, 53]
Gravity	Sedimentation difference	Size, density	Simple, label-free, gentle	Low resolution, sensitive	[54, 55]

The small channel dimensions can lead to clogging by cells or debris, which can disrupt the separation process and necessitate frequent cleaning. Additionally, the microscale dimensions make the system sensitive to external variables such as temperature and pressure. Thus, precise control systems are required, which can increase the complexity and cost of the setup. [7, 24]

Despite these challenges, the specificity and selectivity of microfluidic fractionation are often superior to traditional, binary separation methods, such as FACS, MACS, and panning. However, the heterogeneity in biological samples can also make a fractionation challenging. Cells with similar sizes or overlapping physical characteristics can be difficult to separate distinctly, leading to potential cross-contamination. This necessitates the integration of additional sorting mechanisms or multiple stages of separation to achieve the desired purity/separation efficiency, which can complicate the design and operation of microfluidic devices. [23, 56]

1.2.1 Magnetophoresis-based Cell Sorting

The Fundamentals of Magnetism

Among the active separation techniques, magnetophoresis is increasingly recognized for its diverse applications in cell separation [6, 57]. In magnetophoresis, entities are manipulated within a viscous medium using an inhomogeneous magnetic field [58, 59]. The magnetic field (Figure 1.2 a) can either be generated by permanent magnets, known for their convenience and cost-effectiveness, or electromagnets, which offer higher magnetic field gradients but are limited by issues like joule heating [24]. The magnetic flux represents all magnetic field lines. The magnetic flux density $\vec{B}$ describes the density and direction of the field lines that pass through an imaginary surface in space. Indirectly, $\vec{B}$ is also a measure of the strength of the magnetic field $\vec{H}$ [24]. Both variables can be expressed as:

$$\vec{H} \cdot \mu \cdot \mu_0 = \vec{B} \tag{1.5}$$

Where μ is the material-specific magnetic permeability constant, and μ_0 is the magnetic permeability constant of vacuum. The magnetic susceptibility χ ($\chi = \mu - 1$), which quantifies a material's response to an applied magnetic field, varies among different materials. Diamagnetic materials (e.g., water, cells) exhibit weak magnetization opposite to the magnetic field ($-1 < \chi < 0$), which ceases upon field removal. Paramagnetic materials display a weak but more pronounced magnetization in the field's direction ($0 < \chi < 10^{-2}$), also reversible upon field removal (e.g., manganese ions in magnetic resonance imaging contrast agents). Ferromagnetic materials (e.g., iron, nickel, cobalt) are easily magnetized and retain
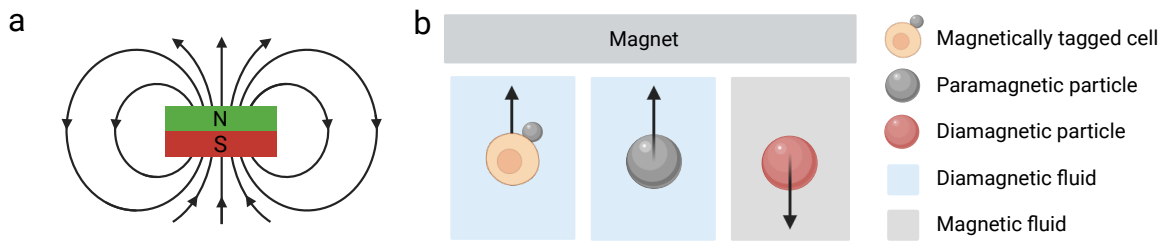
Figure 1.2: (a) Scheme of a magnet with the magnetic field lines from the north pole to the south pole. The field lines are always closed, but can form large loops; inside the magnet they run back from the south pole to the north pole. (b) Schematic depiction of positive and negative magnetophoresis processes. Positive magnetophoresis involves paramagnetic or magnetically tagged cells with higher magnetization than the surrounding diamagnetic fluid, causing them to migrate toward the field maximum. In contrast, in negative magnetophoresis, diamagnetic particles suspended in a magnetic fluid experience a magnetic force in opposition to the magnet. Adapted from [57].

a remanent magnetization even after the field is removed ($\chi > 10^{-1}$ to 10^5). For anti-ferromagnetic materials, the magnetic moment is anti-parallel; for ferrimagnetic materials, the magnetic moments are also anti-parallel but do not cancel each other (Figure 1.3 a). [7, 57, 60, 61] Superparamagnetism is characterized by the absence of remanence, which means that the magnetization becomes zero if the magnetic field is removed (Figure 1.3 b). This is particularly advantageous for magnetophoresis-based cell separation, allowing precise control. Superparamagnetism occurs in ferro- or ferrimagnetic materials, which are composed of a single magnetic domain below a critical size, dependent on the material. In these small particles, magnetization changes require the rotation of the entire particle's magnetic moment, a process hindered in larger particles by significant anisotropy energy barriers (Figure 1.3 c). However, in sufficiently small particles (e.g., Fe = 6 nm at room temperature, 3 – 50 nm for other materials [24]), the anisotropy energy equals the thermal energy $K_{eff} \cdot V \geq 10 \cdot k_B \cdot T$, leading to rapid thermal flipping of the magnetic dipole, making them superparamagnetic. The Néel relaxation time represents the period between two flips. In the absence of a magnetic field, this rapid flipping results in a net zero measured magnetic moment, while in the presence of a field, these particles align like paramagnetic materials but with a higher saturation magnetization M_S. Superparamagnetism is observed below the Curie temperature, defined as the temperature where any ferro- or ferrimagnetic materials undergo a transition to a paramagnetic state, whereas paramagnetism is normally observed above. [58, 61, 64–66]

Superparamagnetic Iron Oxide Nanoparticles

Superparamagnetic nanoparticles, in the following, also referred to as magnetic nanoparticle (MNP)s, are typically composed of magnetite or ferritic oxides like maghemite and exhibit
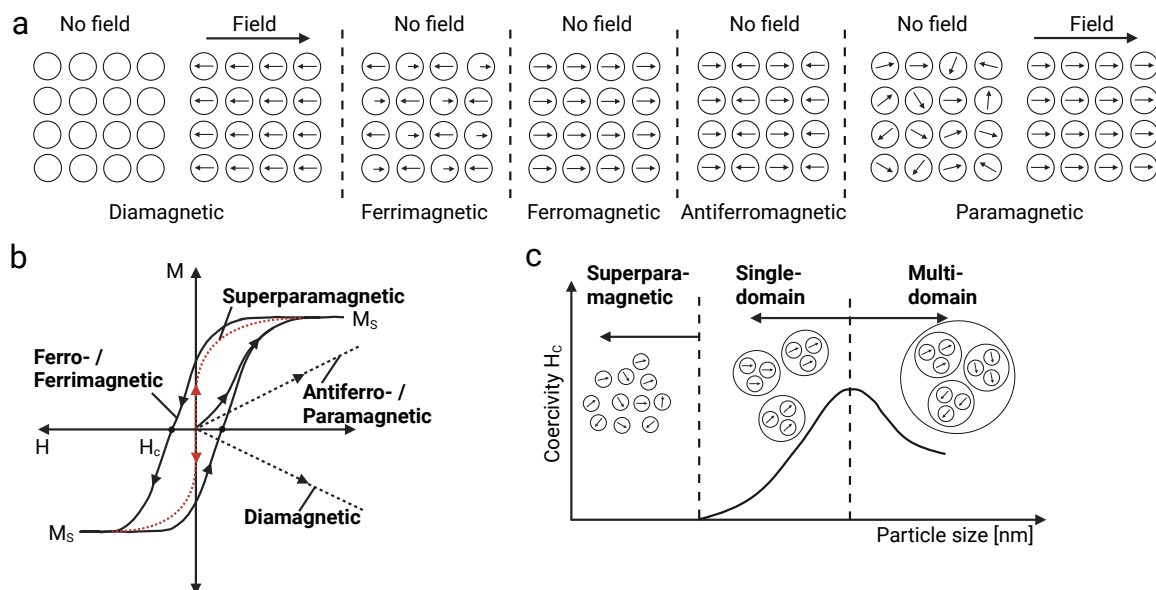
Figure 1.3: (a) Illustration depicting magnetic dipole orientations in five material types, both with and without an external magnetic field. (b) Hysteresis curves, plotting magnetization (M) against magnetic field strength (H), where H_c represents the coercivity for demagnetization and M_S denotes the saturation magnetization, the maximum achievable magnetization with increasing magnetic field strength. (c) Graph showing the relationship between coercivity and particle size, highlighting the absence of coercivity in superparamagnetic particles and its increase with particle size until reaching the energetically favorable multi-domain arrangements. Adapted from [62, 63].

sizes in the nanometer range [61]. Their high surface-to-volume ratio is a key advantage, enabling specific binding of targets via a (un-) functionalized surface with high binding capacities. The size of these MNPs can reach a few micrometers, depending on factors such as the stabilizing matrix, functionalization for specific binding, and the agglomeration of single MNPs [24, 67]. MNP synthesis employs two principal approaches: Bottom-up and top-down. The bottom-up approach assembles MNPs from molecular components using chemical methods like co-precipitation [68], sol-gel [69], and hydrothermal synthesis [70], or biological methods based on the reduction of salts to MNPs using enzymes [71]. Conversely, the top-down approach starts with bulk material and reduces it to nanoscale dimensions based mainly on physical methods, like milling [72], electron beam deposition [73], and laser ablation [74]. Various studies provide comprehensive analyses of these methods, detailing their respective advantages and disadvantages [75–77].

The bottom-up method co-precipitation was first established by Massart [68], and it is one of the most commonly used methods for synthesizing MNPs due to its simplicity, safety, controllability of particle size and distribution, and scalability [76, 78]. This method involves

creating an alkaline environment by adding a base to an iron (II/III) salt solution, enabling the formation of magnetite (Fe_3O_4).

$$Fe_2{}^+ + 2\,Fe_3{}^+ + 8\,OH^- \longrightarrow Fe(OH)_2 + 2\,Fe(OH)_3 \longrightarrow Fe_3O_4 + 4\,H_2O$$
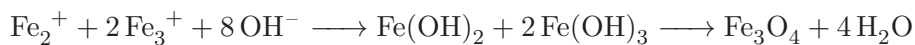
However, the significant surface energy of MNPs, attributed to their high surface-to-volume ratio, predisposes them to form agglomerates consisting of single MNPs [79]. Agglomerates, characterized by weak, reversible physical interactions between particles, can vary in size and shape depending on the surrounding medium, while aggregates consist of irreversible, strongly bonded colloidal particles. This clustering significantly affects the magnetic properties and may result in non-uniform particle size distribution [80]. Preventing spontaneous particle agglomeration during processing is crucial to maintaining colloidal stability in MNP dispersions for specific applications, such as in microfluidic fractionation [81] or drug delivery [82]. Conversely, aggregation or agglomeration enhances the magnetic moment, thereby improving separation efficiency; however, this can also amplify undesired phenomena such as cooperative magnetophoresis (Equation 1.8) or convective motion (Equation 1.10), as described later in this chapter [66].

Colloidal stability of MNPs can be enhanced through various methods, including electrostatic and steric stabilization, mechanical dispersion via ultrasonication, and viscosity increment [67, 83]. Among these approaches, steric stabilization involves modifying the particle surface with coatings such as organic shells (e.g., oleic acid, citric acid), organic polymers (e.g., chitosan, dextran, polyethylene glycol), surfactants, or inorganic metal oxides like silica and noble metals [84]. These coatings prevent particle agglomeration by creating a physical barrier around each particle [79]. Electrostatic stabilization is achieved by imparting a net positive or negative charge to the particles, influenced by environmental factors like pH and ionic strength or through charged macromolecules [76]. However, maintaining colloidal stability becomes challenging at high ionic strengths, where the electrical double layer is easily influenced, leading to particle aggregation and irreversible precipitation. [67, 85, 86]

The surface modification for increasing the colloidal stability of MNPs can also serve as functionalization for specific biomolecular binding, such as proteins, antibodies, deoxyribonucleic acid, lipids, or carbohydrates [87–89]. The binding mechanisms involve hydrogen bonds, electrostatic, hydrophobic, van der Waals interactions, and covalent bonds [87, 90]. Biomolecule adsorption, in particular proteins, enhances nanoparticle agglomeration through hydrophobic interactions, where the protein acts as a glue [91]. The large nanoparticle-protein agglomerate comprises smaller nanoparticle-protein agglomerates [91, 92], and with increasing protein concentration, the nanoparticle surface gets saturated, and repulsive forces prevail, leading then to a decrease in particle-protein agglomerates [90, 91].

In summary, while electrostatic and steric repulsion methods can enhance the colloidal stability of MNPs, the MNPs are susceptible to agglomeration due to attractive forces like van der Waals forces or electrostatic attraction depending on the medium. Additionally, when a magnetic field is present in magnetophoresis-driven processes, magnetic dipole interactions further promote agglomeration (further described on page 12). This presents a dilemma: High colloidal stability is desirable for maximizing surface area, but agglomeration, while often being inevitable, difficult to control, and reducing surface area, enhances separation efficiency in magnetophoretic processes. Thus, in a magnetophoresis-based fractionation process, it is important to control agglomeration and use homogeneous agglomerates, balancing the need for high surface area with efficient but accurate separation/fractionation.

Forces and Characteristics in a Magnetophoresis-based Process

For a magnetophoresis-based process, the classical theory employs the continuum equation as outlined in Equation 1.2. This approach considers the external forces acting on particles, and their movement is governed by Newton's second law, expressed as

$$m\frac{\partial \vec{u_p}}{\partial t} = \vec{F_m} + \vec{F_d} + \vec{F_g} + \vec{F_b} + \vec{F_l} \tag{1.6}$$

where m is the mass of the particle, $\partial \vec{u_p}/\partial t$ its acceleration, $\vec{F_m}$ is the magnetic force, $\vec{F_d}$ is the hydrodynamic force, $\vec{F_g}$ is the gravitational force, $\vec{F_b}$ is the buoyant force, and $\vec{F_l}$ is the lift force that impact the particle. In microfluidic systems, $\vec{F_m}$ and $\vec{F_d}$ are typically dominant, while the others can often be neglected [58].

According to Leong et al., for superparamagnetic particles in an inhomogeneous magnetic field, where $\nabla \times \vec{B}$ is zero and the magnetization $\vec{M}$ is parallel to the magnetic field $\vec{B}$, the magnetic force $\vec{F_m}$ can be described by

$$\vec{F_m} = |\vec{m}(\vec{B})|\vec{\nabla}B = V_m \cdot \rho_m \cdot |\vec{M}(\vec{B})|\vec{\nabla}B \tag{1.7}$$

In this equation, $\vec{\nabla}B$ represents the gradient of the magnetic field B, and $|\vec{m}(\vec{B})|$ is the magnetic dipole moment of the superparamagnetic particle induced by the magnetic field strength $\vec{B}$. The magnetic dipole moment can be quantitatively expressed as a function of the magnetization per unit mass, denoted as $|\vec{M}(\vec{B})|$. This relationship suggests that the resultant force acting upon a magnetic particle is not aligned with the magnetic field vector itself but rather is oriented along the vector gradient of the magnetic field. As a consequence of this orientation, magnetic particles exhibit a spatial migration from zones of lower magnetic field intensity towards areas characterized by higher magnetic field intensities. This migration is governed by a force that is directly proportional to the magnetic field gradient. [66]

The term magnetophoresis describes the movement of an entity experiencing a magnetic force, and it can be classified as negative and positive magnetophoresis (Figure 1.2 b). Negative magnetophoresis operates as a label-free method and separates diamagnetic particles such as cells in a paramagnetic medium (e.g., ferrofluids) [57]. The diamagnetic particles in the ferrofluids act as magnetic holes, and when exposed to an external magnetic field, the imbalance of particle and fluid susceptibility creates a negative magnetophoretic force, dragging the particles away from the magnet. This force is also proportional to the particle size, enabling size-based separation [93, 94]. Conversely, positive magnetophoresis allows paramagnetic particles to accumulate at magnetic field maxima in a diamagnetic medium, facilitating the separation and manipulation of biological samples like oxygen-poor or infected red blood cells [95, 96], magnetotactic bacteria [97], or cells specifically labeled with MNPs [98].

Magnetophoresis is not only based on the classical theory, as displayed in Equations 1.2, 1.6, 1.7, but the movement of magnetic entities in an inhomogeneous field is also influenced by two more phenomena. Leong et al. showed that the separation times of superparamagnetic nanoparticles are substantially quicker (by a factor of about 30) than theoretical predictions applying Equation 1.7 [99]. This increase in separation efficiency is influenced by particle concentration and their dispersion within the solution, meaning that separation velocity increases with particle concentration; furthermore, they revealed that under the assumption of spatially homogeneous concentration, which solely accounts for the magnetic field gradient, there is a temporal decrease in concentration. They presented two primary mechanisms to explain their observations: Magnetic aggregation [100] and magnetic-induced convection [101, 102] (Figure 1.4). Magnetic aggregation is based on magnetic dipole interactions, leading
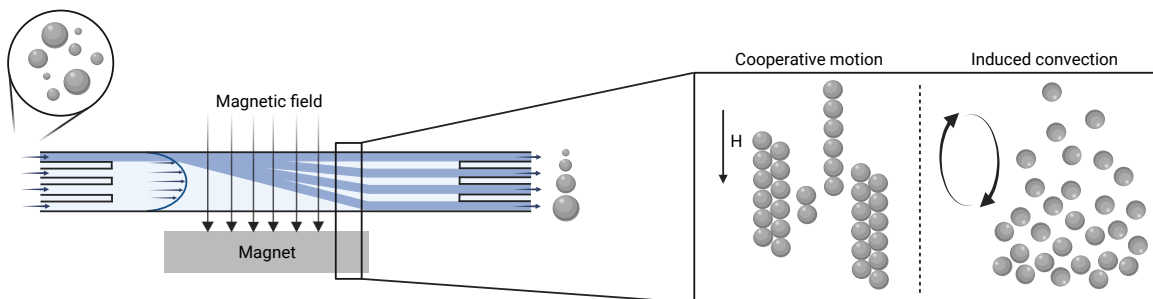
Figure 1.4: Magnetophoresis-based fractionation in a laminar flow channel: Entities with varying magnetic susceptibilities experience a magnetic force when passing the inhomogeneous magnetic field by flowing through the channel. The deflection is increased by an increased magnetic moment because of interacting dipoles, resulting in agglomeration (cooperative magnetophoresis). Because of the inhomogeneous magnetic field, the entities near the magnet experience a larger force compared to those further away, resulting in a concentration gradient inducing a hydrodynamic instability, which leads then to an induced convective motion. Adapted from [66].

to the formation of elongated particle structures aligned with the magnetic field, thereby accelerating magnetophoretic movement [100, 103]. This is quantified by the aggregation parameter N^*, defined as:

$$N^* = \sqrt{\phi_0 \cdot e^{(\Gamma-1)}} \tag{1.8}$$

where ϕ_0 is the initial volume fraction of the MNPs, and Γ is the magnetic coupling parameter given by

$$\Gamma = \frac{\mu_0 \cdot m^{*2}}{2 \cdot \pi \cdot d^3 \cdot k_B \cdot T} \tag{1.9}$$

where μ_0 is the magnetic permeability of free space, m^* presents the induced magnetic dipole, d is the particle diameter, k_B is the Boltzmanns constant, and T the temperature. The critical threshold is $N^* = 1$, as for $N^* > 1$, the particles will start forming chains and bundles, whereas for $N^* < 1$, the thermal energy is stronger than the magnetic interaction.

Magnetic-induced convection is driven by the inhomogeneous magnetic field because entities near the magnet experience a larger magnetic force compared to ones further away from the magnet. Thus, a local concentration gradient is generated and results in a convection flow that further speeds up particle movement [66, 104, 105]. This is characterized by the Grashof number Gr_m, given by

$$Gr_m = \frac{\rho \cdot \nabla B \cdot \left(\frac{\delta M}{\delta c}\right)_H \cdot (c_s - c_\infty) \cdot L^3}{\eta^2} \tag{1.10}$$

where c_s and c_∞ are the particle concentrations at the collection plane and in the bulk solution, respectively [66].

Magnetophoresis-based Cell Separation

In designing a magnetophoresis-based cell separation or fractionation process, not only the classical theory of magnetophoresis (Equation 1.7) has to be taken into account, but also magnetic aggregation (Equation 1.8) and magnetic-induced convection (Equation 1.10). Both phenomena speed up the movement of the magnetic entities in the magnetic field; furthermore, crosslinkage due to magnetic aggregation or turbulences induced by magnetic-induced convection could decrease the separation efficiency. Nevertheless, keeping these characteristics in mind, the advantages are promising. The process is non-invasive, as the magnet does not contact the flow or the sample, and the magnetic force does not affect cell viability or depend on surface charges, ionic strength, or pH of the medium. It is faster, more specific, and less expensive compared to electrophoresis [106]. However, a significant disadvantage is that

most cells lack intrinsic magnetic susceptibility and must be labeled with MNPs in order to manipulate them in a magnetic field. [107, 108]

The labeling with MNPs has to be specific so that cells with distinct characteristics or special exposed epitopes are targeted. The magnetic labeling is achieved through affinity or covalent binding, where ligands such as proteins, antibodies, or synthetic agents like aptamers and peptides can bind to the MNPs but also to the cell, having specific characteristics [11, 60, 109]. It is essential that the entire surface of the MNP is covered to prevent non-specific binding to the cells. Additionally, magnetic labeling methods encompass also direct endocytosis of MNPs for separating cell types like magnetic macrophages from non-magnetic monocytes [48], or the integration of reporter genes that express surface markers for MNP binding following DNA internalization [110].

There are many different designs for magnetophoresis-based cell separation or fractionation processes often tailored for a specific application. In general, parameters such as flow rate, magnet distance, and concentration of magnetic entities are optimized for each process, depending on the MNPs used, labeling methods, and generated magnetic field gradients [48, 57, 111, 112]. Innovations in channel geometry, such as transitioning from classical rectangular to trapezoidal shapes, help in directing less magnetically labeled entities towards regions of higher field gradient [94, 113]. Other proposed designs, such as H-, Y-, U-, and L-shaped channels, are further discussed in [57]. Besides using magnets for sample focusing [108], the introduction of a sheath fluid for hydrodynamic focusing narrows the sample stream, ensuring a consistent magnetic field gradient across the entire sample, which is crucial since the field gradient decreases exponentially with distance from the magnet [95]. Furthermore, multi-step approaches enhance separation efficiency, aiming to reduce the unwanted drag of non-labeled cells by magnetically labeled ones, resulting from magnetic-induced convective motion [98].

1.2.2 Size-based Cell Sorting

Microfluidic size-based cell separations like deterministic lateral displacement, hydrodynamic (pinch-flow fractionation), and inertial (spiral) microfluidics have been developed for multi-cell sorting and are versatile, operating in both passive label-free and labeled modes (Table 1.1). This technology is particularly effective when dealing with cell populations with variations in size or shape. For instance, yeast cells increase in size as they age [109, 114], and the shape of live blood cells differs significantly from that of sickle cells [115]. While deterministic lateral displacement suffers from cell clogging and low throughput, pinch-flow fractionation has evolved to be promising as it can be combined with other separation

techniques [33]. Spiral microfluidics is constrained by channel geometry and a limited flow rate range, and it can only sort particles based on size differences, not on other characteristics like magnetization. In the following, the latter two are explained in more detail, as pinch-flow fractionation can be combined with magnetophoresis, and spiral fractionation is a complete label-free alternative.

Pinch-flow Fractionation

Pinch-flow fractionation (Figure 1.5 a) is a hydrodynamic method where inertial forces play a key role [36]. First presented in 2004 by Yamada et al., this process involves a flowing stream of cells being 'pinched' by a narrow channel cross-section, typically at a T-junction, where they are pressed against one side of the channel by a sheath fluid. The cells' center of mass is positioned at varying distances from the wall, leading to size-based separation as the channel widens and cells follow the hydrodynamic streamlines of the laminar flow profile [22, 24, 36, 107]. Factors influencing separation performance include flow rate ratios, pinched section width, boundary angle, total flow rate, and the geometry of the cell collection area [36]. The design has improved with asymmetric pinch-flow fractionation, which increases particle
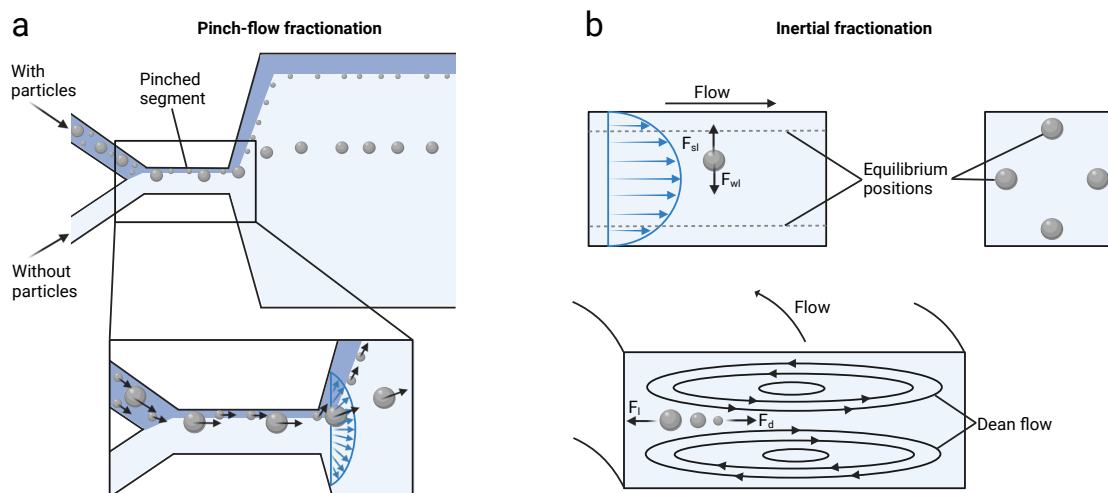
Figure 1.5: (a) Scheme of pinch-flow fractionation: Particles are pinched against the wall in the narrow segment due to a sheath fluid. They are separated according to their size due to the spreading flow profile, as their center of mass differs in their position. (b) Scheme of spiral (inertial) fractionation: Forces on particles in a straight channel result in four equilibrium positions due to counteracting shear-induced (F_{sl}) and wall-induced (F_{wl}) lift forces. In a curved channel, the randomly dispersed particles find their equilibrium positions by their size under the influence of the drag (F_d) and lift (F_l) force within the Dean flow. Adapted from [36, 116].

displacement by altering resistance and flow velocity through broadening and shortening outlet channels. This innovation enabled the separation of particles between 1 µm and 2.1 µm

with an efficiency of 80% [117] compared to 15 and 30 µm before by Yamada et al. [36]. Further enhancements in separation efficiency have been achieved through the introduction of microvalves for precise flow control [118]. This size-based fractionation can also be further improved by combining it with other forces such as sedimentation [119], centrifugal [120], optical [121], and dielectrophoretic forces [122]. Inertia-enhanced pinch-flow fractionation, which elongates the pinch flow segment to increase the lateral distance of the particles due to lift force, could increase the throughput from 2.5×10^4 particles min^{-1} [36] to 1.67×10^5 particles min^{-1}, allowing for higher sample flow rates relative to the sheath flow (often being up to 1:30), thus reducing sample dilution [123].

Recent applications of pinch-shaped channels in cell-based applications include the separation of spermatozoa from erythrocytes [37] and the removal of viruses from semen [124] in a classical pinch-shaped channel; however, the throughput was relatively low with 2.5×10^4 cells min^{-1} and 8.5×10^5 cells min^{-1}, respectively. In another application, low-abundance cells, like circulating tumor cells, have been successfully isolated from diluted blood. By using their size and shape differences, cells were focused in high aspect-ratio microchannels coupled with pinch sections processing 10^8 cells min^{-1} [125]. All these applications have in common that they separate a heterogeneous cell sample into two fractions, having cells with large size and/or shape differences.

The integration of pinch-flow with magnetophoresis offers a finer fractionation, as it combines size and magnetic susceptibility as separation criteria. This combination is particularly beneficial for cells with varying sizes or shapes, where the overall magnetic susceptibility changes. Using these two separation principles, Kumar et al. developed a microfluidic device for the fourplex fractionation of magnetic (5, 11, and 35 µm) and non-magnetic (10 − 19 µm) microparticles, having a high throughput of 1.67×10^7 particles min^{-1} [81]. Both positive and negative magnetophoresis are employed for hydrodynamic separation based on size differences [111]. Zhu et al. demonstrated this by successfully separating label-free yeast from *E. coli* cells in a ferrofluid, achieving a throughput of 1.67×10^4 cells min^{-1} [126].

However, it is important to note that the highest throughput in such systems is achieved when two separation criteria are applied: Size selection alone requires a significant size difference between particles or cells.

Spiral Sorting

Another passive approach, inertial separation technology like a spiral sorter, uses only fluid dynamics to manipulate particles or cells at a high flow rate according to size differentiation. This is achieved through the application of a radially force, known as the Dean force, which acts on fluid traversing a curved channel (Figure 1.5 b). This force arises due to a pressure

gradient created by the differential path lengths of fluid on the inside and outside of the curve, leading to the formation of two counter-rotating vortices (= Dean vortices). These vortices, normal to the angular velocity, form into a top and a bottom vortex, each occupying half of the channel [127, 128].

The strength of this secondary flow is quantified by the dimensionless Dean number De, expressed as

$$De = Re \cdot \sqrt{\frac{D_h}{2R}} \tag{1.11}$$

where R is the radius of curvature and D_h the hydraulic diameter. The average Dean flow velocity u_D for a given De is described by $u_D = 1.8 \cdot 10^{-4} \cdot De^{1.63}$ [128]. Upon the introduction of particles or cells into the microfluidic system, they are subjected to the influence of transverse secondary Dean flows, which effectively guide them into one of the two Dean vortices. Once within these vortices, the particles or cells are dynamically entrained [127]. To quantify the drag force exerted on these particles by the Dean flows, Stokes' law is applied. This dean drag force, denoted as F_d can be calculated using the formula

$$\vec{F_d} = 3 \cdot \pi \cdot \eta \cdot \vec{u_D} \cdot d. \tag{1.12}$$

Additionally, particles are subjected to a net lift force resulting from the shear-induced and wall-induced inertial lift forces, F_{sl} and F_{wl} [129]. In laminar flow, the parabolic velocity profile generates a shear-induced inertial lift force, leading the particles away from the microchannel's center. This force is counterbalanced by the wall-induced inertial lift force, which intensifies as particles near the wall, pushing them away from it. These opposing forces create equilibrium positions along the fluid channel's cross-section (Figure 1.5 b) [129, 130]. In a rectangular cross-section, four equilibrium positions are found [131].

The net lift force (shear- and wall-induced) in relation to the particle position across the cross-section is described as

$$\vec{F_l} = \frac{\rho \cdot \vec{u}_{max}^2 \cdot d^4}{D_h^2} f_l(Re_c, x) \tag{1.13}$$

where $\vec{u}_{max} = 2 \cdot \vec{u}$ is the maximum fluidic flow rate and $f_l(Re_c, x)$ is the lift coefficient, depending on the position x of the particles and here, the Reynolds number $Re_c = \rho \cdot \vec{u}_{max} \cdot D_h/\eta$, displaying the ratio of inertia force to viscosity [116].

The equilibrium of these forces within curved fluidic channels is fundamentally governed by the interplay between $\vec{F_d}$ (Equation 1.12) and the $\vec{F_l}$ (Equation 1.13). Near the outer wall, these forces act in a cumulative manner, whereas in the vicinity of the inner wall,

they effectively counteract each other, thereby inhibiting any further lateral movement of the particles [127]. This dynamic equilibrium leads to a notable reduction in the number of equilibrium positions from four to a singular position proximal to the inner wall of the channel [132]. Both forces are dependent on the particle diameter ($\vec{F_d} \sim d$ and $\vec{F_l} \sim d^4$) leading to different equilibrium positions for particles of varying diameters [127, 133]. Consequently, this effect enables the separation of particles based on size, with larger particles being significantly influenced by $\vec{F_l}$, pushing them near the inner wall, while smaller particles tend to find their equilibrium position closer to the outer wall after a certain channel length (Figure 1.5 b) [127, 132]. The height of a microchannel influences the formation of a single particle stream, whereas its width predominantly affects the inter-stream spacing. Consequently, wider channels lead to greater separation between particle streams, facilitating the differentiation of particles with similar diameters [134]. If $\vec{F_d} >> \vec{F_l}$, no particle focusing is possible, as particles are entrained in the Dean vortices. Conversely, if $\vec{F_d} << \vec{F_l}$, all particles are focused at the same position. Other experimentally determined thresholds for particle equilibration are $d/D_h > 0.07$ and $Re_c > 0.04$, thereby defining the maximum channel geometries for given particle diameters [116]. Below this value, $\vec{F_d}$ exerts $\vec{F_l}$, and another threshold is set to $De > 20$, resulting in a similar effect [131].

Spiral sorters are getting more attention due to their high throughput, label-free properties, and ease of integration into existing systems, making them also potentially usable for process intensification in downstream processing [135]. In a diverse range of applications, the optimization of channel geometry plays a crucial role. This was exemplified in the work of Chiu et al., who successfully isolated B and T cells (7 – 8 µm) from natural killer cells (12– 15 µm). They systematically evaluated various aspect ratios, identifying a channel dimension of 100 x 500 µm as the most effective, resulting in an impressive throughput of 1.3×10^5 cells min^{-1} [136]. For fractionating cells or particles with larger size discrepancies, trapezoidal channels are preferred [137, 138], although these channels primarily focus on larger particles while smaller ones remain in the Dean vortices, which are pushed to the outer wall due to the trapezoidal design. Further advancements include the insertion of trapezoidal cavities to enhance the focusing of *Saccharomyces* cells, though a fractionation has still not been achieved [139]. 3D printing technology has enabled the creation of vertical spirals with constant channel radius, maintaining uniform Dean forces throughout the channel [138]. Commercial chips with various channel dimensions were tested by Natu et al. using particles ranging from 2 – 20 µm in diameter. Their study analyzed focusing and separation behavior based on multiple parameters, such as flow rate, repeatability, blockage, hydraulic diameter, and the confinement ratio of d/H. Generally performing as expected, reaching throughputs between 10^5 – 10^8 particles min^{-1}, issues like clogging and inlet tube leakages negatively influenced the overall performance [140]. In a comprehensive overview, Xu et al. and Shiriny et al. provide existing channel designs and modes for cell and particle separation [116, 141].

Despite the advantages of spiral sorters, challenges persist, such as the fragile balance of forces, dependence on various process parameters, and difficulties in focusing particles with widely varying diameters in a single channel, impacting selectivity [135, 137, 140]. Future advancements may involve integrating inertial technology with other active or passive separation methods to improve purity and efficiency [142]. Current devices are often specialized for specific applications, leading to a lack of universally applicable spiral sorters [116].

1.2.3 Milli- and Microfluidic Fabrication Methods

For microfluidic device fabrication, the creation of milli- and microstructures is a complex challenge, constrained by specific requirements such as the resolution and the challenges associated with handling small sizes [6]. These fabrication methods are broadly classified into two categories: Non-additive and additive manufacturing methods, with the latter commonly known as 3D-printing (Table 1.2) [24, 143].

Non-additive manufacturing methods, such as molding, are commonly used and extensively optimized [24, 144, 145]. Molding includes replica molding, like soft lithography, where a master pattern is created on a silicon wafer using a photomask and photoresist, typically SU-8. The mold is replicated using polydimethylsiloxane (PDMS), subsequently bonded to a glass cover. Injection molding uses a master form, where a heated thermoplastic like polymethylmethacrylate (PMMA) is cooled and compressed around the form, whereas hot embossed replication presses the hot thermoplastic onto the master fold, both followed by thermal bonding [144]. Other common fabrication methods include glass capillaries, etching, laser ablation, and mold fabrication methods [24, 144].

Stereolithography, an additive manufacturing method, employs a high-intensity laser to polymerize photopolymerizable materials, like nylon, polypropylene, and resins, building a 3D structure in a layer-by-layer fashion. The size of the laser spot limits the resolution of this method. To enhance fabrication speed, projections of digital light spots from light-emitting diode (LED) sources are used to polymerize entire layers simultaneously. Here, the resolution depends on the pixel size of the LED sources. Extrusion-based methods, such as fused deposition modeling, involve extruding flowable precursors like melted thermopolymers through a nozzle, sequentially solidified (filament-based). Alternative approaches are non-filament-based and use hydrogels, powders, or pellets. Inkjet printing is another variant, where photopolymer-based inkjet printing uses a computer-controlled array of inkjet heads to dispense and UV-cure liquid acrylate-based photopolymers, differing in support materials such as wax or acrylic monomer mix. In contrast to classical stereolithography, where a large light source cures an entire layer of resin, two types of inkjet printing offer more precise

control. Photopolymer-based printers cure photopolymers with targeted UV through inkjet heads. Powder-based inkjet 3D printing, also known as binder jetting, selectively binds powder material (e.g., ceramics, metals) layer-by-layer using a binding agent but is less suited for fabricating polymer-based microfluidics. Two-photon polymerization achieves nanoscale resolution by employing direct femtosecond laser writing. [6, 143, 144, 146]

Direct printing methods, producing the chip in one piece, are fast but face challenges in removing non-polymerized resin and achieving optical transparency. Hybrid approaches, such as sealing open structures with adhesive tape or PDMS, are employed to mitigate these limitations [44, 146]. Alternatively, 3D printing can be used for non-sacrificial mold production, significantly reducing the time for fabricating devices compared to traditional methods like soft lithography [143].

3D printing, in general, especially stereolithography, offers a convenient, rapid, and cost-effective alternative to traditional soft lithography methods like PDMS molding for producing microfluidic devices. Stereolithography excels in creating complex three-dimensional structures beyond the capabilities of PDMS [147]. Although its minimum resolution is limited by laser beam diameters of approximately 100 µm, however, most of the printable channels are larger than 100 µm [143], stereolithography remains more attractive than PDMS/ resin in terms of throughput rates. However, it falls short of the throughput achievable with high-throughput plastic molding techniques like injection molding. Despite this, stereolithography is particularly accessible for personnel without expert knowledge of fabrication methods, which is important when using molding techniques. In contrast, most microfluidic devices are currently developed using PDMS due to their low cost and suitability for biomedical applications, with their design cycles generally adequate for prototype development [24]. Nevertheless, PDMS molding is slow and unsuitable for high- or medium-volume production, essential for commercialization. While high-throughput techniques like injection molding exist, their high mold and equipment costs are prohibitive, particularly for small startups or research [148]. Additive manufacturing is an automated method that can produce a wide range of 3D shapes in a single material with medium-volume throughput [143]. It has great potential, even if current limitations such as optical transparency, post-processing, surface roughness, bonding, wettability, gas permeability, and sterilization still need to be optimized [143].

Table 1.2: Overview of microfluidic chip fabrication methods. Resolution refers to the minimum channel width for the direct printing approach. [6, 143–145]

Technique	Resolution	Advantages	Disadvantages	Application
Stereolithography	20 – 600 μm	Easy processing, flexible design, biocompatible	Clogging, limited materials, post-processing difficulty, low transparency, surface roughness	[149]
Fused deposition modeling	40 – 1000 μm	Easy processing, flexible design, low cost, robust	Low resolution, fragile, low transparency, surface roughness, limited materials	[150]
Non-filament based	635 – 1000 μm	Flexible design, biocompatible, high resolution, high-throughput	Limited materials, expensive, low transparency, surface roughness, low resolution	[151]
Inkjet printing: Photopolymer-based	130 – 400 μm	High-resolution, multi-material printing, flexible design	Limited materials, post-processing difficulty, surface roughness, low transparency, high cost	[152]
Inkjet printing: Powder-based	130 – 400 μm	Suitable for metals/ ceramics, multi-material printing, no support structures needed	Clogging, time-consuming post-processing, low transparency, surface roughness	[153]
Two-photon polymerization	0.1 – 1 μm	High-resolution, flexible design	Clogging, time-consuming, expensive, limited print volume	[154]
Soft lithography	0.1 – 100 μm	Flexible design, biocompatible, gas permeable, transparent, high resolution, smooth surface	Poor chemical resistance, labor-intense, molecule adsorption, clean room necessary	[155]
Inject molding	0.1 – 100 μm	High-throughput, cost-efficient, high accuracy and resolution, smooth surface	Material restrictions to thermo-plastics, design constraints, expensive mold fabrication	[148]
Hot embossing	0.1 – 100 μm	High-resolution, smooth surface	Material restrictions to thermo-plastics, design constraints, expensive mold fabrication	[156]

1.3 Yeast Cells: An Overview

Yeast cells, predominantly from the species *Saccharomyces cerevisiae*, are single-celled fungi characterized by their eukaryotic nature, possessing a nucleus and other membrane-bound organelles. Yeast is facultatively anaerobic, meaning that it can grow in both aerobic and anaerobic conditions. In aerobic conditions, yeast metabolizes sugar into carbon dioxide and water, a process that is more efficient in terms of energy production, as 32 adenosine triphosphate (ATP) are produced of one sugar molecule. In the absence of oxygen, yeast has the ability to ferment sugar into alcohol and carbon dioxide, but only two ATP are yielded from one sugar molecule. This process is known as alcoholic fermentation and is key for diverse applications in the beverage industry. Even in the presence of oxygen, pyruvate is metabolized to ethanol if the sugar concentration is high enough, known as the Crabtree effect. At low sugar concentrations, the respiratory chain is turned on. [157, 158]

In the beverage industry, strains like *S. pastorianus ssp. carlsbergensis* and *Saccharomyces cerevisiae* are used for alcohol production in beer, wine, and spirits [159]. These strains, classified as top-fermenting (ale yeast, T = 15 – 24°C, e.g., *Saccharomyces cerevisiae*) or bottom-fermenting (lager yeast, T = 7 – 13°C, e.g., *S. pastorianus ssp. carlsbergensis*), contribute significantly to the flavor, aroma, and texture of beverages [2]. Due to their ability to perform post-translational modifications, yeasts are important for producing biopharmaceuticals, including insulin, human growth hormones, vaccines, or other recombinant proteins using strains like *Komagataella phaffi* and *Saccharomyces cerevisiae* in pharmaceutical industry [160]. Similarly, in the baking industry, *Saccharomyces cerevisiae* is essential for bread making, fermenting sugars to produce carbon dioxide and ethanol, which causes the dough to rise and impacts its sensory characteristics [161]. Beyond these applications, yeasts are also key microorganisms in bioethanol production, by fermenting sugars from starch, lignocellulose, or algal biomass sources [158]. Their rapid growth, pH tolerance, robust cultivation in simple media, and genetic engineering potential underscore their industrial significance. In 2024, the global yeast product market was valued at $5.5 billion U.S. dollars, and it will reach $8.5 billion U.S. dollars by 2029 [162].

Their genetic simplicity and eukaryotic nature make them ideal for studying cellular processes in higher organisms, including aging research. Yeasts can act as a model for understanding conserved aging mechanisms, such as DNA damage repair and protein homeostasis, relevant to human aging [1]. Their short lifespan facilitates rapid lifespan analysis, enabling studies on aging and longevity interventions [3, 163, 164]. In aged yeast cells, there is a decline in glucose uptake, energy metabolism, and fermentation rates, which impairs secondary metabolic processes and ester biosynthesis [109, 165, 166]. That is why a deeper understanding of

the underlying aging mechanisms is necessary to develop strategies counteracting these age-associated functional declines.

1.3.1 Yeast Cell Division and Aging

According to Herskowitz, in the asymmetric cell division of yeast, known as budding, the cell cycle is divided into four distinct phases. During the G1 phase, the cell undergoes growth and initiates the formation of a bud, preparing for DNA replication. The S phase involves the replication of chromosomes and the initiation of DNA synthesis. In the G2 phase, the cell continues to grow, and the nucleus migrates to the neck of the cell, with chromosomes starting to elongate; nucleus division occurs at the end of this phase. The M phase, or Mitosis, involves chromosome segregation and nucleus division, followed by cell wall separation. Mitosis itself is subdivided into five stages: Prophase, metaphase, anaphase, telophase, and cytokinesis. After the M phase, the mother cell re-enters the G1 phase, starting a new cell cycle and having a bud scar [167]. This bud scar, rich in chitin and glucan, forms during cytokinesis, with a positive correlation observed between the mean number of bud scars and chitin content [114, 168]. The daughter cell has a similar, but chitin-poor ring [169, 170].

During the yeast cell cycle, chitin synthase generates chitin that is incorporated into the lateral walls and forms a chitin ring at the site of the daughter cell, which is essential for establishing the neck diameter between the mother and daughter cells. As the bud grows, it shifts from apical to isotropic growth, leading to the formation of a primary septum of chitin, subsequently covered by a secondary septum. This primary septum is broken down by chitinase, facilitating daughter-cell separation, and leaving a distinct bud and birth scar on the mother and daughter cell, respectively. [2, 169, 171, 172].

The bud scar number is a well-established indicator for off-line age analysis in yeast cells [168, 173, 174]. Fluorescence bud scar labeling allows for offline analysis of the cells' age, first presented by Kurec et al. in 2009 [174]. For that, bud scars are labeled with expensive fluorescent dyes such as Alexa Fluor 488-coupled wheat-germ agglutinin [17, 174], or Calcofluor White [175]. Often, the number of labeled bud scars per yeast cell is investigated via microscopy. This labor-intensive method makes high-throughput analysis of age distributions difficult. The fluorescence of cells can also be measured via cytometry. However, a correlation between fluorescence and microscopically derived bud scar number is necessary [174]. Additionally, the number of bud scars must be calculated afterwards, so a direct age fractionation via FACS is not yet possible [168, 174].

The aging process in yeast encompasses both replicative and chronological life spans (Figure 1.6). The replicative lifespan is defined by the number of divisions a mother cell undergoes

before senescence. The range of 5 to 25 budding events is influenced by genetic background [114, 168, 176, 177]. Chronological lifespan refers to the duration yeast cells can survive in a non-dividing state when deprived of nutrients. Prolonged chronological aging in the stationary phase leads to a decrease in replicative lifespan [178]. Yeast cell aging is affected
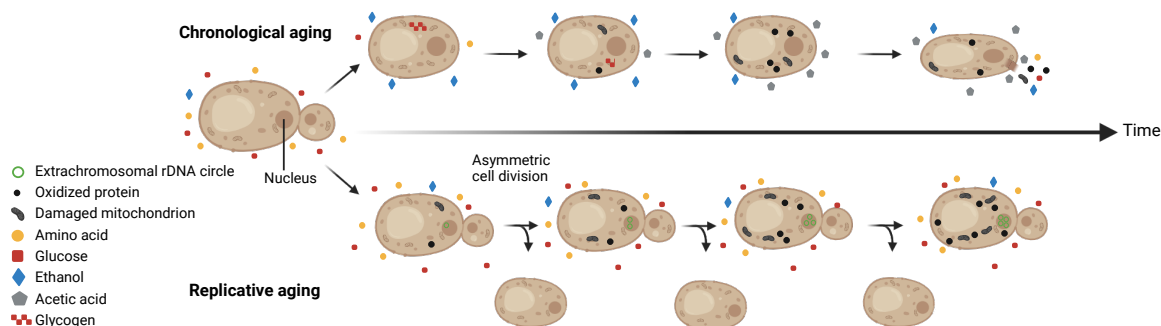
Figure 1.6: Illustration of yeast aging mechanisms: Chronological and replicative aging. Chronological lifespan represents the period yeast cells can endure when deprived of nutrients, triggered by nutrient limitation or external stressors. This phase is marked by increased stress resistance, carbohydrate consumption, a decline in external pH due to ethanol metabolism into acetic acid, protein oxidation, and mitochondrial damage. Upon senescence, the cell lyses. Replicative lifespan, conversely, is determined by the number of cell divisions a mother cell can perform prior to senescence, influenced by factors such as extrachromosomal ribosomal DNA circles, protein oxidation, and mitochondrial damage. Due to the asymmetry in cell division, the daughter cell does not inherit the mother cell's accumulated damages. Adapted from [166].

by endogenous and exogenous stressors, including mutations, oxidative stress, pH stress, and heat stress [3, 166, 179, 180].

Premature cell death can negatively impact fermentation efficiency and quality, but chronological lifespan can be increased by pre-treating cells with nutrient stress during growth, inducing a long-lasting stress response. This adaptation enables cells to more effectively cope with stress conditions, prolonging their lifespan and enhancing cultivation processes [166].

It is important to understand yeast cell aging, as it affects physiology, morphology, gene expression, and consequently, growth during fermentation, which influences sugar uptake, flavor, alcohol production, and flocculation behavior [11, 17]. Concerning age distributions within yeast populations, empirical data [17, 109, 165, 175, 181] differ from theoretical predictions [182], which influences growth during cultivation. Moreover, cell aging influences metabolic activity and protein biogenesis, leading to reduced glucose uptake and metabolic activities for old cells compared to daughter cells [165, 183]. These findings are relevant for brewing or baking industries, where yeast metabolic activity directly affects the production process. Overall, current research indicates clear age-dependent differences in generation

time, metabolic activity, and metabolite formation, underscoring the significant influence of yeast population age distribution on cultivation behavior [17, 165, 174].

1.3.2 Yeast Cell Separation Techniques Based on Age and Size

For a deeper understanding of yeast cell aging, there is a need for age-based separation/fractionation methods, offering the analysis of differently aged cells, but not a whole heterogeneous population. Different methods have been developed, however, most of them work on the analytical scale.

Micromanipulation was the pioneering technique introduced in 1959 by Mortimer and Johnson [176]. This method involves using a micromanipulator to physically separate new daughter cells from mother cells. While it allows for the direct observation of budding events, it is time-consuming and labor-intensive. Moreover, the invasive nature of this technique can damage cells, and its reliance on an arbitrary 2D medium limits its applicability [176].

Centrifugal elutriation, developed in the 1990s, is a mechanical size-based separation method that utilizes centrifugal force and opposed hydrodynamic force. Larger cells are dragged towards the outside of a cone, while smaller cells are moving in the middle due to the counter-flow. However, a significant disadvantage is the shear stress imposed on the cells [184, 185].

Dielectrophoretic separation is particularly effective for separating live and dead cells, but also age-based fractionation is possible. This method uses an electrical field to generate opposing dielectrophoretic forces, leveraging cell geometry for separation [186]. For example, multifrequency dielectrophoresis was used to separate yeast cells in anaphase from a heterogeneous population [187].

Sedimentation in a sucrose gradient is another size-based approach [17]. However, its accuracy is limited as yeast cells grow during their cell cycle and with increasing replicative lifespan [188], and can adapt their size in response to environmental changes [189].

Magnetic separation has been explored through various approaches. On the one hand, the mother cell wall can be biotinylated without inheriting the labeling to daughter cells, allowing only mother cells to bind to streptavidin-coated magnetic beads [190]. On the other hand, genetic enrichment involves inhibiting daughter cell growth with estradiol, facilitating mother cell retention via a MACS system [191]. However, despite the high throughput, the yeast cells have to be genetically modified, and therefore this method is time-consuming. The miniature-chemostat aging device (MAD) improved the magnetic separation, offering high throughput

capabilities up to 10^6 cells min^{-1} and dynamic operation modes, as the daughter cells are eluted, and the retained mother cells can be released by removing the magnetic field [11].

Microfluidics has emerged as a powerful tool for single-cell analysis, enabling live-cell monitoring of physiological changes [192]. For mechanical trapping, mother cells are trapped into pillars [193, 194], between micropads [195], or in cavities [196] while the flow carries away daughter cells. Chemical trapping is performed via mother cell labeling and retention, and daughter cells are flushed away [197]. Despite recent advancements, which increased throughput to 1.9×10^4 cells for one life span experiment [198], the primary limitation of microfluidic yeast cell separation remains the analytical scale.

Apart from age-based separation, other microfluidic approaches also focus on size differentiation of yeast cells. For instance, fractionation based on size and shape in a flow of diluted ferrofluid has been demonstrated, where they distinguished between singlets, duplets, and triplets [199]. In another approach, this fractionation has been reached via a coflowing viscoelastic and Newtonian fluid [200]. However, both methods had low throughputs varying between 75 and 3750 cells min^{-1}.

In summary, various methods have been developed for separating mother from daughter yeast cells, each with its unique advantages and limitations. However, a combined approach that distinguishes precisely between finer, distinct age groups is still not possible. Thus, the ongoing challenge is to develop a method that is both efficient and gentle, ensuring cell viability while providing accurate age-based fractionation.

2 Motivation

Saccharomyces yeast is one of the most important microorganisms. It has been used for beverage production since 7000 B.C., and today it finds its application in the baking industry, for bioethanol production or recombinant protein biosynthesis [1]. Because of these various applications, there is a growing interest in increasing product yields. This can be achieved through methods such as optimizing cultivation parameters [2], metabolic engineering of the strain [9], or investigating the impact of individual cell age on overall productivity [109]. Apart from the industrial applications, *Saccharomyces* serves as a model organism in aging research [1]. Its eukaryotic nature offers profound insights into chronological aging – defined by cell survival time – and replicative aging, characterized by the number of division events a cell can undergo before senescence [163]. This versatility underlines the yeast market's economic footprint, with a valuation of $5.5 billion U.S. dollars in 2024 [162].

The research presented in this thesis introduces a novel approach to performing yeast cell fractionation based on cell age, with the objective of analyzing its impact on metabolic processes and fermentation efficiency. Existing methodologies, predominantly flow cytometry, have been limited to elucidating aspects of the yeast cell cycle without the capability to determine the age of individual cells [174]. Given their analytical scale, further fractionation techniques were based on invasive fluorescence staining or microdissection [4]. Others rely on the correlation between cell size and age [17]. However, this correlation is inconsistent, as cell growth depends not only on age but also on the strain, growth conditions, and growth phase [188]. More established is the method of a binary separation of cells into young daughter cells and old mother cells [165]. The high throughput sorting of yeast cells into different age groups is not provided in current methods [4].

This gap in research methodology inspires the objective of this project: To develop a non-invasive magnetophoretic fractionation process for sorting yeast cells based on their age in high throughput. The primary focus is directed towards the following hypotheses and challenges. Yeast cells, which exhibit more bud scars with increasing age, bind more MNPs via a bifunctional linker-protein [168] capable of binding to yeast cell bud scars on one end, and functionalized magnetic nanoparticles on the other. Four different age fractions ($0, \leqq 5, 5-15,$

> 15 bud scars [114, 168, 176, 177]) of yeast-chitin binding domain (ChBD)-MNP complexes can be magnetically fractionated based on the age-dependent magnetic susceptibility.

For a successful process development, further requirements have to be fulfilled: The binding of functionalized magnetic nanoparticles has to be specific, homogeneous, and non-invasive, targeting only the bud scars through uniformly sized agglomerates to ensure the correlation between age and magnetic susceptibility. That is why the initial stages of the project will involve designing nanoparticles, analyzing bare iron oxide nanoparticles (BION) and ION@Si@EDTA for their agglomeration behavior with and without a magnetic field, and evaluating the specificity and cross-linkage of binding by different yeast-ChBD-MNP ratios (Section 4.1, 4.2).

To enable growth and omics studies, the process was designed at a millifluidic scale for high-throughput fractionation into the four distinct age groups. 3D printing will be used for chip production, favoring its simplicity and adaptability over traditional microfluidic methods [143, 145]. However, the larger scale of this fractionation process will require the assurance of high separation selectivity. Due to the size difference, both hydrodynamics and diffusion should not be significantly altered by the bound MNPs. However, due to the milliliter volumes, the magnetic-induced convection in the millifluidic channel, leading to a potential co-migration of non-labeled daughter cells, should be analyzed (Section 4.4, 4.5). Different chip geometries will be tested to achieve high separation selectivities. A preceding simulation-based approach will support the experimental optimization by investigating the required magnetic field. As an alternative to magnetophoretic fractionation, a label-free, size-based approach will be explored (Section 4.3).

Due to the analytical scale of yeast cell sorting, there is a lack of data regarding the distribution of actual cell age under conditions of stress-induced fermentation and how this age distribution correlates with fermentation performance. This includes understanding the interplay between yeast cell age, viability, vitality, and population dynamics. Furthermore, no information is yet available on the expression of stress-related genes and viability in relation to the age of yeast cells. Closing these research gaps could provide deeper insights into the complex interactions within yeast cell populations during fermentation, potentially leading to enhanced fermentation strategies (Section 4.5).

3 Publications

3.1 The Effect of pH and Viscosity on Magnetophoretic Separation of Iron Oxide Nanoparticles

3.1.1 Summary and Author Contribution

MNPs are widely used in biotechnology and biomedicine, where the medium is of higher viscosity, such as blood in drug delivery or fermentation broths following cultivation. Besides the specific targeting, the colloidal stability and the ability for separation at low magnetic field gradients, typically below 100 T m^{-1}, are important criteria in the application for the mentioned industries. BIONs tend to agglomerate to reduce their surface area for entropic reasons; however, this study shows that agglomeration can be influenced by pH and viscosity. At the same time, the magnetic separation abilities are influenced by the agglomerate's sizes, shown by magnetophoretic sedimentation experiments.

Characterization of the BIONs via transmission electron microscopy (TEM) and super-conducting quantum interference device (SQUID) measurements revealed primary particle diameters of 9.92 nm and a saturation magnetization of 70.84 A m^2 kg^{-1}. The investigation showed that, at the isoelectric point where BIONs attain neutral charge, agglomerates with sizes of up to 3000 nm were formed. Only under pH values below pH 5 and above pH 8, where the zeta potential was below -20 mV or exceeded 20 mV, agglomerate sizes diminished to below 500 nm. Moreover, in solutions with 2.5× higher viscosity than water, these smaller agglomerates formed at pH values less than pH 5 and greater than pH 6. This enhanced colloidal stability was attributed to increased viscosity, potentially resulting from hydration effects or the adsorption of hydroxyl groups. The magnetophoretic sedimentation velocity directly correlated with increasing agglomerate size and was inversely proportional to viscosity. Thus, colloidal stability and viscosity introduce a complex interplay affecting the motion of BIONs, which is additionally influenced by phenomena such as magnetic aggregation, magnetically induced convection, and Brownian motion.

In sum, this work offers a comprehensive overview of the interplay between colloidal stability, surface charge, agglomeration, and viscosity, which influences the separation capabilities of low-gradient magnetic separation processes. These findings provide valuable insights in biotechnology and biomedicine, with implications for applications like cell sorting and drug delivery processes.

The doctoral candidate contributed substantially to this study by conceptualizing and designing the experiments. Following a critical review of the existing literature, she executed out the main part of the presented experiments, analyzed the complete data, and wrote the manuscript. Chiara Turrina was responsible for synthesizing the BIONs used in the work. All authors critically reviewed the manuscript.

3.1.2 Article

Article

The Effect of pH and Viscosity on Magnetophoretic Separation of Iron Oxide Nanoparticles

Leonie Wittmann [iD]**, Chiara Turrina** [iD] **and Sebastian P. Schwaminger ***[iD]

Bioseparation Engineering Group, Department of Mechanical Engineering, Technical University of Munich, Boltzmanstr. 15, 85748 Garching bei München, Germany; l.wittmann@tum.de (L.W.); c.turrina@tum.de (C.T.)
* Correspondence: s.schwaminger@tum.de

Abstract: Magnetic nanoparticles (MNPs) are used for magnetophoresis-based separation processes in various biomedical and engineering applications. Essential requirements are the colloidal stability of the MNPs and the ability to be separated even in low magnetic field gradients. Bare iron oxide nanoparticles (BIONs) with a diameter of 9.2 nm are synthesized via coprecipitation, exhibiting a high saturation magnetization of 70.84 $Am^2 kg^{-1}$ and no remanence. In our study, zeta potential, dynamic light scattering (DLS), and sedimentation analysis show that the aggregation behavior of BIONs is influenced by pH and viscosity. Small aggregate clusters are formed with either low or high pH values or increased viscosity. Regarding magnetophoresis-based separation, a higher viscosity leads to lower magnetophoretic velocities, similar to how small aggregates do. Additionally, cooperative magnetophoresis, the joint motion of strongly interacting particles, affects the separation of the BIONs, too. Our study emphasizes the effect of pH and viscosity on the physicochemical characteristics of MNPs, resulting in different aggregation behavior. Particularly, for high viscous working media in downstream processing and medicine, respectively, the viscosity should be taken into account, as it will affect particle migration.

Keywords: magnetophoresis; magnetic separation process; iron oxide nanoparticles; aggregation; pH; viscosity; sedimentation analyzer; zeta potential; hydrodynamic diameter

1. Introduction

Magnetic nanoparticles (MNPs) have become an important nanomaterial in biotechnology, in chemistry, and in medicine [1–6]. They entail characteristics such as biocompatibility, high binding capacities, and cost-efficient production via coprecipitation. Moreover, their superparamagnetic properties are advantageous during the separation process, as the MNPs show no remanence at room temperature. However, when applying a magnetic field, they possess a high magnetic susceptibility and can be easily separated [7,8]. For biological samples, it is challenging to separate a target entity from a complex mixture with different components. Here, magnetophoresis-based processes provide a simple and efficient method, where the desired entity (magnetic or magnetically labeled with MNPs) is isolated by applying an external magnetic field [9–11]. For the method of High Gradient Magnetic Separation (HGMS), a suspension containing the magnetic material is pumped through a separation chamber, and it is trapped by a magnetically susceptible matrix due to high magnetic field gradients (10^2–10^4 T m^{-1}) [9,11,12]. In contrast, low magnetic field gradients (<100 T m^{-1}) are used for Low Gradient Magnetic Separation (LGMS), where a magnet is placed outside the particle suspension without contacting the particles [13]. Both modes of operation can be realized with either a permanent magnet or an electromagnet. However, the latter brings up several challenges. The installation costs are higher than a permanent magnet, and cooling might be necessary to counteract the Joule heating. Thus, water usage is required besides energy consumption [14]. Therefore, a permanent magnet might be preferred in the biomedical field. Moreover, in microfluidics, the implementation

3.2 Magnetophoresis in Microfluidic Applications: Influence of Magnetic Convection in Hydrodynamic Fields

3.2.1 Summary and Author Contribution

In the fields of biomedicine and biotechnology, magnetophoretic separation processes miniaturized on lab-on-a-chip platforms have emerged as useful techniques. These platforms are advantageous due to their minimal sample volume requirements, accelerated analysis time, enhanced sensitivity, and selectivity. Typically, these microfluidic devices operate at low Reynolds numbers, ranging from 10^{-6} to 10. A major challenge in utilizing MNPs in these contexts is the lack of a comprehensive theory to predict and understand their motion in magnetic fields.

The experimental setup of this study employed a millifluidic, rectangular channel. The findings demonstrated high and constant separation efficiencies for non-magneto-responsive nanoparticles (fluorescent silica nanoparticles) with increasing Péclet number. However, at lower concentrations of magneto-responsive nanoparticles (silica-coated iron oxide nanoparticles), the separation efficiency diminished. As their concentration increased, the efficiency improved due to enhanced dipole-dipole interactions leading to an increased magnetic dipole moment. In a mixture of both nanoparticle types, the presence of non-magneto-responsive nanoparticles did not affect the separation efficiency of the magneto-responsive ones when increasing magnetic field strength. Conversely, the separation efficiency of non-magneto-responsive nanoparticles decreased with rising magnetic field strength. Despite this, the process purities of the magneto-responsive nanoparticles remained constant, even as their separation efficiency improved with increasing Péclet number. This indicated that non-magneto-responsive nanoparticles were dragged along by the magneto-responsive ones. That effect is attributed to the hydrodynamic force induced by the magneto-responsive nanoparticles. Increasing the shear by increasing the volumetric buffer flow enhanced separation efficiency and reduced diffusive effects onto non-magneto-responsive nanoparticles. However, in mixtures containing both particle types, the purity of magneto-responsive nanoparticles was compromised due to increased shear counteracting the magnetophoretic force.

Large-scale Brownian motion simulations, extending beyond the experimentally tested parameters, affirmed that this convective motion was intrinsic to the system's dynamics and remained consistent across varying particle concentrations and magnetic field gradients. The simulations suggested that reducing the magnetic field gradient minimized the average velocity of non-magneto-responsive particles in the field direction, but this also decreased the responsiveness of magneto-responsive particles, leading to lower separation efficiency.

In summary, this study's experimental and simulative results underscore the significant impact of the motion of magneto-responsive nanoparticles on the separation efficiency and purity of both nanoparticle species in microfluidic systems. The hydrodynamic motion induced by magneto-responsive nanoparticles substantially influences the separation process. To mitigate the magnetic-induced convection of non-magneto-responsive entities, a practical approach might involve a multi-step process, including a prior static batch separation, to reduce their concentration, enhancing overall separation efficiency and purity.

The substantial contributions of the doctoral candidate were the conceptualization and design of all the experiments. She carried out all the experiments together with Laura Westphal and Julia Schaupp. The doctoral candidate analyzed the experimental data. Emily Krucker-Velasquez contributed equally to the manuscript by designing, executing, and analyzing the simulations. The doctoral candidate served as the leading author writing the manuscript, excluding the sections related to the simulations. All authors critically reviewed the manuscript.

3.2.2 Article

Check for updates

Influence of magnetic convection on separation efficiency in magnetophoretic microfluidic processes: a combined simulation and experimental study†

Leonie Wittmann, [ID] ‡[a] Emily Krucker-Velasquez, [ID] ‡[b] Julia Schaupp,[a] Laura Westphal,[a] James W. Swan, [ID] §[b] Alfredo Alexander-Katz, [ID] [c] Martin Z. Bazant, [ID] [b] Sebastian P. Schwaminger [ID] *[a,d,e] and Sonja Berensmeier [ID] [a,f]

This work explores the complex hydrodynamics in magnetophoretic microfluidic processes, focusing on the interplay of forces and particle concentrations. The study employs a combined simulation and experimental approach to investigate the impact of magnetophoresis on magneto-responsive nanoparticles (MNPs) and their environment, including non-magneto-responsive nanoparticles (non-MNPs) in a microfluidic system. Our findings reveal that the motion of MNPs induces a hydrodynamic convective motion of non-MNPs, significantly affecting the separation efficiency and purity of the particles. The separation efficiency of MNPs increases with the Péclet number, reflecting the increase in the magnetophoretic force, but decreases with lower concentrations. Conversely, non-MNPs exhibit high and constant separation efficiency with increasing Péclet number, independent of the magnetophoretic force. In a mixture, the separation efficiency of non-MNPs decreases, suggesting that non-MNPs drag along MNPs. The Mason number, representing the ratio between shear and magnetophoretic force, also plays a crucial role in the separation process. The results underscore the need for careful control and optimization of the Péclet and Mason numbers, as well as particle concentrations, for efficient magnetophoretic microfluidic processes. This study provides valuable information on the underlying principles of magnetophoresis in microfluidic applications, with implications for biochemistry, biomedicine, and biotechnology.

1 Introduction

In recent years, the development of lab-on-a-chip platforms has garnered significant attention in the field of biomedical research, including disease diagnosis, drug development, and personalized medicine. These miniaturized analytical devices offer a range of advantages over traditional laboratory techniques, including reduced sample volumes, faster analysis times, and improved sensitivity and selectivity.[1,2]

The basic principle of a lab-on-a-chip platform involves the integration of multiple laboratory functions onto a single microchip, allowing the parallel processing of multiple samples having a high degree of controllability and optimization. This integration is achieved through the use of microfluidics, which enables manipulation at the microscale level[2,3] and precise control of fluid flow with low Reynolds numbers[4] ranging from 10^{-6} to 10. Using microfluidic technology, lab-on-a-chip platforms are capable of performing a range of functions, including magnetophoresis-based cell sorting and detection,[5] DNA sequencing,[6] and protein analysis.[7] The potential impact of lab-on-a-chip platforms in biomedical research is huge. For example, using them for point-of-care diagnostics could greatly improve access to medical care in low-resource settings, where traditional laboratory techniques are often prohibitively expensive or logistically challenging.[8,9] Similarly, performing high-throughput drug screening on a microfluidic platform could greatly accel-

[a]Technical University of Munich, TUM School of Engineering and Design, Chair of Bioseparation Engineering, Boltzmannstr. 15, 85748 Garching, Germany. E-mail: s.schwaminger@tum.de

[b]Department of Chemical Engineering, Massachusetts Institute of Technology, Cambridge, Massachusetts 02139, USA

[c]Department of Materials Science and Engineering, Massachusetts Institute of Technology, Cambridge, Massachusetts 02139, USA

[d]Medical University Graz, Otto-Loewi Research Center, Division of Medicinal Chemistry, Neue Stiftingtalstr. 6, 8010 Graz, Austria. E-mail: sebastian.schwaminger@medunigraz.at

[e]BioTechMed-Graz, Mozartgasse 12, 8010 Graz, Austria

[f]Technical University of Munich, Munich Institute of Integrated Materials, Energy and Process Engineering, Lichtenberstr. 4a, 85748 Garching, Germany

† Electronic supplementary information (ESI) available. See DOI: https://doi.org/10.1039/d4nr02225d

‡ These authors contributed equally to this work.

§ Deceased author.

3.3 Studying the Impact of Cell Age on the Yeast Growth Behaviour of *Saccharomyces pastorianus var. carlsbergensis* by Magnetic Separation

3.3.1 Summary and Author Contribution

In biotechnology, particularly in the food, beverage, and pharmaceutical industries, yeast is an important microorganism. However, the yeast's viability, age distribution, and effects on cultivation performance have not been fully elucidated. Recent research has underscored the significance of the ratio between daughter and mother yeast cells in controlled fermentation processes.

Yeast cultures with lower viability and a higher proportion of daughter cells exhibited similar cultivation behaviors to those with better viability and a lower daughter cell count. Conversely, a low ratio of both cell types and poor viability affected cultivation. To optimize this ratio, low-viability yeast had to undergo aerobic cultivation, which, after 60 – 72 h, yielded both high viability and an optimal daughter-to-mother cell ratio.

This study introduced an innovative magnetic labeling technique that used ethylenediaminetetraacetic acid (EDTA)-functionalized, silica-coated iron oxide nanoparticles. These particles bind to the chitin in yeast cell bud scars by a linker-protein, enabling specific bud scar labeling. The binding capacity achieved was 0.0877 ± 0.0062 $g_{Linker-protein}$ per $g_{Nanoparticle}$. The specificity of this binding was confirmed through a combination of cytometry, light microscopy, and scanning electron microscopy. A magnetic batch separation process was used to differentiate between non-magnetic daughter cells and magnetically labeled mother cells.

Regarding growth characteristics, no significant differences were observed under aerobic conditions. However, under anaerobic conditions at T = 14°C, where the energy production is more complex compared to aerobic conditions, mother cells exhibited a markedly reduced growth rate of $\mu_{max} = 0.00907 \pm 0.00045$ h^{-1}, in contrast to daughter cells, which showed a growth rate of $\mu_{max} = 0.01853 \pm 0.00017$ h^{-1}. These novel insights suggest that industrial yeast cell-based cultivation processes, such as in beverage and pharmaceutical production, could enhance the efficiency of these processes by using a higher proportion of daughter cells to inoculate the cultivation broth.

The doctoral candidate's substantial contribution encompassed the conception and design of experiments related to synthesizing and characterizing the MNPs, their binding to the bud

scars, and the batch separation. She executed all corresponding experiments and performed data analysis. In parallel, Marco Eigenfeld executed viability and fermentation experiments involving yeast cells, contributing equally to the experimental procedures and manuscript composition. Moreover, Marco Eigenfeld contributed to the manuscript's conceptualization. All authors actively participated in critically reviewing the manuscript.

3.3.2 Article

Biotechnology
Journal

RESEARCH ARTICLE

Studying the impact of cell age on the yeast growth behaviour of *Saccharomyces pastorianus* var. *carlsbergensis* by magnetic separation

Marco Eigenfeld[1] ⓘ | **Leonie Wittmann**[2] ⓘ | **Roland Kerpes**[1] ⓘ |
Sebastian P. Schwaminger[2,3,4] ⓘ | **Thomas Becker**[1] ⓘ

[1]TUM School of Life Science, Technical Chair of Brewing and Beverage Technology, University of Munich, Freising, Germany

[2]TUM School of Engineering and Design, Technical University of Munich, Chair of Bioseparation Engineering, Garching, Germany

[3]Otto-Loewi Research Center, Medical Division of Medicinal Chemistry, University of Graz, Graz, Austria

[4]BioTechMed-Graz, Graz, Austria

Correspondence
Roland Kerpes, TUM School of Life Science, Technical Chair of Brewing and Beverage Technology, University of Munich, Weihenstephaner Steig 20, 85354 Freising, Germany.
Email: roland.kerpes@tum.de

Sebastian P. Schwaminger, TUM School of Engineering and Design, Technical University of Munich, Chair of Bioseparation Engineering, Boltzmannstr. 15, 85748 Garching, Germany.
Email: sebastian.schwaminger@medunigraz.at

Funding information
Deutsche Forschungsgemeinschaft, Grant/Award Number: 441672360

Abstract

Despite the fact that yeast is a widely used microorganism in the food, beverage, and pharmaceutical industries, the impact of viability and age distribution on cultivation performance has yet to be fully understood. For a detailed analysis of fermentation performance and physiological state, we introduced a method of magnetic batch separation to isolate daughter and mother cells from a heterogeneous culture. By binding functionalised iron oxide nanoparticles, it is possible to separate the chitin-enriched bud scars by way of a linker protein. This reveals that low viability cultures with a high daughter cell content perform similarly to a high viability culture with a low daughter cell content. Magnetic separation results in the daughter cell fraction (>95%) showing a 21% higher growth rate in aerobic conditions than mother cells and a 52% higher rate under anaerobic conditions. These findings emphasise the importance of viability and age during cultivation and are the first step towards improving the efficiency of yeast-based processes.

KEYWORDS
bioseparation, fermentation, magnetic separation, physiological state, yeast

1 | INTRODUCTION

Saccharomyces yeast is an essential microorganism for food production, and is used in food supplements,[1] biofuels, and chemicals – especially bioethanol – to replace high-energy-density fuels with biobased resources.[2] They are the ones most widely used in pure cultures, especially in the beverage and baking industries, as well as in cocul-tures in mixed fermentation processes.[3] In particular, *Saccharomyces* species are a key factor in biotechnical applications, due to their high fermentative capacity.[4]

There is a growing interest in increasing the product yields of current fermentation procedures. This can be achieved by optimising fermentation performance either by metabolic/genetic engineering[5,6] or by focussing on the production quantity in dependence on singular cell age.

Marco Eigenfeld and Leonie Wittmann contributed equally to this study.

3.4 Millifluidic Magnetophoresis-based Chip for Age-specific Fractionation: Evaluating the Impact of Age on Metabolomics and Gene Expression in Yeast

3.4.1 Summary and Author Contribution

Saccharomyces yeast is a model organism for aging research, but it is used in various industries, such as in the beverages industry for brewing processes or in the pharmaceutical industry for recombinant protein production. Until now, most studies investigated either a heterogeneous culture or relied on the inconsistent size-age correlation to distinguish between old mother and young daughter cells. Although magnetic separation techniques have enabled the binary separation of a heterogeneous yeast population, the ability to sort yeast cells by a specific age, as determined by bud scar numbers, is not yet possible.

This study has introduced a multi-step process for age-based fractionation of yeast cells relying on their bud scar numbers. During process development, the linker-protein to particle ratio was considered, which was optimized to achieve the desired MNP agglomerate size while minimizing cross-linkage (R = 0.25). To mitigate the co-migration of non-magnetic daughter cells along with magnetically labeled mother cells, owing to magnetically induced convection in the 3D-printed millifluidic chip, a preliminary static batch separation step was employed before the mother cells underwent fractionation. Ensuring concentration homogeneity involved mechanical dispersion, achieved by introducing a sphere into the sample-containing syringe placed on a rocker shaker. Three distinct chip designs were evaluated: A classical rectangular shape, a trapezoidal geometry, and a pinch-shaped configuration. Among these, the pinch-shaped geometry combined size-based and magnetophoretic sorting principles and yielded the most promising results. This design increased the average bud scar number from 2.33 ± 0.82 in fraction A (furthest from the magnet) to 6.27 ± 0.45 in fraction D (nearest to the magnet), indicative of enriched old cells. The process demonstrated reproducibility, a high throughput of $1.90 \times 10^6 \pm 5.71 \times 10^5$ cells min^{-1}, and remarkable separation efficiencies (1.00 ± 0.00 for fraction A, 0.95 ± 0.02 for fraction B, and 0.97 ± 0.00 and 0.84 ± 0.08 for fractions C and D, respectively). Subsequent metabolomic studies unveiled age-related declines in specific amino acids and an increase in nicotinamide adenine dinucleotide (NAD$^+$) production, likely attributed to the metabolic activities of younger cells. Gene expression analyses further underscored age-related alterations, particularly in genes associated with metabolism and stress response. Aging cells appeared to adapt their metabolic pathways, suggesting potential energy inefficiencies.

This study has introduced a non-invasive method for age-based sorting of *S. pastorianus ssp. carlsbergensis* yeast cells, involving batch separation and subsequent fractionation within a 3D-printed millifluidic chip. This innovative and high-throughput process could be used for applications in aging research and the beverages and pharmaceutical industries, offering new ways for age analysis and optimization of production processes.

The doctoral candidate's substantial contributions were the experiments' conception and design. She and Jennifer Meiler conducted the experiments involving the loading of the yeast cells with the MNPs, as well as the separation and fractionation in the millifluidic chips. The doctoral candidate analyzed the corresponding data, including the cytometry data, and served as the leading author of the manuscript. Marco Eigenfeld and the doctoral candidate contributed equally, with Marco Eigenfeld primarily responsible for the conception and design of the gene analysis experiments. Marco Eigenfeld and Kai Büchner conducted these experiments and composed the manuscript sections about the gene and metabolomic analysis. Hansjörg Habisch performed the metabolomics study at the Medical University of Graz. All authors critically reviewed the manuscript.

3.4.2 Article

Lab on a Chip

ROYAL SOCIETY
OF CHEMISTRY

PAPER

Check for updates

Millifluidic magnetophoresis-based chip for age-specific fractionation: evaluating the impact of age on metabolomics and gene expression in yeast†

L. Wittmann, [iD] ‡[a] M. Eigenfeld, [iD] ‡[bc] K. Büchner, [iD] [b] J. Meiler,[a] H. Habisch, [iD] [c]
T. Madl, [iD] [cd] R. Kerpes, [iD] *[b] T. Becker, [iD] [ce]
S. Berensmeier [iD] [ae] and S. P. Schwaminger [iD] *[acd]

A novel millifluidic process introduces age-based fractionation of *S. pastorianus* var. *carlsbergensis* yeast culture through magnetophoresis. *Saccharomyces* yeast is a model organism for aging research used in various industries. Traditional age-based cell separation methods were labor-intensive, but techniques like magnetic labeling have eased the process by being non-invasive and scalable. Our approach introduces an age-specific fractionation using a 3D-printed millfluidic chip in a two-step process, ensuring efficient cell deflection in the magnetic field and counteracting magnetic induced convection. Among various channel designs, the pinch-shaped channel proved most effective for age differentiation based on magnetically labeled bud scar numbers. Metabolomic analyses revealed changes in certain amino acids and increased NAD^+ levels, suggesting metabolic shifts in aging cells. Gene expression studies further underlined these age-related metabolic changes. This innovative platform offers a high-throughput, non-invasive method for age-specific yeast cell fractionation, with potential applications in industries ranging from food and beverages to pharmaceuticals.

[a] *TUM School of Engineering and Design, Chair of Bioseparation Engineering, Technical University of Munich, Boltzmannstr. 15, 85748 Garching, Germany. E-mail: s.schwaminger@tum.de*

[b] *TUM School of Life Science, Chair of Brewing and Beverage Technology, Technical University of Munich, Weihenstephaner Steig 20, 85354 Freising, Germany. E-mail: roland.kerpes@tum.de*

[c] *Otto-Loewi Research Center, Division of Medicinal Chemistry, Medical University of Graz, Neue Stiftingtalstr. 6, 8010 Graz, Austria*

[d] *BioTechMed-Graz, Mozartgasse 12/II, 8010 Graz, Austria. E-mail: sebastian.schwaminger@medunigraz.at*

[e] *Munich Institute of Integrated Materials, Energy and Process Engineering, Technical University of Munich, Lichtenberstr. 4a, 85748 Garching, Germany*

† Electronic supplementary information (ESI) available. See DOI: https://doi.org/10.1039/d4lc00185k

‡ All authors contributed equally.

A Introduction

Saccharomyces yeast is a valuable model organism for aging research, offering insights into two distinct aging processes: chronological aging, which is defined by the survival time of the cell, and replicative aging, characterized by the number of division events a cell undergoes before reaching senescence. Senescence, a key aging marker, impedes cellular repair and is linked to age-related diseases.[1] The process of asymmetric cell division in yeast, wherein mother cells generate a finite number of daughter cells, presents a unique opportunity to gain a deeper understanding of these aging dynamics.[2]

Numerous studies have investigated cellular aging by analyzing heterogeneous cultures or relying on the variable correlation between cell size and age, often employing a sucrose gradient method.[3–8] However, the direct link between cell age, its metabolome, and gene expression remains a topic of debate, because of the lack of methodology, specifically sorting cells by their replicative age. Recent studies have shown that external factors, such as growth rate and stressors like formic acid, influence yeast metabolic reactions, impacting both oxidative stress response and protein biosynthesis.[6,7] Correia-Melo *et al.* highlighted the connection between metabolism and chronological aging, marked by shifts in intracellular metabolic processes and signaling pathways.[8] Thus, there is a need for a reliable, age-specific fractionation method of yeast cells to advance aging research concerning the replicative lifespan.

Historically, age-based cell separation was labor-intensive, relying on microdissection.[2] Modern microfluidic platforms, leveraging cell size differences or surface adhesion, have simplified this process.[9–11] However, these techniques can be invasive, potentially compromising age-analysis accuracy, and often lack scalability, making growth and omics studies difficult.[12,13] High-throughput technologies, like magnetic

4 Discussion

4.1 Magnetic Nanoparticle Design and Agglomeration Behavior

For the magnetophoretic fractionation process of a heterogeneous yeast population based on age, the MNPs had to meet certain requirements to ensure a high separation efficiency. First, the MNPs should bind specifically to the chitin-enriched bud scars of the yeast cells, by a bifunctional linker-protein. It comprised of a ChBD and a histidine (his) tag [168]. The ChBD enabled the specific labeling of the chitin-enriched ring present around the bud scars, while the his tag bound either to a functionalized MNP surface by a chelate complex of EDTA and Ni^{2+} ions or on the surface of BIONs [92]. Furthermore, the MNPs should form homogeneous agglomerates with the linker-protein in the chosen buffer (pH $6-8$), which had to enable the binding of the linker-protein to both the MNPs and the yeast cells' bud scars. This homogeneity in agglomeration should ensure consistent susceptibility across yeast cells with a defined bud scar number; thereby, magnetic manipulation by age was possible. Moreover, the agglomeration process should be independent of time, maintaining homogeneity throughout the duration of the magnetophoretic process. This consistency ensured reproducible separation efficiencies in the fractionation process. The hydrodynamic diameter of the MNP@linker-protein agglomerates should be > 300 nm for the used analytics of light microscopy. Additionally, the MNPs had to be colloidal stable ($-20 > \chi > 20$ mV) to minimize unwanted aggregation with and without magnetic fields [66, 85, 201]. When exposed to a magnetic field gradient, aggregation of MNPs leads to bundle formation [100] and magnetically induced convection [66] (Equations 1.10, 1.8). To counteract this, a steric stabilization of the BIONs may be necessary. However, the smaller the agglomerates, the stronger the magnetic field gradient must be to enable effective manipulation due to their reduced magnetic moment compared to larger agglomerates. A higher concentration of MNPs leads to increased volumetric magnetization, which in turn enhances the magnetic force exerted on the particles (Equation 1.7). Both, magnetic aggregation and magnetically induced convection contribute to increasing the velocity of MNPs in the magnetic field within the millifluidic channel (Subsection 1.2.1).

The dilemma of colloidal stability and magnetic manipulation shows that the design and agglomeration of the MNPs in this application are essential for the age-dependent fractionation. Thus, BIONs and ION@Si@EDTAs are compared regarding their suitability (Table 4.1).

Table 4.1: Nanoparticle requirements for the age-specific labeling of the yeast cells' bud scars and the subsequent magnetophoretic fractionation process in the millifluidic chip.

Agglomerate diameter at pH 6-8 [nm]	1000 – 2000
Monomodality of agglomerates	High
Magnetic aggregation [-]	N* <1
Magnetically induced convection [-]	Gr <1
Binding specificity to bud scar	High

One of the primary advantages of using BIONs was their straightforward, not labor-intensive, and cost-effective synthesis process by the Massart process [68, 75]. Furthermore, Wittmann et al. demonstrated that the agglomeration behavior of BIONs could be effectively controlled by manipulating the viscosity and pH of the solution. Increasing the viscosity $2.5\times$ compared to water altered the isoelectric point from 6.69 to 6.07. At that point, particle agglomerates up to 3000 nm were formed due to their low surface charge. However, the agglomeration was less pronounced in solutions with higher viscosity, particularly for $4 > $ pH $ > 7$ due to potential hydration effects or steric hindrance by hydroxyl groups in the magnetic field [202, 203]. Additionally, with decreasing agglomerate size and increasing viscosity, the magnetophoretic sedimentation velocity decreased, as the drag force is directly proportional to viscosity [83].

However, BIONs also exhibited significant disadvantages. As reported by Eigenfeld et al., BIONs tended to bind unspecifically to yeast cells at a pH of 7.4 in 3-(N-morpholino)propane sulfonic acid (MOPS) buffer. This was attributed to the only slightly negative charge ($\chi \sim -8$ mV) of the yeast cell surface at that pH, leading to potential electrostatic interactions ($\chi_{BIONs} = -24.98 \pm 2.07$ mV) [204]. To prevent unspecific binding apart from the bud scars, functionalization of the BIONs with EDTA was necessary. Additionally, they were highly prone to magnetic agglomeration and tended to form bundles along the local magnetic field lines [100] resulting in an increase in the average hydrodynamic diameter, as displayed in Figure 4.1. When moved into the magnetic field, an increase in agglomerate size could be observed in water for pH 4 and pH 10, although they possessed a charged surface [83]. This magnetic agglomeration was reversible, as the average diameter decreased when the magnetic field was removed. However, at pH 7, where the BIONs surface was neutrally charged even in the higher viscous solution, large agglomerates were built within the magnetic field, as the attractive forces prevailed. Additionally, aggregates were built as the particle accumulation is irreversible. In contrast, MNPs with a silica shell, which increased their

colloidal stability [79], did not show such agglomeration in the magnetic field even at pH 7 (isoelectric point ∼pH 4 [205]), as illustrated in Figure A.1. The derived counts in water slightly increased in the magnetic field, which indicated particle interaction; however, the hydrodynamic diameter did not increase.

When considering the buffer's role in the agglomeration behavior, an increase in viscosity led to a reduction in the BIONs agglomerate size across all buffers (Figure 4.2) [202, 203]. Different buffers were chosen all near the neutral pH having low molarity as under these conditions Eigenfeld et al. observed preferred binding of the ChBD to the chitin-enriched bud scars [168]. For potassium phosphate (KPP), and MOPS buffer, the average diameter was decreased for the higher viscosity; however, some larger agglomerates persisted, resulting in a multimodal distribution. In contrast, buffers like 2-(N-morpholino)ethane sulfonic acid (MES), tris(hydrocymethyl)aminomethane (TRIS), and phosphare buffered saline (PBS) yielded a more monomodal and narrower distribution with increased viscosity. Furthermore, higher viscosity buffers exhibited a time-independent agglomeration behavior for MES, TRIS, and PBS. For the low viscosity buffers, the BIONs showed a time-dependent agglomeration behavior with multimodal distributions [206]. Consequently, low viscosity buffers were deemed unsuitable, and only MES, TRIS, and PBS buffers were considered viable in highly viscous solutions.

So, while BIONs offered certain advantages in terms of simplicity of synthesis and controllable agglomeration by pH and viscosity, they were not ideally suited for age-based yeast cell labeling due to their tendency for magnetic aggregation and unspecific binding to the yeast cell surface. The increase in viscosity, although it prevented magnetic agglomeration and led to monomodal, time-independent agglomeration in specific buffers would necessitate a buffer exchange after fractionation for further processing and analytics. Additionally, even if yeast cells could handle high osmolarity by producing the compatible solute glycerol [158, 207], the increase in viscosity leads to a stress response, contradicting the need for a non-invasive fractionation method. To address these challenges, enhancing colloidal stability through steric hindrance with a silica shell could reduce magnetic aggregation, and functionalization with EDTA would enable specific binding to the yeast cells' bud scars.

These ION@Si@EDTA were produced in three synthesis steps. In the first step, BIONs [83] were synthesized via the Massart process [68], followed by the introduction of a silica shell with amino groups using (3-aminopropyl)triethoxysilane (APTES) by a modified Stöber process [208, 209]. This functionalization enabled the covalent binding of EDTA via amide bonding [109, 209]. Two different silica shell thicknesses were compared to increase the colloidal stability (Figure A.2 a and b) [79, 205]. However, this resulted in a decrease in saturation magnetization from 70.84 m^2 kg^{-1} for the BIONs to 13.23 Am^2 kg^{-1} (normal = 178 mg BIONs) and 17.57 Am^2 kg^{-1} (thin = 235 mg BIONs) for the ION@Si@EDTA. That is why
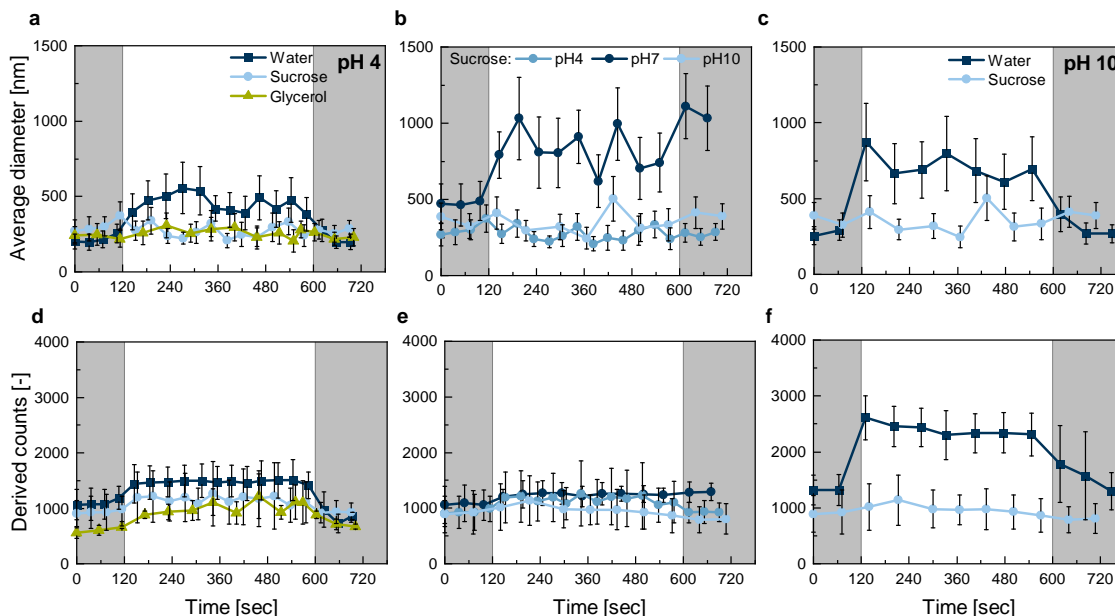
Figure 4.1: Dynamic light scattering (DLS) kinetic measurement of BIONs (c = 1 g L^{-1}) at pH 4, 7, and 10 in water (η = 0.888 mPas), glycerol, or sucrose (both η = 2.774 mPas). The sample was measured without the magnetic field for 120 s (grey area), then it was moved into the homogeneous magnetic field (H = 180 mT) for 480 sec, and finally, the field was removed again for 120 sec. The average diameter corresponds to the intensity-weighted mean hydrodynamic diameter. The derived count rate reflects the scattering intensity. In DLS, variations in scattering intensity over time are analyzed to determine the range of diffusion coefficients for particles within a dispersion. The standard deviation represents the width of the distribution of a triplicate measurement.

they had to be centrifuged for washing after the synthesis instead of applying magnetic decantation which resulted in a particle loss of 53% and 59%, respectively, for the normal and thin silica-coated nanoparticles (Table 4.2). In the next step, EDTA was bound onto the surface of the silica-coated magnetic nanoparticles (MNP@Si@NH$_2$), optimal at 60°C under acidic conditions [209]. This step was critical, as the particles dissolved depending on the synthesis time (2 – 8 h), silica coating thickness (m$_{BION, normal}$ = 178 mg vs. m$_{BION, thin}$ = 235 mg for 6.94 mL tetraethyl orthosilicate (TEOS)), and strength of the ultrasonic dispersion (132 kHz vs. 45 kHz). Figure 4.3 d shows that the highest and fastest particle loss of $\sim$ 80% occurred at the stronger dispersion with the thinner silica coating because the high energy input and the reduced protective coating led to the dissolution of the BIONs under the acidic synthesis conditions [210]. According to Salman et al., the EDTA binding is successful after 2 h of synthesis, which resulted in a particle loss between 10 – 20% under all applied conditions. A temperature increase to 80°C resulted in a dissolution of 84% (45 kHz) and 86% (132 kHz) of the normal coated particles after 2 h synthesis time and the thinner coated ones dissolved completely at the same conditions. Thus, depending on the coating thickness, all of these
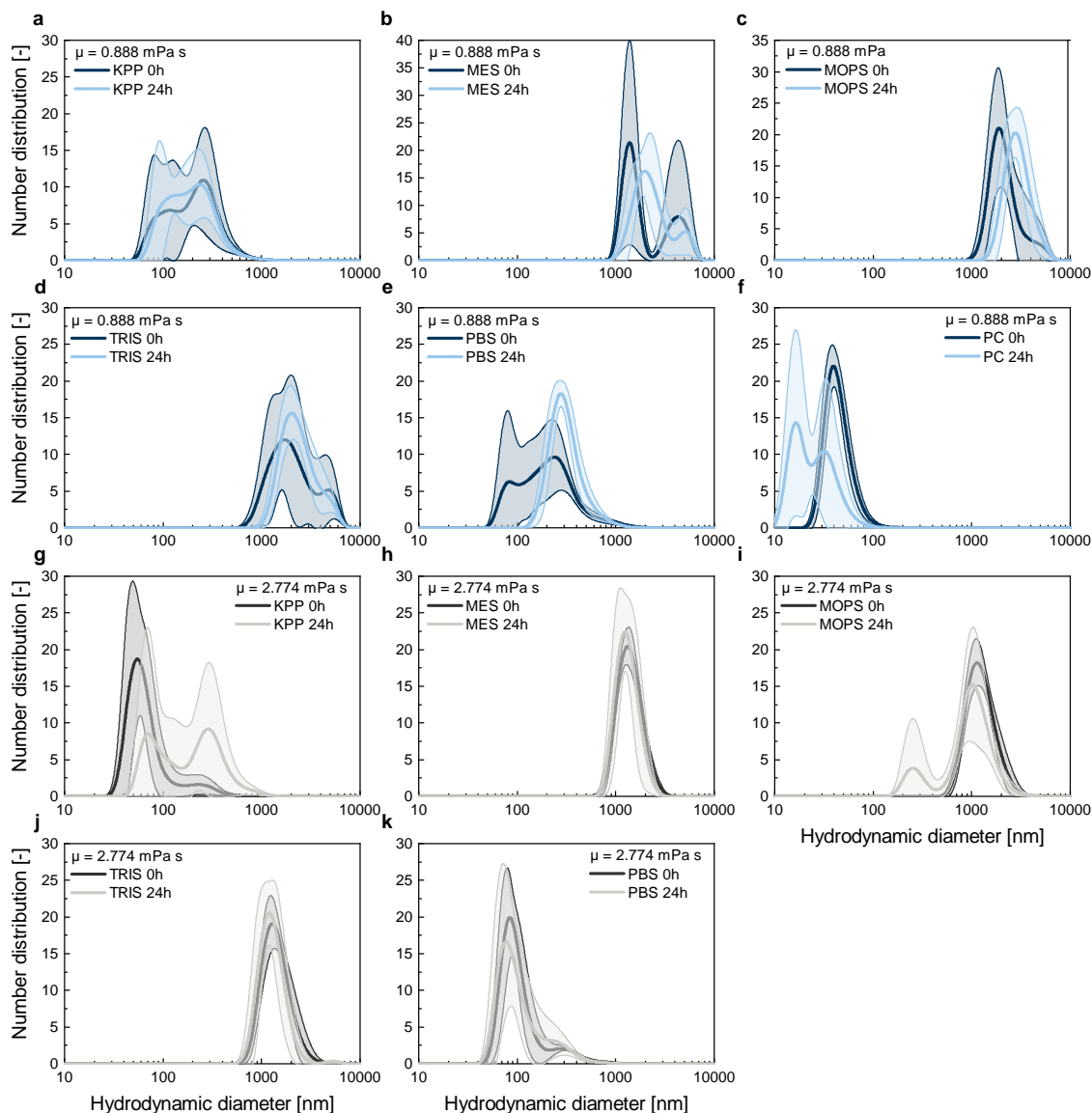
Figure 4.2: DLS measurement of BIONs (c = 1 g L^{-1}) in KPP pH = 8 (a, g), MES pH = 6.5 (b, h), MOPS pH = 7.3 (c, i), TRIS pH = 8 (d, j), PBS pH = 7.4 (e, k), phosphate citrate (PC) pH = 8 (f), all at c = 20 mM at a viscosity of $\eta = 0.888$ mPas and $\eta = 2.774$ mPas measured directly, and 24 h after incubation. The shaded area represents the standard deviation of an analytical triplicate measurement.

parameters had to be controlled carefully, with the temperature being the most important one. Table 4.2 compares the yield of the second and third synthesis steps, indicating a lower yield of 41% (132 kHz) and 34% (45 kHz) for the normal ION@Si@EDTA compared to the thinner ones with 51% (132 kHz) and 34% (40 kHz), respectively.

Table 4.2: Synthesis yields after washing of the silica coating with the introduction of the amino groups MNP@Si@NH$_2$ and the subsequent amide bonding of EDTA at 60°C under weak (132 kHz) and strong (45 kHz) ultrasonic dispersion resulting in the final thin (m$_{BION}$ = 235 mg) and normal (m$_{BION}$ = 178 mg) silica shell ION@Si@EDTA. The overall yield refers to both synthesis steps.

m$_{BION}$ [mg]	Yield MNP@Si@NH$_2$ [%]	Ultrasonic dispersion [kHz]	Yield ION@Si@EDTA [%]	Overall synthesis yield [%]
178	53	132	88	41
178		45	65	34
235	59	132	87	51
235		45	68	40
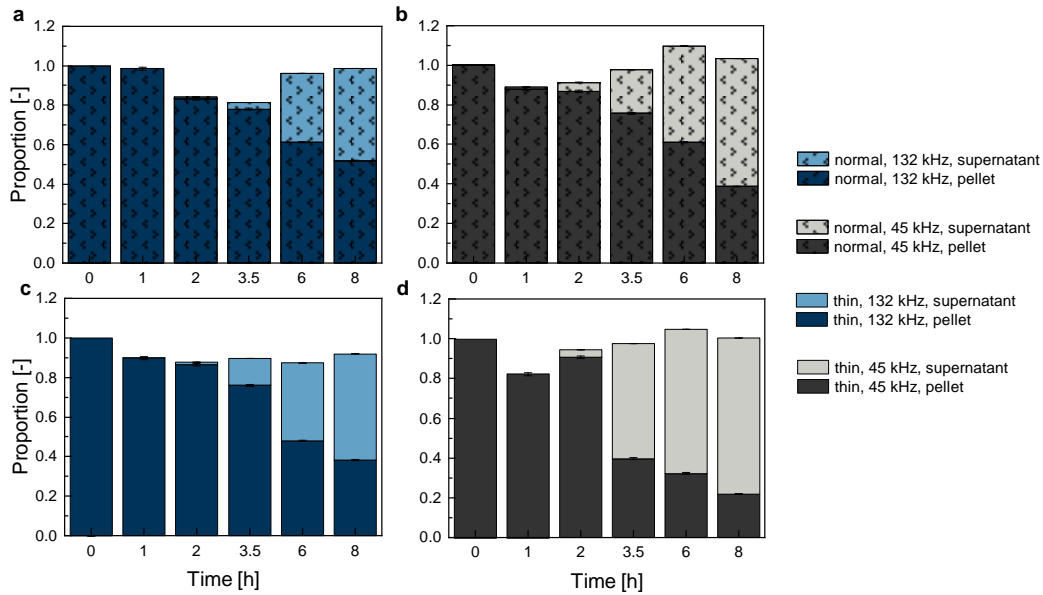
Figure 4.3: Synthesis yields (m$_{after\ washing}$ / m$_{before\ washing}$) after washing of the silica coating with the introduction of the amino groups MNP@Si@NH$_2$ and the subsequent amide bonding of EDTA at T = 60°C under weak (132 kHz) (a, c) and strong (45 kHz) (b, d) ultrasonic dispersion resulting in the final thin (m$_{BION}$ = 235 mg) (c, d) and normal (m$_{BION}$ = 178 mg) (a, b) silica shell ION@Si@EDTA nanoparticles. The overall yield refers to both synthesis steps.

Subsequently, the resulting nanoparticles were characterized. As expected, TEM analysis (Figure A.3 and A.2) showed a smaller primary particle diameter of d$_{TEM}$ = 72 ± 12 nm for the thinner coated MNP@Si@NH$_2$ compared to the normal ones (d$_{TEM}$ = 114 ± 18 nm) [79]. However, both particle species encapsulated same sized BIONs (d$_{thin}$ = 11.4 ± 0.32 nm vs. d$_{normal}$ = 11.93 ± 0.49 nm) derived from X-ray diffraction (XRD)

measurement, in detail discussed in [211]. DLS measurements after synthesis in Figure A.4 revealed slightly smaller agglomerates for the normal MNP@Si@NH$_2$ ones ($d_{DLS,\ thin}$ = 1783 $\pm$ 122 nm, pH = 9.13, ζ = –7.73 $\pm$ 0.63 mV vs. $d_{DLS,\ normal}$ = 1456 $\pm$ 18 nm, pH = 9.43, ζ = –4.01 $\pm$ 0.50 mV), as the thicker coating increases the colloidal stability of the nanoparticles [205]. After EDTA functionalization both resulting ION@Si@EDTAs exhibited similar number distributions of the DLS measurement of $\sim$200 nm (Figure A.4 b and c), but differences in TEM diameters ($d_{TEM,\ thin}$ $\sim$89 nm vs. $d_{TEM,\ normal}$ $\sim$102 nm). This underlines again the difference in colloidal stability depending on the sterically stabilizing silica shell. Despite the differences in synthesis yield and dissolution, the primary particle and hydrodynamic diameters of both particles did not vary for the used ultrasonic dispersion methods, thus, only the particles synthesized in 132 kHz dispersion were further characterized. SQUID measurement revealed a higher saturation magnetization of the thinner coated ION@Si@EDTA with 17.57 Am^2 kg^{-1} compared to the normal ones with 13.23 Am^2 kg^{-1}, resulting in differences in the magnetophoretic sedimentation velocity ($v_{mag,\ thin}$ = 9.88 µm s^{-1} vs. $v_{mag,\ normal}$ = 4.61 µm s^{-1}). The Fourier-transform infrared spectroscopy (FT-IR) spectra showed the characteristic peaks for the different functionalization steps, in detail discussed in [109] [212]. Preserving the colloidal stability was the most important criterion for the development of the magnetophoretic fractionation process. Therefore, the thicker coated ION@Si@EDTA were selected for further studies.

The reproducibility of the synthesis was examined to ensure that the particles for subsequent binding to the yeast via the linker-protein had similar properties. In particular, the agglomeration behavior should be comparable in order to achieve a uniform magnetization of the bud scars. Table 4.3 summarizes five different synthesis batches for the ION@Si@EDTA. The conductivity, pH, and zeta potential only showed slight variations, whereas the primary particle diameter varied between 102 – 219 nm. The hydrodynamic diameter ranged between 223 – 288 nm. These variations could mainly be attributed to the second synthesis step, as the addition of TEOS was done manually with a syringe and directly influenced the shell thickness. The FT-IR spectra in Figure A.7 confirmed this, as the characteristic peak for the Si-O-Si stretching vibration at 1080 cm^{-1} differed slightly in intensity. In summary, despite slight batch-to-batch variations, a well-characterized synthesis of ION@Si@EDTA has been developed. As will be shown in the following chapters, the slightly different properties had no negative influence on the magnetophoretic fractionation process.

As shown in Wittmann and Eigenfeld et al., the silica shell ensured high colloidal stability so that a stable hydrodynamic diameter can be preserved for 28 days in water [211]. To enable the binding of the particles to the linker-protein via the his tag, 4 mg$_{Ni}$ g$_{Particle}^{-1}$ complying with 0.40 nickel ions nm$_{Particle}^{-2}$, could be complexed by the functionalized particle surface within minutes [213] [211].

Table 4.3: Conductivity, pH, zeta potential, hydrodynamic diameter, and primary particle diameter for six different synthesis batches for ION@Si@EDTA production.

	#1	**#2**	**#3**	**#4**	**#5**
Conductivity [µS cm]	51.9	41.6	43.1	14.7	27.7
pH [-]	4.86	4.83	4.57	5.74	5.04
Zeta potential [mV]	27.25 ± 0.80	28.58 ± 1.15	38.47 ± 0.85	26.78 ± 0.38	22.42 ± 0.28
Hydrodynamic diameter [nm]	227.40 ± 5.57	227.97 ± 2.85	287.7 ± 5.31	222.90 ± 7.26	219.33 ± 6.68
Primary particle diameter [nm]	142.66 ± 19.80	126.02 ± 20.45	102.28 ± 19.04	120.62 ± 16.86	219.30 ± 53.38

The ionic strength of buffers significantly influenced the agglomeration behavior of the ION@Si@EDTA. According to the Derjaguin, Landau, Verwey and Overbeek (DLVO) theory, the colloidal stability of particles is dependent on the attractive van der Waals forces and the repulsive forces of the electric double layer [214]. A higher ionic strength reduces the zeta potential of the nanoparticles, and decreases the electric double-layer thickness, promoting their agglomeration [215]. Figure 4.4 and A.8 demonstrate that nanoparticles in all buffers agglomerated, but in higher ionic strength (c = 50 mM) buffers the agglomerates increased in size to > 1000 nm. At lower ionic strength (c = 20 mM), the nanoparticles showed differences in their agglomeration behavior depending on whether they were loaded with nickel or not. Most particles formed agglomerates of ~1000 nm, however, the ones loaded with nickel ions decreased in hydrodynamic diameter for PBS, PC, KPP, and TRIS after t = 24 h [216–218]. For MOPS, directly after incubation, small agglomerates between 100 − 200 nm were formed and preserved for 24 h. Only for RS, and MES, no decrease in agglomerate size was observed when the nanoparticles were loaded with nickel [216–218]. For almost all tested buffers, the agglomeration behavior changed over time. The storage in the corresponding buffer led to a variation of agglomeration behavior, which could not guarantee a reproducible labeling process of the yeast cells' bud scars. Therefore, the particles had to be loaded with nickel and dispersed in the corresponding buffer every time before usage [211].

In summary, a robust synthesis process was developed for the production of colloidal stable ION@Si@EDTA being able to complex nickel ions for the subsequent binding to the his tag of the linker-protein. The nanoparticles differed in their agglomeration behavior depending on the buffer species, ionic strength, their incubation time and whether they were loaded with nickel ions or not. So far, MES, and TRIS were excluded as they exhibited a multimodal
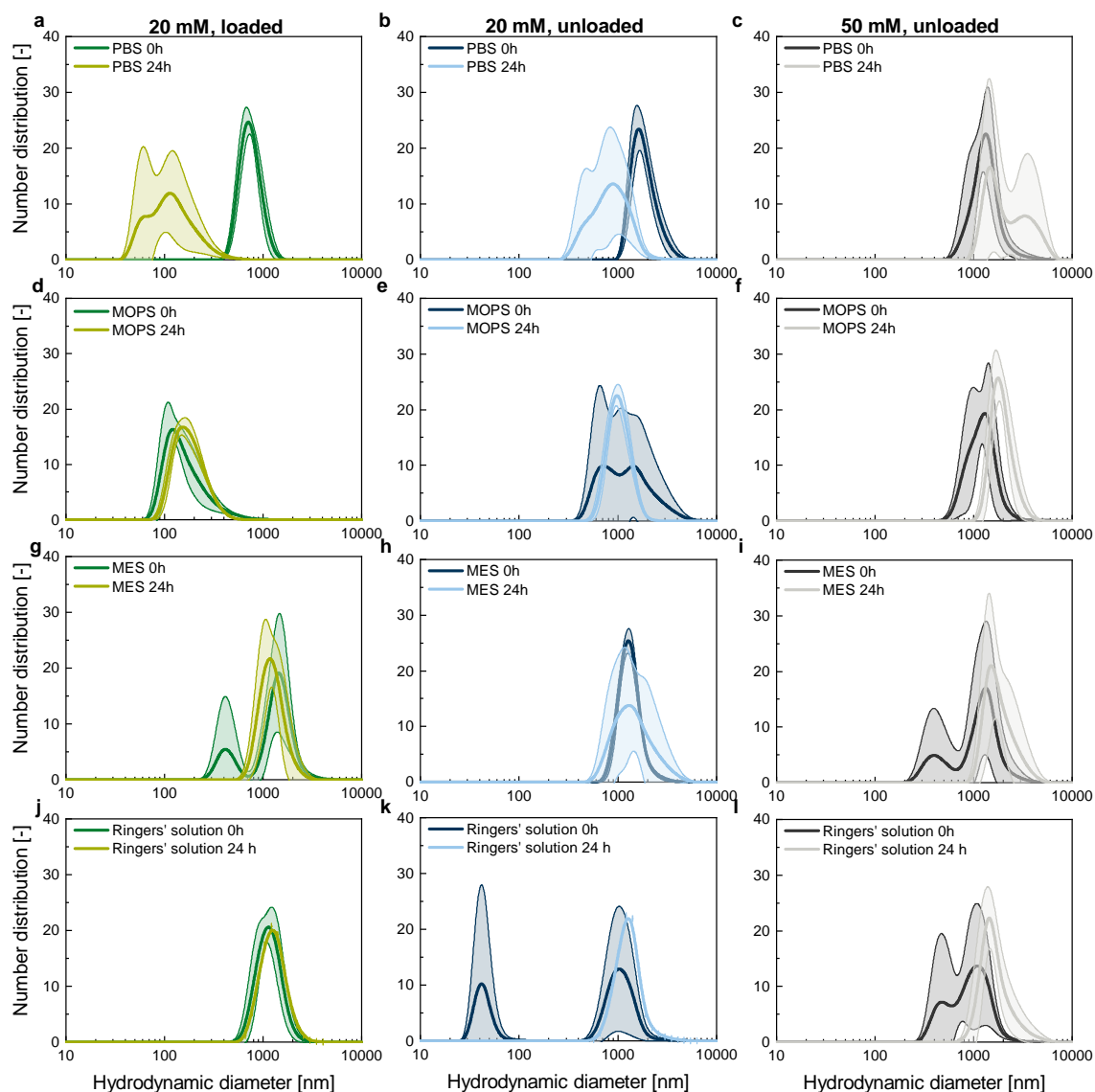
Figure 4.4: DLS measurement of ION@Si@EDTAs ($c = 1$ g L^{-1}) in PBS pH = 7.4 (a, b, c), MOPS pH = 7.3 (d, e, f), MES pH = 6.5 (g, h, i), and Ringers solution (RS) pH = 7.2 (j, k, l) at concentrations of c = 20 and 50 mM loaded with nickel ions or unloaded measured directly and 24 h after incubation. Instead of a concentration of 50 mM, 1x PBS and 1x RS was used. The shaded area represents the standard deviation of an analytical triplicate measurement.

particle distribution initially after incubation. In addition to the agglomeration, it had to be ensured that no unspecific binding to the yeast cell surface occurred. Therefore, the binding behavior of the nickel-loaded nanoparticles to the linker-protein was analyzed in various buffers, further described in the subsequent section.

4.2 Age-specific Labeling of Yeast Cell Bud Scars Using Magnetic Nanoparticles

Upon analyzing the agglomeration behavior of the ION@Si@EDTA (hereafter referred to as nanoparticles), the subsequent objective involved the specific targeting of yeast cells' bud scars with these nanoparticles by the linker-protein. Therefore, the chair of Brewing and Beverages Technology investigated the binding of the linker-protein to the yeast cells' bud scar, and the chair of Bioseparation Engineering analyzed the binding of the linker-protein to the nanoparticles. Our focus was on quantifying the maximum binding capacity and assessing the agglomeration dynamics under varying buffer conditions, alongside concentration and temporal dependencies of the process. Subsequently, we characterized the entire system – comprising yeast cells, linker protein, and nanoparticles – in terms of binding specificity, meaning whether the linker-protein@nanoparticle agglomerate bound specifically to the yeast cells' bud scar. For this analysis, cytometry and microscopy techniques were implemented as orthogonal methods [109, 219]. Given that the nanoparticles were completely coated with the linker-protein, the possibility of unintended cross-linkage between yeast cells, mediated by the linker-protein-nanoparticle agglomerates, was also considered. Finally, in preparation for the subsequent age analysis of the yeast cells, a method for the efficient elution of nanoparticles was developed.

First, the binding of the linker-protein to the nanoparticles (MNP@Si and ION@Si@EDTA) was analyzed, concurrently determining the hydrodynamic diameter of the resulting linker-protein@nanoparticle agglomerates (Figure 4.5). As expected, only the silica-coated nanoparticles, possessing a negatively charged surface, exhibited negligible binding to the linker protein, primarily due to the repulsive forces of the imidazole rings of histidine [205]. Consequently, the hydrodynamic diameters of these agglomerates remained between 200 – 300 nm. Further analysis of ION@Si@EDTA revealed that linker-protein binding was independent of the nickel source (either $NiCl_2$ or $NiSO_4$). Higher loading of linker-protein on the nanoparticles resulted in smaller agglomerates, particularly in PBS and TRIS buffers. These linker-protein@nanoparticle agglomerates, primarily composed of small-sized protein-particle agglomerates, were built via hydrophobic interactions [92]. At a certain linker-protein to nanoparticle ratio, however, a saturation of the nanoparticle surface occurs, leading to inhibited bridging interactions due to repulsive forces [90, 91] [211]. Moreover, the binding capacity of the linker-protein to the nanoparticles decreased for increased ionic strength of the buffer (PBS, MES, MOPS, and RS) [91]. For PC, MES, MOPS, RS, and KPP, independent of the protein load, linker-protein@nanoparticle agglomerates around 1500 nm were formed, optimal for labeling the yeast cells' bud scars having a size between 1.9 – 2.3 μm [17]. These conditions achieved the highest binding loads, 0.0877 ± 0.0062 $g_{Linker-protein}$ $g_{Particle}^{-1}$,

ensuring complete nanoparticle surface coverage [211]. Research with the cooperating partner
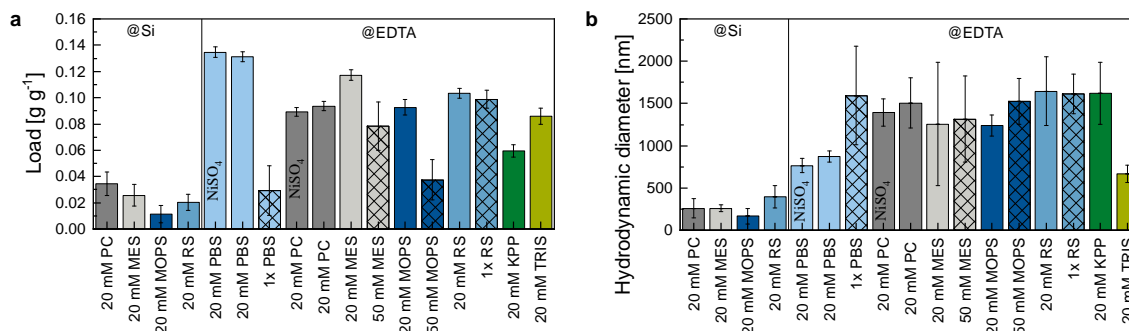
Figure 4.5: (a) Linker-protein load per $g_{Particle}$ and (b) number distribution of the DLS measurement is presented for the buffers PC pH = 8, MES pH = 6.5, MOPS pH = 7.3, KPP pH = 8 and TRIS pH = 8 for 20 and 50 mM ionic strength. For PBS pH = 7.4 and RS pH = 7, 20 mM and 1x concentration is used. As a reference, only silica @Si nanoparticles were analyzed. @EDTA refers to the final, with nickel ions loaded ION@Si@EDTA nanoparticles. The error bar presents the standard deviation from a technical triplicate measurement.

indicated that in MES and KPP buffers, the linker-protein did not bind to yeast cells' bud scars. Furthermore, yeast cell viability was highest with 75% in 20 mM MOPS buffer after 25h, starting from an initial viability of 89.99%. It was also important to ascertain that in the absence of linker-protein, no unspecific binding occurred. As presented in Figure A.9, this was the case for the higher concentrated MES buffer and the calcium-containing RS. Therefore, both were excluded as potential buffers. In all other buffers, no unspecific binding could be observed.

Taking all these results together, these findings establish MOPS buffer as the most suitable buffer for the specific binding of the linker-protein@nanoparticle agglomerate to yeast cells' bud scars, with a maximum binding capacity of 0.0877 ± 0.0062 $g_{Linker-protein}$ $g_{Particle}^{-1}$ [219]. Next, it was the aim to minimize nanoparticle concentration to reduce undesirable cross-linkage and magnetically-induced convection, both of which are concentration-dependent. Wittmann and Eigenfeld et al. reported that increasing the linker-protein@nanoparticle ratio led to a decrease in agglomerate size, from 1112.0 ± 36.2 nm to 695.6 ± 40.0 nm at a ratio of R = 0.25 to R = 2, respectively. At the same time, depending on this ratio, the agglomerates changed their size with time. A lower ratio was associated with more dynamic behavior. But, for a ratio of R = 0.25, uniform agglomerates were formed for the 5 h, which ensured homogeneous agglomerates during the magnetophoretic fractionation process [211].

Combining all three components – linker protein, nanoparticles, and yeast cells – cytometry, microscopy, and scanning electron microscopy confirmed the specificity of the binding, further detailed in [219]. A daughter cell proportion of ∼60%, a first generation mother cell proportion of ∼25%, and ∼15% second generation mother cells were measured. Compared to

previous studies [17, 174], our analysis revealed a different age distribution in *S. pastorianus ssp. carlsbergensis*, with a lower proportion of higher-generation mother cells. This could be attributed to strain differences, growth conditions, differences in cell cycle durations with increasing replicative aging, and the analytical constraints [219].

Wittmann and Eigenfeld et al. also found that 45% of the cells were single, and 55% were budding. However, when being labeled, at a low linker-protein@nanoparticle ratio of R = 0.04, the single cell content was less than 40%, because 10% of the labeled yeast cells formed part of larger cross-linked cell agglomerates, reducing the single cell proportion. In contrast, the crosslinked proportion was below 10% for a higher ratio of R = 0.25, meaning that fewer nanoparticles were present in the system. A time dependence could not be observed for both ratios. Therefore, a consistent linker-protein@particle ratio of 0.25 in subsequent processes was employed to ensure optimal agglomerate size and reduced crosslinkage [211].

For the subsequent age analysis, the nanoparticles were eluted using imidazole, dissociating the linker-protein from the nanoparticles, similar to immobilized metal affinity chromatography. Following the procedure outlined in [211], $100.00 \pm 0.00\%$ of nanoparticles were separated (compare Figure A.9 h and i), and $77.00 \pm 2.15\%$ of unlabeled yeast cells were recovered for further analysis.

In conclusion, the linker-protein bound specifically to the yeast cells' bud scar in MOPS buffer, forming homogeneous agglomerates. Despite the low molarity, the yeast cell viability could be maintained, and the heterogeneous yeast cell culture was successfully labeled according to the number of bud scars so that each yeast cell exhibited an age-specific susceptibility.

4.3 Sized-based Yeast Cell Fractionation via a Spiral Sorter

Size-based yeast cell fractionation was explored as an alternative label-free method alongside magnetophoretic fractionation. The primary goal was to achieve fractionation based on age, leveraging the known correlation between cell size and age [17, 109]. The secondary objective was to separate cell-cell agglomerates or budding cells from single cells for the magnetophoretic fractionation. This step was essential, as cell-cell agglomerates or budding cells exhibited different ages, potentially leading to non-age-specific binding of the linker-protein@nanoparticle agglomerate. Consequently, the selectivity of the magnetophoretic fractionation process would be reduced, as the resulting magnetophoretic force would not be proportional to the age anymore.

As detailed in Section 4.2, the cell population consisted of 45% single cells and 55% budding cells, necessitating the separation of these budding cells [211]. Size distribution analysis (Figure 4.6 a) revealed that single cells ranged between 7 – 8 µm and agglomerated cells between 9 – 10 µm. Thus, a 9 µm threshold was chosen for efficient separation; cells smaller than 9 µm comprised predominantly single cells (80.84%), while cells larger than 9 µm were mostly budding or agglomerated (89.75%).
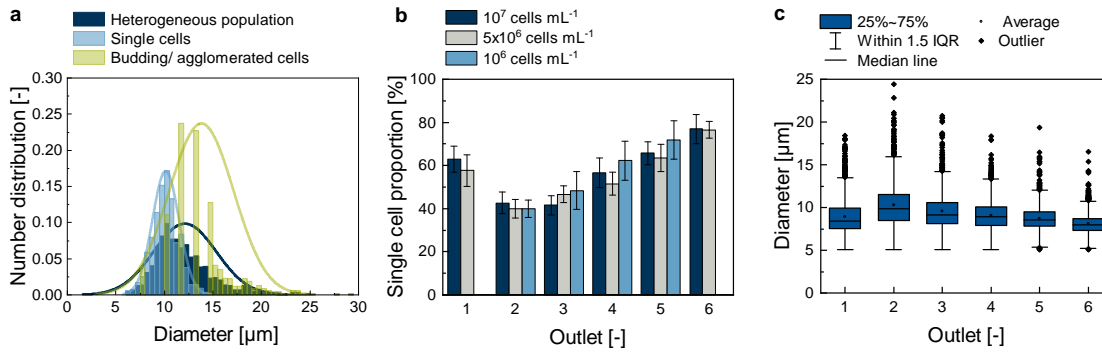
Figure 4.6: (a) Size distribution of a heterogeneous yeast cell population and categorized into single cells and agglomerated/budding cells. Cell diameters were determined from light microscopic imaging and subsequent processing 849 cells of each group by ImageJ analysis. Data of a single measurement used. (b) Single cell proportion of three different cell concentrations over the different outlets using the 500 x 120 µm spiral chip at 1.5 mL min^{-1}. Error bars represent the standard deviation of a triplicate measurement. (c) Boxplot for the yeast cell diameter using 10^7 cells mL^{-1} for fractionation. The outlets are numbered in ascending order starting from the inside of the channel with outlet 1. Data of a triplicate measurement was used. The cell concentration of outlets 7 and 8 was too low to get a representative number of cells for analysis.

Two commercially available microfluidic spiral chip sizes (Figure A.10) for inertia-based cell separation were selected (500 $\times$ 120 µm, and 300 $\times$ 80 µm) based on their ability to separate fluorescent polystyrene particles of differing sizes (7.3 µm and 15.25 µm) according to the supplier's information [220]. The 500 $\times$ 120 µm chip was initially tested at a flow rate of 1.5 mL min^{-1} (a_p / D_h > 0.07 for a_p = 13.60 µm). First, the cell throughput, a known limitation in such processes [136, 140], was assessed at varying concentrations (10^6, 5 $\times$ 10^6 and 10^7 cell mL^{-1}) presented in Figure 4.6 b and A.11. The proportion of single cells increased from outlet 2 (approximately 40%) to outlet 6 (nearly 80%) independent of the used cell concentration. The corresponding average cell diameter decreased from 9.84 $\pm$ 2.61 µm in outlet 2 to 7.94 $\pm$ 1.24 µm in outlet 6, shown in Figure 4.6 c, suggesting potential size and age fractionation. Cells in outlet 1 were primarily smaller than 9 µm, likely entrained in Dean vortices rather than achieving an equilibrium position. Figure A.11 confirmed the collection of cells larger than 9 µm predominantly in outlets 2, 3, and 4, regardless of cell concentration. The separation criterion was 9 µm, in order to separate larger from small

single cells. In outlets 5 and 6, mostly cells smaller than 9 µm could be selected; however, the collected proportion was below 10%. Contrary to expectations under the applied conditions, the smaller cells were still entrained in the Dean vortices and distributed across all outlets, but not focused. A fractionation with the 300×80 µm channel (Figure 4.7 a and b, a_p / D_h >
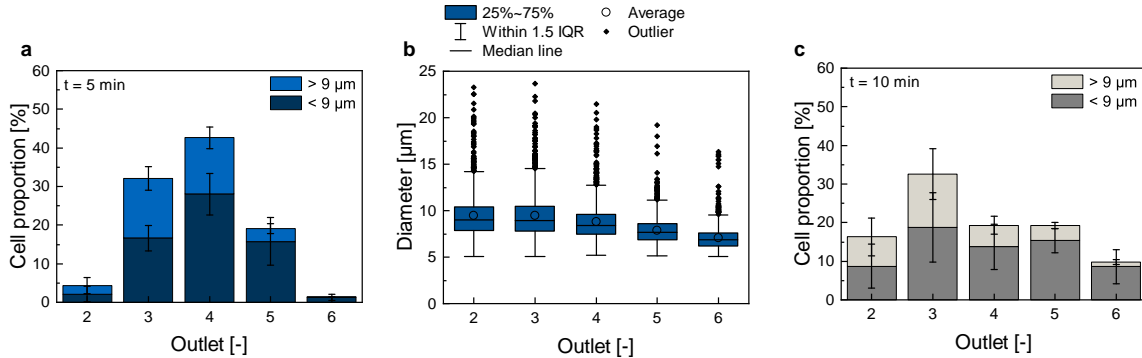
Figure 4.7: Yeast cell fractionation using the 500 x 120 µm spiral chip at 1.5 mL min^{-1}. (a) Cell proportion of cells < and > 9 µm are shown for the different outlets for process time t = 5 min. 1231 cells were analyzed per outlet 2 – 6. The error bar represents the standard deviation of a triplicate measurement. (b) Boxplot for the yeast cell diameter using 10^7 cells mL^{-1} for fractionation. Data of a triplicate used. (c) Cell proportion of cells < and > 9 µm are shown for the different outlets for process time t = 10 min. 1452 cells were analyzed per outlet 2 – 6. The error bar represents the standard deviation of a triplicate measurement. The cell concentration of outlets 1, 7 and 8 was too low to get a representative number of cells for analysis. The outlets are numbered in ascending order starting from the inside of the channel with outlet 1.

0.07 for $a_p = 8.90$ µm) at the same flow rate resulted in a similar pattern: Smaller cells were distributed across all outlets due to inadequate net lift forces compared to Dean drag forces. However, the larger cells were mainly focused in outlets 3 and 4, so that in outlets 5 and 6 almost only single cells were collected. The average diameter decreased from 9.44 ± 2.41 µm in outlet 2 to 7.04 ± 1.28 µm in outlet 6. Figure 4.7 c shows the same experiment performed as triplicate, but for a longer process time of t = 10 min instead of t = 5 min (Figure 4.7 a). The distribution changed significantly for the longer processing time, highlighting the sensitivity of the fractionation process to external factors like chip blockage because of dust [140]. Thus, careful handling, consequent microscopic monitoring of the chips, and working in a clean room evolved to be essential for having a reproducible process.

Despite the successful application of Dean vortices in particle separation [137], the size difference among yeast cells was not sufficient for effective separation. The efficiency of binary separation of two distinct sizes of PMMA particles (8.8 and 14.1 µm, Figure A.12) was higher than that of yeast fractionation, which was not higher than $83 - 87\%$ under all conditions tested (Table A.1). The wide size distribution of yeast cells (5 µm to over 20 µm in some agglomerates), but the main proportion between 7 and 11 µm, and their non-uniform

shape (elliptical, budding, or irregular in agglomerates) presented additional challenges not encountered with spherical PMMA particles. Age analysis by cytometry was not possible because of a handling fault. Thus, a statement about the capability of age fractionation by spiral sorting was not possible.

Using only outlets 5 and 6 for the separation of single cells, the throughput would be $3.07 \pm 1.24 \times 10^6$ cells min^{-1} for t = 5 min, and $4.36 \pm 1.36 \times 10^6$ cells min^{-1} for t = 10 min. It would be possible to collect mainly single yeast cells for further processing; however, a lot of yeast cells would be lost to other fractions. To separate enough cells for the subsequent magnetophoretic fractionation, the process would take up to $2-3$ h (for needed 3.5×10^8 cells for magnetophoretic fractionation, washing steps included). This process was considered too long; an acceptable time would be 30 minutes. Thus, the focus was solely on magnetophoretic cell fractionation.

4.4 Simulative and Experimental Process Development of the Magnetophoretic Yeast Cell Fractionation

In the size-based yeast cell fractionation using the spiral sorter, it evolved that while agglomerate separation is feasible, the enrichment of single cells at high throughput remains inefficient. Consequently, a model-based approach was employed to assess the potential (negative) impact of cell enlargement due to budding or agglomeration on fractionation efficiency in a magnetophoretic fractionation process. A simulation-based approach was employed to reduce the experimental effort.

The used model was composed of a heterogeneous yeast cell population comprising 100 spherical cells, reflecting an experimentally determined age distribution (61% daughter cells, 28% first generation, 7% second generation, and 3% third generation mother cells), consistent with previous experimental findings [109] [211]. Each age group exhibited a size distribution derived from ImageJ analysis, with a total permeability of magnetically-labeled yeast cells derived from nanoparticle and linker-protein@nanoparticle characterization data (Sections 4.1, 4.2). Given the simulation of only 100 cells and known concentration-dependent effects like magnetic convection and aggregation [66], a black box model was used. This model assumed scaled-up volumes and permeabilities to replicate real flow channel deflection (further details given in the Materials and Methods Section A.5). The simulation, featuring increased cell volumes to represent agglomerated or budding cells, was focused on their collection in different outlets (Figure 4.8 a). A single-point release method was utilized for precise volume comparison, detailed in the Appendix A.5. Results indicated that in outlet A, volume increase

led to a minor deviation of 5%; however, cell proportion in outlet B diminished with volume increase due to greater magnetophoretic force (Equation 1.7), causing higher deflection to outlets C and D. Notably, in outlet D, the proportion of the largest cells was 13% higher compared to originally sized cells. Although experimental data suggested that agglomerated or cross-linked cells constituted less than 10% of a heterogeneous yeast population, budding cells accounted for approximately 45% [211]. According to Zakhartsev et al., the volume increase resulting from budding was up to 13%. Additionally, same-aged cells exhibited growth during the G1 phase, with size control influenced by nutrient conditions [189]. As presented in Figure 4.8 a, a volume increase of only 20% resulted in small deviations in cell proportions between 2 to 5%.
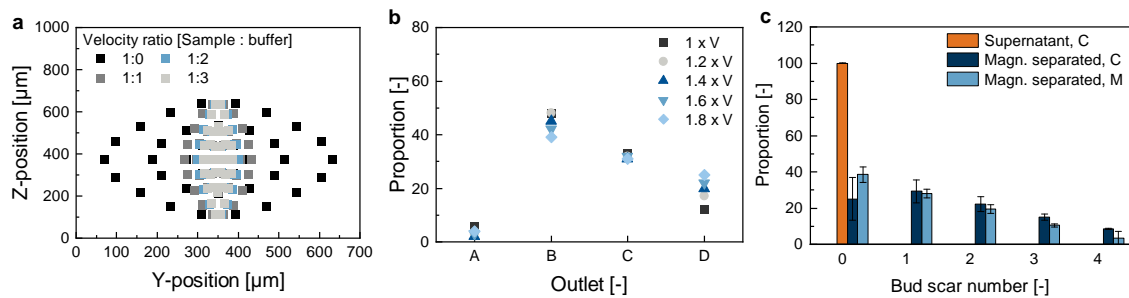
Figure 4.8: (a) Simulation of particle deflection behavior in a rectangular channel, using a model of 100 yeast cells with incrementally increased volumes. The simulation follows a single point release approach, with additional details provided in Section A.5. (b) Simulation of hydrodynamic focusing in both straight (with a sample to sheath flow velocity ratio of 1:0) and Y-shaped channels (featuring various other ratios). Z- and Y-positions of fluidic streamlines within these channels are visualized. (c) Proportion of the different age distribution of yeast cells in a batch culture, categorized by the number of bud scars. It differentiates between the supernatant (non-magnetically separated fraction) and the magnetically separated fraction. The age distribution was determined using both cytometry (C) and microscopy (M) [109].

The influence of volume increase on magnetophoretic fractionation was initially assessed using a single-point release. However, the sample inlet size of the 3D-printed channel, ranging from 400 to 700 μm depending on the geometry [211], indicated that a single point release might not accurately represent real inlet flow dynamics. The magnetophoretic force, as described in Equation 1.7, diminishes with increasing distance from the magnet due to the exponential decay of the magnetic field gradient [211]. Consequently, hydrodynamic focusing via sheath flow was necessary to counteract this effect [95, 221]. As depicted in Figure 4.8 b and further demonstrated in Figure 4.9 a, the introduction of a Y-shaped channel successfully focused the sample flow. This design narrowed the flow width from 600 μm in a straight channel to 200 μm by only introducing a Y-shaped channel, while maintaining a 1:1 flow velocity ratio between the sheath and sample flows [222, 223]. Additionally, increasing the sheath-to-sample

flow ratio further concentrated the sample stream, a result confirmed by both simulations (Figure 4.8 a) and experimental observations (Figure 4.9 a and b). However, beyond a specific flow rate ratio of 1:3, the sample stream became disrupted, as evidenced experimentally but not predicted in the simulations (Figure 4.9 c). These findings necessitated modifications to the initially used rectangular channel, which had a sample width of 500 µm, constrained by the resolution and cleaning capabilities of the 3D printer. For other channel geometries, such as trapezoidal and pinch-shaped, a sheath fluid velocity ratio of 1:1 was successfully implemented [211].
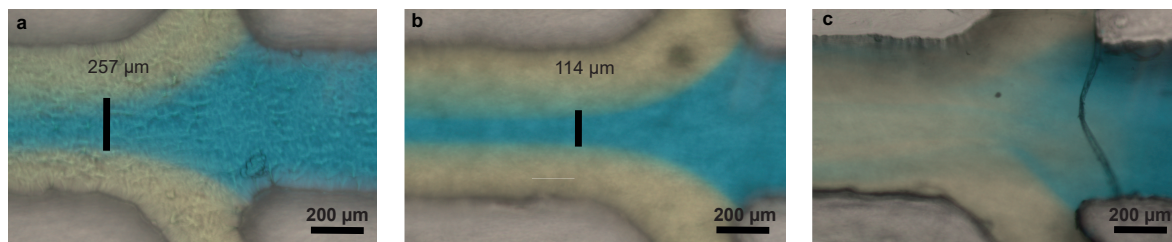
Figure 4.9: Light microscopy images of the hydrodynamic focusing of the sample stream in a Y-shaped channel using blue food colorant at a 1:1 (a), 1:2 (b), and 1:3 (c) sample to sheath flow velocity.

As Wittmann and Eigenfeld et al. highlighted, there was a need for sample homogenization to avoid sedimentation of the yeast cells and to optimize the magnetophoretic fractionation process. Ensuring a uniform yeast cell concentration in the input sample is essential, as the magnetic dipole moment influencing the magnetophoretic force on labeled yeast cells is a function of both concentration and agglomerate size (Equation 1.7). In brewing, both top-fermenting *S. cerevisiae* and bottom-fermenting *S. pastorianus var. carlsbergensis strains* are used, differing in their flocculation and sedimentation characteristics [2]. The *S. pastorianus ssp. carlsbergensis* strain used in this study, primarily non-flocculating and consisting of single or budding cells, showed significant sedimentation in the absence of a dispersion method, leading to concentration inhomogeneities. Traditional magnetic stirring for mixing was unsuitable due to the usage of magnetic nanoparticles. Alternative methods included using a shaker and a teetering rocker with an internal sphere for mechanical mixing. The latter proved most effective, uniformly dispersing yeast cells and preserving nearly 100% of the initial cell count without compromising cell viability or magnetic labeling [211].

Wittmann and Eigenfeld et al. demonstrated that magnetically labeled yeast cells, subjected to the inhomogeneous magnetic field in the magnetophoretic fractionation process, experience a magnetophoretic force leading to their motion. This motion was increased by interparticle and hydrodynamic interactions, namely, cooperative and convective magnetophoresis [100–103]. The tendency of particles to aggregate is measured by the aggregation parameter (N*) [66], with a calculated value of N* = 0.01 for the ION@Si@EDTA under the applied

conditions; values above 1 would lead to particle agglomeration. The magnetic nanoparticles used in the study encapsulated in a silica shell with a low saturation magnetization, showed reduced magnetic dipole coupling. Despite this, the induced convective motion due to hydrodynamic interaction was significant, as indicated by a high magnetic Grashof number of Gr = 603.2 [66] [211]. Preliminary experiments assessed the impact of convective motion on separation efficiency, comparing the behavior of yeast cells alone, nanoparticles alone, and a mixture of both without linker-protein. Results showed that yeast cells were unaffected by the magnetic field in absence of nanoparticles, while the nanoparticles were significantly deflected to a specific chip outlet under magnetophoretic force. When mixed, the non-magnetic yeast cells were influenced by the nanoparticles' movement. This magnetic-induced convective motion could reduce the separation efficiency in a heterogeneous culture, possibly causing the comigration of non-magnetically labeled daughter and magnetically labeled mother cells [211]. This phenomenon was further explored in another study by Wittmann and Krucker-Velasquez et al., employing a model system of non-magnetic and magnetic nanoparticles [212]. Modifying the hydrodynamic force or magnetic field strength did not effectively counteract this effect, as these changes only amplified the magnetically induced hydrodynamic force without surpassing the magnetophoretic force's threshold [211]. An experimentally validated simulation using this nanoparticle model system within the millifluidic channel indicated that the entrainment of non-magnetic entities by magnetic ones was unavoidable across a wide range of Péclet and Mason numbers, representing the interplay between magnetic versus diffusive, and shear versus magnetic dipole forces [212].

Magnetophoretic microfluidic platforms employing magnetic labeling are commonly used in fractionation processes [48, 107, 108]. An example is the work of Robert et al., who effectively separated magnetic macrophages from non-magnetic monocytes using a lower magnetic field strength (H = 0.26 T) compared to that employed in our study (H = 0.41 T) [48]. In contrast, our approach involved the use of larger, centimeter-scale millifluidic channels. These channels enabled higher throughput, concentrations, and flow rates, but necessitated a stronger magnetic field, thereby inducing significant magnetic convective motion [211]. Therefore, Lin et al. developed a two-stage method for separating magnetically labeled white blood cells from co-migrating red blood cells [98]. Following these precedents, Wittmann and Eigenfeld et al. implemented a two-step process for age-based fractionation. Initially, a batch separation was performed outside the chip, separating non-magnetic daughter cells from magnetically labeled mother cells, as depicted in Figure 4.8 c. Subsequently, the magnetically enriched fraction, predominantly comprising mother cells, was subjected to further age-based fractionation within the chip, avoiding the comigration of daughter cells [211]. This sequential approach integrated the initial preparatory separation with the refined, in-chip fractionation, thereby enhancing the specificity and efficiency of the process, as described in the following section.

4.5 Advancing to a Millifluidic Multistep Process for Age-specific Yeast Cell Fractionation

Using three different 3D-printed, millifluidic platforms (Figure 4.10), Wittmann and Eigenfeld et al. conducted a comparative analysis to assess their efficacy in age-based fractionation of yeast cells. Each geometry incorporated four outlets, with outlet A, the furthest from the magnet, expected to collect the youngest mother cells, and outlet D, nearest to the magnet, collecting the oldest cells. The geometries examined included a classical rectangular channel [48, 224], a trapezoidal channel for enhanced magnetic field gradient exposure [113], and a pinch-shaped channel designed to facilitate dual criteria separation [36, 81, 199]. [211]
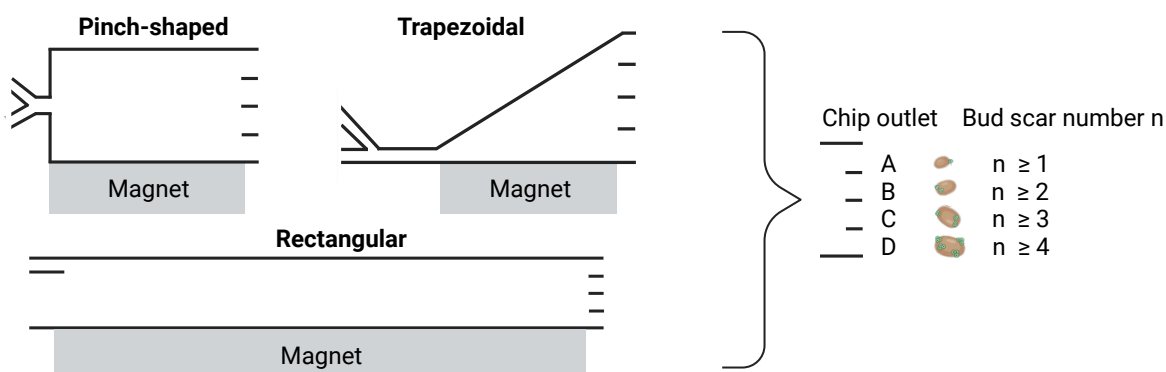
Figure 4.10: Scheme of the three different millifluidic chips (rectangular, trapezoidal, and pinch-shaped) used for age-based fractionation. All chips were produced by 3D printing. [211]

According to Wittmann and Eigenfeld et al., the pinch-shaped channel proved particularly effective, as yeast cells, which enlarge with age as detailed in Section 1.3.1, were fractionated using both magnetophoresis and size-based criteria. It also revealed that batch separation across all chip geometries successfully separated the daughter cells, evident from the negligible average bud scar numbers. However, the trapezoidal channel was not able for age-based fractionation, contrary to the rectangular channel, where the bud scar count increased from 2.08 ± 0.41 at outlet A to 3.67 ± 1.55 at outlet D. The high standard deviation, attributed to the low number of yeast cells collected in outlet D, was further reinforced by the extended chip length in the millifluidic design, leading to increased magnetically-induced convection and diffusion [212]. Consequently, separation selectivities were relatively low, at 0.48 for outlet A and 0.66 for outlet D. Conversely, the pinch-shaped channel demonstrated better separation efficacy, with selectivities of 1.00 ± 0.00 for outlet A and 0.84 ± 0.08 for outlet D. An increase in average bud scar numbers from 2.33 ± 0.82 in fraction A to 6.27 ± 0.45 in fraction D indicated an effective enrichment of older cells. Despite this

advancement, a precise bud scar number fractionation per outlet remained unfeasible, owing to the intrinsic limitations imposed by the millifluidic scale, such as unavoidable magnetically induced convective movements. Furthermore, the variability in cell size during different stages of the cell cycle [189, 225] influenced the fractionation process as well. Remarkably, the pinch-shaped channel was able to collect $1.18 \times 10^6 \pm 1.54 \times 10^5$ cells mL^{-1}, compared to the lower throughput of $8.73 \times 10^3 \pm 8.00 \times 10^3$ cells min^{-1} in the rectangular channel. This innovative approach using a pinch-shaped channel, enhanced known throughputs for yeast cell fractionations between $10 - 3.75 \times 10^4$ cells min^{-1} [199, 200] up to $1.90 \times 10^6 \pm 5.71 \times 10^5$ cells min^{-1}. This novel age-based fractionation method, using a 3D-printed chip that sorts yeast cells by bud scar count, is a high-throughput millifluidic platform, enabling growth, metabolomics, and gene expression studies. [211].

Simulative studies contrast the experimental findings predicting the highest bud scar number increase in the rectangular channel from 1.04 to 3.73, whereas the pinch-shaped channel only increased from 1.09 to 3.70 (Figures A.13 and A.14). A clear size increase could be observed with channel outlets nearer to the magnet. The simulation of the trapezoidal fractionation completely contradicts the experimental results, as all cells were collected in outlet D. This further emphasizes that magnetically induced effects like convection and diffusion can not be neglected in millifluidic processes, as discussed in Subsection 1.2.1, Section 4.4, and [212]. Unlike simulated magnetophoretic microfluidic fractionations [199, 226, 227], where these effects were less pronounced, millifluidic systems have to include them due to their larger scale (Equations 1.10, 1.8).

Using the fractionated cells of the pinch-shaped channel, metabolomic studies conducted by Wittmann and Eigenfeld et al. revealed that older cells exhibited increased levels of NAD$^+$, lactic acid, and formic acid, along with a five-fold increase in adenosine diphosphate (ADP). This suggested a decline in ATP levels, ATPase activity, and an increase in intracellular acidification [228]. The study also found age-related changes in amino acid levels, with essential amino acids like leucine, methionine, phenylalanine, tryptophan, and tyrosine increasing in older cells, while isoleucine and valine remained consistent. This could be due to younger cells using more amino acids for protein synthesis and other growth-related activities [109, 229], indicating a metabolic shift. These pathways might encompass energy production, nucleotide synthesis, or alcohol formation, reducing the accumulation of specific amino acids. Notably, the synthesis of esters, an energy-intensive process demanding cofactors, could be linked to this hypothesis [230]. Regarding gene expression levels, a 50% upregulation in genes ADH1 and MEP2 in older cells was observed, and a two-fold increase in GCR1, HSP12, HXK2, and PHO5, indicating changes in metabolism and energy regulation in aging cells. However, HSP104 expression remained consistent. These findings highlighted the impact of aging on cellular processes, particularly metabolism and stress response [180, 231] with older cells

potentially requiring increased glycolytic activities [232–235] to meet energy needs. Stress conditions, especially during anaerobic fermentations, can reduce growth and biomass due to energy shortages [109], affecting processes like aroma or protein production. [211] As Eigenfeld and Wittmann et al. found out, daughter cells exhibit a 27% higher growth rate in aerobic conditions than mother cells and a 104% higher growth rate under anaerobic conditions [109].

In sum, age-related changes in gene expression, particularly in genes governing metabolism and stress response, could be identified. Aging cells appeared to modulate their metabolic pathways, potentially reflecting energy inefficiencies. Therefore, the developed 3D-printed millifluidic platform offers a non-invasive, high-throughput approach for age-based fractionation of yeast cells. This technique, utilizing a pinch-shaped channel geometry for combined magnetophoretic and size-based sorting, could enable in-line age analysis and yeast processing techniques, with significant implications for the beverage and pharmaceutical industries.

5 Summary and Outlook

Saccharomyces yeast is an important microorganism, as it is used in many industries and serves as a model organism in aging research. To elucidate the correlation between the age of individual yeast cells and parameters such as cultivability, production rate, growth dynamics, metabolomic profiles, and gene expression patterns, it is necessary to selectively enrich yeast cells of a specific age in high throughput. That is why this project aimed to develop an age-based fractionation process of a heterogeneous yeast cell population. Yeast cells proliferate by budding during their replicate lifespan, so they possess bud scars depending on age. This project utilized these bud scars to magnetically label these individual cells based on age, enabling their sorting in a flow channel within a magnetic field. The labeling involved a bifunctional protein-linker: One end bound to the chitin-rich bud scars via a ChBD, while the other end, featuring a his tag, attached to MNPs. The magnetic bud scar targeted labeling resulted in each cell's age-specific magnetic susceptibility, with older cells having more bud scars for MNP agglomerate binding, thus increasing their magnetic deflection.

In this study, the bottom-fermenting *S. pastorianus ssp. carlsbergensis* TUM 34/70 strain was used, and the Chair of Brewing and Beverage Technology supplied the linker-protein.

For the efficient age-based magnetophoretic separation of the yeast cells, MNPs had to meet specific criteria to ensure consistent magnetic response relative to the number of bud scars. This included precise bud scar binding via the linker-protein and uniform linker-protein@nanoparticle agglomerates in pH 6 – 8 buffer. Additionally, time-stable agglomerate homogeneity, colloidal stability of MNPs, and steric stabilization were essential to prevent undesirable agglomeration in magnetic fields. However, the smaller and more stable the agglomerates are, the stronger magnetic fields are required for manipulation due to their lower magnetic moments. Additionally, higher MNP concentrations increase the volumetric magnetization, and the particle velocity in the magnetophoretic millifluidic channel rises. That is why the first part of this thesis dealt with the nanoparticle design and its analysis under process conditions.

Meeting these criteria, BIONs emerged as potential MNPs. Their agglomeration behavior could be controlled via pH and viscosity. However, they agglomerated under magnetic fields

and bound non-specifically to yeast cell surfaces in certain buffers. As a mitigation, adding a silica shell increased the colloidal stability of BIONs. The additional surface functionalization with EDTA for nickel ion chelation facilitated the linker-protein binding. A robust synthesis method was established for these ION@Si@EDTA nanoparticles in milli- to liter-scale. It turned out that future enhancements should include automation of the synthesis process to minimize variations in particle characteristics, as in this project, e.g. due to the manual TEOS addition. Moreover, more nanoparticles must be supplied if the yeast cell fractionation process should be further scaled up.

Next, the binding behavior of the linker-protein to the ION@Si@EDTA was analyzed in various buffers. The highest binding was achieved with a 20 mM MOPS buffer at pH 7.3. The binding specificity was confirmed using microscopy and cytometry, the latter of which was developed by the cooperation partner. Contrary to expectations, the maximum number of bud scars was 5 – 7, as it is strain-dependent on the one hand, and on the other hand, old cells make up only $< 3 – 5$ % of the total population, which are lost in the cytometric analysis in the signal-to-noise ratio. Furthermore, to reduce cross-linkage, an optimal linker-protein@nanoparticle ratio was determined. Future efforts should optimize the labor-intense binding processes to increase the overall process efficiency. Therefore, the data analysis for age determination should be further improved to be fully automatic and robust.

For the magnetophoretic fractionation, a millifluidic chip design was favored over microfluidic alternatives, enabling higher cell throughput and more straightforward production via 3D printing. Key process improvements included developing a dispersion method for uniformly concentrated yeast samples and a rocker shaker mechanism to prevent sedimentation without impacting cell labeling or viability. An alternative to the magnetophoretic fractionation, label-free sorting based on size-age correlation, was also explored but found to be less effective due to minor size differences in aged or agglomerated cells. Future research might examine separating large agglomerates before magnetophoretic fractionation, requiring new spiral geometries and intense studying of the generated Dean and lift forces. In contrast, simulative studies indicated minimal impact of large agglomerates on the fractionation process.

The colloidal stability of the used ION@Si@EDTA avoided magnetic aggregation successfully; however, because of the millimeter scale of the flow channels, magnetically induced convection was unavoidable in reasonable process conditions. This was evaluated by a model system consisting of non-magneto-responsive and magneto-responsive nanoparticles. The results showed that non-magneto-responsive nanoparticles maintained high and constant separation efficiencies with increasing Péclet numbers. Conversely, the separation efficiency of magneto-responsive nanoparticles initially decreased at lower concentrations but improved at higher concentrations due to enhanced dipole-dipole interactions. In mixed nanoparticle systems, increasing magnetic field strength did not impact the separation efficiency of

magneto-responsive nanoparticles, but it reduced the efficiency of non-magneto-responsive nanoparticles. Interestingly, the process purity of magneto-responsive nanoparticles remained stable, indicating hydrodynamic forces from magneto-responsive nanoparticles influenced the non-magneto-responsive ones. Brownian motion simulations extended beyond experimental parameters confirmed these dynamics, revealing that the magnetic field gradient and separation efficiency decreased proportionally.

So, despite varying the Péclet and Mason numbers, the non-magnetically young daughter cells would always comigrate along with the hydrodynamically generated motion of the magnetically labeled mother cells. That is why a multi-step approach, consisting of a static batch separation, separated the non-magnetically labeled daughter cells from the magnetically labeled mother cells. These were then introduced for further age-based sorting in the flow channel. A rectangular, a trapezoidal, and a pinch-shaped channel were tested using a simulative and experimental approach. The simulative model used a black box model to summarize the described magnetic effects besides the magnetophoretic force; however, it proved not robust enough. Here, replacing the particle-based approach and modeling the magnetic effects in detail would be useful. Then, the simulation can help optimize and understand the magnetophoretic process. To achieve the highest possible separation selectivities, the three chip geometries resulting in four age groups (≥ 1, ≥ 2, ≥ 3, ≥ 4) were compared in the experimental approach. The pinch-shaped channel, relying on the magnetophoretic and the size-based sorting principle, proved to be the best geometry, increasing the average bud scar number from 2.33 ± 0.82 in fraction A to 6.27 ± 0.45 in fraction D, indicating an effective enrichment of older cells. The reproducible process reached high selectivities and a high throughput of $1.9 \times 10^6 \pm 5.71 \times 10^5$ cells min^{-1}.

Subsequent metabolomic analysis of the pinch-channel sorted cells highlighted age-related changes, suggesting potential application for optimizing yeast-based processes in various industries. In detail, older cells showed increases in NAD$^+$, lactic acid, and formic acid levels, suggesting decreased ATP levels and intracellular acidification. Younger cells, characterized by increased growth and division, likely exhibit decreased amino acid levels due to increased utilization for protein synthesis while also undergoing a metabolic shift that prioritizes pathways like energy production and nucleotide synthesis, leading to reduced amino acid accumulation. Genomic analysis revealed that genes related to the glycolytic pathway and stress regulation were upregulated for older cells. This indicated that these aged cells try to maintain their cellular functionality under stress conditions. Future work should focus on age-dependent aroma analysis for beverage products and transcriptome studies to further understand age-based cellular differences.

The process was designed at a millifluidic scale for high-throughput fractionation instead of a traditional microfluidic chip to enable growth and omics studies. 3D printing to produce

a millifluidic chip presents a robust alternative to traditional microfluidic chips, facilitating that high-throughput fractionation [143, 145]. However, the larger centimeter scale is not without challenges, and future improvements in printing accuracy promise even smaller and more complex geometries, potentially replacing conventional non-additive manufacturing methods.

Extending the developed method to strains like *Komagataella phaffi* used in recombinant protein production demands optimization and adaptation. While successful in batch separation, further refinement is required to accommodate differences in cell size, bud scar size, and chitin content.

The separation and usage of young daughter cells, which have been shown to grow faster, could be used in pharmaceutical or beverage industries, as they can enhance product yields [109]. Here, the separation process would be only binary, so one does not have to distinguish between differently aged mother cells. Separated young cells could be used as inoculum to control the overall production process. This would enable the study of the effects of the adapted inoculum on end-product quality and yeast degeneration. The usage in industry would necessitate an upscale of the established batch separation method, possibly realized through high-gradient magnetic separation or expanded bed chromatography [236–238]. The high-gradient magnetic separator could use the existing labeling method, separating the non-labeled young daughter cells from the magnetically labeled older mother cells. However, this process needs to be newly designed, as nanoparticle agglomeration does not have to be prevented anymore, but it would be beneficial to increase the magnetic moment. To increase the magnetization, the silica shell size has to be decreased, and the bud scar-specific binding has to be ensured. As a nanoparticle-free alternative, expanded bed chromatography is a potentially scalable method, where cells possessing a bud scar bind to a stationary phase like cellulose by a similar linker protein, and daughter cells are washed out.

From an economic point of view, using an adapted inoculum brings advantages such as time savings, cost reduction, sustainability through multiple uses of yeast cultures, consistent product quality, and capacity expansion through shorter process times. An accelerated fermentation using technologically adapted yeast cultures by 20 % would correspond to cost savings of € 170.000 – € 850.000, considering a production value of € 42.5 – 212.5 hl^{-1} in a micro, small, and medium-sized (SME) breweries (10.000 – 50.000 hl) [239]. Alternatively, the increased efficiency, which saves time, can also lead to increased product diversification due to shorter tank filling times. Another aspect is sustainability through a reduction in energy consumption. At the same time, refining the harvested yeast can reduce the material outflow from production or increase the value of reuse within the company. By reducing the time required, the brewery can benefit from the flexibility of its production volume with the same plant capacity. The technology of yeast separation can be integrated on a pilot scale

as part of a scale-up, as shown earlier [238]. For example, with a yeast cell concentration of 12 million cells mL^{-1} and a flow rate of 2 m h^{-1}, a volume of 300 hl could be processed in 5 days with six columns (diameter 0.5 m) connected in parallel.

The knowledge and technological control of the cell age would directly improve the existing yeast management and create the basis for the specialized application. Additionally, the fine age-based fractionation achieved through millifluidics opens new ways for exploring aging processes, offering potential insights into cellular dynamics and longevity. In conclusion, the thesis not only offers practical solutions for industrial processes but also contributes to the broader scientific understanding of cellular aging.

6 Bibliography

1. Nielsen, J. Yeast systems biology: model organism and cell factory. *Biotechnology Journal* **14,** 1–9. ISSN: 18607314 (9 2019).

2. Stewart, G. *Brewing and Distilling Yeasts* ISBN: 9783319691244 (Springer International Publishing AG 2017, 2017).

3. Lippuner, A. D., Julou, T. & Barral, Y. Budding yeast as a model organism to study the effects of age. *FEMS Microbiology Reviews* **38,** 300–325. ISSN: 01686445 (2 2014).

4. O'Laughlin, R., Jin, M., Li, Y., Pillus, L., Tsimring, L. S., Hasty, J. & Hao, N. Advances in quantitative biology methods for studying replicative aging in saccharomyces cerevisiae. *Translational Medicine of Aging* **4,** 151–160. ISSN: 24685011 (2020).

5. Henley, E. J., Seader, J. D. & Roper, D. K. *Separation process principles* 3rd ed. ISBN: 9780470646113 (Wiley, 2011).

6. Gharib, G., Bütün, İ., Muganlı, Z., Kozalak, G., Namlı, İ., Sarraf, S. S., Ahmadi, V. E., Toyran, E., van Wijnen, A. J. & Koşar, A. Biomedical applications of microfluidic devices: a review. *Biosensors* **12.** ISSN: 20796374 (11 2022).

7. Lee, W., Tseng, P. & Carlo, D. D. *Microtechnology for Cell Manipulation and Sorting* (eds Howe, R. T. & Ricco, A. J.) ISBN: 978-3-319-44137-5 (Springer Internationsal Publishing Switzerland, 2017).

8. Herzenberg, L. A., Sweet, R. G. & Herzenberg, L. A. Fluorescence-activated cell sorting. *Scientific American* **234,** 108–118. ISSN: 00368733, 19467087 (1976).

9. Mapelli, V. & Bettiga, M. *Yeast Metabolic Engineering Methods and Protocols* 2nd ed., 39–58. ISBN: 978-1-0716-2398-5 (Springer Nature, 2022).

10. Miltenyi, S., Müller, W., Weichel, W. & Radbruch, A. High gradient magnetic cell separation with macs. *Cytometry* **11,** 231–238. ISSN: 10970320 (2 1989).

11. Hendrickson, D. G., Soifer, I., Wranik, B. J., Kim, G., Robles, M., Gibney, P. A. & McIsaac, R. S. A new experimental platform facilitates assessment of the transcriptional and chromatin landscapes of aging yeast. *eLife* **7,** 1–31. ISSN: 2050084X (2018).

12. Picot, J., Guerin, C. L., Kim, C. L. V. & Boulanger, C. M. Flow cytometry: retrospective, fundamentals and recent instrumentation. *Cytotechnology* **64,** 109–130. ISSN: 09209069 (2 2012).

13. Sutermaster, B. A. & Darling, E. M. Considerations for high-yield, high-throughput cell enrichment: fluorescence versus magnetic sorting. *Scientific Reports* **9.** ISSN: 20452322 (1 2019).

14. Chai, M., Ye, Y. & Chen, V. Application of rotational vibration in a submerged hollow fibre membrane system for bioseparation of high concentration yeast suspensions. *Journal of Membrane Science* **573,** 145–156. ISSN: 18733123 (2019).

15. Lieblová, J., Beran, K. & Streiblová, E. Fractionation of a population saccharomyces cerevisiae yeasts by centrifugation in a dextran gradient. *Folia Microbiologica* **9,** 205–213 (1964).

16. Sebastian, J., Carter, B. L. & Halvorson, H. O. Use of yeast populations fractionated by zonal centrifugation to study the cell cycle. *Journal of Bacteriology* **108,** 1045–1050. ISSN: 00219193 (3 1971).

17. Powell, C. D., Quain, D. E. & Smart, K. A. The impact of brewing yeast cell age on fermentation performance, attenuation and flocculation. *FEMS Yeast Research* **3,** 149–157. ISSN: 15671356 (2 2003).

18. Wang, Y., Lilley, K. S. & Oliver, S. G. A protocol for the subcellular fractionation of saccharomyces cerevisiae using nitrogen cavitation and density gradient centrifugation. *Yeast,* 191–198 (February 2008).

19. Lange, H., Taillandier, P. & Riba, J.-P. Effect of high shear stress on microbial viability. *Journal of Chemical Technology and Biotechnology* **76** (5 2001).

20. Chlup, P. H., Bernard, D. & Stewart, G. G. Disc stack centrifuge operating parameters and their impact on yeast physiology. *Journal of the Institute of Brewing* **114,** 45–61. ISSN: 00469750 (1 2008).

21. Correia-Melo, C. *et al.* Cell-cell metabolite exchange creates a pro-survival metabolic environment that extends lifespan. *Cell* **186,** 63–79.e21. ISSN: 10974172 (1 2023).

22. Iv, C. W. S., Reyes, C. D. & López, G. P. Microfluidic cell sorting: a review of the advances in the separation of cells from debulking to rare cell isolation. *Lab on a Chip* **15,** 1230–1249. ISSN: 14730189 (5 2015).

23. Shen, Y., Yalikun, Y. & Tanaka, Y. Recent advances in microfluidic cell sorting systems. *Sensors and Actuators, B: Chemical* **282,** 268–281. ISSN: 09254005 (2019).

24. Ruffert, C. *Mikrofluidische Separationsverfahren und -systeme* 1–130. ISBN: 9783662564486 (Springer-Verlag GmbH Deutschland, 2018).

25. Jones, J. E. On the determination of molecular fields.— i. from the variation of the viscosity of a gas with temperature. *Proceedings of the Royal Society of London. Series A, Containing Papers of a Mathematical and Physical Character* **106,** 441–462 (738 1924).

26. Jones, J. E. On the determination of molecular fields. — ii. from the equation of state of a gas. *Proceedings of the Royal Society of London. Series A, Containing Papers of a Mathematical and Physical Character* **106,** 463–477 (738 1924).

27. Stokes, G. G. On the theories of the internal friction of fluids in motion and of the equilibrium and motion of elastic solids. *Trans. Cambridge Philos. Soc.* **8,** 287–319 (1845).

28. Squires, T. M. & Quake, S. R. Microfluidics: fluid physics at the nanoliter scale. *Reviews of modern physics* **77** (3 2005).

29. Ismagilov, R. F., Stroock, A. D., Kenis, P. J., Whitesides, G. & Stone, H. A. Experimental and theoretical scaling laws for transverse diffusive broadening in two-phase laminar flows in microchannels. *Applied Physics Letters* **76,** 2376–2378. ISSN: 00036951 (17 2000).

30. Kamholz, A. E. & Yager, P. Theoretical analysis of molecular diffusion in pressure-driven laminar flow in microfluidic channels. *Biophysical Journal* **80,** 155–160. ISSN: 00063495 (1 2001).

31. Agnihotri, P. Analysis of interfacial mixing zone and mixing index in microfluidic channels. *Microfluidics and Nanofluidics* **27.** ISSN: 16134990 (2 2023).

32. Huysmans, M. & Dassargues, A. Review of the use of péclet numbers to determine the relative importance of advection and diffusion in low permeability environments. *Hydrogeology Journal* **13,** 895–904. ISSN: 14312174 (5-6 2005).

33. Nasiri, R., Shamloo, A., Ahadian, S., Amirifar, L., Akbari, J., Goudie, M. J., Lee, K. J., Ashammakhi, N., Dokmeci, M. R., Carlo, D. D. & Khademhosseini, A. Microfluidic-based approaches in targeted cell/particle separation based on physical properties: fundamentals and applications. *Small* **16.** ISSN: 16136829 (29 2020).

34. Zheng, S., Lin, H., Liu, J. Q., Balic, M., Datar, R., Cote, R. J. & Tai, Y. C. Membrane microfilter device for selective capture, electrolysis and genomic analysis of human circulating tumor cells. *Journal of Chromatography A* **1162,** 154–161. ISSN: 00219673 (2 SPEC. ISS. 2007).

35. Chen, X., Cui, D. F., Liu, C. C. & Li, H. Microfluidic chip for blood cell separation and collection based on crossflow filtration. *Sensors and Actuators, B: Chemical* **130,** 216–221. ISSN: 09254005 (1 2008).

36. Yamada, M., Nakashima, M. & Seki, M. Pinched flow fractionation: continuous size separation of particles utilizing a laminar flow profile in a pinched microchannel. *Analytical Chemistry* **76,** 5465–5471. ISSN: 00032700 (18 2004).

37. Berendsen, J. T., Eijkel, J. C., Wetzels, A. M. & Segerink, L. I. Separation of spermatozoa from erythrocytes using their tumbling mechanism in a pinch flow fractionation device. *Microsystems and Nanoengineering* **5.** ISSN: 20557434 (1 2019).

38. Loutherback, K., D'Silva, J., Liu, L., Wu, A., Austin, R. H. & Sturm, J. C. Deterministic separation of cancer cells from blood at 10 ml/min. *AIP Advances* **2.** ISSN: 21583226 (4 2012).

39. Liu, Z., Huang, F., Du, J., Shu, W., Feng, H., Xu, X. & Chen, Y. Rapid isolation of cancer cells using microfluidic deterministic lateral displacement structure. *Biomicrofluidics* **7.** ISSN: 19321058 (1 2013).

40. Shevkoplyas, S. S., Yoshida, T., Munn, L. L. & Bitensky, M. W. Biomimetic autoseparation of leukocytes from whole blood in a microfluidic device. *Analytical Chemistry* **77,** 933–937. ISSN: 00032700 (3 2005).

41. Guo, Q., Duffy, S. P., Matthews, K., Deng, X., Santoso, A. T., Islamzada, E. & Ma, H. Deformability based sorting of red blood cells improves diagnostic sensitivity for malaria caused by plasmodium falciparum. *Lab on a Chip* **16,** 645–654. ISSN: 14730189 (4 2016).

42. Tsukamoto, M., Taira, S., Yamamura, S., Morita, Y., Nagatani, N., Takamura, Y. & Tamiya, E. Cell separation by an aqueous two-phase system in a microfluidic device. *Analyst* **134,** 1994–1998. ISSN: 13645528 (10 2009).

43. SooHoo, J. R. & Walker, G. M. Microfluidic aqueous two phase system for leukocyte concentration from whole blood. *Biomedical Microdevices* **11,** 323–329. ISSN: 13872176 (2 2009).

44. Bazaz, S. R., Rouhi, O., Raoufi, M. A., Ejeian, F., Asadnia, M., Jin, D. & Warkiani, M. E. 3d printing of inertial microfluidic devices. *Scientific Reports* **10.** ISSN: 20452322 (1 2020).

45. Al-Halhouli, A., Albagdady, A., Al-Faqheri, W., Kottmeier, J., Meinen, S., Frey, L. J., Krull, R. & Dietzel, A. Enhanced inertial focusing of microparticles and cells by integrating trapezoidal microchambers in spiral microfluidic channels. *RSC Advances* **9,** 19197–19204. ISSN: 20462069 (33 2019).

46. Shim, S., Stemke-Hale, K., Noshari, J., Becker, F. F. & Gascoyne, P. R. Dielectrophoresis has broad applicability to marker-free isolation of tumor cells from blood by microfluidic systems. *Biomicrofluidics* **7.** ISSN: 19321058 (1 2013).

47. Song, H., Rosano, J. M., Wang, Y., Garson, C. J., Prabhakarpandian, B., Pant, K., Klarmann, G. J., Perantoni, A., Alvarez, L. M. & Lai, E. Continuous-flow sorting of stem cells and differentiation products based on dielectrophoresis. *Lab on a Chip* **15,** 1320–1328. ISSN: 14730189 (5 2015).

48. Robert, D., Pamme, N., Conjeaud, H., Gazeau, F., Iles, A. & Wilhelm, C. Cell sorting by endocytotic capacity in a microfluidic magnetophoresis device. *Lab on a Chip* **11,** 1902–1910. ISSN: 14730189 (11 2011).

49. Kang, B., Han, S., Son, H. Y., Mun, B., Shin, M. K., Choi, Y., Park, J., Min, J. K., Park, D., Lim, E. K., Huh, Y. M. & Haam, S. Immunomagnetic microfluidic integrated system for potency-based multiple separation of heterogeneous stem cells with high throughput capabilities. *Biosensors and Bioelectronics* **194.** ISSN: 18734235 (2021).

50. Petersson, F., Åberg, L., Swärd-Nilsson, A. M. & Laurell, T. Free flow acoustophoresis: microfluidic-based mode of particle and cell separation. *Analytical Chemistry* **79,** 5117–5123. ISSN: 00032700 (14 2007).

51. Ding, X., Peng, Z., Lin, S. C. S., Geri, M., Li, S., Li, P., Chen, Y., Dao, M., Suresh, S. & Huang, T. J. Cell separation using tilted-angle standing surface acoustic waves. *Proceedings of the National Academy of Sciences of the United States of America* **111,** 12992–12997. ISSN: 10916490 (36 2014).

52. Qi, X., Carberry, D. M., Cai, C., Hu, S., Yuan, Z., Rubinsztein-Dunlop, H. & Guo, J. Optical sorting and cultivation of denitrifying anaerobic methane oxidation archaea. *Biomedical Optics Express* **8,** 934. ISSN: 2156-7085 (2 2017).

53. Chen, Y., Wu, T. H., Kung, Y. C., Teitell, M. A. & Chiou, P. Y. 3d pulsed laser-triggered high-speed microfluidic fluorescence-activated cell sorter. *Analyst* **138,** 7308–7315. ISSN: 13645528 (24 2013).

54. Ozcelik, A., Gucluer, S. & Keskin, T. Continuous flow separation of live and dead cells using gravity sedimentation. *Micromachines* **14.** ISSN: 2072666X (8 2023).

55. Norouzi, N., Bhakta, H. C. & Grover, W. H. Sorting cells by their density. *PLoS ONE* **12.** ISSN: 19326203 (7 2017).

56. Bhagat, A. A. S., Bow, H., Hou, H. W., Tan, S. J., Han, J. & Lim, C. T. Microfluidics for cell separation. *Medical and Biological Engineering and Computing* **48,** 999–1014. ISSN: 01400118 (10 2010).

57. Alnaimat, F., Dagher, S., Mathew, B., Hilal-Alnqbi, A. & Khashan, S. Microfluidics based magnetophoresis: a review. *Chemical Record* **18,** 1596–1612. ISSN: 15280691 (11 2018).

58. Furlani, E. P. Analysis of particle transport in a magnetophoretic microsystem. *Journal of Applied Physics* **99,** 1–35. ISSN: 00218979 (2 2006).

59. Gooding, D. Final steps to the field theory: faraday's study of magnetic phenomena. *Historical Studies in the Physical Sciences,* **11,** 231–275 (2 1981).

60. Frenea-Robin, M. & Marchalot, J. Basic principles and recent advances in magnetic cell separation. *Magnetochemistry* **8,** 11 (1 2022).

61. Hajalilou, A., Mahmoud, T. & Elahe, P. *Magnetic Nanoparticles - Synthesis, Characterization, and Applications* ISBN: 978-3-527-35097-1 (Wiley-VCH, 2022).

62. Du, H., Akakuru, O. U., Yao, C., Yang, F. & Wu, A. Transition metal ion-doped ferrites nanoparticles for bioimaging and cancer therapy. *Translational Oncology* **15.** ISSN: 19365233 (1 2022).

63. Pekarsky, A. & Spadiut, O. Intrinsically magnetic cells: a review on their natural occurrence and synthetic generation. *Frontiers in Bioengineering and Biotechnology* **8.** ISSN: 22964185 (2020).

64. Nicholas, K. *Selected works of Louis Néel (Translation from the French authorized by the centre national de la recherche scientifique)* (Gordon and Breach Science Publishers, 1988).

65. Furlani, E. P. Magnetic biotransport: analysis and applications. *Materials* **3,** 2412–2446. ISSN: 19961944 (4 2010).

66. Leong, S. S., Ahmad, Z., Low, S. C., Camacho, J., Faraudo, J. & Lim, J. K. Unified view of magnetic nanoparticle separation under magnetophoresis. *Langmuir* **36,** 8033–8055. ISSN: 15205827 (28 2020).

67. Yeap, S. P., Lim, J. K., Ooi, B. S. & Ahmad, A. L. Agglomeration, colloidal stability, and magnetic separation of magnetic nanoparticles: collective influences on environmental engineering applications. *Journal of Nanoparticle Research* **19.** ISSN: 1572896X (11 2017).

68. Massart, R. Preparation of aqueous magnetic liquids in alkaline and acidic media. *IEEE Transactions on Magnetics* **17.** - Urquelle MNP Herstellung, 1247–1248. ISSN: 19410069 (2 1981).

69. Hu, P., Chang, T., Chen, W. J., Deng, J., Li, S. L., Zuo, Y. G., Kang, L., Yang, F., Hostetter, M. & Volinsky, A. A. Temperature effects on magnetic properties of fe3o4 nanoparticles synthesized by the sol-gel explosion-assisted method. *Journal of Alloys and Compounds* **773,** 605–611. ISSN: 09258388 (2019).

70. Li, S., Zhang, T., Tang, R., Qiu, H., Wang, C. & Zhou, Z. Solvothermal synthesis and characterization of monodisperse superparamagnetic iron oxide nanoparticles. *Journal of Magnetism and Magnetic Materials* **379,** 226–231. ISSN: 03048853 (2015).

71. Sundaram, P. A., Augustine, R. & Kannan, M. Extracellular biosynthesis of iron oxide nanoparticles by bacillus subtilis strains isolated from rhizosphere soil. *Biotechnology and Bioprocess Engineering* **17,** 835–840. ISSN: 12268372 (4 2012).

72. Schobesberger, M., Helmhagen, S., Mende, S., Berensmeier, S. & Fraga-García, P. From micro to nano: grinding natural magnetite ore for microalgae harvesting. *Magnetochemistry* **9.** ISSN: 23127481 (6 2023).

73. Kurapov, Y. A., Lytvyn, S. Y., Didikin, G. G. & Romanenko, S. M. Electron-beam physical vapor deposition of iron nanoparticles and their thermal stability in the fe–o system. *Powder Metallurgy and Metal Ceramics* **60,** 451–463. ISSN: 15739066 (7-8 2021).

74. Svetlichnyi, V. A., Shabalina, A. V., Lapin, I. N., Goncharova, D. A., Kharlamova, T. S. & Stadnichenko, A. I. Comparative study of magnetite nanoparticles obtained by pulsed laser ablation in water and air. *Applied Surface Science* **467-468,** 402–410. ISSN: 01694332 (2019).

75. Niculescu, A. G., Chircov, C. & Grumezescu, A. M. Magnetite nanoparticles: synthesis methods – a comparative review. *Methods* **199,** 16–27. ISSN: 10959130 (2022).

76. Ling, W., Wang, M., Xiong, C., Xie, D., Chen, Q., Chu, X., Qiu, X., Li, Y. & Xiao, X. Synthesis, surface modification, and applications of magnetic iron oxide nanoparticles. *Journal of Materials Research* **34,** 1828–1844. ISSN: 20445326 (11 2019).

77. Wu, W., Wu, Z., Yu, T., Jiang, C. & Kim, W. S. Recent progress on magnetic iron oxide nanoparticles: synthesis, surface functional strategies and biomedical applications. *Science and Technology of Advanced Materials* **16.** ISSN: 14686996 (2 2015).

78. Roth, H. C., Schwaminger, S. P., Schindler, M., Wagner, F. E. & Berensmeier, S. Influencing factors in the co-precipitation process of superparamagnetic iron oxide nano particles: a model based study. *Journal of Magnetism and Magnetic Materials* **377,** 81–89. ISSN: 03048853 (2015).

79. Favela-Camacho, S. E., Samaniego-Benítez, E. J., Godínez-García, A., Avilés-Arellano, L. M. & Pérez-Robles, J. F. How to decrease the agglomeration of magnetite nanoparticles and increase their stability using surface properties. *Colloids and Surfaces A: Physicochemical and Engineering Aspects* **574,** 29–35. ISSN: 18734359 (April 2019).

80. Gutiérrez, L., Cueva, L. D. L., Moros, M., Mazarío, E., Bernardo, S. D., Fuente, J. M. D. L., Morales, M. P. & Salas, G. Aggregation effects on the magnetic properties of iron oxide colloids. *Nanotechnology* **30.** ISSN: 13616528 (11 2019).

81. Kumar, V. & Rezai, P. Multiplex inertio-magnetic fractionation (mimf) of magnetic and non-magnetic microparticles in a microfluidic device. *Microfluidics and Nanofluidics* **21.** ISSN: 16134990 (5 2017).

82. Turrina, C., Klassen, A., Milani, D., Rojas-González, D. M., Ledinski, G., Auer, D., Sartori, B., Cvirn, G., Mela, P., Berensmeier, S. & Schwaminger, S. P. Superparamagnetic iron oxide nanoparticles for their application in the human body: influence of the surface. *Heliyon* **9.** ISSN: 24058440 (6 2023).

83. Wittmann, L., Turrina, C. & Schwaminger, S. P. The effect of ph and viscosity on magnetophoretic separation of iron oxide nanoparticles. *Magnetochemistry* **7,** 80. ISSN: 23127481 (6 2021).

84. Liu, S., Yu, B., Wang, S., Shen, Y. & Cong, H. Preparation, surface functionalization and application of fe3o4 magnetic nanoparticles. *Advances in Colloid and Interface Science* **281,** 102165. ISSN: 00018686 (2020).

85. Yeap, S. P., Ahmad, A. L., Ooi, B. S. & Lim, J. Electrosteric stabilization and its role in cooperative magnetophoresis of colloidal magnetic nanoparticles. *Langmuir* **28,** 14878–14891. ISSN: 07437463 (42 2012).

86. Lim, J. K., Majetich, S. A. & Tilton, R. D. Stabilization of superparamagnetic iron oxide core-gold shell nanoparticles in high ionic strength media. *Langmuir* **25,** 13384–13393. ISSN: 07437463 (23 2009).

87. Abarca-cabrera, L., Fraga-garcía, P. & Berensmeier, S. Bio-nano interactions : binding proteins , polysaccharides , lipids and nucleic acids onto magnetic nanoparticles. *Biomaterials Research,* 1–18 (2021 2022).

88. Wang, Z., Wu, R., Chen, H., Sun, N. & Deng, C. Synthesis of zwitterionic hydrophilic magnetic mesoporous silica materials for endogenous glycopeptide analysis in human saliva. *Nanoscale* **10,** 5335–5341. ISSN: 20403372 (11 2018).

89. Roth, H. C., Schwaminger, S. P., Peng, F. & Berensmeier, S. Immobilization of cellulase on magnetic nanocarriers. *ChemistryOpen* **5,** 183–187. ISSN: 21911363 (3 2016).

90. Nienhaus, K. & Nienhaus, G. U. *Mechanistic understanding of protein corona formation around nanoparticles: old puzzles and new insights* 2023.

91. Wang, H., Ma, R., Nienhaus, K. & Nienhaus, G. U. Formation of a monolayer protein corona around polystyrene nanoparticles and implications for nanoparticle agglomeration. *Small* **15.** ISSN: 16136829 (22 2019).

92. Schwaminger, S. P., Blank-Shim, S. A., Scheifele, I., Pipich, V., Fraga-García, P. & Berensmeier, S. Design of interactions between nanomaterials and proteins: a highly affine peptide tag to bare iron oxide nanoparticles for magnetic protein separation. *Biotechnology Journal* **14,** 1–7. ISSN: 18607314 (3 2019).

93. Shiriny, A. & Bayareh, M. On magnetophoretic separation of blood cells using halbach array of magnets. *Meccanica* **55,** 1903–1916. ISSN: 15729648 (10 2020).

94. Zhao, W., Zhu, T., Cheng, R., Liu, Y., He, J., Qiu, H., Wang, L., Nagy, T., Querec, T. D., Unger, E. R. & Mao, L. Label-free and continuous-flow ferrohydrodynamic separation of hela cells and blood cells in biocompatible ferrofluids. *Advanced Functional Materials* **26,** 3990–3998. ISSN: 16163028 (22 2016).

95. Nam, J., Huang, H., Lim, H., Lim, C. & Shin, S. Magnetic separation of malaria-infected red blood cells in various developmental stages. *Analytical Chemistry* **85,** 7316–7323. ISSN: 00032700 (15 2013).

96. Furlani, E. P. Magnetophoretic separation of blood cells at the microscale. *Journal of Physics D: Applied Physics* **40,** 1313–1319. ISSN: 00223727 (5 2007).

97. Schuerle, S., Soleimany, A. P., Yeh, T., Anand, G. M., Häberli, M., Fleming, H. E., Mirkhani, N., Qiu, F., Hauert, S., Wang, X., Nelson, B. J. & Bhatia, S. N. Synthetic and living micropropellers for convection-enhanced nanoparticle transport. *Sciences Advances* **5** (2019).

98. Lin, S., Zhi, X., Chen, D., Xia, F., Shen, Y., Niu, J., Huang, S., Song, J., Miao, J., Cui, D. & Ding, X. A flyover style microfluidic chip for highly purified magnetic cell separation. *Biosensors and Bioelectronics* **129,** 175–181. ISSN: 18734235 (2019).

99. Leong, S. S., Ahmad, Z., Camacho, J., Faraudo, J. & Lim, J. K. Kinetics of low field gradient magnetophoresis in the presence of magnetically induced convection. *Journal of Physical Chemistry C* **121,** 5389–5407. ISSN: 19327455 (9 2017).

100. Cuevas, G. D. L., Faraudo, J. & Camacho, J. Low-gradient magnetophoresis through field-induced reversible aggregation. *Journal of Physical Chemistry C* **112,** 945–950. ISSN: 19327447 (4 2008).

101. Kitenbergs, G. & Cēbers, A. Rivalry of diffusion, external field and gravity in micro-convection of magnetic colloids. *Journal of Magnetism and Magnetic Materials* **498,** 166247. ISSN: 03048853 (2020).

102. Lee, J. G., Porter, V., Shelton, W. A. & Bharti, B. Magnetic field-driven convection for directed surface patterning of colloids. *Langmuir* **34,** 15416–15424. ISSN: 15205827 (50 2018).

103. Faraudo, J., Andreu, J. S., Calero, C. & Camacho, J. Predicting the self-assembly of superparamagnetic colloids under magnetic fields. *Advanced Functional Materials* **26,** 3837–3858. ISSN: 16163028 (22 2016).

104. Fratzl, M., Delshadi, S., Devillers, T., Bruckert, F., Cugat, O., Dempsey, N. M. & Blaire, G. Magnetophoretic induced convective capture of highly diffusive superparamagnetic nanoparticles. *Soft Matter* **14,** 2671–2681. ISSN: 17446848 (14 2018).

105. Sun, J., Shi, Z., Chen, S. & Jia, S. Experimental and numerical analysis of the magnetophoresis of magnetic nanoparticles under the influence of cylindrical permanent magnet. *Journal of Magnetism and Magnetic Materials* **475,** 703–714. ISSN: 03048853 (2019).

106. Salafi, T., Zeming, K. K. & Zhang, Y. Advancements in microfluidics for nanoparticle separation. *Lab on a Chip* **17,** 11–33. ISSN: 14730189 (1 2017).

107. Dalili, A., Samiei, E. & Hoorfar, M. A review of sorting, separation and isolation of cells and microbeads for biomedical applications: microfluidic approaches. *Analyst* **144,** 87–113. ISSN: 13645528 (1 2019).

108. Alnaimat, F., Karam, S., Mathew, B. & Mathew, B. Magnetophoresis and microfluidics: a great union. *IEEE Nanotechnology Magazine* **14,** 24–41. ISSN: 19427808 (3 2020).

109. Eigenfeld, M., Wittmann, L., Kerpes, R., Schwaminger, S. P. & Becker, T. Studying the impact of cell age on the yeast growth behaviour of saccharomyces pastorianus var. carlsbergensis by magnetic separation. *Biotechnology Journal* **18.** ISSN: 1860-6768 (2023).

110. David, R., Groebner, M. & Franz, W.-M. Magnetic cell sorting purification of differentiated embryonic stem cells stably expressing truncated human cd4 as surface marker. *STEM CELLS* **23,** 477–482. ISSN: 1066-5099 (4 2005).

111. Munaz, A., Shiddiky, M. J. & Nguyen, N. T. Recent advances and current challenges in magnetophoresis based micro magnetofluidics. *Biomicrofluidics* **12.** ISSN: 19321058 (3 2018).

112. Shih, P. H., Shiu, J. Y., Lin, P. C., Lin, C. C., Veres, T. & Chen, P. On chip sorting of bacterial cells using sugar-encapsulated magnetic nanoparticles. *Journal of Applied Physics* **103,** 2006–2009. ISSN: 00218979 (7 2008).

113. Shen, F. & Park, J. K. Toxicity assessment of iron oxide nanoparticles based on cellular magnetic loading using magnetophoretic sorting in a trapezoidal microchannel. *Analytical Chemistry* **90,** 920–927. ISSN: 15206882 (1 2018).

114. Powell, C. D., Quain, D. E. & Smart, K. A. Chitin scar breaks in aged saccharomyces cerevisiae. *Microbiology* **149,** 3129–3137. ISSN: 13500872 (11 2003).

115. Kose, A. R., Birgit, F., Mao, L. & Koser, H. Label-free cellular manipulation and sorting via biocompatible ferrofluids. *Proceedings of National Academy of Sciences of the United States of America* **106,** 21478–21483 (51 2009).

116. Xu, X., Huang, X., Sun, J., Wang, R., Yao, J., Han, W., Wei, M., Chen, J., Guo, J., Sun, L. & Yin, M. Recent progress of inertial microfluidic-based cell separation. *Analyst* **146,** 7070–7086. ISSN: 13645528 (23 2021).

117. Takagi, J., Yamada, M., Yasuda, M. & Seki, M. Continuous particle separation in a microchannel having asymmetrically arranged multiple branches. *Lab on a Chip* **5,** 778–784. ISSN: 14730189 (7 2005).

118. Sai, Y., Yamada, M., Yasuda, M. & Seki, M. Continuous separation of particles using a microfluidic device equipped with flow rate control valves. *Journal of Chromatography A* **1127,** 214–220. ISSN: 00219673 (1-2 2006).

119. Vig, A. L. & Kristensen, A. Separation enhancement in pinched flow fractionation. *Applied Physics Letters* **93.** ISSN: 00036951 (20 2008).

120. Morijiri, T., Sunahiro, S., Senaha, M., Yamada, M. & Seki, M. Sedimentation pinched-flow fractionation for size- and density-based particle sorting in microchannels. *Microfluidics and Nanofluidics* **11,** 105–110. ISSN: 16134982 (1 2011).

121. Lee, K. H., Kim, S. B., Lee, K. S. & Sung, H. J. Enhancement by optical force of separation in pinched flow fractionation. *Lab on a Chip* **11,** 354–357. ISSN: 14730189 (2 2011).

122. Khashei, H., Latifi, H., Seresht, M. J. & Ghasemi, A. H. B. Microparticles manipulation and enhancement of their separation in pinched flow fractionation by insulator-based dielectrophoresis. *Electrophoresis* **37,** 775–785. ISSN: 15222683 (5-6 2016).

123. Lu, X. & Xuan, X. Inertia-enhanced pinched flow fractionation. *Analytical Chemistry* **87,** 4560–4565. ISSN: 15206882 (8 2015).

124. Hamacher, T., Berendsen, J. T., Dongen, J. E. V., Hee, R. M. V. D., Cornelissen, J. J., Broekhuijse, M. L. & Segerink, L. I. Virus removal from semen with a pinched flow fractionation microfluidic chip. *Lab on a Chip* **21,** 4477–4486. ISSN: 14730189 (22 2021).

125. Bhagat, A. A. S., Hou, H. W., Li, L. D., Lim, C. T. & Han, J. Pinched flow coupled shear-modulated inertial microfluidics for high-throughput rare blood cell separation. *Lab on a Chip* **11,** 1870–1878. ISSN: 14730189 (11 2011).

126. Zhu, T., Cheng, R., Lee, S. A., Rajaraman, E., Eiteman, M. A., Querec, T. D., Unger, E. R. & Mao, L. Continuous-flow ferrohydrodynamic sorting of particles and cells in microfluidic devices. *Microfluidics and Nanofluidics* **13,** 645–654. ISSN: 16134982 (4 2012).

127. Bhagat, A. A. S., Kuntaegowdanahalli, S. S. & Papautsky, I. Continuous particle separation in spiral microchannels using dean flows and differential migration. *Lab on a Chip* **8,** 1906–1914. ISSN: 14730189 (11 2008).

128. Ookawara, S., Higashi, R., Street, D. & Ogawa, K. Feasibility study on concentration of slurry and classification of contained particles by microchannel. *Chemical Engineering Journal* **101,** 171–178. ISSN: 13858947 (1-3 2004).

129. Matas, J.-P., Morris, J. F., Guazzelli, E. & E, B. J. Inertial migration of rigid spherical particles in poiseuille flow. *Journal of Fluid Mechanics* **515,** 171–195 (2003).

130. Segre, G. & Silberberg, A. Behaviour of macroscopic rigid spheres in poiseuille flow part 2. experimental results and interpretation. *Journal of Fluid Mechanics,* 136–157 (1962).

131. Carlo, D. D., Irimia, D., Tompkins, R. G. & Toner, M. Continuous inertial focusing, ordering, and separation of particles in microchannels. *Proceedings of the National Academy of Sciences of the United States of America* **104** (48 2007).

132. Martel, J. M. & Toner, M. Inertial focusing in microfluidics. *Annual Review of Biomedical Engineering* **16,** 371–396. ISSN: 15454274 (2014).

133. Cruz, J. & Hjort, K. High-resolution particle separation by inertial focusing in high aspect ratio curved microfluidics. *Scientific reports* **11,** 13959. ISSN: 20452322 (1 2021).

134. Kuntaegowdanahalli, S. S., Bhagat, A. A. S., Kumar, G. & Papautsky, I. Inertial microfluidics for continuous particle separation in spiral microchannels. *Lab on a Chip* **9,** 2973–2980. ISSN: 14730189 (20 2009).

135. Herrmann, N., Neubauer, P. & Birkholz, M. Spiral microfluidic devices for cell separation and sorting in bioprocesses. *Biomicrofluidics* **13.** ISSN: 19321058 (6 2019).

136. Chiu, P. L., Chang, C. H., Lin, Y. L., Tsou, P. H. & Li, B. R. Rapid and safe isolation of human peripheral blood b and t lymphocytes through spiral microfluidic channels. *Scientific Reports* **9.** ISSN: 20452322 (1 2019).

137. Moloudi, R., Oh, S., Yang, C., Teo, K. L., Lam, A. T. L., Warkiani, M. E. & Naing, M. W. Inertial-based filtration method for removal of microcarriers from mesenchymal stem cell suspensions. *Scientific Reports* **8.** ISSN: 20452322 (1 2018).

138. Lee, W., Kwon, D., Choi, W., Jung, G. Y., Au, A. K., Folch, A. & Jeon, S. 3d-printed microfluidic device for the detection of pathogenic bacteria using size-based separation in helical channel with trapezoid cross-section. *Scientific Reports* **5.** ISSN: 20452322 (September 2018 2015).

139. Al-Halhouli, A., Albagdady, A., Al-Faqheri, W., Kottmeier, J., Meinen, S., Frey, L. J., Krull, R. & Dietzel, A. Enhanced inertial focusing of microparticles and cells by integrating trapezoidal microchambers in spiral microfluidic channels. *RSC Advances* **9,** 19197–19204. ISSN: 20462069 (33 2019).

140. Natu, R., Guha, S., Dibaji, S. A. R. & Herbertson, L. Assessment of flow through microchannels for inertia-based sorting: steps toward microfluidic medical devices. *Micromachines* **11.** ISSN: 2072666X (10 2020).

141. Shiriny, A. & Bayareh, M. Inertial focusing of ctcs in a novel spiral microchannel. *Chemical Engineering Science* **229.** ISSN: 00092509 (2021).

142. Ozkumur, E. *et al.* Inertial focusing for tumor antigen-dependent and -independent sorting of rare circulating tumor cells. *Science Translational Medicine* **5.** ISSN: 19466234 (179 2013).

143. Mehta, V. & Rath, S. N. 3d printed microfluidic devices: a review focused on four fundamental manufacturing approaches and implications on the field of healthcare. *Bio-Design and Manufacturing* **4,** 311–343. ISSN: 25228552 (2 2021).

144. Gale, B. K., Jafek, A. R., Lambert, C. J., Goenner, B. L., Moghimifam, H., Nze, U. C. & Kamarapu, S. K. A review of current methods in microfluidic device fabrication and future commercialization prospects. *Inventions* **3.** ISSN: 24115134 (3 2018).

145. Chen, L., Yang, C., Xiao, Y., Yan, X., Hu, L., Eggersdorfer, M., Chen, D., Weitz, D. A. & Ye, F. Millifluidics, microfluidics, and nanofluidics: manipulating fluids at varying length scales. *Materials Today Nano* **16.** ISSN: 25888420 (2021).

146. Nielsen, A. V., Beauchamp, M. J., Nordin, G. P. & Woolley, A. T. 3d printed microfluidics. *Annual Review ofAnalytical Chemistry* **13,** 45–65 (2020).

147. Au, A. K., Lee, W. & Folch, A. Mail-order microfluidics: evaluation of stereolithography for the production of microfluidic devices. *Lab on a Chip* **14,** 1294–1301. ISSN: 14730189 (7 2014).

148. Lee, U. N., Su, X., Guckenberger, D. J., Dostie, A. M., Zhang, T., Berthier, E. & Theberge, A. B. Fundamentals of rapid injection molding for microfluidic cell-based assays. *Lab on a Chip* **18,** 496–504. ISSN: 14730189 (3 2018).

149. Kuo, A. P., Bhattacharjee, N., Lee, Y. S., Castro, K., Kim, Y. T. & Folch, A. High-precision stereolithography of biomicrofluidic devices. *Advanced Materials Technologies* **4.** ISSN: 2365709X (6 2019).

150. Romanov, V., Samuel, R., Chaharlang, M., Jafek, A. R., Frost, A. & Gale, B. K. Fdm 3d printing of high-pressure, heat-resistant, transparent microfluidic devices. *Analytical Chemistry* **90,** 10450–10456. ISSN: 15206882 (17 2018).

151. Ching, T., Li, Y., Karyappa, R., Ohno, A., Toh, Y. C. & Hashimoto, M. Fabrication of integrated microfluidic devices by direct ink writing (diw) 3d printing. *Sensors and Actuators, B: Chemical* **297.** ISSN: 09254005 (2019).

152. Vasilescu, S. A., Khorsandi, S., Ding, L., Bazaz, S. R., Nosrati, R., Gook, D. & Warkiani, M. E. A microfluidic approach to rapid sperm recovery from heterogeneous cell suspensions. *Scientific Reports* **11.** ISSN: 20452322 (1 2021).

153. Chin, S. Y., Dikshit, V., Priyadarshini, B. M. & Zhang, Y. Powder-based 3d printing for the fabrication of device with micro and mesoscale features. *Micromachines* **11.** ISSN: 2072666X (7 2020).

154. Huang, C., Wippold, J. A., Stratis-Cullum, D. & Han, A. Eliminating air bubble in microfluidic systems utilizing integrated in-line sloped microstructures. *Biomedical Microdevices* **22.** ISSN: 15728781 (4 2020).

155. Bazaz, S. R., Kashaninejad, N., Azadi, S., Patel, K., Asadnia, M., Jin, D. & Warkiani, M. E. Rapid softlithography using 3d-printed molds. *Advanced Materials Technologies* **4.** ISSN: 2365709X (10 2019).

156. Çoğun, F., Yıldırım, E. & Arikan, M. A. S. Investigation on replication of microfluidic channels by hot embossing. *Materials and Manufacturing Processes* **32,** 1838–1844. ISSN: 15322475 (16 2017).

157. Satyanarayana, T. & Kunze, G. *Yeast Diversity in Human Welfare* ISBN: 9789811026218 (Springer Science+Business Media Singapore 2017, 2017).

158. Parapouli, M., Vasileiadis, A., Afendra, A. S. & Hatziloukas, E. Saccharomyces cerevisiae and its industrial applications. *AIMS Microbiology* **6,** 1–31. ISSN: 24711888 (1 2020).

159. *Yeasts in Food and Beverages* (eds Querol, A. & Fleet, G. H.) (Springer, 2006).

160. Karbalaei, M., Rezaee, S. A. & Farsiani, H. Pichia pastoris: a highly successful expression system for optimal synthesis of heterologous proteins. *Journal of Cellular Physiology* **235,** 5867–5881. ISSN: 10974652 (9 2020).

161. Heitmann, M., Zannini, E., Axel, C. & Arendt, E. Correlation of flavor profile to sensory analysis of bread produced with different saccharomyces cerevisiae originating from the baking and beverage industry. *Cereal Chemistry* **94,** 746–751. ISSN: 19433638 (4 2017).

162. MarketsandMarkets. *Yeast market by type (baker's yeast, brewer's yeast, wine yeast, probiotic yeast), application (food, feed), form (fresh, instant, active), genus (saccharomyces, kluveromyces), yeast extract (qualitative) and region - global forecast to 2029* 2024. https://www.marketsandmarkets.com/Market-Reports/yeast-industry-268.html#:~:text=The%20global%20yeast%20market%20is,a%20promising%20CAGR%20of%208.9%25..

163. Replicative and chronological aging in saccharomyces cerevisiae. *Cell Metabolism* **16,** 18–31. ISSN: 15504131 (1 2012).

164. Kaeberlein, M. Lessons on longevity from budding yeast. *Nature* **464,** 513–519. ISSN: 00280836 (7288 2010).

165. Leupold, S., Hubmann, G., Litsios, A., Meinema, A. C., Takhaveev, V., Papagiannakis, A., Niebel, B., Janssens, G., Siegel, D. & Heinemann, M. Saccharomyces cerevisiae goes through distinct metabolic phases during its replicative lifespan. *eLife* (2019).

166. Wauters, R., Britton, S. J. & Verstrepen, K. J. Old yeasts, young beer—the industrial relevance of yeast chronological life span. *Yeast* **38,** 339–351. ISSN: 10970061 (6 2021).

167. Herskowitz, I. Life cycle of the budding yeast saccharomyces cerevisiae. *Microbiological Reviews,* 536–553 (1988).

168. Eigenfeld, M., Kerpes, R. & Becker, T. Recombinant protein linker production as a basis for non-invasive determination of single-cell yeast age in heterogeneous yeast populations. *RSC Advances* **11,** 31923–31932. ISSN: 20462069 (51 2021).

169. Cabib, E. & Bowers, B. Chitin and yeast budding: localization of chitin in yeast bud scars. *The Journal of Biological Chemistry* **246,** 152–159 (1 1971).

170. Schekman, R. & Brawley, V. Localized deposition of chitin on the yeast cell surface in response to mating pheromone. *Biochemistry* **76,** 645–649 (2 1979).

171. Cabib, E. The septation apparatus, a chitin-requiring machine in budding yeast. *Archives of Biochemistry and Biophysics* **426,** 201–207. ISSN: 00039861 (2 2004).

172. Cabib, E. & Durán, A. Synthase iii-dependent chitin is bound to different acceptors depending on location on the cell wall of budding yeast. *Journal of Biological Chemistry* **280,** 9170–9179. ISSN: 00219258 (10 2005).

173. Bühligen, F., Lindner, P., Fetzer, I., Stahl, F., Scheper, T., Harms, H. & Müller, S. Analysis of aging in lager brewing yeast during serial repitching. *Journal of Biotechnology* **187,** 60–70. ISSN: 18734863 (2014).

174. Kuřec, M., Baszczyňski, M., Lehnert, R., Mota, A., Teixeira, J. A. & Brányik, T. Flow cytometry for age assessment of a yeast population and its application in beer fermentations. *Journal of the Institute of Brewing* **115,** 253–258. ISSN: 00469750 (3 2009).

175. Cipollina, C., Vai, M., Porro, D. & Hatzis, C. Towards understanding of the complex structure of growing yeast populations. *Journal of Biotechnology* **128,** 393–402. ISSN: 01681656 (2 2007).

176. Mortimer, R. K. & Johnston, J. R. Life soan of individual yeast cells. *Nature* **183.** - erste Erfindung der Mikrodissektion, 1751–1752 (4677 1959).

177. Stumpferl, S. W., Brand, S. E., Jiang, J. C., Korona, B., Tiwari, A., Dai, J., Seo, J. G. & Jazwinski, S. M. Natural genetic variation in yeast longevity. *Genome Research* **22,** 1963–1973. ISSN: 10889051 (10 2012).

178. Aranda, A., Orozco, H., Picazo, C. & Matallana, E. Yeast life span and its impact on food fermentations. *Fermentation* **5.** ISSN: 23115637 (2 2019).

179. Eigenfeld, M., Kerpes, R. & Becker, T. Understanding the impact of industrial stress conditions on replicative aging in saccharomyces cerevisiae. *Frontiers in Fungal Biology* **2** (June 2021).

180. Morano, K. A., Grant, C. M. & Moye-Rowley, W. S. The response to heat shock and oxidative stress in saccharomyces cerevisiae. *Genetics* **190,** 1157–1195. ISSN: 00166731 (4 2012).

181. Bühligen, F., Lindner, P., Fetzer, I., Stahl, F., Scheper, T., Harms, H. & Müller, S. Analysis of aging in lager brewing yeast during serial repitching. *Journal of Biotechnology* **187,** 60–70. ISSN: 18734863 (2014).

182. Wang, Y., Lo, W. C. & Chou, C. S. A modeling study of budding yeast colony formation and its relationship to budding pattern and aging. *PLoS Computational Biology* **13.** ISSN: 15537358 (11 2017).

183. Janssens, G. E., Meinema, A. C., lez, J. G., Wolters, J. C., Schmidt, A., Guryev, V., Bischoff, R., Wit, E. C., Veenhoff, L. M. & Heinemann, M. Protein biogenesis machinery is a driver of replicative aging in yeast. *eLife* (2015).

184. Woldringh, C. L., Fluiter, K. & Huls, P. G. Production of senescent cerevisiae by centrifugal cells of saccharomyces elutriation. *Yeast* **11,** 361–369 (1995).

185. Egilmez, N. K., Chen, J. B. & Jazwinski, S. M. Preparation and partial characterization of old yeast cells. *Journal of Gerontology: Biological Sciences* **45,** 9–16 (1990).

186. Asami, K., Gheorghiu, E. & Yonezawa, T. Real-time monitoring of yeast cell division by dielectric spectroscopy. *Biophysical Journal* **76,** 3345–3348. ISSN: 00063495 (6 1999).

187. Valero, A., Braschler, T., Rauch, A., Demierre, N., Barral, Y. & Renaud, P. Tracking and synchronization of the yeast cell cycle using dielectrophoretic opacity. *Lab on a Chip* **11,** 1754–1760. ISSN: 14730189 (10 2011).

188. Ferrezuelo, F., Colomina, N., Palmisano, A., Garí, E., Gallego, C., Csikász-Nagy, A. & Aldea, M. The critical size is set at a single-cell level by growth rate to attain homeostasis and adaptation. *Nature Communications* **3.** ISSN: 20411723 (2012).

189. Turner, J. J., Ewald, J. C. & Skotheim, J. M. Cell size control in yeast. *Current Biology* **22,** R350–R359. ISSN: 09609822 (9 2012).

190. Smeal, T., Claus, J. & Kennedy, B. Loss of transcriptional silencing causes sterility in old mother cells of s. cerevisiae. *Cell* **84,** 633–642 (1996).

191. Lindstrom, D. L. & Gottschling, D. E. The mother enrichment program: a genetic system for facile replicative life span analysis in saccharomyces cerevisiae. *Genetics* **183,** 413–422. ISSN: 00166731 (2 2009).

192. Microfluidic technologies for yeast replicative lifespan studies. *Mechanisms of Ageing and Development* **161,** 262–269. ISSN: 18726216 (2017).

193. Durán, D. C., Hernández, C. A., Suesca, E., Acevedo, R., Acosta, I. M., Forero, D. A., Rozo, F. E. & Pedraza, J. M. Slipstreaming mother machine: a microfluidic device for single-cell dynamic imaging of yeast. *Micromachines* **12,** 1–11. ISSN: 2072666X (1 2021).

194. Li, Y., Jin, M., O'Laughlin, R., Bittihn, P., Tsimring, L. S., Pillus, L., Hasty, J. & Hao, N. Multigenerational silencing dynamics control cell aging. *Proceedings of the National Academy of Sciences of the United States of America* **114,** 11253–11258. ISSN: 10916490 (42 2017).

195. Lee, S. S., Vizcarra, I. A., Huberts, D. H., Lee, L. P. & Heinemann, M. Whole lifespan microscopic observation of budding yeast aging through a microfluidic dissection platform. *Proceedings of the National Academy of Sciences of the United States of America* **109,** 4916–4920. ISSN: 00278424 (13 2012).

196. Fehrmann, S., Paoletti, C., Goulev, Y., Ungureanu, A., Aguilaniu, H. & Charvin, G. Aging yeast cells undergo a sharp entry into senescence unrelated to the loss of mitochondrial membrane potential. *Cell Reports* **5,** 1589–1599. ISSN: 22111247 (6 2013).

197. Xie, Z., Zhang, Y., Zou, K., Brandman, O., Luo, C., Ouyang, Q. & Li, H. Molecular phenotyping of aging in single yeast cells using a novel microfluidic device. *Aging cell* **11,** 599–606. ISSN: 15378276 (4 2012).

198. Thayer, N. H., Robles, M., Xu, J., Schinski, E. L., Hotz, M., Keyser, R., Millett-Sikking, A., Okreglak, V., Rogers, J. V., Waite, A. J., Wranik, B. J., York, A. G., Mcisaac, R. S. & Gottschling, D. E. The yeast lifespan machine: a microfluidic platform for automated replicative lifespan measurements. *bioRxiv* (2022).

199. Chen, Q., Li, D., Zielinski, J., Kozubowski, L., Lin, J., Wang, M. & Xuan, X. Yeast cell fractionation by morphology in dilute ferrofluids. *Biomicrofluidics* **11.** ISSN: 19321058 (6 2017).

200. Liu, P., Liu, H., Yuan, D., Jang, D., Yan, S. & Li, M. Separation and enrichment of yeast saccharomyces cerevisiae by shape using viscoelastic microfluidics. *Analytical Chemistry* **93,** 1586–1595. ISSN: 15206882 (3 2021).

201. Lim, E. W. C. & Feng, R. Agglomeration of magnetic nanoparticles. *Journal of Chemical Physics* **136.** ISSN: 00219606 (12 2012).

202. Sun, X., Zheng, C., Zhang, F., Yang, Y., Wu, G., Yu, A. & Guan, N. Size-controlled synthesis of magnetite (fe3o4) nanoparticles coated with glucose and gluconic acid from a single fe(iii) precursor by a sucrose bifunctional hydrothermal method. *Journal of Physical Chemistry C* **113,** 16002–16008. ISSN: 19327447 (36 2009).

203. Benítez, E. I., Genovese, D. B. & Lozano, J. E. Effect of typical sugars on the viscosity and colloidal stability of apple juice. *Food Hydrocolloids* **23,** 519–525. ISSN: 0268005X (2 2009).

204. Schwegmann, H., Feitz, A. J. & Frimmel, F. H. Influence of the zeta potential on the sorption and toxicity of iron oxide nanoparticles on s. cerevisiae and e. coli. *Journal of Colloid and Interface Science* **347,** 43–48. ISSN: 00219797 (1 2010).

205. Turrina, C., Oppelt, A., Mitzkus, M., Berensmeier, S. & Schwaminger, S. P. Silica-coated superparamagnetic iron oxide nanoparticles: new insights into the influence of coating thickness on the particle properties and lasioglossin binding. *MRS Communications* **12,** 632–639. ISSN: 21596867 (5 2022).

206. Cross, S. N., Al-Feghali, A. H. & Blum, A. S. Interactions of common biological buffers with iron oxide nanoparticles. *Langmuir.* ISSN: 0743-7463 (2023).

207. Hohmann, S. Osmotic adaptation in yeast-control of the yeast osmolyte system. *International Review of Cytology* **215,** 149–187. ISSN: 00747696 (2002).

208. Stober, W., Fink, A. & Bohn, D. E. Controlled growth of monodisperse silica spheres in the micron size range. *Journal of Colloid and Interface Science* **26,** 62–69 (1968).

209. Salman, D., Juzsakova, T., Al-Mayyahi, M. A., Akos, R., Mohsen, S., Ibrahim, R. I., Mohammed, H. D., Abdullah, T. A., Domokos, E. & Korim, T. Synthesis, surface modification and characterization of magnetic fe3o4@sio2core-shell nanoparticles. *Journal of Physics: Conference Series* **1773,** 0-12. ISSN: 17426596 (1 2021).

210. Misra, S. K., Dybowska, A., Berhanu, D., Luoma, S. N. & Valsami-Jones, E. The complexity of nanoparticle dissolution and its importance in nanotoxicological studies. *Science of the Total Environment* **438,** 225–232. ISSN: 00489697 (2012).

211. Wittmann, L. †., Eigenfeld, M. †., Büchner, K., Meiler, J., Habisch, H., Madl, T., Kerpes, R., Becker, T., Berensmeier, S. & Schwaminger, S. P. Millifluidic magnetophoresis: an innovative approach for age-specific fractionation and analysis of saccharomyces yeast cells. *Lab on a Chip [Unpublished manuscript]* (2024).

212. Wittmann, L. †., Krucker-Velasquez, E. †., Schaupp, J., Westphal, L., Swan, J. W., Alexander-Katz, A. Z., Bazant, M., Schwaminger, S. P. & Sonja, B. Magnetophoresis in microfluidic applications: influence of magnetic convection in hydrodynamic fields. *Small [Unpublished manuscript]* (2024).

213. Chen, J., Hao, Y. & Chen, M. Rapid and efficient removal of ni2+ from aqueous solution by the one-pot synthesized edta-modified magnetic nanoparticles. *Environmental Science and Pollution Research* **21,** 1671–1679. ISSN: 09441344 (3 2014).

214. Derjaguin, B. & Landau, L. Theory of the stability of strongly charged lyophobic sols and of the adhesion of strongly charged particles in solutions of electrolytes. *Acta Physico Chemica URSS,* 30–59 (1941).

215. Dickson, D., Liu, G., Li, C., Tachiev, G. & Cai, Y. Dispersion and stability of bare hematite nanoparticles: effect of dispersion tools, nanoparticle concentration, humic acid and ionic strength. *Science of the Total Environment* **419,** 170–177. ISSN: 00489697 (2012).

216. Fischer, B. E., Häring, U. K., Tribolet, R. & Sigel, H. Metal ion / buffer interactions. *European Journal of Biochemistry* **94,** 523–530 (1979).

217. Pfeiffer, C., Rehbock, C., Hühn, D., Carrillo-Carrion, C., Aberasturi, D. J. D., Merk, V., Barcikowski, S. & Parak, W. J. Interaction of colloidal nanoparticles with their local environment: the (ionic) nanoenvironment around nanoparticles is different from bulk and determines the physico-chemical properties of the nanoparticles. *Journal of the Royal Society Interface* **11.** ISSN: 17425662 (96 2014).

218. Ferreira, C. M., Pinto, I. S., Soares, E. V. & Soares, H. M. (un)suitability of the use of ph buffers in biological, biochemical and environmental studies and their interaction with metal ions-a review. *RSC Advances* **5,** 30989–31003. ISSN: 20462069 (39 2015).

219. Eigenfeld, M., Kerpes, R., Whitehead, I. & Becker, T. Autofluorescence prediction model for fluorescence unmixing and age determination. *Biotechnology Journal* **17.** ISSN: 18607314 (12 2022).

220. Microfluidic ChipShop. *Application note-spiral sorter chip fluidic 382 sorting 7 μm and 15 μm beads* https://www.microfluidic-chipshop.com/catalogue/microfluidic-chips/polymer-chips/particle-cell-sorting-chips/particle-cell-sorting-chips-fluidic-382/.

221. Wang, H., Enders, A., Preuss, J. A., Bahnemann, J., Heisterkamp, A. & Torres-Mapa, M. L. 3d printed microfluidic lab-on-a-chip device for fiber-based dual beam optical manipulation. *Scientific Reports* **11.** ISSN: 20452322 (1 2021).

222. Mehendale, N. D. & Paul, D. *Hydrodynamic flow focusing for microfluidic cell sorting chip* 2014.

223. Selamat, N., Rahim, M. S. B. & Ehsan, A. A. *Effect of microchannel sizes on 3d hydrodynamic focusing of a microflow cytometer* in. **2016-September** (Institute of Electrical and Electronics Engineers Inc., 2016), 109–112. ISBN: 9781509023837.

224. Ngamsom, B., Esfahani, M. M. N., Phurimsak, C., Lopez-martinez, M. J., Raymond, J.-c., Broyer, P., Patel, P. & Pamme, N. Multiplex sorting of foodborne pathogens by on-chip free-flow magnetophoresis. *Analytica Chimica Acta* **918,** 69–76. ISSN: 0003-2670. http://dx.doi.org/10.1016/j.aca.2016.03.014 (2016).

225. Zakhartsev, M. & Reuss, M. Cell size and morphological properties of yeast saccharomyces cerevisiae in relation to growth temperature. *FEMS Yeast Research* **18,** 1–16. ISSN: 15671364 (6 2018).

226. Xu, Y., Zhang, Z., Su, Z., Zhou, X., Han, X. & Liu, Q. Continuous microfluidic purification of dna using magnetophoresis. *Micromachines* **11,** 2–6. ISSN: 2072666X (2 2020).

227. Wu, J., Yan, Q., Xuan, S. & Gong, X. Size-selective separation of magnetic nanospheres in a microfluidic channel. *Microfluidics and Nanofluidics* **21,** 1–12. ISSN: 16134990 (3 2017).

228. Kasamo, K. Regulation of plasma membrane h+-atpase activity by the membrane environment. *Journal of Plant Research* **116,** 517–523. ISSN: 09189440 (6 2003).

229. Papagiannakis, A., Niebel, B., Wit, E. C. & Heinemann, M. Autonomous metabolic oscillations robustly gate the early and late cell cycle. *Molecular Cell* **65,** 285–295. ISSN: 10974164 (2 2017).

230. Saerens, S. M., Delvaux, F. R., Verstrepen, K. J. & Thevelein, J. M. Production and biological function of volatile esters in saccharomyces cerevisiae. *Microbial Biotechnology* **3,** 165–177. ISSN: 17517907 (2 2010).

231. Herrero, P., Galíndez, J., Ruiz, N., Martínez-Campa, C. & Moreno, F. Transcriptional regulation of the saccharomyces cerevisiae hxk1, hxk2 and glk1 genes. *Yeast* **11,** 137–144. ISSN: 10970061 (2 1995).

232. Raj, S. B., Ramaswamy, S. & Plapp, B. V. Yeast alcohol dehydrogenase structure and catalysis. *Biochemistry* **53,** 5791–5803. ISSN: 15204995 (36 2014).

233. Dickinson, J. R., Salgado, L. E. J. & Hewlins, M. J. The catabolism of amino acids to long chain and complex alcohols in saccharomyces cerevisiae. *Journal of Biological Chemistry* **278,** 8028–8034. ISSN: 00219258 (10 2003).

234. Uemura, H. & Fraenkel, D. P. Gcr2, a new mutation affecting glycolytic gene expression in saccharomyces cerevisiae. *Molecular and cellular biology* **10,** 6389–6396 (12 1990).

235. Clifton, D., Weinstock, S. B. & Fraenkel, D. G. Glycolysis mutants in saccharomyces cerevisiae. *Genetics* **88,** 1–11 (1978).

236. Ge, W., Encinas, A., Araujo, E. & Song, S. Magnetic matrices used in high gradient magnetic separation (hgms): a review. *Results in Physics* **7,** 4278–4286 (2017).

237. Ameskamp, N., Priesner, C., Lehmann, J. & Lütkemeyer, D. Pilot scale recovery of monoclonal antibodies by expanded bed ion exchange adsorption. *Bioseparation* **8,** 169–188 (1-5 1999).

238. Smith, M. P., Bulmer, M. A., Hjorth, R. & Titchener-Hooker, N. J. Hydrophobic interaction ligand selection and scale-up of an expanded bed separation of an intracellular enzyme from saccharomyces cerevisiae. *Journal of Chromatography A* **968,** 121–128 (1-2 2002).

239. Statistischer Bericht - Brauwirtschaft 2022, F. 7.-0. *Bierausstoß von kleinbrauereien in deutschland in den jahren 2005 bis 2022(in hektoliter)* 2023. `https : / / de . statista . com/statistik/daten/studie/294710/umfrage/bierausstoss - von - kleinbrauereien-in-deutschland/`.

List of Figures

List of Tables

A Appendix

A.1 Supporting Information

A.1.1 The Effect of pH and Viscosity on Magnetophoretic Separation of Iron Oxide Nanoparticles

MDPI

Article

The Effect of pH and Viscosity on Magnetophoretic Separation of Iron Oxide Nanoparticles

Leonie Wittmann , **Chiara Turrina** and **Sebastian P. Schwaminger** *

Bioseparation Engineering Group, Department of Mechanical Engineering, Technical University of Munich, Boltzmanstr. 15, 85748 Garching bei München, Germany; l.wittmann@tum.de (L.W.); c.turrina@tum.de (C.T.)
* Correspondence: s.schwaminger@tum.de

Abstract: Magnetic nanoparticles (MNPs) are used for magnetophoresis-based separation processes in various biomedical and engineering applications. Essential requirements are the colloidal stability of the MNPs and the ability to be separated even in low magnetic field gradients. Bare iron oxide nanoparticles (BIONs) with a diameter of 9.2 nm are synthesized via coprecipitation, exhibiting a high saturation magnetization of 70.84 $Am^2 kg^{-1}$ and no remanence. In our study, zeta potential, dynamic light scattering (DLS), and sedimentation analysis show that the aggregation behavior of BIONs is influenced by pH and viscosity. Small aggregate clusters are formed with either low or high pH values or increased viscosity. Regarding magnetophoresis-based separation, a higher viscosity leads to lower magnetophoretic velocities, similar to how small aggregates do. Additionally, cooperative magnetophoresis, the joint motion of strongly interacting particles, affects the separation of the BIONs, too. Our study emphasizes the effect of pH and viscosity on the physicochemical characteristics of MNPs, resulting in different aggregation behavior. Particularly, for high viscous working media in downstream processing and medicine, respectively, the viscosity should be taken into account, as it will affect particle migration.

Keywords: magnetophoresis; magnetic separation process; iron oxide nanoparticles; aggregation; pH; viscosity; sedimentation analyzer; zeta potential; hydrodynamic diameter

check for
updates

1. Introduction

Magnetic nanoparticles (MNPs) have become an important nanomaterial in biotechnology, in chemistry, and in medicine [1–6]. They entail characteristics such as biocompatibility, high binding capacities, and cost-efficient production via coprecipitation. Moreover, their superparamagnetic properties are advantageous during the separation process, as the MNPs show no remanence at room temperature. However, when applying a magnetic field, they possess a high magnetic susceptibility and can be easily separated [7,8]. For biological samples, it is challenging to separate a target entity from a complex mixture with different components. Here, magnetophoresis-based processes provide a simple and efficient method, where the desired entity (magnetic or magnetically labeled with MNPs) is isolated by applying an external magnetic field [9–11]. For the method of High Gradient Magnetic Separation (HGMS), a suspension containing the magnetic material is pumped through a separation chamber, and it is trapped by a magnetically susceptible matrix due to high magnetic field gradients (10^2–10^4 T m^{-1}) [9,11,12]. In contrast, low magnetic field gradients (<100 T m^{-1}) are used for Low Gradient Magnetic Separation (LGMS), where a magnet is placed outside the particle suspension without contacting the particles [13]. Both modes of operation can be realized with either a permanent magnet or an electromagnet. However, the latter brings up several challenges. The installation costs are higher than a permanent magnet, and cooling might be necessary to counteract the Joule heating. Thus, water usage is required besides energy consumption [14]. Therefore, a permanent magnet might be preferred in the biomedical field. Moreover, in microfluidics, the implementation

of a permanent magnet with a high magnetic field gradient is more advantageous, as Alnaimat et al. summarize [15].

For LGMS or HGMS applications, such as in microfluidics [16] or in medicine [17–22], it is important to have a defined and stable particle size. Hence, MNPs need to meet the following requirements. On the one hand, they should be colloidal stable and not form aggregates so that they remain their defined size during fractionation or separation [5]. Particularly, for medical purposes, such as hyperthermia treatment or magnetic resonance imaging, the particle diameter should be smaller than 100 nm without forming large aggregates [17,19,23,24]. On the other hand, it should be possible to isolate the colloidal stable MNPs with the respective magnetic field gradient [25].

Regarding downstream processing, the handled liquids, e.g., cell lysates or hydrolysates coming out of fermentation, pose another challenge. Viscosity becomes an essential factor, influencing the separation performance [26–28]. Furthermore, in medical applications, the medium blood exhibits a higher viscosity, being fivefold higher than the one of water [29]. In addition to the higher viscosity, serum proteins or other blood components might influence the aggregation behavior [20,21]. However, the so-called biocorona, which is determined by the liquid components such as biomolecules, bacterial debris, proteins, or lipids, could also prevent the aggregation of MNPs [30]. Socoliuc et al. recently emphasized the importance of characterizing the aggregation behavior of MNPs in the respective medium, e.g., cell culture media, and not only in water [18]. Besides the intrinsic characteristics of the working liquid, an increase in viscosity could be advantageous for the microfluidic processing of magnetic particles [31]. In order to avoid sedimentation effects during the process, Solsona et al. developed a microfluidic chip for the magnetophoretic sorting of single-catalyst particles composed of iron [31]. Hence, working with different viscosities might facilitate process handling, or a specific medium might give another viscosity. We would like to point out that besides other parameters, e.g., pH, the viscosity might influence the particle aggregation behavior as well.

Concerning an LGMS process, the control of aggregation is important, as it has been shown that, despite low magnetic field gradients, the particles can be separated, mainly due to cooperative magnetophoresis [32–34]. By extending the DLVO theory with the magnetic interaction, this phenomenon can be explained [35]. Here, particles form aggregates because of the magnetic field gradient, as their magnetic dipoles align, and the cooperative effect speeds up the magnetophoretic separation. According to Faraudo et al., these aggregates are reversible for high zeta potentials. Electrostatic repulsion and magnetic attraction form a secondary minimum besides the primary one, separated by a potential barrier [35]. The magnetic Bjerrum length poses a parameter, which enables the evaluation of aggregation throughout a magnetophoretic process. It describes the distance of two parallel dipoles, where the magnetic force equals the thermal energy. Due to this parameter, it can be estimated if the magnetic dipoles are interacting with each other or not.

$$\lambda_B = \left(\frac{\mu_0 \cdot m^2}{2 \cdot \pi \cdot k_B \cdot T} \right)^{\frac{1}{3}} \qquad (1)$$

The Bjerrum length is dependent on the permeability of free space $\mu_0 = 4\pi \times 10^{-7}$ H m^{-1}, the Boltzmann's constant $k_B = 1.381 \times 10^{-23}$ J K^{-1}, the temperature T, and the magnetic dipole, which is written as

$$m = M_S \cdot \rho_P \cdot \frac{4}{3} \cdot \pi \cdot r^3, \qquad (2)$$

where the saturation magnetization per unit mass of colloid is M_S, the particle density is ρ_P, and the particle radius is r.

101

This study emphasizes the importance of understanding the aggregation behavior of bare iron oxide nanoparticles (BIONs) in different viscosities. The influence on a separation process in a low magnetic field gradient is investigated by the magnetophoretic sedimentation velocity with a sedimentation analyzer. The following hypotheses are proposed:

1. The aggregation behavior of BIONs in the gravity field is dependent on pH and viscosity, respectively. Therefore, the colloidal stability can be selectively controlled.
2. During magnetophoresis, these effects directly influence the separation process. The aggregate size, as well as viscosity, result in different magnetophoretic velocities.

Four different pH values between 4 and 9, which clearly show the pH's influence on aggregate size and therefore on magnetophoretic sedimentation velocity, are chosen. The viscosity of water (η = 0.888 mPa s) is compared with the 2.5-fold viscosity. A higher viscosity can be beneficial for magnetophoretic sorting processes, as field-induced aggregation and convection only play a minor role at elevated viscosities [31,33]. The higher viscosity is obtained by adding sucrose (η = 2.227 mPa s).

2. Results and Discussion

2.1. Particle Characterization

BIONs are synthesized via coprecipitation. They exhibit a high saturation magnetization of 70.84 Am^2 kg^{-1} (Figure 1a), no remanence and no hysteresis at 0 Oe [36–38]. The chemical composition and the crystalline spinel structure were previously described by Schwaminger et al. [39]. With Transmission Electron Microscopy (TEM) (Figure 1b), the optical diameter of the BIONs is examined, resulting in an average single particle diameter of 9.92 nm, which is similar to previous measurements of BIONs [38–40].

(**a**)	(**b**)
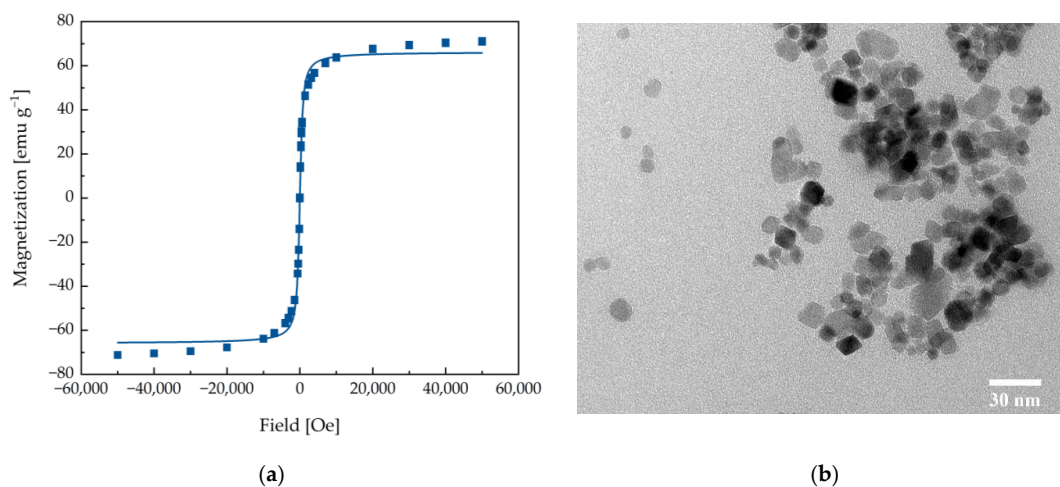
Figure 1. (**a**) Superconducting quantum interference (SQUID) measurement for the bare iron oxide nanoparticles (BIONs) at 300 K with a LangevinMod fit. (**b**) Transmission Electron Microscopy (TEM) image of the BIONs.

2.2. Influencing the Colloidal Stability of the BIONs due to Viscosity and pH

Zeta potential is the electrostatic potential at the particle's slipping plane, which presents the interface between the moving fluid and the fluid attached to the particle surface. Therefore, the zeta potential is used as a relative measurand for the surface potential and, thus, for the magnitude of a particle's charge. Due to the extent of electric repulsion between the particles in the solution, the colloidal stability can be evaluated. The repulsion energy is thereby dependent on the particles' radius and the extent of shielding, which is affected by the ionic strength of the solvent [41]. Figure 2 illustrates the course

of zeta potential versus pH and presents the amphiphilic character of the BIONs' surface. At very low and high pH, it ranges between 20 and 35 mV or −20 and −35 mV, meaning the BIONs' net charge is positive or negative, respectively. Thus, the particles' repulsion is high, and they are colloidally stable, leading to less aggregation. The hydrodynamic diameter measurement goes in line with this assumption, as it shows low diameters for low and high pH values. While the isoelectric point (IEP), where the potential is 0, is 6.69 for the low viscous solution (η = 0.888 mPa s) (Figure 2a), it is 6.07 for the high viscous solution (η = 2.227 mPa s) (Figure 2b) [42]. Here, the particles form aggregates up to 3000 nm in both liquids because of their low superficial charge. Comparing the particle distributions of both solutions, the one with the low viscosity (Figure 2a) exhibits a wide distribution over pH. In contrast, for the other one (Figure 2b), large aggregates can only be observed at pH 5 and 6. Thus, in the higher viscous solution, the colloidal stability of the BIONs is given over a broader pH range from pH 2 to 4 and pH 7 to 10. In addition, the polydispersity index (PDI) of the measured samples (Figure S1) confirms these results, as it is between 0.18 ± 0.09 and 0.24 ± 0.04 for the high viscous solution, whereas it is between 0.22 ± 0.03 and 0.54 ± 0.20 for the low viscous solution. Compared to the literature, a PDI below 0.7 is considered as nearly monodisperse [43]. For pH 2, 3, 9, and 10, the PDI for both solutions is similar; however, for the low viscous samples, the PDI at pH 5, 6, 7, and 8 is higher. This indicates that the BIONs around the IEP possess a higher heterogeneity in aggregate size. Additionally, this effect can be seen in the intensity distributions of all samples in Figures S2 and S3. For the water solution, heterogeneous aggregates are detected between pH 4 and 8, while the particle distributions for the higher viscosity are uniform. Particularly, for low pH values, the particles might react with the acid and therefore possess a higher stability.
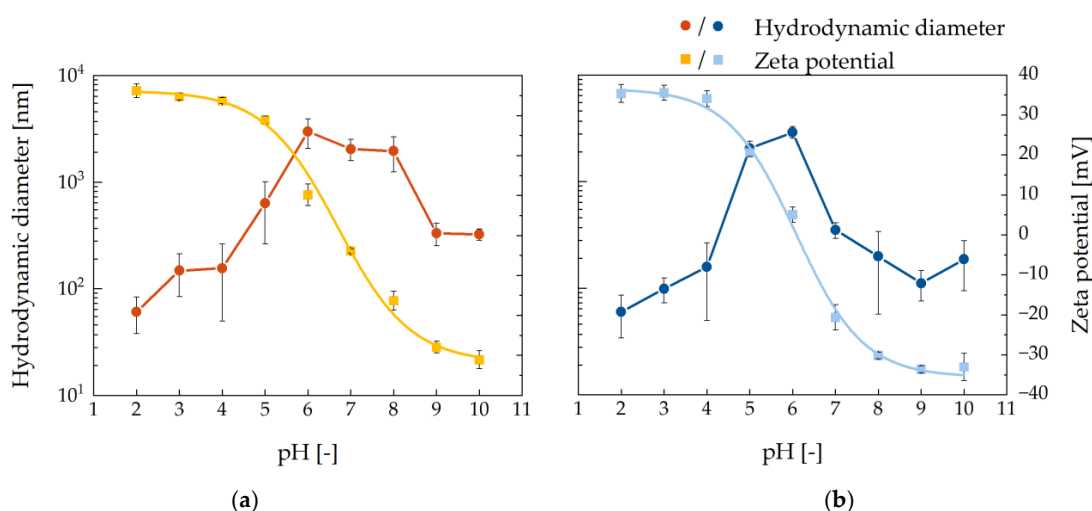
Figure 2. Hydrodynamic diameter and zeta potential measurements of BION suspension in pH 2 to 10 (**a**) in deionized water (η = 0.888 mPa s) (**b**) and sucrose solution (η = 2.227 mPa s).

The analysis of BIONs in other sugar solutions, such as fructose and glucose, at pH 7 resulted in similar particle distributions as sucrose (Figure S4). In the literature, the effect on the colloidal stability of particles due to higher viscosity by sugars, such as sucrose, is confirmed. Previously, Szalai et al. synthesized ex situ coated magnetite nanoparticles with gelatin and sucrose. They reported higher colloidal stability of their particles when adding sucrose [44]. Sun et al. propose that the multiple hydroxyl groups, as they are present in sucrose, can adsorb or chelate onto the magnetite surface, resulting in steric hindrance, as it is known to conventional surfactants [45,46]. Benítez et al. describe another effect of sugars,

where they claim that sucrose might influence particles' colloidal stability because of the hydration capacity. They extend the DLVO theory by the hydration repulsive energy, which occurs as water molecules around the particle surface restrict them in their motion, known as hydration pressure [47,48]. We assume that stabilization due to the higher viscosity with sucrose is reached because of a synergy of the mentioned effects.

2.3. Dependence of the Magnetophoretic Velocity on Aggregate Size and Viscosity

The effect of pH and viscosity on the aggregation behavior of our BIONs indicates that it is essential to evaluate the influence of different aggregate sizes regarding a magnetophoresis-based separation process. The Space-and-Time-resolved Extinction Profiles (STEP) technology is based on the sedimentation of particles due to magnetophoresis. It describes the particles' movement towards the magnetic field direction if the buoyancy and friction force is overcome (Figure 3).

(a)   **(b)**   **(c)**
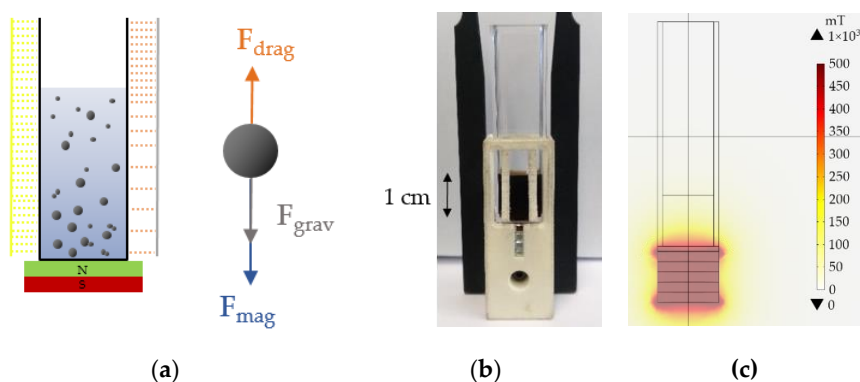
Figure 3. (**a**) Schematic illustration of the sedimentation analyzer (LUMiReader) with the involved forces (magnetic force F_{mag}, the gravitational force F_{grav}, and the drag force F_{drag}). (**b**) Experimental set-up. The cuvette filled with sample fluid is placed on a magnet, and parallel light with a wavelength of 870 nm transmits the sample. A light sensor records transmission profiles, and the magnetophoretic velocity of the particles is calculated. The magnetic flux density in the direction of the particle movement is 40 mT at the sample top and 350 mT at the sample bottom. (**c**) Calculated magnetic flux density along the *y*-axis. Calculations were performed with COMSOL Multiphysics 5.6.

Figure 4 presents the magnetophoretic velocity derived from STEPs over pH 4, 6, 7, and 9 at η = 0.888 and η = 2.227 mPa s. For pH 4 and 9, the magnetophoretic velocity is noticeably lower than for pH 6 and 7, which goes in line with the measured particle size distributions via dynamic light scattering (DLS) measurement (Figure 5). The latter pH values show around one power of ten higher diameters than pH 4 and 9 because the surface of the BIONs is charged positively or negatively, respectively. Hence, the attractive forces major the repulsive ones so that the particles do not resist aggregation. The same pattern can be observed for the high viscous samples. Here, at pH 6, which is almost the IEP of the BIONs, aggregates with a hydrodynamic diameter of 2764 ± 446 nm show a higher magnetophoretic velocity in contrast to other pH values where the hydrodynamic diameter is smaller (Figure 5b). Here, for pH 4, 7, and 9, a second mode with larger aggregates is detected, which is not visible in the intensity distributions (Figure S2). Even if the amount of these larger aggregates is lower compared to the first mode, they might influence the measured magnetophoretic velocity. The velocity differences are lower compared to the less viscous samples. Following Equation (7), the particle radius is directly proportional to the magnetophoretic force during the sedimentation process. Therefore, the measured velocities are in line with the theoretical assumptions.
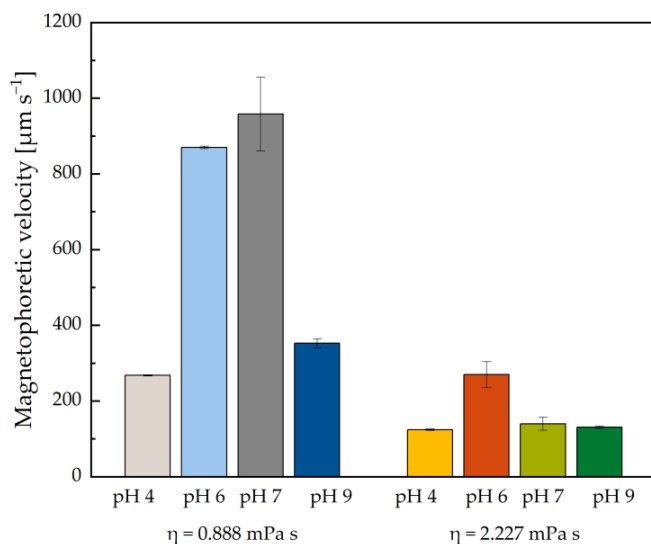
Figure 4. Magnetophoretic velocity over pH 4, 6, 7, and 9 of BION suspension in deionized water (η = 0.888 mPa s) and sucrose solution (η = 2.227 mPa s) with a corresponding mean diameter of DLS measurement.

(**a**) (**b**)
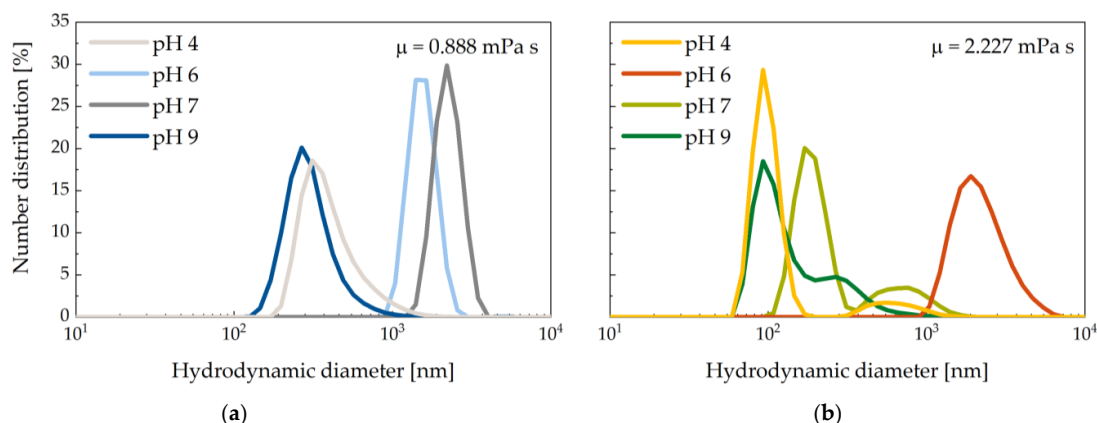
Figure 5. Particle size distribution at pH 4, 6, 7, and 9 of BION suspension (**a**) in deionized water (η = 0.888 mPa s) (**b**) and sucrose solution (η = 2.227 mPa s).

Besides the aggregate size, viscosity is another parameter that influences the separation process. The magnetophoretic velocities of all measured pH values are lower for the higher viscosity (η = 2.227 mPa s) compared to the lower one (η = 0.888 mPa s), as the viscosity is indirectly proportional to the velocity, as written in Equation (10). Due to the higher viscosity, the drag force increases and slows down the particle motion along the magnetic field gradient. The gravitational force does not influence this effect, as values for the sedimentation velocity show very low values for both viscosities (Table 1). Here, the sedimentation velocity is similar when having the same size of aggregates at different pH values only in a gravitational field.

Taking these findings together, the viscosity influences the colloidal stability of the particles and the magnetophoresis process itself. These effects should be taken into account when working with high viscous liquids, such as cell lysates or blood, in order to obtain a distinct separation process.

Table 1. Measurement of the sedimentation velocity and the corresponding hydrodynamic diameter of the samples in the sedimentation analyzer.

pH	η = 0.888 mPa s		η = 2.227 mPa s	
	Sedimentation Velocity (µm s^{-1})	Hydrodynamic Diameter (nm)	Sedimentation Velocity (µm s^{-1})	Hydrodynamic Diameter (nm)
4	1.57 ± 0.09	156 ± 106	0.88 ± 0.70	158 ± 108
6	3.82 ± 0.85	2986 ± 920	2.30 ± 0.01	2764 ± 446
7	3.69 ± 0.14	2047 ± 461	0.33 ± 0.28	351 ± 58
9	1.43 ± 0.37	331 ± 79	0.31 ± 0.06	111 ± 35

Regarding a LGMS process, the particle size poses an essential factor in the kinetics of the separation and the resulting process efficiency. As mentioned above, mainly the cooperative effect of magnetic aggregation speeds up the magnetophoretic motion of the particles [49]. Here, the Bjerrum length can be used in order to evaluate the formation of aggregates in a magnetic field [9,50]. Therefore, we calculate the ratio of the Bjerrum length λ_B and the particle diameter d (Figure 6). As seen in Figure 6, particles do not form aggregates in a magnetic field if $\lambda_B \, d^{-1} < 1$ with a saturation magnetization of 70.84 Am^2 kg^{-1} [49]. For our BIONs with a particle diameter of 9.92 nm, the ratio is 1.12, which implies magnetic aggregate formation. This value, measured by TEM, is close to one; however, this is the minimal limit, as the particle diameter in suspension is >100 nm, depending on the buffer conditions. Hence, the magnetophoretic velocity might be additionally influenced by this effect, but from a practical process view, cooperative magnetophoresis might be beneficial to implement such an LGMS process because the separation efficiency increases.
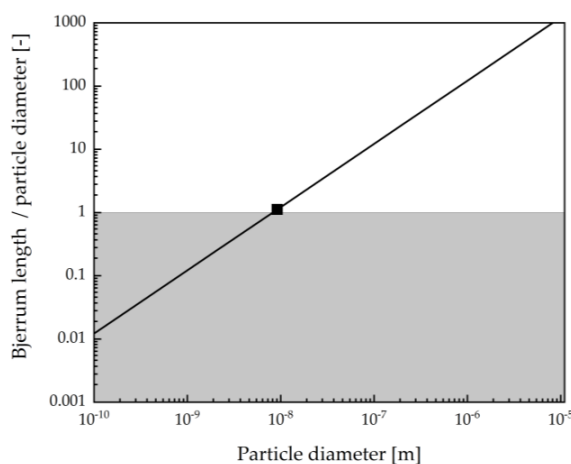
Figure 6. Log–log plot of the ratio of the Bjerrum length and the particle diameter over the particle diameter. The shaded region corresponds to particle diameters where no aggregation due to a magnetic field occurs, and the solid line describes the Bjerrum length for particles with the same magnetization. The symbol represents our particle size and indicates that magnetic aggregation takes place (transparent region).

Besides the cooperative magnetophoresis, Leong et al. recently discussed the effect of convective magnetophoresis [33,41]. They introduce the dimensionless Grashof number Gr$_m$ (Equation (3)), which is dependent on the magnetic field gradient ∇B, the volumetric

magnetization M, the particle concentration difference between the bulk solution, the collection plane $c_s - c_\infty$ and the length of the analyzed system L_c.

$$Gr_m = \frac{\rho \cdot \nabla B \cdot \left(\frac{\partial M}{\partial c}\right)_H \cdot (c_s - c_\infty) \cdot L_c^3}{\eta^2} \tag{3}$$

It describes the convection induced by an external magnetic field, which happens due to the rapid acceleration of the particles. Leong et al. state that the Grashof number is mostly dependent on the concentration, resulting in a higher magnetophoretic velocity for higher particle concentrations. However, in our study, all parameters are kept constant besides the viscosity. Its square is indirectly proportional to the dimensionless number, so one can say that an increase in viscosity lowers the convection and therefore, the magnetophoretic velocity as well.

In addition to both discussed effects, the cooperative and the convective magnetophoresis, the diffusion, described by the Stokes–Einstein Equation, is influenced by viscosity as shown in Equation (4) [51]:

$$D_o = \frac{k_B \cdot T}{6 \cdot \pi \cdot r \cdot \eta} \tag{4}$$

According to Equation (4), the diffusion coefficient is decreasing with a higher viscosity and thus, Brownian motion is lower as well. Hence, it evolves that viscosity noticeably influences various parameters during a magnetophoresis-based process and should be always considered.

To sum up, the colloidal stability of BIONs is controllable due to a change in pH value, but also a higher viscosity leads to stabilization. The former is based on electrostatic stabilization effects, whereas the various latter effects, such as a steric hindrance and/or hydration repulsion due to sucrose, might be involved. The different aggregate sizes and the viscosity influences the magnetophoresis process (Equations (5)–(10)). Particularly, for a separation process with high viscous liquids, the efficiency is lower [26]. Moreover, depending on the aggregate size, MNP–MNP interactions, as cooperative or convective magnetophoresis and Brownian motion, have to be considered, as these effects influence magnetophoretic processes, e.g., a microfluidic fractionation.

3. Materials and Methods

Coprecipitation of $Fe^{2+}/^{3+}$ ions was used to synthesize the BIONs [38]. For this, 28.9 g of sodium hydroxide (722 mmol, 4.10 equivalents (eq.), Carl Roth GmbH + Co. KG, Karlsruhe, Germany) was dissolved in 400 mL of degassed water under a nitrogen atmosphere. A solution, containing 86.6 g of $FeCl_3 \cdot 6H_2O$ (320 mmol, 1.82 eq., Sigma Aldrich Merck KGaA, Darmstadt, Germany) and 35.0 g of $FeCl_2 \cdot 4H_2O$ (176 mmol, 1.0 eq., Sigma Aldrich Merck KGaA, Darmstadt, Germany) in 160 mL of degassed water, was added slowly under continuous stirring. The temperature was kept constant at 27 °C via a water bath. A black precipitate built up immediately, and the reaction was continued under stable conditions for a further 30 min. Then, the precipitate was washed ~15 times with deionized water via magnetic decantation with a neodymium iron boron magnet in a glass bottle until the conductivity was below 200 µS cm^{-1}. The BIONs were stored under a nitrogen atmosphere at 4 °C. The magnetic susceptibility was analyzed by the SQUID device Quantum Design MPMS XL-7 (Quantum Design GmbH, Darmstadt, Germany). Therefore, the particles were lyophilized, and then they were glued into a small tube. TEM was performed with the JEM 1400 Plus microscope (JEOL GmbH, Freising, Germany), and the recorded images were subsequently evaluated by using ImageJ software.

All experiments were performed either in water ($\eta = 0.888$ mPa s, 25 °C) or in a 24% (w/w) sucrose solution ($\eta = 2.227$ mPa s, 25 °C, Carl Roth GmbH + Co. KG, Karlsruhe, Germany), fructose solution ($\eta = 1.9858$ mPa s, Carl Roth GmbH + Co. KG), or glucose solution ($\eta = 2.1201$ mPa s, AppliChem GmbH, Darmstadt, Germany). The pH was

adjusted by adding 0.1 M or 1 M sodium hydroxide (Carl Roth GmbH + Co. KG, Karlsruhe, Germany) or hydrochloric acid (VWR International GmbH, Darmstadt, Germany). A solution of 1 g L^{-1} BIONs was used, dispersed via an ultrasonication probe (5 min, 10 s on, 15 s off, 20%, Branson Ultrasonics Corporation, Danbury, United States of America). For zeta potential and hydrodynamic diameter by DLS evaluation, a ZetaSizer XS (Malvern Panalytical GmbH, Kassel, Germany) was used. Both measurements were performed at 25 °C in 1 mL of a 1 g L^{-1} solution in five and three measuring cycles in duplicates, respectively. The IEP was determined by applying a Boltzmann fit.

STEPs were recorded in duplicates at an optical wavelength of 870 nm (LUMiReader, LUM GmbH, Berlin, Germany) to calculate the magnetophoretic velocity. According to Newton's second law of motion, magnetophoresis is composed of the gravitational force F_{grav}, the magnetic force F_{mag} and the viscous drag force F_{drag}, pointing in the opposite direction of the former two forces.

$$\frac{m_P du}{dt} = F_{grav} + F_{mag} + F_{drag} \tag{5}$$

Here, m_P and u are the mass and the velocity of the particle, respectively. For simplicity, the inertial term can be neglected [49,52].

$$0 = F_{grav} + F_{mag} + F_{drag} \tag{6}$$

The magnetic force is determined by the magnetic field gradient ∇H, the permeabilities μ_0 and μ_r, the relative permittivity K, and the particle radius r:

$$F_{mag} = 3 \cdot \mu_0 \cdot \mu_r \cdot K \cdot \nabla H^2 \cdot 2 \cdot \pi \cdot r^3 \tag{7}$$

According to Stokes' law, the movement of a spherical particle in an incompressible fluid can be described as follows, where η corresponds to the fluid viscosity:

$$F_{drag} = -6 \cdot u \cdot \pi \cdot \eta \cdot r \tag{8}$$

The gravitational force is based on Newton's law of gravitation,

$$F_{grav} = \frac{4}{3} \left(\rho_p - \rho_f \right) \cdot g \cdot \pi \cdot r^3, \tag{9}$$

which is dependent on the density difference of particle and fluid $\rho_p - \rho_f$ and the free-fall acceleration g. The force balance, as written in Equations (6)–(9), can be solved for the velocity as written in Equation (10):

$$v = \frac{2 \cdot \left(\rho_p - \rho_f \right) \cdot g \cdot r^2}{9 \cdot \eta} + \frac{\mu_0 \cdot \mu_r \cdot K \cdot \nabla H^2 \cdot r^2}{2 \cdot \eta} \tag{10}$$

For the measurement, a disposable cuvette (1 × 1 × 4.4 cm) filled with 1 mL of solution was placed onto a stack of five cylindrical neodymium boron ferrite (NdFeB) magnets (diameter = 12 mm, height = 2 mm, N45, Webcraft GmbH, Gottmadingen, Germany). The built-in temperature control assured a constant temperature of 25 °C. The magnetic flux density was measured with a Hall detector PCE-MF M 3000 (PCE Instruments UK Limited, Southampton Hampshire, United Kingdom). The obtained transmittance profiles were integrated over the sample height, leading to an integral transmittance for each measurement time. For data evaluation, it was converted into an integral extinction value, which is directly proportional to the particle concentration after Lambert–Beer's law. Particle movement due to the magnetic and gravitational force induces the change in particle concentration. Therefore, the time-dependent variation of the extinction enables

calculating the magnetophoretic velocity v_{mag}, where L is the mean length defined by half of the sample height.

$$v = \frac{<L>}{t} \qquad (11)$$

A cumulative distribution function ϕ (v_{mag}) is obtained by plotting the relative extinction over the magnetophoretic velocity [53]. The relative extinction E_{rel} is determined by the initial extinction of the sample E_0 and the minimal extinction E_{min} at the end of magnetophoresis measurement.

$$E_{rel}(t) = \frac{E - E_{min}}{E_0 - E_{min}}, \qquad (12)$$

For better comparability, the value at $t_{0.5}$ was used, which is the distribution function's median. It describes the velocity of 50% of the particles at the time $t_{0.5}$, where the extinction has fallen by half. The sedimentation analysis experiments were performed with a magnetic flux density between 40 and 350 mT, which corresponds to a magnetization between 29.31 and 54.40 Am^2 kg^{-1}.

4. Conclusions

BIONs with an average diameter of 9.2 nm were synthesized via coprecipitation, showing a high saturation magnetization [38]. Zeta potential and hydrodynamic diameter measurements showed that pH and viscosity influence the colloidal stability of the particles. pH values close to the IEP resulted in large particle agglomerates; however, electrostatic stabilization was observed for high and low pH values. The particle distribution over different pHs narrowed due to the increase in viscosity with sucrose. This could be explained by the hydration repulsion and the steric stabilization effect of sucrose. The aggregate size and viscosity directly influence a magnetophoretic process. The particle diameter is proportional to the magnetophoretic velocity, which results in high velocities for large aggregates and lower velocities for small particle diameters. By increasing the viscosity, the drag force counteracts the magnetophoretic force and decreases the magnetophoretic velocity of all aggregate sizes. This study emphasizes the underestimated effect of viscosity by using the simple method of sedimentation analysis, in addition to zeta potential and DLS measurement. In downstream processing or medical applications, liquids such as cell suspension or blood will affect particle migration, resulting in a lower separation. Particularly, the stabilizing effect of sucrose should be further examined, as the formation of aggregates is one of the main reasons for using different coatings for the steric stabilization of the BIONs [54]. In further studies, these new findings can be used to control the aggregation behavior for applications in medicine or biotechnology.

References

1. Fraga-García, P.; Kubbutat, P.; Brammen, M.; Schwaminger, S.; Berensmeier, S. Bare Iron Oxide Nanoparticles for Magnetic Harvesting of Microalgae: From Interaction Behavior to Process Realization. *Nanomaterials* **2018**, *8*, 292. [CrossRef]
2. Schnell, F.; Kube, M.; Berensmeier, S.; Schwaminger, S.P. Magnetic Recovery of Cellulase from Cellulose Substrates with Bare Iron Oxide Nanoparticles. *ChemNanoMat* **2019**, *5*, 422–426. [CrossRef]
3. Zhang, H.; Ding, W.; Li, S.; Ya, S.; Li, F.; Qiu, B. On-chip analysis of magnetically labeled cells with integrated cell sorting and counting techniques. *Talanta* **2020**, *220*, 121351. [CrossRef]
4. Puddu, M.; Paunescu, D.; Stark, W.J.; Grass, R.N. Magnetically Recoverable, Thermostable, Hydrophobic DNA/Silica Encapsulates and Their Application as Invisible Oil Tags. *ACS Nano* **2014**, *8*, 2677–2685. [CrossRef]
5. Ling, W.; Wang, M.; Xiong, C.; Xie, D.; Chen, Q.; Chu, X.; Qiu, X.; Li, Y.; Xiao, X. Synthesis, surface modification, and applications of magnetic iron oxide nanoparticles. *J. Mater. Res.* **2019**, *34*, 1828–1844. [CrossRef]
6. Liu, S.; Yu, B.; Wang, S.; Shen, Y.; Cong, H. Preparation, surface functionalization and application of Fe3O4 magnetic nanoparticles. *Adv. Colloid Interface Sci.* **2020**, *281*, 102165. [CrossRef]
7. Kodama, R. Magnetic nanoparticles. *Magnetochemistry* **2020**, *6*. [CrossRef]
8. Massart, R. Preparation of aqueous magnetic liquids in alkaline and acidic media. *IEEE Trans. Magn.* **1981**, *17*, 1247–1248. [CrossRef]
9. Leong, S.S.; Yeap, S.P.; Lim, J. Working principle and application of magnetic separation for biomedical diagnostic at high- and low-field gradients. *Interface Focus* **2016**, *6*, 20160048. [CrossRef]
10. Lozar, T.; Jesenko, T.; Prevodnik, V.K.; Cemazar, M.; Hosta, V.; Jericevic, A.; Nolde, N.; Kuhar, C.G. Preclinical and Clinical Evaluation of Magnetic-Activated Cell Separation Technology for CTC Isolation in Breast Cancer. *Front. Oncol.* **2020**, *10*, 1–10. [CrossRef]
11. Miltenyi, S.; Müller, W.; Weichel, W.; Radbruch, A. High gradient magnetic cell separation with MACS. *Cytometry* **1990**, *11*, 231–238. [CrossRef]
12. Fratzl, M.; Delshadi, S.; Devillers, T.; Bruckert, F.; Cugat, O.; Dempsey, N.M.; Blaire, G. Magnetophoretic induced convective capture of highly diffusive superparamagnetic nanoparticles. *Soft Matter* **2018**, *14*, 2671–2681. [CrossRef]
13. Corchero, J.L.; Villaverde, A. Biomedical applications of distally controlled magnetic nanoparticles. *Trends Biotechnol.* **2009**, *27*, 468–476. [CrossRef] [PubMed]
14. Toh, P.Y.; Yeap, S.P.; Kong, L.P.; Ng, B.W.; Chan, D.J.C.; Ahmad, A.L.; Lim, J.K. Magnetophoretic removal of microalgae from fishpond water: Feasibility of high gradient and low gradient magnetic separation. *Chem. Eng. J.* **2012**, *211-212*, 22–30. [CrossRef]
15. Alnaimat, F.; Karam, S.; Mathew, B.; Mathew, B. Magnetophoresis and Microfluidics: A Great Union. *IEEE Nanotechnol. Mag.* **2020**, *14*, 24–41. [CrossRef]
16. Robert, D.; Pamme, N.; Conjeaud, H.; Gazeau, F.; Iles, A.; Wilhelm, C. Cell sorting by endocytotic capacity in a microfluidic magnetophoresis device. *Lab. Chip* **2011**, *11*, 1902–1910. [CrossRef] [PubMed]
17. Kievit, F.M.; Zhang, M. Surface Engineering of Iron Oxide Nanoparticles for Targeted Cancer Therapy. *Acc. Chem. Res.* **2011**, *44*, 853–862. [CrossRef]
18. Socoliuc, V.; Peddis, D.; Petrenko, V.I.; Avdeev, M.V.; Susan-Resiga, D.; Szabó, T.; Turcu, R.; Tombácz, E.; Vékás, L. Magnetic Nanoparticle Systems for Nanomedicine—A Materials Science Perspective. *Magnetochemistry* **2020**, *6*, 2. [CrossRef]
19. Dulińska-Litewka, J.; Łazarczyk, A.; Hałubiec, P.; Szafrański, O.; Karnas, K.; Karewicz, A. Superparamagnetic Iron Oxide Nanoparticles—Current and Prospective Medical Applications. *Materials* **2019**, *12*, 617. [CrossRef]
20. Ansari, S.A.M.K.; Ficiarà, E.; Ruffinatti, F.A.; Stura, I.; Argenziano, M.; Abollino, O.; Cavalli, R.; Guiot, C.; D'Agata, F. Magnetic Iron Oxide Nanoparticles: Synthesis, Characterization and Functionalization for Biomedical Applications in the Central Nervous System. *Materials* **2019**, *12*, 465. [CrossRef]
21. Vangijzegem, T.; Stanicki, D.; Laurent, S. Magnetic iron oxide nanoparticles for drug delivery: Applications and characteristics. *Expert Opin. Drug Deliv.* **2019**, *16*, 69–78. [CrossRef]
22. Soetaert, F.; Korangath, P.; Serantes, D.; Fiering, S.; Ivkov, R. Cancer therapy with iron oxide nanoparticles: Agents of thermal and immune therapies. *Adv. Drug Deliv. Rev.* **2020**, *163-164*, 65–83. [CrossRef] [PubMed]

23. Belanova, A.A.; Gavalas, N.; Makarenko, Y.M.; Belousova, M.M.; Soldatov, A.V.; Zolotukhin, P.V. Physicochemical Properties of Magnetic Nanoparticles: Implications for Biomedical Applications In Vitro and In Vivo. *Oncol. Res. Treat.* **2018**, *41*, 139–143. [CrossRef]
24. Nam, J.; Huang, H.; Lim, H.; Lim, C.; Shin, S. Magnetic Separation of Malaria-Infected Red Blood Cells in Various Developmental Stages. *Anal. Chem.* **2013**, *85*, 7316–7323. [CrossRef] [PubMed]
25. Pamme, N.; Wilhelm, C. Continuous sorting of magnetic cells via on-chip free-flow magnetophoresis. *Lab. Chip* **2006**, *6*, 974–980. [CrossRef] [PubMed]
26. Roth, H.-C.; Prams, A.; Lutz, M.; Ritscher, J.; Raab, M.; Berensmeier, S. A high-gradient magnetic separator for highly viscous process liquors in industrial biotechnology. *Chem. Eng. Technol.* **2016**, *39*, 469–476. [CrossRef]
27. Mishima, F.; Hayashi, S.; Akiyama, Y.; Nishijima, S. Development of a Superconducting High Gradient Magnetic Separator for a Highly Viscous Fluid. *IEEE Trans. Appl. Supercond.* **2011**, *22*, 3700204. [CrossRef]
28. Gupta, A.K.; Gupta, M. Synthesis and surface engineering of iron oxide nanoparticles for biomedical applications. *Biomaterials* **2005**, *26*, 3995–4021. [CrossRef]
29. Coppola, L.; Caserta, F.; De Lucia, D.; Guastafierro, S.; Grassia, A.; Coppola, A.; Marfella, R.; Varricchio, M. Blood viscosity and aging. *Arch. Gerontol. Geriatr.* **2000**, *31*, 35–42. [CrossRef]
30. Alphandéry, E. Bio-synthesized iron oxide nanoparticles for cancer treatment. *Int. J. Pharm.* **2020**, *586*, 119472. [CrossRef]
31. Solsona, M.; Nieuwelink, A.-E.; Meirer, F.; Abelmann, L.; Odijk, M.; Olthuis, W.; Weckhuysen, B.M.; Berg, A.V.D. Magnetophoretic Sorting of Single Catalyst Particles. *Angew. Chem. Int. Ed.* **2018**, *57*, 10589–10594. [CrossRef] [PubMed]
32. Faraudo, J.; Andreu, J.S.; Calero, C.; Camacho, J. Predicting the Self-Assembly of Superparamagnetic Colloids under Magnetic Fields. *Adv. Funct. Mater.* **2016**, *26*, 3837–3858. [CrossRef]
33. Leong, S.S.; Ahmad, Z.; Low, S.C.; Camacho, J.; Faraudo, J.; Lim, J. Unified View of Magnetic Nanoparticle Separation under Magnetophoresis. *Langmuir* **2020**, *36*, 8033–8055. [CrossRef]
34. Yavuz, C.T.; Mayo, J.T.; Yu, W.W.; Prakash, A.; Falkner, J.C.; Yean, S.; Cong, L.; Shipley, H.J.; Kan, A.; Tomson, M.; et al. Low-Field Magnetic Separation of Monodisperse Fe3O4 Nanocrystals. *Science* **2006**, *314*, 964–967. [CrossRef]
35. Faraudo, J.; Camacho, J. Cooperative magnetophoresis of superparamagnetic colloids: Theoretical aspects. *Colloid Polym. Sci.* **2009**, *288*, 207–215. [CrossRef]
36. Schwaminger, S.P.; Fraga-García, P.; Selbach, F.; Hein, F.G.; Fuß, E.C.; Surya, R.; Roth, H.-C.; Blank-Shim, S.A.; Wagner, F.E.; Heissler, S.; et al. Bio-nano interactions: Cellulase on iron oxide nanoparticle surfaces. *Adsorption* **2016**, *23*, 281–292. [CrossRef]
37. Bean, C.P.; Livingston, J.D. Superparamagnetism. *J. Appl. Phys.* **1959**, *30*, S120–S129. [CrossRef]
38. Turrina, C.; Berensmeier, S.; Schwaminger, S. Bare Iron Oxide Nanoparticles as Drug Delivery Carrier for the Short Cationic Peptide Lasioglossin. *Pharmaceuticals* **2021**, *14*, 405. [CrossRef]
39. Schwaminger, S.; Syhr, C.; Berensmeier, S. Controlled Synthesis of Magnetic Iron Oxide Nanoparticles: Magnetite or Maghemite? *Crystals* **2020**, *10*, 214. [CrossRef]
40. Schwaminger, S.P.; Bauer, D.; Fraga-García, P.; Wagner, F.E.; Berensmeier, S. Oxidation of magnetite nanoparticles: Impact on surface and crystal properties. *CrystEngComm* **2016**, *19*, 246–255. [CrossRef]
41. Schwaminger, S.P.; Schwarzenberger, K.; Gatzemeier, J.; Lei, Z.; Eckert, K. Magnetically Induced Aggregation of Iron Oxide Nanoparticles for Carrier Flotation Strategies. *ACS Appl. Mater. Interfaces* **2021**, *13*, 20830–20844. [CrossRef] [PubMed]
42. Schwaminger, S.P.; Blank-Shim, S.A.; Scheifele, I.; Fraga-García, P.; Berensmeier, S. Peptide binding to metal oxide nanoparticles. *Faraday Discuss.* **2017**, *204*, 233–250. [CrossRef] [PubMed]
43. Stetefeld, J.; McKenna, S.; Patel, T.R. Dynamic light scattering: A practical guide and applications in biomedical sciences. *Biophys. Rev.* **2016**, *8*, 409–427. [CrossRef] [PubMed]
44. Szalai, A.J.; Manivannan, N.; Kaptay, G. Super-paramagnetic magnetite nanoparticles obtained by different synthesis and separation methods stabilized by biocompatible coatings. *Colloids Surfaces A Physicochem. Eng. Asp.* **2019**, *568*, 113–122. [CrossRef]
45. Sun, X.; Zheng, C.; Zhang, F.; Yang, Y.; Wu, G.; Yu, A.; Guan, N. Size-Controlled Synthesis of Magnetite (Fe3O4) Nanoparticles Coated with Glucose and Gluconic Acid from a Single Fe(III) Precursor by a Sucrose Bifunctional Hydrothermal Method. *J. Phys. Chem. C* **2009**, *113*, 16002–16008. [CrossRef]
46. Cushing, B.L.; Kolesnichenko, V.; O'Connor, C.J. Recent Advances in the Liquid-Phase Syntheses of Inorganic Nanoparticles. *Chem. Rev.* **2004**, *104*, 3893–3946. [CrossRef] [PubMed]
47. Benítez, E.I.; Genovese, D.B.; Lozano, J.E. Effect of typical sugars on the viscosity and colloidal stability of apple juice. *Food Hydrocoll.* **2009**, *23*, 519–525. [CrossRef]
48. Chalikian, T.V. Ultrasonic and Densimetric Characterizations of the Hydration Properties of Polar Groups in Monosaccharides. *J. Phys. Chem. B* **1998**, *102*, 6921–6926. [CrossRef]
49. Leong, S.S.; Ahmad, Z.; Lim, J. Magnetophoresis of superparamagnetic nanoparticles at low field gradient: Hydrodynamic effect. *Soft Matter* **2015**, *11*, 6968–6980. [CrossRef]
50. Cuevas, G.D.L.; Faraudo, J.; Camacho, J. Low-Gradient Magnetophoresis through Field-Induced Reversible Aggregation. *J. Phys. Chem. C* **2008**, *112*, 945–950. [CrossRef]
51. Einstein, A. Über die von der molekularkinetischen Theorie der Wärme geforderte Bewegung von in ruhenden Flüssigkeiten suspendierten Teilchen. *Ann. Phys.* **1905**, *322*, 549–560. [CrossRef]
52. Furlani, E.P. Analysis of particle transport in a magnetophoretic microsystem. *J. Appl. Phys.* **2006**, *99*, 024912. [CrossRef]

53. Mykhaylyk, O.; Lerche, D.; Vlaskou, D.; Schoemig, V.; Detloff, T.; Krause, D.; Wolff, M.; Joas, T.; Berensmeier, S.; Plank, C.; et al. Biomagnetic Particles Magnetophoretic Velocity Determined by Space- and Time-Resolved Extinction Profiles. *IEEE Magn. Lett.* **2015**, *6*, 1–4. [CrossRef]
54. Laurent, S.; Forge, D.; Port, M.; Roch, A.; Robic, C.; Elst, L.V.; Muller, R.N. Erratum: Magnetic Iron Oxide Nanoparticles: Synthesis, Stabilization, Vectorization, Physicochemical Characterizations, and Biological Applications. *Chem. Rev.* **2008**, *110*, 2574. [CrossRef]

Supplementary Materials: The Effect of pH and Viscosity on Magnetophoretic Separation of Iron Oxide Nanoparticles

Leonie Wittmann, Chiara Turrina and Sebastian P. Schwaminger *

Bioseparation Engineering Group, Department of Mechanical Engineering, Technical University of Munich, Boltzmanstr. 15, 85748 Garching b. München, Germany; l.wittmann@tum.de (L.W.); c.turrina@tum.de (C.T.)
* Correspondence: s.schwaminger@tum.de
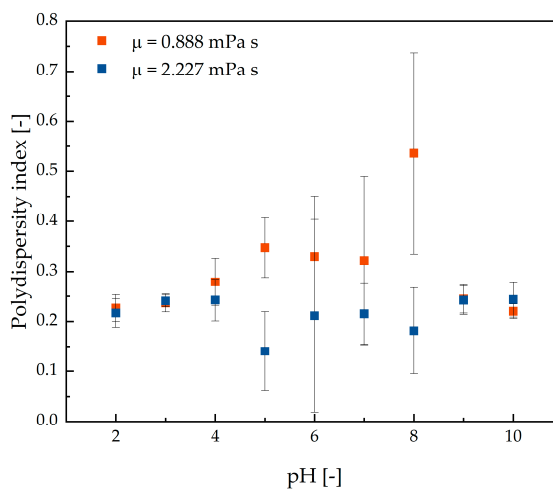
Figure S1. Polydispersity Index of BION suspension from pH 2 to 10 in deionized water (η = 0.888 mPa s) and sucrose solution (η = 2.227 mPa s).
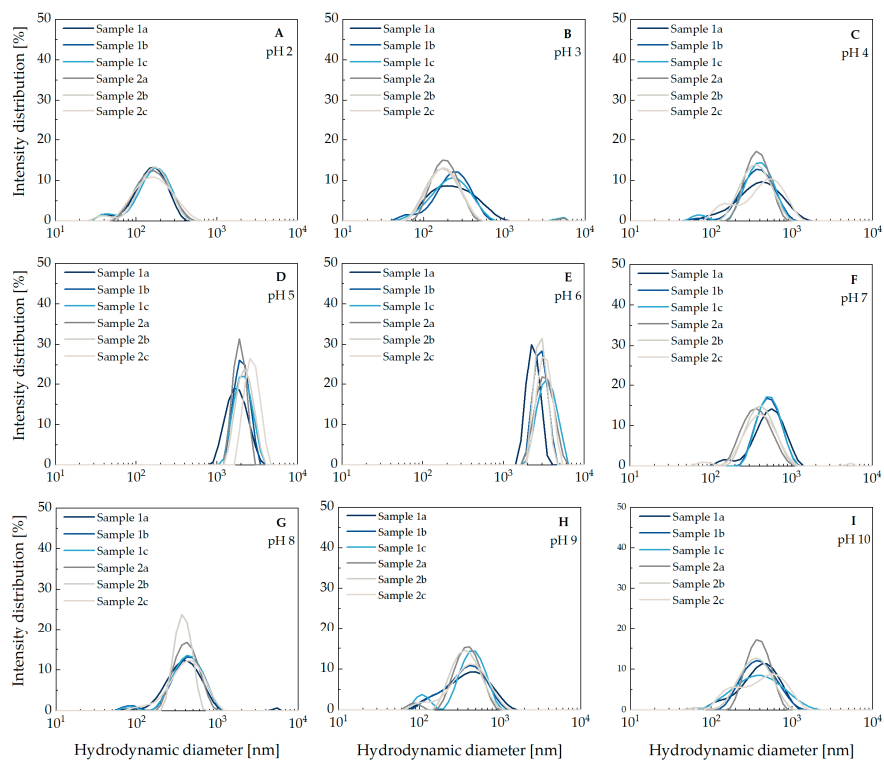
Figure S2. Intensity distribution data of pH 2 to 10 for high viscous BION suspension. Technical triplicates are shown for each duplicate.
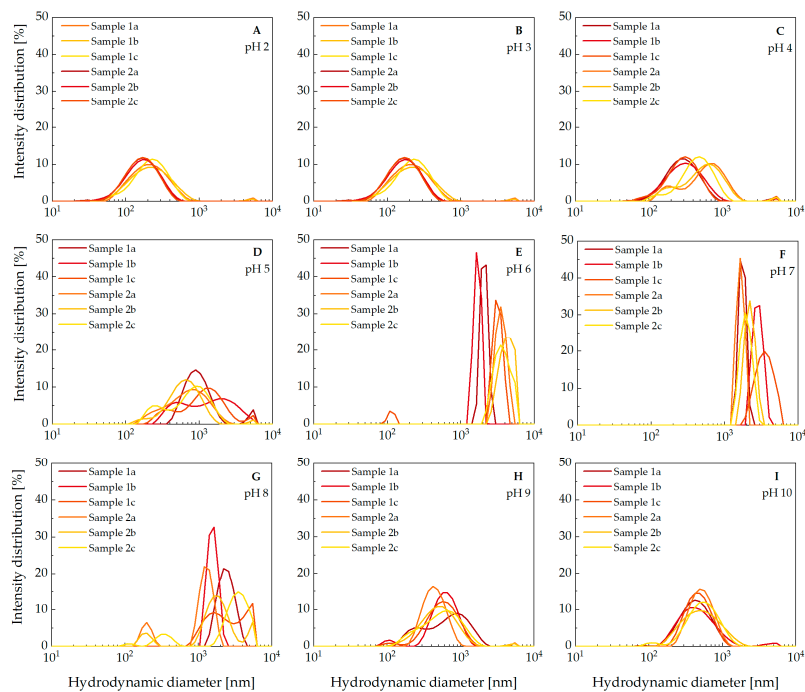
Figure S3. Intensity distribution data of pH 2 to 10 for low viscous BION suspension. Technical triplicates are shown for each duplicate.
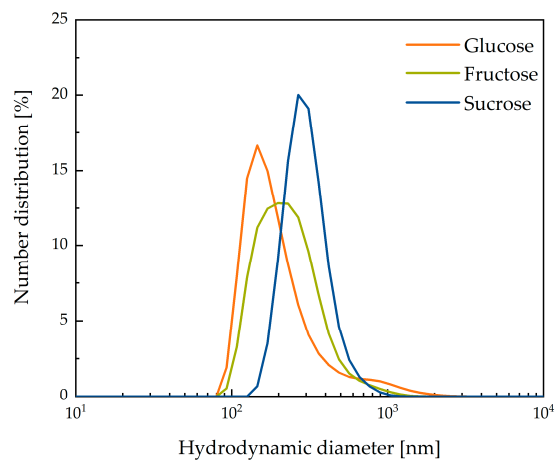
Figure S4. Number distribution of BIONS in fructose, glucose and sucrose solution at pH 7.

115

A.1.2 Magnetophoresis in Microfluidic Applications: Influence of Magnetic Convection in Hydrodynamic Fields

Nanoscale

PAPER

Check for updates

Influence of magnetic convection on separation efficiency in magnetophoretic microfluidic processes: a combined simulation and experimental study†

Leonie Wittmann, [ID] ‡[a] Emily Krucker-Velasquez, [ID] ‡[b] Julia Schaupp,[a] Laura Westphal,[a] James W. Swan, [ID] §[b] Alfredo Alexander-Katz, [ID] [c] Martin Z. Bazant, [ID] [b] Sebastian P. Schwaminger [ID] *[a,d,e] and Sonja Berensmeier [ID] [a,f]

This work explores the complex hydrodynamics in magnetophoretic microfluidic processes, focusing on the interplay of forces and particle concentrations. The study employs a combined simulation and experimental approach to investigate the impact of magnetophoresis on magneto-responsive nanoparticles (MNPs) and their environment, including non-magneto-responsive nanoparticles (non-MNPs) in a microfluidic system. Our findings reveal that the motion of MNPs induces a hydrodynamic convective motion of non-MNPs, significantly affecting the separation efficiency and purity of the particles. The separation efficiency of MNPs increases with the Péclet number, reflecting the increase in the magnetophoretic force, but decreases with lower concentrations. Conversely, non-MNPs exhibit high and constant separation efficiency with increasing Péclet number, independent of the magnetophoretic force. In a mixture, the separation efficiency of non-MNPs decreases, suggesting that non-MNPs drag along MNPs. The Mason number, representing the ratio between shear and magnetophoretic force, also plays a crucial role in the separation process. The results underscore the need for careful control and optimization of the Péclet and Mason numbers, as well as particle concentrations, for efficient magnetophoretic microfluidic processes. This study provides valuable information on the underlying principles of magnetophoresis in microfluidic applications, with implications for biochemistry, biomedicine, and biotechnology.

1 Introduction

In recent years, the development of lab-on-a-chip platforms has garnered significant attention in the field of biomedical research, including disease diagnosis, drug development, and

[a]Technical University of Munich, TUM School of Engineering and Design, Chair of Bioseparation Engineering, Boltzmannstr. 15, 85748 Garching, Germany. E-mail: s.schwaminger@tum.de
[b]Department of Chemical Engineering, Massachusetts Institute of Technology, Cambridge, Massachusetts 02139, USA
[c]Department of Materials Science and Engineering, Massachusetts Institute of Technology, Cambridge, Massachusetts 02139, USA
[d]Medical University Graz, Otto-Loewi Research Center, Division of Medicinal Chemistry, Neue Stiftingtalstr. 6, 8010 Graz, Austria. E-mail: sebastian.schwaminger@medunigraz.at
[e]BioTechMed-Graz, Mozartgasse 12, 8010 Graz, Austria
[f]Technical University of Munich, Munich Institute of Integrated Materials, Energy and Process Engineering, Lichtenberstr. 4a, 85748 Garching, Germany
†Electronic supplementary information (ESI) available. See DOI: https://doi.org/10.1039/d4nr02225d
‡These authors contributed equally to this work.
§Deceased author.

personalized medicine. These miniaturized analytical devices offer a range of advantages over traditional laboratory techniques, including reduced sample volumes, faster analysis times, and improved sensitivity and selectivity.[1,2]

The basic principle of a lab-on-a-chip platform involves the integration of multiple laboratory functions onto a single microchip, allowing the parallel processing of multiple samples having a high degree of controllability and optimization. This integration is achieved through the use of microfluidics, which enables manipulation at the microscale level[2,3] and precise control of fluid flow with low Reynolds numbers[4] ranging from 10^{-6} to 10. Using microfluidic technology, lab-on-a-chip platforms are capable of performing a range of functions, including magnetophoresis-based cell sorting and detection,[5] DNA sequencing,[6] and protein analysis.[7] The potential impact of lab-on-a-chip platforms in biomedical research is huge. For example, using them for point-of-care diagnostics could greatly improve access to medical care in low-resource settings, where traditional laboratory techniques are often prohibitively expensive or logistically challenging.[8,9] Similarly, performing high-throughput drug screening on a microfluidic platform could greatly accel-

erate the drug development process, leading to more efficient and cost-effective drug discovery.[1]

In transport processes, the Péclet number describes the ratio of convective to diffusive forces. Controlling the Péclet number is crucial in microfluidic devices to optimize either a sorting process or to achieve efficient mixing in reaction processes.[4,10] In magnetophoresis-based processes, one key challenge is the need for a comprehensive theory for predicting and understanding the dynamic behavior of magneto-responsive nanoparticles (MNPs).[11–13] These magneto-responsive nanoparticles can be engineered with different surface coatings and functionalizations to serve as carriers for a particular substance or to specifically target cells.[14–17] Moreover, the presence of magnetic fields can lead to complex emergent behavior; such as spontaneous pattern formation and self-assembly.[18] When this magnetic field varies in space, MNPs will experience a force that causes them to migrate. This phenomenon is commonly referred to as magnetophoresis, which, similar to its analogous "electrophoresis" for charged nanoparticles,[19] has frequently been modeled *via* mean-field approximations.[20] Nonetheless, thermal fluctuations and discrete particle interactions are essential at the mesoscale, making classic mean-field theories poorly equipped to accurately simulate and predict the transport and equilibrium properties of magnetic colloidal suspensions. Particle-based simulations, such as molecular or Brownian dynamics simulations, can provide a picture of the underlying physical phenomena present in colloidal suspensions. However, due to the long-ranged and many-bodied nature of the hydrodynamic and magnetic forces present in magnetophoretic processes, previous computational work has only considered magnetic species and mainly focused on the aggregation kinetics of magnetic agglomerates.[16,21]

This study aims to explore the transport mechanisms in colloidal dispersions of MNPs and non-MNPs in the presence of a spatially varying magnetic field, particle concentration, and particle solution flow and their effect on the separation efficiency (schematically shown in Fig. 1). Notably, the influence of magnetic convection in a hydrodynamic system comprising magnetic and non-magneto-responsive entities in a

microfluidic or millifluidic chip has yet to be previously investigated.[3,22,23] We compliment and support our findings with large-scale Brownian dynamics simulations coupled to the magnetic equivalent of Poisson's equation to solve for the magnetostatic field of a mixture of magneto-responsive and non-magneto-responsive nanoparticles in the presence of a magnetic field gradient. The hydrodynamic forces between colloidal particles are computed using a positively split Ewald method[24] and the magnetostatic potential is computed using a spectral Ewald method.[25,26] We present a combined simulation and experimental approach to demonstrate that convection motion is an underappreciated effect in magnetohydrodynamic systems.

2 Theory and numerical methods

2.1 Brownian dynamics simulation

We model the mixture of MNP and non-MNP as a suspension of charged, hard, spherical particles of radius a. We assume that these particles are suspended in a continuum Newtonian fluid such that the colloids interact with the solvent only *via* stochastic Brownian forces from fluctuations in the thermal energy or fluctuating hydrodynamics due to the momentum relaxation of the solvent molecules.[27] Under these assumptions we can start with Langevin's equation to derive our equations of motion:

$$\mathbf{m} \cdot \frac{d\mathbf{u}_\alpha}{dt} = \mathbf{F}_\alpha^H + \mathbf{F}_\alpha^I + \mathbf{F}_\alpha^M + \mathbf{F}_\alpha^B, \qquad (1)$$

where $\mathbf{u}_\alpha$ is the velocity of the αth colloid, $\mathbf{F}_\alpha^H$ is the hydrodynamic force acting on the αth colloid, $\mathbf{F}_\alpha^I$ accounts for forces arising from a generic conservative potential, $\mathbf{F}_\alpha^M$ is the magnetophoretic force due to the magnetic field gradient[28] and $\mathbf{F}_\alpha^B$ is the stochastic Brownian force. The last force satisfies the fluctuation–dissipation theorem[19] with ensemble average:

$$\langle \mathbf{F}^B(t) \rangle = 0; \quad \langle \mathbf{F}^B(t)\mathbf{F}^B(t+\tau) \rangle = 2k_B T(\mathbf{M}^H)^{-1}\delta(\tau) \qquad (2)$$

where $\mathbf{F}^B(t) = [\mathbf{F}_1{}^B(t), \mathbf{F}_2{}^B(t),...]$, $\langle \cdot \rangle$ indicates the expectation value, δ is the Dirac delta function, and $\mathbf{M}^H$ is the hydrodyn-
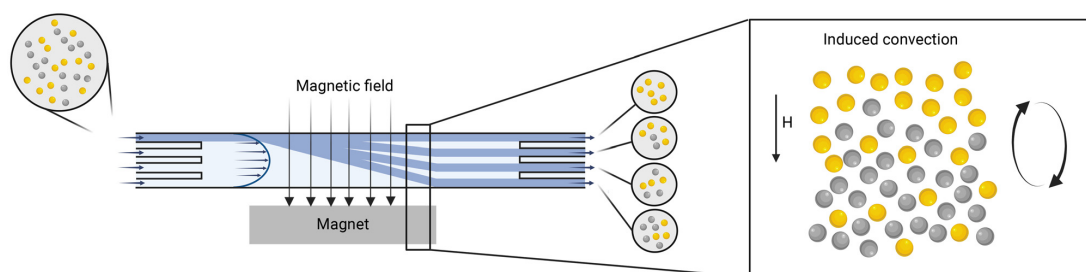
Fig. 1 Scheme of the microfluidic chip sorting a mixture of MNPs (grey) and non-MNPs (yellow) within a spatially varying magnetic field. The MNPs generate a hydrodynamic force influencing the non-MNPs, resulting in their co-migration alongside the MNPs. This magnetically induced convective motion is analyzed through both experimentally and large-scale Brownian dynamic simulation. Created with Biorender.com.

amic mobility tensor. This formulation ensures that any energy a colloid gains from a thermal fluctuation is dissipated as drag to the solvent.

A more mathematically rigorous formulation states that the Brownian force, consistent with the distribution in the second term of eqn (2), is sampled from a collection of independent Wiener processes, $\mathbf{W}(t)$, expressed as

$$\mathbf{F}^{B} = \sqrt{2k_{B}T}\left(\mathbf{M}^{H}\right)^{-1/2} \cdot \frac{d\mathbf{W}}{dt}. \tag{3}$$

Here, the square root of the inverse of the mobility matrix, $(\mathbf{M}^{H})^{-1/2}$, satisfies the relation $(\mathbf{M}^{H})^{-1/2} \cdot (\mathbf{M}^{H})^{-1/2\dagger} = (\mathbf{M}^{H})^{-1}$, where $\dagger$ denotes the adjoint (or conjugate transpose).

At the colloidal scale, inertial relaxation occurs on time scales orders of magnitude smaller than those governing colloidal motion. Consequently, any perturbation to the particle's momentum dissipates almost instantaneously. Rigorous integration of eqn (1) results in a set of stochastic differential-algebraic equations (SDAE) that faithfully capture the *overdamped* Langevin dynamics:

$$\mathbf{u}_{\alpha}(t) = \mathbf{M}_{\alpha\beta}^{H} \cdot \left(\mathbf{F}_{\beta}^{I} + \mathbf{F}_{\beta}^{M}\right) + \sqrt{2k_{B}T\mathbf{M}_{\alpha\beta}^{H}} \cdot \frac{d\mathbf{W}}{dt} \\ + k_{B}T\nabla \cdot \mathbf{M}_{\alpha\beta}^{H} \tag{4}$$

The final term in eqn (4), often referred to as the Brownian or thermal drift, emerges from integrating out the inertial degrees of freedom in eqn (1). Physically, this drift introduces an additional flux that actively displaces particles from regions of low mobility,[29] preventing their accumulation and ensuring a uniform exploration of the system's phase space.

Good agreement between experimental measurements and simulation results for a suspension of colloidal particles (including concentrated ones) can be achieved with a relatively coarse approximation for the interparticle hydrodynamic interactions. The fields generated by beads in a Newtonian fluid can be approximated as the superposition of the field generated by a point particle and a point quadrupole.[24] When all colloidal particles are of the same size, the hydrodynamic fields are given by the Rotne–Prager–Yamakawa mobility tensor:[19]

$$\mathbf{M}_{\alpha\beta}^{H} = \frac{1}{\gamma} \begin{cases} \left(\frac{3a}{4r} + \frac{a^3}{2r^3}\right)\mathbf{I} + \left(\frac{3a}{4r} - \frac{2a^3}{2r^3}\right)\hat{\mathbf{r}}\hat{\mathbf{r}}, & r > 2a \\ \left(1 - \frac{9r}{32a}\right)\mathbf{I} + \left(\frac{3r}{32a}\right)\hat{\mathbf{r}}\hat{\mathbf{r}}, & r \leq 2a \end{cases}. \tag{5}$$

Naive evaluation of the mobility tensor involves computational operations scaling as $O(N_2)$, while its inversion, necessary for calculating the Brownian displacements in eqn (2), incurs a complexity of $O(N_3)$. This computational burden often limits the feasibility of simulating large-scale systems. However, a substantial reduction in numerical complexity can be achieved by recognizing that the mobility tensor is positive-definite.[30]

This positive-definiteness allows for fast algorithms, such as those yielding $O(N\log N)$ scaling for evaluating particle vel-

ocities from applied forces.[24] Furthermore, the Positively Split Ewald (PSE) method, introduced by Fiore, Swan, and colleagues, enables linear scaling in the sampling of Brownian displacements.[31]

In periodic systems, the mobility tensor in eqn (5) exhibits translational invariance, making it divergence-free and resulting in a zero Brownian drift term in eqn (4). In this case, the trajectories over time can be numerically solved *via* a forward Euler–Maruyama integration scheme:

$$\mathbf{x}_{\alpha}(t + \Delta t) = \mathbf{x}_{\alpha}(t) + \mathbf{u}_{\alpha}(t)\Delta t \tag{6}$$

where Δt is the time step over which ion trajectories are advanced. Nonetheless, the situation becomes more intricate when simulating bounded geometries or employing more sophisticated hydrodynamic models. For example, in confined environments[32–34] or higher-order approximations,[35,36] the mobility tensor may lose its divergence-free character. In such cases, additional corrections are required. For example, when employing *constrained* Rotne–Prager–Yamakawa (RPY) hydrodynamics, it becomes essential to account for the Brownian drift to ensure the accurate resolution of particle dynamics and the generation of physically consistent trajectories.[29,36,37]

Forces arising from conservative interactions among colloidal particles are represented as the gradient of a potential energy $U(\mathcal{X})$, which is a function of the coordinates of all ions $\mathcal{X} \equiv [x_1, x_2, \ldots, x_N]^{T}$,

$$\mathbf{F}_{\alpha}^{I/M}(\mathcal{X}) \equiv -\nabla_{x_{\alpha}}U^{I/E}(\mathcal{X}), \tag{7}$$

where the gradient is taken with respect to the position of the αth particle. While the electrostatic interactions between the charged species can be taken into account as described by the Gouy–Champman model, the electromagnetic interactions and the influence of the magnetic field gradient are obtained by solving Maxwell's equations in the form

$$\nabla \cdot \mathbf{B} = 0, \quad \mathbf{B} = \mu\mathbf{H} \tag{8}$$

Paramagnetic particles of magnetic permeability μ_{p} in a solvent of permeability μ_{s}. By defining a magnetic scalar potential ψ, the problem reduces to Laplace's equation:

$$\nabla^{2}\psi = 0 \tag{9}$$

subject to

$$\left(\mathbf{B}_{f} - \mathbf{B}_{p}\right) \cdot \hat{n} = 0. \tag{10}$$

where $\mathbf{B}_{p}$ and $\mathbf{B}_{f}$ are the magnetic fluxes inside and outside of the particle. These equations are valid in the limit that the magnetic relaxation time inside of the particle and fluid is significantly smaller than the time scale of the study. As we are interested in timescales of particle motion $O(1s)$, the system is said to be pseudosteady. Thus, time dependence arises solely due to the time-varying boundary conditions in 10 as particles move around or the external field varies. A multipole expansion of the integral representation of Laplace's equation can be used to derive a linear system of equations that couples the magnetic flux moments on the particle to the magnetic poten-

Paper

tial and potential gradients on the fluid.[28] Considering the dipole contribution and ignoring quadrupoles and higher-order moments, we obtain:

$$\mathbf{H}_0 = \sum_{\alpha,\beta}^{N} \mathbf{M}_{\alpha\beta} \cdot \mathbf{m}_i, \quad (11)$$

where $\mathbf{M}_{\alpha\beta}$, the magnetic flux moments of particle β with particle α in a periodic box

$$\mathbf{M}_{\alpha\beta} = \frac{3\mathbf{I}\delta_{\alpha\beta}}{4\pi a^3 \left(\mu_p - \mu_f\right)} + \frac{9}{a^2 \mu_f V} \sum_{\mathbf{k} \neq 0} \frac{e^{i\mathbf{k}\cdot\left(x_\alpha - x_\beta\right)}}{k^2} j_1^2(k_a)\hat{\mathbf{k}}\hat{\mathbf{k}}, \quad (12)$$

where $j_1(x) = \sin(x)/x^2 - \cos(x)/x$ is the first order spherical Bessel function of the first kind, and $\mathbf{k} = [2\pi\kappa_x/L_x, 2\pi\kappa_y/L_y, 2\pi\kappa_z/L_z]$ for integers κ_i. The dipole–dipole interactions contribution to the potential energy can be obtained *via* the sum of the pairwise interactions given by

$$U^M = -\frac{1}{2}\sum_{\alpha=1}^{N} \mathbf{H}_0 \cdot \mathbf{m}_\alpha = -\frac{1}{2}\sum_{\alpha,\beta}^{N} \mathbf{M}_{\alpha\beta} : \mathbf{m}_\alpha\mathbf{m}_\beta. \quad (13)$$

Similarly, the resulting magnetic force acting on the α_{th} particle is

$$\mathbf{F}^M = -\nabla_\alpha U^M = -\frac{1}{2}\sum_{\alpha,\beta}^{N} \frac{\partial \mathbf{M}_{\alpha\beta}}{\partial x_\alpha} : \mathbf{m}_\alpha\mathbf{m}_\beta \quad (14)$$

We simulate a mixture of MNPs and non-MNPs of the equal radius, $\alpha \approx 47$ nm, in water a room temperature. We assume that the solvent behaves as a Newtonian fluid, with a viscosity of $\mu = 1$ cp, constant magnetic permeability, $\mu_f \approx 1.25 \times 10^3$ H nm^{-1}, and constant permittivity $\varepsilon_f = 80$. Furthermore, the colloidal particles are electrostatically stabilized in a binary electrolyte, such as NaCl, which is simulated implicitly. The concentration of the implicit ions is estimated using Graham's equation[38] based on the experimental zeta potential of $\zeta_{\text{MNP}} = -24.26$ mV and $\zeta_{\text{non-MNP}} = -43.48$ mV.

2.2 Characterization of the magneto-responsive suspension using Péclet and Mason number

The displacement of the magneto-responsive particles results in a perturbation of the microstructure of the suspension which can be characterized by the Péclet number.[39] This non-dimensional number expresses the importance of the external force deforming the system, F^{ext}, with respect to the restoration of entropic spring forces from Brownian motion,[30,40,41]

$$\text{Pe} = \frac{F^{\text{ext}}}{2k_B T/a} \quad (15)$$

where F^{ext} is any externally applied force to the suspension of interest, $k_B T$, is the thermal energy, and a is the hydrodynamic radius of the particles. In our analysis, the external force is the magnetophoretic force, defined as the dot product of the

induced dipole on the αth colloid, $\mathbf{m}_\alpha$, and the magnetic field gradient: $\nabla\mathbf{H} = G \cdot \hat{\mathbf{H}}_0$, where $\hat{\mathbf{H}}_0 = \mathbf{H}_0/H_0$ is the unit vector of the externally applied magnetic field of magnitude $H_0 = |\mathbf{H}_0|$. In our simulations, the field is applied on the $\hat{\mathbf{z}}$ direction.

For paramagnetic particles, the magnetic dipole is *induced* by the field and assumed to be perfectly aligned with the field. Moreover, in our simulations, the magnetic field only varies in the direction of the applied field, $\hat{\mathbf{z}}$. Then, the only non-zero components of the field gradient 2-tensor $\nabla\mathbf{H}$ are those in the $\hat{\mathbf{z}}$ direction. To facilitate our analysis, we define a gradient vector containing the gradient direction and field magnitude, $G = \nabla H\hat{\mathbf{z}} = G\hat{\mathbf{z}}$. By definition, $\mathbf{m}_\alpha = \frac{4}{3}\pi a^3 \mu_f\chi\mathbf{H}_0$, where μ_f is the fluid permittivity, and $\chi = 3(\mu_p/\mu_f - 1)/(\mu_p/\mu_f + 2)$ is the susceptibility, with μ_p being the particle's permittivity. Then, this *magnetic* Péclet number is given by Pe $= (4\pi a^3 \mu_f\chi\nabla|\mathbf{H}|^2)/3k_B T \sim (a^4 \mu_f\chi G H_0)/k_B T$, where G is the field gradient magnitude. This equation tells us that in the limit of very small Péclet numbers, the deformation of the particle arrangement within the suspension, and consequently the local polarization density, due to the externally imposed magnetic gradient is easily restored by the Brownian bath. On the other hand, high Péclet numbers indicate that the arrangement of particles and thus the macroscopic properties of the suspension are defined by the magnetophoretic process.

In our experimental set-up, the presence of no-slip boundary conditions in a Newtonian fluid results in an additional tangential force due to momentum transfer (a shear force), which further deforms the suspension. Assuming that the shear force is orthogonal to the magnetic gradient, as in our experimental set-up, this deformation will be opposed in the simplest of cases by the dipole–dipole interactions of the magnetic particles. The competition of both forces is given by a Mason number,[42,43] defined as

$$\text{Ma} = \frac{6\pi\eta a^2 \dot{\gamma}}{F_{\text{dip}}}, \quad (16)$$

where $\dot{\gamma}$ is the shear rate and F_{dip} is obtained by taking the gradient of the potential energy with respect to the distance between a pair of magnetic interacting dipoles.[44] In the context of microfluidic devices employed for separation processes, performance evaluation revolves around two key metrics: Purity and separation efficiency. The purity, P, of the outlet streams is quantified, where the ratio of concentration to velocity serves as the defining factor for mass flux $\dot{n}$ of components A and B: $P_A = \dot{n}_{\text{out,A}}/(\dot{n}_{\text{out,A}} + \dot{n}_{\text{out,B}})$. The separation efficiency S is defined as $S_A = \dot{n}_{\text{out,A}}/\dot{n}_{\text{in,A}}$.

3 Experimental methods

3.1 Microfluidic platform

The microfluidic chip was designed in SolidWorks 2021 and printed by a FormLabs 3B + printer using clear resin (Formlabs, RS-F2-GPCL-04). The chip was placed horizontally and twisted in every direction to facilitate the later washing

process. When the print was finished, the uncured resin was flushed out with 100% 2-propanol *via* a syringe. Then, the chip was washed for 15 min in a 2-propanol bath and cured by UV light at 60 °C for 20 min. Finally, the supporting structures were removed, and the printed M5 threads were drilled into the in- and outlets, enabling the connection of the silicon tubes (1.3 mm, VWR) *via* Luer lock tubing adapters (male, 1.6 mm, Reichelt Chemie Technik GmbH & Co.).

The experiments were performed at a viscosity η of 2.2274 mPa s, increasing the colloidal stability of the nanoparticles.[45] Therefore, the nanoparticles are dissolved in 24 wt% D(+)-sucrose (Carl Roth) at pH 7. The concentration stayed the same for the mixture experiments as for the single experiments per particle species. This means the overall particle mass flux for a mixture experiment was twice the one of the single experiment ($\dot{m}_{\mathrm{single,SFP}} = \dot{m}_{\mathrm{mix,SFP}}$). The density for the particles is 2650 for the non-magneto-responsive and 4870 kg m^{-3} for the MNPs, respectively. For the experimental set-up, the chip and the neodymium iron boron magnet (4 × 0.5 × 1.5 cm, N40, supermagnete) were placed in the holder, and the tubes were connected. The sample was pumped at 52 μL min^{-1} (u = 0.00107 m s^{-1}) by a syringe pump (kdScientific), the buffer *via* a peristaltic pump (ISMATEC) with 37% (u = 0.00425 m s^{-1}), and the outlet samples were removed with 229 μL min^{-1} by a self-made multi-syringe adapter for a syringe pump (Krüss, Havard Apparatus) as presented in Fig. 2 and in the ESI section.† The flow of the viscous solution should be higher than the sample flow to minimize the transverse diffusional migration of the nano-

particles. For running the experiments, the chip was first slowly filled with the viscous solution, then the sample was connected, avoiding bubble formation. After 30 s of equilibration time, the outlet tubes were connected, and each experiment was run for 4 min in triplicates (n = 3, error bars presenting the standard deviation). The outlets A/B and C/D are combined to calculate the process purity and selectivity.

The nanoparticle concentration was analyzed in triplicates *via* UV absorbance at 400 nm and fluorescent measurement (excitation wavelength 488 nm, emission wavelength 520 nm) in a plate reader (Tecan Infinite M200 Microplate Reader). They were compared to standard calibration curves; if necessary, the samples were centrifugally concentrated and resuspended in an ultrasonication bath (132 kHz, Sonorex) for 15 min.

The details of nanoparticle synthesis are provided in the ESI section.†

4 Results

4.1 Exploring the dependence of magnetophoresis on magnetic field and nanoparticle concentration

The separation efficiencies and purities for separating non-MNPs from MNPs are investigated using a magnetophoretic microfluidic platform as presented in Fig. 1 and in the ESI section,† characterized by a laminar flow with a Reynold's number of 0.53. A detailed characterization of the nanoparticles used is given in the ESI section.†
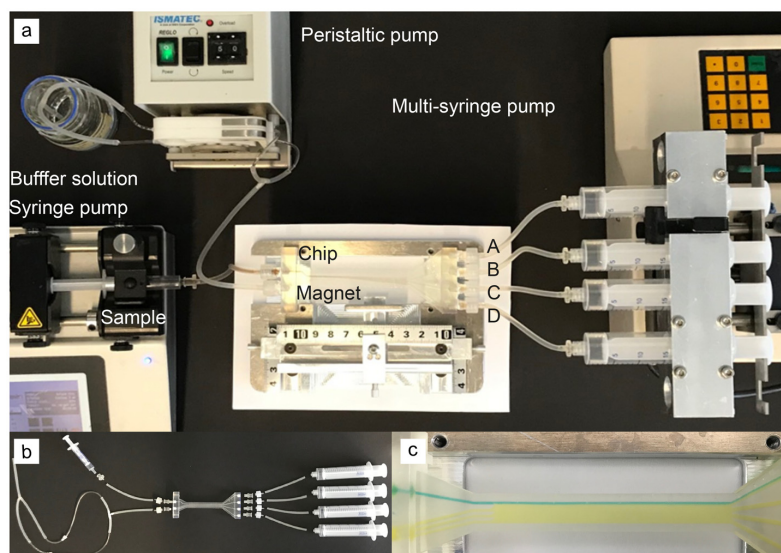
Fig. 2 (a) Experimental set-up consisting of the chip placed in the holder together with the magnet, the syringe pumps for the sample inlet, and the multi-syringe pump for the outlet. The viscous solution is pumped *via* a peristaltic pump. (b) The 3D-printed chip is connected to the tubes *via* printed threads and Luer lock adapters. (c) The flow profile of the chip is shown by food coloring (sample inlet = green, viscous solution inlet = yellow).
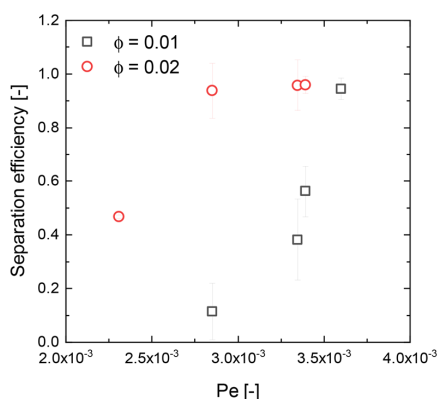
Fig. 3 The separation efficiency of soley MNPs determined with microfluidic experiments is presented as a function of the Péclet number for two different concentrations, namely $\phi = 0.02$ and $\phi = 0.01$.

Fig. 3 depicts the separation efficiency of the MNPs over varying Péclet numbers. For the lower concentration of $\phi = 0.01$, the separation efficiency is $S = 0.11 \pm 0.10$ for Pe = 2.85×10^{-3}. By increasing the Péclet number from Pe = 3.35×10^{-3} to Pe = 3.6×10^{-3}, the separation efficiency increases from $S = 0.38 \pm 0.15$ to $S = 0.94 \pm 0.04$. However, the results show that for a higher concentration, only a lower Péclet number is required to achieve higher separation efficiencies. Here, for $\phi = 0.02$, a separation efficiency of $S = 0.94 \pm 0.10$ is already reached at a Péclet number of Pe = 2.85×10^{-3}. Elevated particle concentrations promote dipole–dipole particle interactions, leading to aggregation and, therefore, an increased

magnetic moment. Consequently, these clusters experience an augmented magnetic force, which drives them towards regions of higher magnetic field intensity.

Fig. 4 compares the separation efficiencies (a and e) and purities (b and f) for varying Péclet numbers achieved by using only one particle species *versus* a mixture of both in the microfluidic chip. Fig. 4(a) refers to the separation efficiency for the non-MNPs, and Fig. 4(e) shows the separation efficiency for the magneto-responsive ones. The separation efficiency for the non-magneto-responsive particles varies little for the applied Péclet numbers but increases from $S = 0.75 \pm 0.13$ to $S = 0.86 \pm 0.05$ by halving the concentration from $\phi = 0.02$ to $\phi = 0.01$ (shaded). However, being within a mixture of both particle species, the separation efficiency decreases from $S = 0.57 \pm 0.13$ to $S = 0.24 \pm 0.01$ as the Péclet number increases. In contrast to the MNPs, it evolves for the non-MNPs that a lower concentration favors a higher separation efficiency at a constant Péclet number. For $\phi = 0.01$ (shaded), the separation efficiency reaches $S = 0.59 \pm 0.1$, compared to $S = 0.24 \pm 0.01$ for $\phi = 0.02$, both at Pe = 3.39×10^{-3}. As the separation efficiency decreases with increasing Péclet numbers for $\phi = 0.02$, the purity of the non-MNPs rises from $P = 0.51 \pm 0.13$ to 0.88 ± 0.1. For the lower concentration of $\phi = 0.01$, it decreases to a purity of $P = 0.52 \pm 0.1$.

From the perspective of the MNPs (Fig. 4e), independent of being present in a particle mixture or not, their separation efficiencies show a similar trend. As the Péclet number rises, signifying an increase in the magnetophoretic force, a notable enhancement in the separation efficiency is observed from $S = 0.44 \pm 0.07$ for Pe = 2.31×10^{-3} to $S = 0.97 \pm 0.02$ for Pe = 3.39×10^{-3} for the particles in the mixture. But again, by decreasing the concentration at a Péclet number of Pe = 3.39×10^{-3}, the
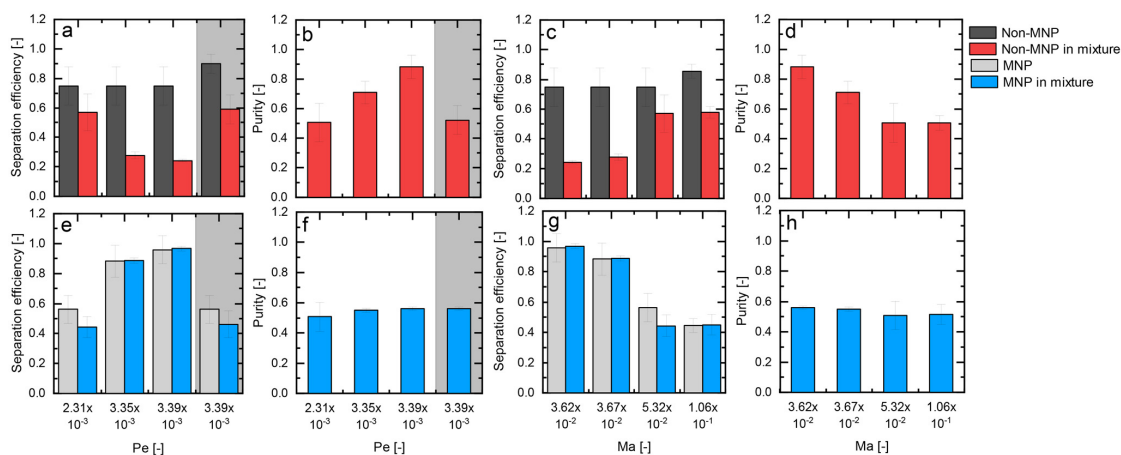
Fig. 4 Figures (a, and b) illustrate the purity and separation efficiency of the non-MNPs obtained with microfluidic separation experiments, whereas figures (e, and f) refer to the MNPs over the Péclet number. The concentration of $\phi = 0.02$ is shown in white, $\phi = 0.01$ in shaded. The mixture always has the same particle concentration as the single experiment for each component. The separation efficiency of solely non-MNPs at $\phi = 0.04$ was $S = 0.66 \pm 0.01$. Figures (c, and d) illustrate the purity and the separation efficiency of the non-MNPs, whereas figures (g, and h) refer to the MNPs over the Mason number for the concentration of $\phi = 0.02$. The mixture always has the same particle concentration as the single experiment for each component.

separation efficiency decreases from $S = 0.97 \pm 0.02$ ($\phi = 0.02$) to $S = 0.46 \pm 0.1$ ($\phi = 0.01$). For separating a mixture with both particle species, the purity (Fig. 4f) is approximately 0.5 for all applied Péclet numbers. This finding aligns with the outcomes observed for non-MNPs, as their separation efficiency diminishes with increasing Péclet numbers. Conversely, higher Péclet numbers exhibit enhanced separation capabilities for the MNPs. This implies that these non-MNPs tend to migrate alongside their magneto-responsive counterparts, consequently compromising the purity of the MNPs. As the magnetic field gradient induces the movement of the MNPs, a hydrodynamic instability appears, generating a convective flow. This flow also instigates a hydrodynamic force on non-MNPs in the direction of the moving MNPs.

4.2 The impact of hydrodynamic forces on magnetic particle interactions

The influence of varying Mason numbers on separation efficiency and purities is depicted in Fig. 4, where it serves as a metric for the ratio of shear to magnetic forces. It evolves that for the non-MNPs in Fig. 4(c), the separation efficiency is around 0.7 for all applied Mason numbers. However, when being present in a mixture with MNPs, it is $S = 0.24 \pm 0.01$ at Ma $= 3.62 \times 10^{-2}$, but increases to $S = 0.58 \pm 0.04$ at Ma $= 1.06 \times 10^{-1}$. At the same time, the purity of the non-MNPs fraction decreases from $P = 0.88 \pm 0.08$ to $P = 0.51 \pm 0.05$.

Since the shear force prevails the magnetophoretic force, the separation efficiency for the magneto-responsive nanoparticles decreases from $S = 0.97 \pm 0.02$ at Ma $= 3.62 \times 10^{-2}$ to $S = 0.45 \pm 0.07$ at Ma $= 1.06 \times 10^{-1}$, depicted in Fig. 4(g) and (h). This decline is observed irrespective of whether the particles are in a mixture with non-magneto-responsive entities or not, the same as for the variation of the Péclet number. Even if the separation efficiency for Ma $= 3.62 \times 10^{-2}$ is high, the purity is $P = 0.56 \pm 0.01$. The observed reduction in separation efficiency for non-MNPs, presented in Fig. 4(c), implies their tendency to be concurrently entrained with MNPs, which is indicative of the resultant low purity in the separation process. Under increased shear conditions, represented by the highest Mason number (Ma $= 1.06 \times 10^{-1}$), it is noteworthy that although the MNPs in the mixture exhibit a lower separation efficiency ($S = 0.45 \pm 0.07$), the non-MNPs align their movement with the MNPs again. Consequently, this leads to a purity level of only $P = 0.52 \pm 0.07$, which is comparable to the purity achieved at the lowest Mason number (Fig. 4(d)).

To further investigate the hydrodynamically induced transport of non-MNPs alongside MNPs, as suggested by the experimental observations, we employ large-scale Brownian dynamic simulations. They are designed to analyze the interplay between the nanoparticles depending on the magnetophoretic forces that contribute to the co-transport phenomenon.

4.3 Hydrodynamically induced transport of undesired species: large-scale Brownian dynamic simulations

Fig. 5(e) shows a snapshot of the simulation box in the absence of shear for a mixture of MNPs (in blue, magneto-responsive nanoparticles) and non-MNPs (in gray, non-magneto-responsive nanoparticles). Such a simple simulation, is similar to the flow present at the geometric symmetric axis along the developing convective flow ($\hat{\mathbf{z}}$). The applied magnetic field in the z direction (outward page) is $\mathbf{H}_0 = 0.4\sqrt{k_B T/a^3 \mu_f}\hat{\mathbf{z}}$, and the gradient $G = 0.02$. The gradient in units of $\sqrt{k_B T/a^5 \mu_f}$.

The motion of MNPs in the presence of a nonuniform magnetic field is known as magnetophoresis. While this topic is a meticulously studied field of study, see ref. 20 and 46 here we are interested on the importance of hydrodynamically induced transport of potentially undesired species (non-magnetic particles) in microfluidic devices. If the components of the applied field gradient $\nabla\mathbf{H}_0$ are small compared to H_0/a, the steady-state structure of the dispersion is only weakly perturbed by the magnetophoretic forces. Under these assumptions, the magnetophoretic force felt by the α_{th} colloid is equal to $\mathbf{F}_\alpha^P = (\nabla\mathbf{H}_0) \cdot \mathbf{m}_\alpha \equiv G(\hat{\mathbf{H}}_0 \cdot \mathbf{m}_\alpha)$, where $G = \nabla H_0$ and $\hat{\mathbf{H}}_0 = \mathbf{H}_0/H_0$. Similar to our magnetic Péclet number estimation, we do not need to consider the field gradient tensor, which has both the field and the gradient directions, but rather the field gradient vector, $\mathbf{G}$. This would not be the case if there is there was any permanent magnetization, for which we would need the complete tensorial expression for the force.

The velocities of the magneto-responsive particles depend on the magnetophoretic forces on the colloids, $\mathcal{F}^P = [\mathbf{F}_1, \mathbf{F}_2, \ldots, \mathbf{F}_N]^T = G(\mathcal{I} \cdot \hat{\mathbf{H}}_0)$, where $\mathcal{I}$ is a list containing the induced dipole moments, and magnetophoretic mobility, $\mathcal{U} = \mathcal{M}^H \cdot \mathcal{F}^P$. The average magnetophoretic velocity will then be given by $\langle u \rangle = \sum_\alpha^{N_M} u_\alpha/N_M$, where u_α is the velocity of the α_{th} colloid.

The first two Fig. 5(a) and (b), show the average colloid velocity of the non-MNPs and MNPs in the direction of the field as a function of the Péclet number. Concentrations vary from $\phi_{mag} = 0.01$ ($\phi_{non-mag} = 0.022$) to $\phi_{mag} = 0.08$ ($\phi_{non-mag} = 0.178$) and field gradient magnitude from $|\nabla H|/H_0 = 0.01$ to $|\nabla H|/H_0 = 0.20$. The field strength increases with the Péclet number and is varied from $O(10^{-6})$ to $O(10^{-2})$. As expected, the velocity of the magneto-responsive particles in the direction of the field (Fig. 5d) increases with the magnetophoretic force (proportional to the Péclet number). Non-MNPs do not show any clear displacement for values of Péclet numbers less than $\mathcal{O}(10^{-4})$, that is, at low-field and/or low-field gradients. The increase in the velocity of the non-MNPs, subpanel (a), with values of Péclet numbers greater than $\mathcal{O}(10^{-4})$ suggests the existence of motion induced by the hydrodynamic interactions between particles in the direction of the field. In consistency with what has been found in magnetophoretic separations,[20] Fig. 5(a) suggests low field gradients are more efficient at reducing the transport of unwanted species (represented by the non-magnetic nanoparticles). In contrast, the orthogonal component of the velocity, as shown in Fig. 5(c) and (d) for the non-MNPs and MNPs, respectively, display no dependence on the applied field or
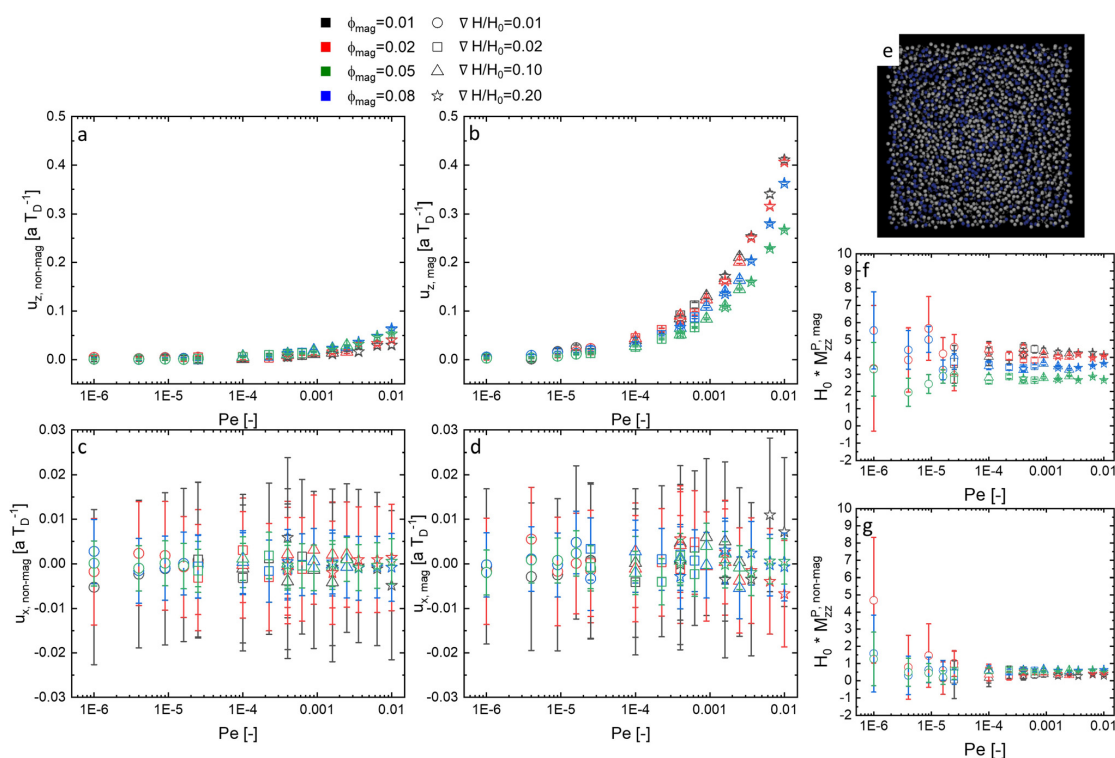
Fig. 5 (a) and (b) Simulated average particle velocity in the direction of the applied field, u_z, and (c) and (d) orthogonal, u_x, to the field as a function of the Péclet number. (a) and (c) Correspond to the average velocities of the non-magnetic particles and (b) and (d) to the magnetic particles, respectively. The concentrations of $\phi_{mag} = 0.01$ ($\phi_{non-mag} = 0.022$), $\phi_{mag} = 0.02$ ($\phi_{non-mag} = 0.044$), $\phi_{mag} = 0.05$ ($\phi_{non-mag} = 0.111$), and $\phi_{mag} = 0.08$ ($\phi_{non-mag} = 0.178$) are colored as dark gray, light gray, blue, and red respectively. The circled, squared, triangled and starred markers correspond to field gradients of $|\nabla H|/H_0 = 0.01$, $|\nabla H|/H_0$, $|\nabla H|/H_0$, and $|\nabla H|/H_0$, respectively. (e) Snapshot of a slice of the xy plane simulated mixture of MNP and non-MNPs in the absence of shear. Non- and magneto-responsive nanoparticles are shown in gray and blue, respectively. Snapshot corresponds to simulation of filling fraction $\phi_{mag} = 0.05$ ($\phi_{non-mag} = 0.111$), field $H_0 = 0.4 k_B T/a_3 \mu_f$ in the z direction, with constant gradient in z given by $|\nabla H|/H_0 = 0.02$. (f) zz component of the mobility matrix, M_{zz}, for the magnetoresponsive particles, computed using eqn (17) (g) zz component of the mobility matrix, M_{zz}, for the non-magnetoresponsive particles, computed using eqn (17) of the MNPs as a function of the Péclet number. Concentrations of $\phi_{mag} = 0.01$ ($\phi_{non-mag} = 0.022$), $\phi_{mag} = 0.02$ ($\phi_{non-mag} = 0.044$), $\phi_{mag} = 0.05$ ($\phi_{non-mag} = 0.111$), and $\phi_{mag} = 0.08$ ($\phi_{non-mag} = 0.178$) are shown in blue, orange, green, and red, respectively. Circled, squared, triangle, and starred markers correspond to field gradients of $|\nabla H|/H_0 = 0.01$, $|\nabla H|/H_0 = 0.02$, $|\nabla H|/H_0 = 0.10$, and $|\nabla H|/H_0 = 0.20$ respectively.

the field gradients and the average velocities of both species are negligible.

From the average velocity, we can compute the approximate magnetophoretic mobility by introducing a summation tensor, Σ;[47] we find

$$\mathbf{u} = \mathbf{M}^P \cdot \mathbf{G}, \quad \mathbf{M}^P \equiv \Sigma \cdot \mathcal{M}^H \cdot \mathcal{I} \cdot \hat{\mathbf{H}}_0 \qquad (17)$$

where magnetophoretic mobility $\mathbf{M}^P$ is a 2-tensor whose elements $M_{\gamma\zeta}^P$ couple the gradient in direction ζ to the velocity in direction γ. Considering the field and the field gradient is only nonzero in the z direction, the dominant term is the "self-term" of the magnetophoretic mobility tensor M_{zz}^P. The results for the zz component of the magnetophoretic mobility tensor for non-MNPs and MNPs are shown in Fig. 5(f) and (g), respectively. The self-term of the mobility tensor for the non-

MNPs, $M_{zz}^{P,non-MNP}$, exhibits little dependence on the Péclet number and field gradient. When $Pe > 10^{-4}$, this component appears to slightly increase in value with the concentration of *magnetic species*, underscoring the cooperative nature of the transport process. In contrast, the self-term of the magnetophoretic mobility tensor of the magneto-responsive, $M_{zz}^{P,MNP}$, nanoparticles slightly decreases with concentration.

5 Discussion

The hydrodynamics in magnetophoretic microfluidic separation processes are characterized by a complex interplay of forces that influence the overall process efficiency. Our experimental results show high and constant separation efficiencies

for solely non-magneto-responsive nanoparticles with increasing Péclet number, indicating that their separation is independent of the magnetic force when no magneto-responsive entities are present. But, keeping a constant Péclet number, a higher separation selectivity is achieved for lower concentrations due to the reduction of diffusive effects.[10,48] Conversely, at low concentrations of magneto-responsive nanoparticles, the separation efficiency is reduced. When a magnetic field is applied at low Péclet numbers, the separation efficiency of MNPs initially remains limited due to the predominance of thermal fluctuations over magnetic forces. However, as the Péclet number increases, enhanced dipole–dipole interactions lead to aggregation, amplifying the magnetic moment and enabling more efficient separation by the magnetic field gradient. Also, raising their concentration amplifies their total magnetic moment. These aggregates, larger in size and showing reduced Brownian motion, are more effectively moved by the magnetic field gradient towards areas of higher magnetic field intensity, resulting in improved separation.[22,49]

In a mixture of both particle species, the presence of non-magneto-responsive nanoparticles does not influence the separation efficiency of the magneto-responsive ones with rising magnetic field strength. However, the reverse is not true. The separation efficiency of non-MNPs decreases with increasing magnetic field strength (increasing Péclet number). The process purities of the MNPs are constant even though the separation efficiency of MNPs improves with increasing Péclet number, suggesting that non-MNPs drag along MNPs. That happens as the magneto-responsive nanoparticles induce a hydrodynamic force acting on the non-magneto-responsive entities, influencing the separation process significantly.[23,50] The simulation integrates and extends beyond the experimentally tested parameters of magnetic field strength and concentration, showing that this convective motion is an intrinsic aspect of the system's dynamics. Focusing on the direct interplay of the magneto-responsive entities and the non-magneto-responsive ones, the simulation confirms that the magnetic field gradient primarily induces the motion of the MNPs, as the orthogonal velocity to the field is constant for both particle species. However, the influence of magneto-responsive particles on their non-magneto-responsive counterparts is significant. Although the motion of non-MNPs is an order of magnitude smaller, it is evident that the movement of the magneto-responsive entities leads to a hydrodynamic convective motion that entrains the non-magneto-responsive particles. Since experimental measurements could only be performed offline, after the magnetophoretic process, direct experimental observation of this interaction within the magnetic field is challenging. Simulations are thus essential for capturing and analyzing the underlying dynamics comprehensively. The simulations allowed us to directly investigate the dynamic behavior within the magnetic field, providing valuable insights into parameter regimes that are costly to explore experimentally. Across all simulated particle concentrations and magnetic field gradients the hydrodynamic effect remains consistent. Exceeding the experimentally tested parameters, the average

velocity of the non-magneto responsive particle in the direction of the field can be minimized by decreasing the magnetic field gradient. However, this will lead to a reduced responsiveness (velocity) of the magneto-responsive ones as well, resulting in a lower separation efficiency.[22] Experimentally, increasing the shear by increasing the volumetric buffer flow leads to an improved separation efficiency and fewer diffusive effects of the non-MNPs.[10,48] But again, in a mixture where both particle species are present, the purity of MNPs is reduced. Due to the increased shear counteracting the magnetophoretic force, the magneto-responsive nanoparticles are less attracted toward higher magnetic fields.[11]

Magnetic separation techniques are widely used in biochemistry, biomedicine, and biotechnology. Applications range from the purification of biomolecules[51] to targeted drug delivery.[52] These techniques rely on applying a magnetic field to manipulate magneto-responsive particles, most commonly superparamagnetic particles, in a non-magnetic environment. In this study, we evaluate the impact of magnetophoresis on magneto-responsive entities, which are nanoparticles in our case but can be modified for other purposes, for instance, through drug functionalization. This happens in a non-magneto-responsive environment, which is represented by non-magneto-responsive particles in a microfluidic system. The magnetic-induced convective motion is a promising technique for nanoparticle manipulation due to its simple and effective separation mechanism.[49,50,53] However, the induced hydrodynamic force acting on the non-magneto-responsive entities has to be considered when it comes to a lab-on-a-chip separation process or application in biomedicine.[25,54] For targeted processes, e.g., drug delivery, mixing motion should be avoided, allowing effective delivery and localization in the body.[55,56]

Given the complexity of the hydrodynamics in magnetophoretic microfluidic processes, it is crucial to consider strategies that could enhance the separation efficiency and purity of the particles. In the study of Solsona et al., a 3D-printed magnetophoretic chip was developed to sort catalyst particles by their magnetic moment; however, they could not see a difference in the magnetic susceptibility between the different fractions. Besides their discussion that the formation of nanoclusters agglomerates accounts for this observation, the induced convective motion reduced the purity of their fractions.[57] As investigated by Robert et al., the separation efficiency could be improved by an increased flow and a decrease in magneto-responsive entities. Their study successfully differentiated between non-magnetic monocytes and magnetic macrophages; however, they noted that during the separation process, fractions may tend to overlap due to the convective motion engendering mixing and generation of a current.[5] In another approach, the purity of a microfluidic separation process of red (non-magnetic) and white (magnetically labeled) blood cells decreased with a higher flow as the hydrodynamic drag force prevails the magnetophoretic force. Therefore, Lin et al. implemented a two-stage cell separation strategy in their chip, preventing the undesired motion of the red blood cells along with the white ones.[25]

6 Conclusion

In conclusion, our experimental and simulative results highlight that the motion of magneto-responsive nanoparticles induces a hydrodynamic motion that entrains the non-magneto-responsive ones. This interaction significantly influences the separation efficiency and purity of both nanoparticle species in the microfluidic system. The simulations directly investigated these dynamic behaviors within the magnetic field and provided insights that are difficult to obtain experimentally. Besides the careful control of the Péclet and Mason number, a practical approach to minimize the unavoidable magnetic-induced convection of non-magneto-responsive entities may include a multi-step process. Here, a prior static batch separation reduces the concentration of non-magneto-responsive nanoparticles in the system, thereby enhancing the overall separation efficiency and purity.

Author contributions

L.W., E.K., M.B., J.W.S., and S.S. conceptualization, methodology; L.W., J.S., La.W. and E.K. data curation, investigation; L.W. and E.K. formal analysis, visualization; M.B., A.A., S.S. and S.B. writing – review and editing, supervision, project administration; L.W. and E.K. writing – original draft.

Data availability

The data supporting this article have been included as part of the ESI.†

Conflicts of interest

There are no conflicts to declare. All data is available upon request.

Acknowledgements

References

1 S. Gupta, K. Ramesh, S. Ahmed and V. Kakkar, *Int. J. Bio-Sci. Bio-Technol.*, 2016, **8**, 311–322.

2 G. Gharib, İ. Bütün, Z. Muganl, G. Kozalak, İ. Naml, S. S. Sarraf, V. E. Ahmadi, E. Toyran, A. J. van Wijnen and A. Koşar, *Biosensors*, 2022, **12**, 1–60.

3 W. H. Chong, S. S. Leong and J. K. Lim, *Electrophoresis*, 2021, **42**, 2303–2328.

4 T. M. Squires and S. R. Quake, *Rev. Mod. Phys.*, 2005, **77**, 977–1026.

5 D. Robert, N. Pamme, H. Conjeaud, F. Gazeau, A. Iles and C. Wilhelm, *Lab Chip*, 2011, **11**, 1902–1910.

6 Y. Zhao, D. Chen, H. Yue, J. B. French, J. Rufo, S. J. Benkovic and T. J. Huang, *Lab Chip*, 2013, **13**, 2183–2198.

7 A. Thiha and F. Ibrahim, *Sensors*, 2015, **15**, 11431–11441.

8 R. Augustine, A. Hasan, S. Das, R. Ahmed, Y. Mori, T. Notomi, B. D. Kevadiya and A. S. Thakor, *Biology*, 2020, **9**, 1–17.

9 E. K. Theel and S. P. Schwaminger, *Int. J. Mol. Sci.*, 2022, **23**, 1–22.

10 R. F. Ismagilov, A. D. Stroock, P. J. Kenis, G. Whitesides and H. A. Stone, *Appl. Phys. Lett.*, 2000, **76**, 2376–2378.

11 Y. W. Tan, S. S. Leong, J. K. Lim, W. M. Yeoh and P. Y. Toh, *Electrophoresis*, 2022, **43**, 2234–2249.

12 E. P. Furlani, *J. Appl. Phys.*, 2006, **99**, 1–35.

13 A. O. Ayansiji, A. V. Dighe, A. A. Linninger and M. R. Singh, *Proc. Natl. Acad. Sci. U. S. A.*, 2020, **117**, 30208–30214.

14 R. K. Singh, T. H. Kim, K. D. Patel, J. C. Knowles and H. W. Kim, *J. Biomed. Mater. Res., Part A*, 2012, **100 A**, 1734–1742.

15 J. P. Steimel, J. L. Aragones and A. Alexander-Katz, *Phys. Rev. Lett.*, 2014, **113**, 178101.

16 S. E. Favela-Camacho, E. J. Samaniego-Benítez, A. Godínez-García, L. M. Avilés-Arellano and J. F. Pérez-Robles, *Colloids Surf., A*, 2019, **574**, 29–35.

17 M. Eigenfeld, L. Wittmann, R. Kerpes, S. P. Schwaminger and T. Becker, *Biotechnol. J.*, 2023, **18**, 1–11.

18 S. A. Majetich, T. Wen and R. A. Booth, *ACS Nano*, 2011, **5**, 6081–6084.

19 D. Saville, W. Russel and R. William, *Colloidal Dispersions*, Cambridge University Press, 1989.

20 T. B. Jones, *Electromechanics of Particles*, Cambridge University Press, 1st edn, 1995.

21 R. G. Gontijo and F. R. Cunha, *Phys. Fluids*, 2017, **29**, 062004.

22 S. S. Leong, Z. Ahmad, S. C. Low, J. Camacho, J. Faraudo and J. K. Lim, *Langmuir*, 2020, **36**, 8033–8055.

23 G. Kitenbergs and A. Cēbers, *J. Magn. Magn. Mater.*, 2020, **498**, 166247.

24 J. W. Swan and G. Wang, *Phys. Fluids*, 2016, **28**, 011902.

25 S. Lin, X. Zhi, D. Chen, F. Xia, Y. Shen, J. Niu, S. Huang, J. Song, J. Miao, D. Cui and X. Ding, *Biosens. Bioelectron.*, 2019, **129**, 175–181.

26 E. S. Krucker-Velasquez, Z. Sherman and J. W. Swan, *Immersed Boundary Method for Dynamic Simulation of Polarizable Colloids of Arbitrary Shape in Explicit Ion Electrolytes*, Ssrn preprint, 2023.

27 D. Frenkel and B. Smit, *Understanding molecular simulation: from algorithms to applications*, Academic Press, 2002.

28 Z. Sherman, PhD Thesis, Massachusets Institute of Technology, 2019.

29 A. M. Fiore and J. W. Swan, *J. Fluid Mech.*, 2019, **878**, 544–597.

30 S. Kim and S. J. Karrila, *Microhydrodynamics: principles and selected applications*, Dover Publications, Mineola, N.Y, 2005.

31 A. M. Fiore, F. B. Usabiaga, A. Donev and J. W. Swan, *J. Chem. Phys.*, 2017, **146**, 124116.

32 A. Gubbiotti, M. Chinappi and C. M. Casciola, *Phys. Rev. E*, 2019, **100**, 053307.

33 S. Delong, F. B. Usabiaga, R. Delgado-Buscalioni, B. E. Griffith and A. Donev, *J. Chem. Phys.*, 2014, **140**, 134110.

34 S. Delong, F. Balboa Usabiaga and A. Donev, *J. Chem. Phys.*, 2015, **143**, 144107.

35 E. E. Keaveny, *J. Comput. Phys.*, 2014, **269**, 61–79.

36 A. M. Fiore and J. W. Swan, *J. Chem. Phys.*, 2018, **148**, 044114.

37 A. W. C. Lau and T. C. Lubensky, *Phys. Rev. E: Stat. Phys., Plasmas, Fluids, Relat. Interdiscip. Top.*, 2007, **76**, 011123.

38 J. N. Israelachvili, *Intermolecular and surface forces*, Academic Press London, San Diego, 2nd edn, 1991.

39 P. Moritz, A. Gonon, T. Blon, N. Ratel-Ramond, F. Mathieu, P. Farger, J. M. Asensio-Revert, S. Cayez, D. Bourrier, D. Saya, L. Nicu, G. Viau, T. Leïchlé and L. M. Lacroix, *ACS Nano*, 2021, **15**, 5096–5108.

40 R. Zwanzig, *Nonequilibrium statistical mechanics*, Oxford University Press, Oxford, New York, 2001.

41 J. W. Swan, R. N. Zia and J. F. Brady, *J. Rheol.*, 2014, **58**, 1–41.

42 G. Bossis, O. Volkova, S. Lacis and A. Meunier, *Magnetorheology: Fluids, Sturcutres and Rheology*, Springer-Verlag Berlin Heidelberg, 2002, vol. 594, pp. 202–233.

43 Z. Varga, V. Grenard, S. Pecorario, N. Taberlet, V. Dolique, S. Manneville, T. Divoux, G. H. McKinley and J. W. Swan, *Proc. Natl. Acad. Sci. U. S. A.*, 2019, **116**, 12193–12198.

44 J. D. Jackson, *Classical electrodynamics*, John Wiley I& Sons, 1999.

45 L. Wittmann, C. Turrina and S. P. Schwaminger, *Magnetochemistry*, 2021, **7**, 80.

46 R. Cobos and A. S. Khair, *J. Fluid Mech.*, 2023, **968**, A14.

47 E. Krucker-Velasquez and J. W. Swan, *J. Chem. Phys.*, 2021, **155**, 134903.

48 P. Agnihotri, *Microfluid. Nanofluid.*, 2023, **27**, 1–15.

49 M. Fratzl, S. Delshadi, T. Devillers, F. Bruckert, O. Cugat, N. M. Dempsey and G. Blaire, *Soft Matter*, 2018, **14**, 2671–2681.

50 J. G. Lee, V. Porter, W. A. Shelton and B. Bharti, *Langmuir*, 2018, **34**, 15416–15424.

51 A. Shiriny and M. Bayareh, *Meccanica*, 2020, **55**, 1903–1916.

52 T. Vangijzegem, D. Stanicki and S. Laurent, *Expert Opin. Drug Delivery*, 2019, **16**, 69–78.

53 S. Schuerle, A. P. Soleimany, T. Yeh, G. M. Anand, M. Häberli, H. E. Fleming, N. Mirkhani, F. Qiu, S. Hauert, X. Wang, B. J. Nelson and S. N. Bhatia, *Sci. Adv.*, 2019, **5**, 1–10.

54 S. S. Leong, S. P. Yeap and J. Lim, *Interface Focus*, 2016, **6**, 1–20.

55 X. Li, W. Li, M. Wang and Z. Liao, *J. Controlled Release*, 2021, **335**, 437–448.

56 P. M. Martins, A. C. Lima, S. Ribeiro, S. Lanceros-Mendez and P. Martins, *ACS Appl. Bio Mater.*, 2021, **4**, 5839–5870.

57 M. Solsona, A. E. Nieuwelink, F. Meirer, L. Abelmann, M. Odijk, W. Olthuis, B. M. Weckhuysen and A. van den Berg, *Angew. Chem., Int. Ed.*, 2018, **57**, 10589–10594.

Electronic supporting information

Influence of Magnetic Convection on Separation Efficiency in Magnetophoretic Microfluidic Processes: A Combined Simulation and Experimental Study

Simulation

Furthermore, the susceptibility in conjunction with the applied magnetic field controls the strength between dipolar interactions. By comparing the potential energy between dipoles of particle α and β aligned tip-to-tail versus the thermal energy at contact,

$$\lambda = -\frac{U_{\alpha,\beta}}{k_\mathrm{B}T} = \frac{\pi\mu_0 a^3 \chi^2 H^2}{9k_\mathrm{B}T}. \tag{1}$$

When $\lambda \ll 1$, dipolar interactions can be easily overcome by Brownian forces. In contrast, when $\lambda \gg 1$ dipole-dipole interactions are so strong that chains of magneto-responsive particles grow in the field direction.[1,2] The force arising from the interaction between dipole α and dipole β, $U_{\alpha\beta}$, is obtained by taking the gradient with respect to the interparticle distance.[3]

Non-magneto-responsive particles

As a first approximation, we will use the dressed ion theory to model the charged colloidal particles. Due to the presence of the ionic shell, the interparticle potential among the colloidal particles is purely repulsive. This allows us to assume the charged particles (equal in sign) exist in an oppositely charge continuum, which neutralizes the charge and the importance of counterions is indirectly captured by the screening length of electrostatic interactions. Thus, the potential between the equally charged particles α and β is simply given by

$$u_{\alpha,\beta}(r) = \frac{q^2}{4\pi\varepsilon_f r} \exp(-\kappa_\mathrm{D} r). \tag{2}$$

where κ_D is the inverse Debye screening length, $\kappa_\mathrm{D} = \sqrt{4\pi n_i q_i^2 / k_\mathrm{B}T}$.

We will assume that when immersed in the dielectric fluid, the non-MNPs acquire a charge distribution due to the bound charge localized at the surface, and counterions are released in the dielectric. These free ions determine the Debye screening length, $\lambda_\mathrm{D}^{-1} = \kappa_\mathrm{D}$.

Because of charge conservation we know that the sum of the particle's net charge, Q, must equal the total free charge. That is,

$$Q_\mathrm{tot} = N_\mathrm{Si} \int_S \sigma(\mathrm{r})\mathrm{d}S. \tag{3}$$

Assuming a constant charge density distribution, the total charge is given by $Q_\mathrm{tot} = N_\mathrm{Si} 4\pi a^2 \langle\sigma\rangle$. The charge density bounded to the non-MNPs is $\langle\rho_\mathrm{Si}\rangle = n_\mathrm{Si} 4\pi a^2 \langle\sigma\rangle$. Let us approximate the number of ions in the solution as $n_i = 2Q_\mathrm{tot}/eV$. Thus the inverse Debye screening length becomes

$$\kappa_\mathrm{D} = \sqrt{\frac{4\pi(2Q_\mathrm{tot}/eV)(ze)^2}{k_\mathrm{B}T}}; \tag{4}$$

where e is the fundamental charge.

Poisson-Boltzmann equation for the electric double layer

The potential for the double layer structure in the non-MNP-solution interface can be modeled using Poisson's equation

$$\nabla^2 \psi = \frac{\rho}{\varepsilon_\mathrm{f}}. \tag{5}$$

If we neglect the curvature, Equation 5 can be simplified to a $1-$D differential equation. Letting the x coordinate origin be located at the surface of the coated particle, the ODE to be solved is

$$\frac{\mathrm{d}^2\psi}{\mathrm{d}x} = -\frac{\sigma}{\varepsilon_\mathrm{f}}; \tag{6}$$

subject to

$$\psi(0) = \xi; \quad \psi(x \to \infty) = 0. \tag{7}$$

Solving this ODE allows us to get the particle's charge density as a function of the solution's charge density.

$$\frac{d\psi}{dx}\bigg|_{x=0} = -\operatorname{sgn}\xi\sqrt{-\frac{2}{\varepsilon_f}\int_0^\xi d\psi\rho(\psi)};\tag{8}$$

or, equivalently

$$\sigma = \operatorname{sgn}\xi\sqrt{-2\varepsilon_f\int_0^\xi d\psi\rho(\psi)};\tag{9}$$

we need a way to relate the zeta potential, *xi*, to the Debye screening length. Now **we need a model to relate the potential to the charge distribution in the solution**. In the **Gouy-Chapman** model, ions behave ideally, thus the charge density will be given by[4]

$$\sigma_{GC} = 4n_iq_i\lambda_D\sinh\frac{q_i\xi}{2k_BT}\tag{10}$$

Brownian dynamics Simulations of colloidal dispersions

   We model the mixture of MNP and non-MNP as a suspension of charged, hard, spherical particles of radius a. We assume that these particles are suspended in a continuum Newtonian fluid such that the colloids interact with the solvent only via stochastic Brownian forces from fluctuations in the thermal energy or fluctuating hydrodynamics due to the momentum relaxation of the solvent molecules.[5] On the colloidal scale, inertial relaxation occurs on time scales orders of magnitude smaller than those on which colloids move. In this regime, any perturbation to the momentum of the particle is felt almost instantaneously. Consequently, the colloids are said to move at their terminal velocity, allowing us to neglect inertial effects. These assumptions lead to the *overdamped* Langevin equation:

$$0 = \mathbf{F}_\alpha^H + \mathbf{F}_\alpha^I + \mathbf{F}_\alpha^E + \mathbf{F}_\alpha^B,\tag{11}$$

where $\mathbf{F}_\alpha^H$ is the hydrodynamic force acting on the αth colloid, $\mathbf{F}_\alpha^I$ accounts for forces arising from a generic conservative potential, $\mathbf{F}_\alpha^M$ is the magnetophoretic force due to the magnetic field gradient[6] and $\mathbf{F}_\alpha^B$ is the stochastic Brownian force. The last force satisfies the fluctuation-dissipation theorem[4] with ensemble average:

$$\left\langle\mathbf{F}^B(t)\right\rangle = 0;\quad\left\langle\mathbf{F}^B(t)\mathbf{F}^B(t+\tau)\right\rangle = 2k_BT(\mathbf{M}^H)^{-1}\delta(\tau),\tag{12}$$

where $\mathbf{F}^B(t) = [\mathbf{F}_1^B(t),\mathbf{F}_2^B(t),\ldots]$, $\langle\cdot\rangle$ indicates the expectation value, δ is the Dirac delta function, and $\mathbf{M}^H$ is the hydrodynamic mobility tensor. This formulation ensures that any energy a colloid gains from a thermal fluctuation is dissipated as drag to the solvent.

   The hydrodynamic mobility tensor projects from the space of the nonhydrodynamic forces, $\mathbf{F}_\beta = \mathbf{F}_\beta^I + \mathbf{F}_\beta^E + \mathbf{F}_\beta^B$; to the space of the velocity of the αth colloid:

$$\mathbf{u}_\alpha(t) = \sum_{\beta=1}^N\mathbf{M}_{\alpha\beta}^H\cdot\mathbf{F}_\beta(t).\tag{13}$$

   The many-body hydrodynamic interactions require some level of approximation. The simplest assumption in colloidal suspensions is the freely draining (FD) model. The freely draining model assumes that each of the individual beads' respective hydrodynamic fields does not interact with the rest of the particles. Thus, the drag on each bead is decoupled from all the others and is equal to the Stokes drag,

$$\mathbf{M}_{\alpha\beta}^H = 0, \alpha\neq\beta;\quad\mathbf{M}_{\alpha\alpha}^H = \mathbf{I}/\gamma,\tag{14}$$

where all colloids are assigned the same drag coefficient, γ.

   While this assumption is valid at low concentrations, it is no longer valid at high concentrations. This is because the average interparticle distance between the colloids decreases. Consequently, the hydrodynamic fields generated by the colloids are likely to interact with each other. Good agreement between experimental measurements and simulation results for a suspension of beads (including concentrated ones) can be achieved with a relatively coarse approximation for the interparticle hydrodynamic interactions. The fields generated by beads in a Newtonian fluid can be approximated as the superposition of the field generated by a point particle and a point quadrupole.[7] When all colloidal particles are of the same size, the hydrodynamic fields are given by the Rotne-Prager-Yamakawa mobility tensor:[4]

$$\mathbf{M}_{\alpha\beta}^H = \frac{1}{\gamma}\begin{cases}(\frac{3a}{4r}+\frac{a^3}{2r^3})\mathbf{I}+(\frac{3a}{4r}-\frac{2a^3}{2r^3})\hat{\mathbf{r}}\hat{\mathbf{r}}, & r > 2a\\(1-\frac{9r}{32a})\mathbf{I}+(\frac{3r}{32a})\hat{\mathbf{r}}\hat{\mathbf{r}}, & r\leq 2a\end{cases}.\tag{15}$$

Naive evaluation of the mobility tensor requires $O(N^2)$ operations and its inversion, required to compute the Brownian displacements in Equation 12 require $O(N^3)$ operations. This commonly precludes researchers from simulating large systems. However, the numerical

complexity of its computation can be significantly improved by noticing the mobility tensor as in Equation 15 is positive-definite.[8] This property can be leveraged to obtain a numerical complexity of $O(N \log N)$ to calculate particle velocities from the forces exerted on them[7] and a linear scaling sampling of Brownian displacements can be obtained using the Positively Split Ewald method developed by Fiore, Swan and coworkers.[9]

Equation 11 can be numerically solved via a forward Euler-Maruyama integration scheme[10],[11],[12]:

$$\mathbf{x}_\alpha(t + \Delta t) = \mathbf{x}_\alpha(t) + \mathbf{u}_\alpha(t)\Delta t, \tag{16}$$

where Δt is the time step over which ion trajectories are advanced.

Forces arising from conservative interactions among colloidal particles are represented as the gradient of a potential energy $U(\mathscr{X})$, which is a function of the coordinates of all ions $\mathscr{X} \equiv [\mathbf{x}_1, \mathbf{x}_2, \ldots, \mathbf{x}_N]^T$,

$$\mathbf{F}_\alpha^{\mathrm{I/M}}(\mathscr{X}) \equiv -\nabla_{\mathbf{x}_\alpha} U^{\mathrm{I/E}}(\mathscr{X}), \tag{17}$$

where the gradient is taken with respect to the position of the αth particle.

While the electrostatic interactions between the charged species can be taken into account as described by the Gouy-Champman model, the electromagnetic interactions and the influence of the magnetic field gradient are obtained by solving Maxwell's equations in the form

$$\nabla \cdot \mathbf{B} = 0, \quad \mathbf{B} = \mu \mathbf{H}. \tag{18}$$

Paramagnetic particles of magnetic permeability μ_p in a solvent of permeability μ_s. By defining a magnetic scalar potential ψ, the problem reduces to Laplace's equation:

$$\nabla^2 \psi = 0, \tag{19}$$

subject to

$$(\mathbf{B}_f - \mathbf{B}_p) \cdot \hat{\mathbf{n}} = 0. \tag{20}$$

Where $\mathbf{B}_p$ and $\mathbf{B}_f$ are the magnetic fluxes inside and outside of the particle. These equations are valid in the limit that the magnetic relaxation time inside of the particle and fluid is significantly smaller than the time scale of the study. As we are interested in timescales of particle motion $O(1s)$, the system is said to be pseudosteady. Thus, time dependence arises solely due to the time-varying boundary conditions in 20 as particles move around or the external field varies.

A multipole expansion of the integral representation of Laplace's equation can be used to derive a linear system of equations that couples the magnetic flux moments on the particle to the magnetic potential and potential gradients on the fluid.[6] Considering the dipole contribution and ignoring quadrupoles and higher-order moments, we obtain:

$$\mathbf{H}_0 = \sum_{\alpha,\beta}^{N} \mathbf{M}_{\alpha\beta} \cdot \mathbf{m}_i, \tag{21}$$

where $\mathbf{M}_{\alpha\beta}$, the magnetic flux moments of particle β with particle α in a periodic box

$$\mathbf{M}_{\alpha\beta} = \frac{3\mathbf{I}\delta_{\alpha\beta}}{4\pi a^3(\mu_p - \mu_f)} + \frac{9}{a^2 \mu_f V} \sum_{\mathbf{k} \neq 0} \frac{e^{i\mathbf{k} \cdot (\mathbf{x}_\alpha - \mathbf{x}_\beta)}}{k^2} j_1^2(ka) \hat{\mathbf{k}}\hat{\mathbf{k}}, \tag{22}$$

where $j_1(x) = \sin(x)/x^2 - \cos(x)/x$ is the first order spherical Bessel function of the first kind, and $\mathbf{k} = [2\pi \kappa_x / L_x, 2\pi \kappa_y / L_y, 2\pi \kappa_z / L_z]$ for integers κ_i.

The dipole-dipole interactions contribution to the potential energy can be obtained via the sum of the pairwise interactions given by

$$U^{\mathrm{M}} = -\frac{1}{2} \sum_{\alpha=1}^{N} \mathbf{H}_0 \cdot \mathbf{m}_\alpha = -\frac{1}{2} \sum_{\alpha,\beta}^{N} \mathbf{M}_{\alpha\beta} : \mathbf{m}_\alpha \mathbf{m}_\beta. \tag{23}$$

Similarly, the resulting magnetic force acting on the αth particle is

$$\mathbf{F}^{\mathrm{M}} = -\nabla_\alpha U^{\mathrm{M}} = -\frac{1}{2} \sum_{\alpha,\beta}^{N} \frac{\partial \mathbf{M}_{\alpha\beta}}{\partial \mathbf{x}_\alpha} : \mathbf{m}_\alpha \mathbf{m}_\beta \tag{24}$$

Experiments

130

Particle synthesis

The non-magneto-responsive fluorescent silica nanoparticles were synthesized according to Mahon et al.[13]. Briefly, the fluorescent core consisting of N-1-(3-trimethoxysilylpropyl)-N'-fluorescein thiourea was formed by dissolving 4 mg of FITC (Sigma Aldrich) in 2 mL of ethanol abs. (Sigma Aldrich). Then, 20 μl of APTMS (Sigma Aldrich) was added, and the mixture was shaken at room temperature in darkness for four hrs. Next, 0.5 mL of the conjugate is mixed with 0.91 g aq. ammonia in 24.5 mL ethanol abs. in a magnetically stirred glass vial at 25°C. Subsequently, 0.95 mL of TEOS was added, and the mixture was stirred at 600 rpm for 20 hrs. The silica shell was grown by adding 50 μL TEOS 29x every 15 min, growing the particle to the desired size of approximately 30 nm, thereby avoiding secondary nucleation. After the reaction, the nanoparticles were washed by centrifugation at 14000 rpm for 30 min with resuspension in EtOH abs. (3x) and Millipore water (3x) using bath sonication (45 kHz, VWR). The concentration was determined gravimetrically by drying 300 μL of solution.

The magneto-responsive silica-coated iron oxide nanoparticles (MNPs) were produced by an adapted recipe described in Turrina et al.[14]. Therefore, solution A was prepared by dispersing 115 mg of the bare iron oxide nanoparticles in 0.100 L of Millipore water. Subsequently, the suspension is dispersed via ultrasonication on ice (3 min, 20%, 10 sec on, 15 sec off, 20 kHz, Branson Ultrasonics). For solution B, 0.25 g citric acid (Carl Roth) were dissolved in 22.5 mL Millipore water and ultrasonicated (3 min, 20%, 10 sec on, 15 sec off). Both (= solution C) were mixed and ultrasonicated again (5 min, 20%, 10 sec on, 15 sec off). After 15 min of incubation, the pH was adjusted to pH 11 with 25% tetramethylammonium hydroxide (Sigma Aldrich). Then, 0.34 L of ethanol abs. (99%, VWR), 0.09 L of Millipore water, 0.0225 L of ammonia solution (25%, Carl Roth), and 0.0225 L of solution C were filled in a nitrogen evacuated 0.5 L flask. 108.5 μL of TEOS were added via a syringe through the septum, and the reaction was continued for 1 h at 11°C under continuous dispersion via ultrasonication. Afterward, the coated nanoparticles were washed with ethanol abs. either by centrifugation (4600 xg, 20 min) or magnetic decantation until pH 9 is reached. Next, the washing was continued using degassed Millipore water until the conductivity was < 150 μS cm^{-1}. The concentration was analyzed as described above and stored under a nitrogen atmosphere at 4°C. Before usage, the particles were redispersed by ultrasonication (132 kHz, Sonorex) for 15 min at 11°C.

Both nanoparticle species were characterized by FT-IR (Alpha II, Bruker) using 64 scans per sample, subtracting the background by the concave rubber band method in the software OPUS 8.1. DLS and zeta potential measurement (Zetasizer Ultra, Malvern Panalytical) were conducted in the viscous solution at a concentration of 1 g L^{-1} (η = 2.2274 mPa s, T = 25°C, pH = 7). The magnetic susceptibility was analyzed via SQUID Quantum Design MPMS XL-7 at 300 K, varying the magnetic field from -50 kOe to 50 kOe. Therefore, frozen particles (T = -80°C) are lyophilized and glued into a small tube. For TEM (JEM 1400 Plus, JEOL) measurement, 10 μL of sample is dried on a carbon copper grid, that has been glow discharged via plasma. A minimum of 100 particles were analyzed using the software ImageJ to determine the primary particle diameter.

Particle characterization

Colloidally stable nanoparticles were synthesized and characterized. The Fourier-transform infrared spectrum (FT-IR) of the fluorescent silica nanoparticles (= non-magneto-responsive nanoparticles (non-MNPs)) reveal peaks at 1082, and 794 cm^{-1}, which correspond to the Si-O-Si stretching and bending vibrations, respectively and thereby confirming the existence of silica (**Figure 1 a**). The peak located at 972 cm^{-1} signifies the Si-OH stretching vibration, while the relatively low intensity of the peak at 2926 cm^{-1} suggests a minimal presence of bound water. The same peaks are observed in the spectrum of silica-coated iron oxide nanoparticles (= magneto-responsive nanoparticles (MNPs)) in **Figure 1 b**, which also exhibit the Fe-O vibration at 570 cm^{-1}, which corroborates the presence of an iron oxide core enveloped by a thin silica shell. The Si-O-Fe stretching vibration is also observed at 1082 cm^{-1}. Additionally, the band at 1603 cm^{-1} confirms the presence of hydroxyl groups. These observations align with previous studies[15–17]. The superparamagnetic properties of the MNPs were verified through superconducting quantum interference device (SQUID) measurements, which revealed no remanence at 0 Oe (as shown in **Figure 1 c**). The saturation magnetization was determined to be 66.10 emu g^{-1}.

The primary particle diameters of the MNPs (**Figure 2 a**) and non-MNPs (**Figure 2 b**) are estimated to be 11.7 $\pm$ 3.6 nm and 26.6 $\pm$ 5.0 nm, respectively, based on transmission electron microscopy (TEM) images. In the viscous solution at pH 7, agglomerates with a hydrodynamic diameter of 45.1 $\pm$ 8.0 nm are formed for the MNPs and 63.9 $\pm$ 6.6 nm for the non-magneto-responsive ones. Dynamic light scattering (DLS) measurements (**Figure 1 d**) show that both particle species exhibit a monomodal distribution with a polydispersity index of 0.36 $\pm$ 0.05 and 0.21 $\pm$ 0.01, respectively. The colloidal stability of the nanoparticles, as characterized by their zeta potentials, describing the electrostatic potential at the particle's slipping plane, depends on the pH, meaning the ionic strength of the solvent. **Figure 1 e** and **f** present the zeta potential and hydrodynamic diameter over pH. The zeta potential of the MNPs **Figure 1 d** is below -20 mV for pH > 4, indicating electrostatic repulsion between the particles. For the non-MNPs **Figure 1 d**, the zeta potential is -43.68 ± 3.12 mV at pH 7, indicating high colloidal stability. This is verified by the hydrodynamic diameter, which decreases from 2870 $\pm$ 1637 nm at pH 4 to 83 $\pm$ 3 nm at pH 10. The experiments were performed at pH 7, where the zeta potential is -24.26 ± 0.61 mV for the MNPs and -43.68 ± 3.12 mV for the non-MNPs. The latter is highly colloidally stable, as a hydrodynamic diameter of $\sim$40

131
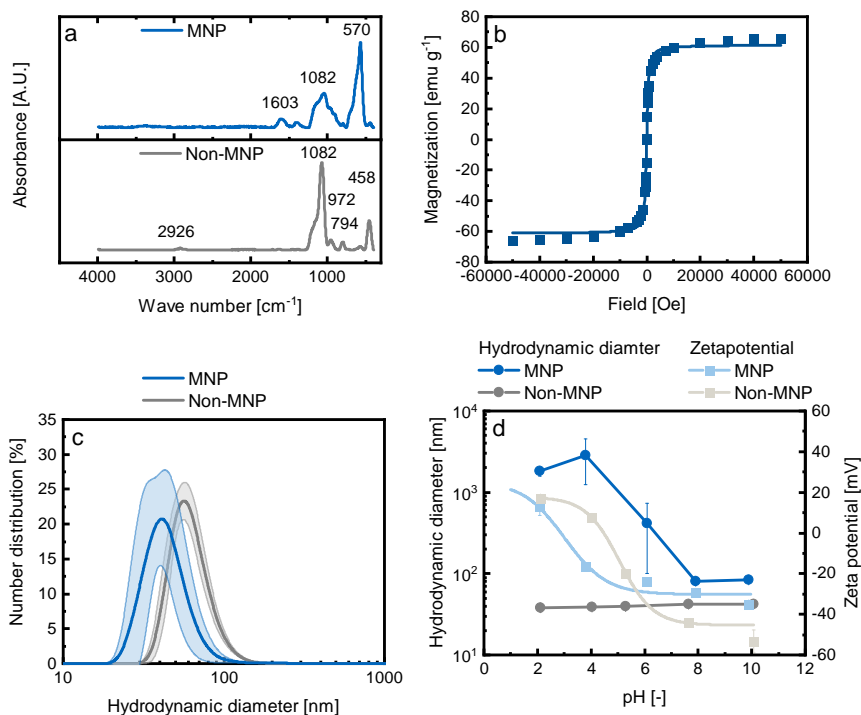
Fig. 1 (a) displays the Fourier-transform infrared spectra of the non-MNPs and MNPs, respectively, measured from 400 to 4000 cm^{-1}. The superconducting quantum interference device measurement of MNPs is shown in (b). (c) presents the average particle size distribution measured in triplicate for the MNPs (blue) and the non-magneto-responsive ones (grey) at a concentration of 1 g L^{-1} in buffer, with the standard deviation shown in the shaded form. (d) shows the hydrodynamic diameter and zeta potential measurements of the non-MNPs (grey) and the non-magneto-responsive (blue) suspensions at a concentration of 1 g L^{-1} in buffer solutions with a pH range of 2 to 10 and a viscosity of 2.227 mPa s.

nm is observed for the whole pH range; nevertheless, the zeta potential is below -20 mV for pH values > 5.5 **Figure 1 f**.
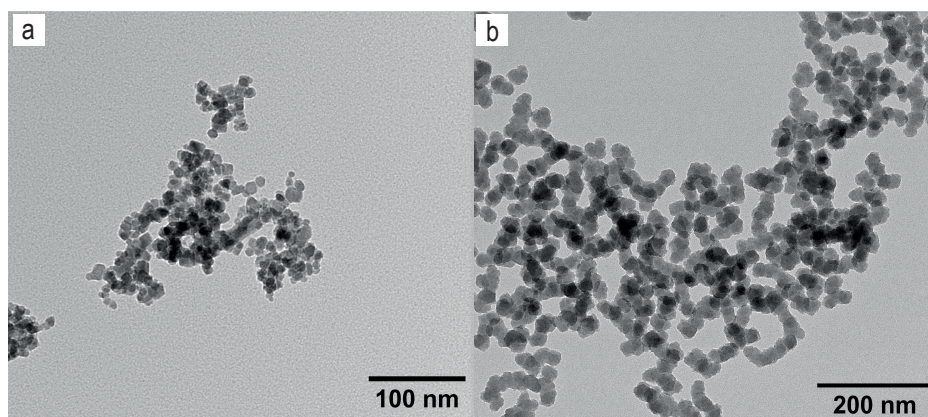
Fig. 2 TEM image of the magneto-responsive nanoparticles (a) at 100000× magnification and for the non-magneto-responsive ones (b) at 60000× magnification.

133

Microfluidic set-up
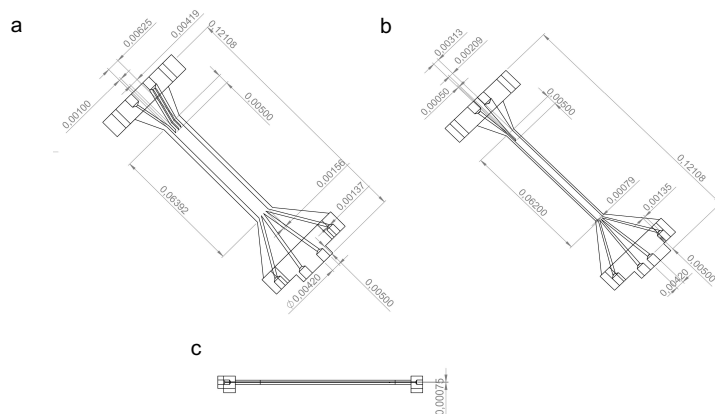
Fig. 3 (a) CAD drawing showing the chip with a height of 750 μm. (b) CAD drawing of the printed chip for two different Péclet numbers by width variation. (c) Side view of the printed chips.

134

References

1 E. M. Furst and A. P. Gast, *Physical Review E*, 2000, **61**, 6732–6739.

2 Z. M. Sherman and J. W. Swan, *ACS Nano*, 2019, **13**, 764–771.

3 J. D. Jackson, *Classical electrodynamics*, John Wiley I& Sons, 1999.

4 D. Saville, W. Russel and R. William, *Colloidal Dispersions*, Cambridge University Press, 1989.

5 D. Frenkel and B. Smit, *Understanding molecular simulation: from algorithms to applications*, Academic Press, 2002.

6 Z. Sherman, *PhD Thesis*, Massachusets Institute of Technology, 2019.

7 J. W. Swan and G. Wang, *Physics of Fluids*, 2016, **28**, 011902.

8 S. Kim and S. J. Karrila, *Microhydrodynamics: principles and selected applications*, Dover Publications, Mineola, N.Y, 2005.

9 A. M. Fiore, F. B. Usabiaga, A. Donev and J. W. Swan, *The Journal of Chemical Physics*, 2017, **146**, 124116.

10 A. W. C. Lau and T. C. Lubensky, *Physical review. E, Statistical, nonlinear, and soft matter physics*, 2007, **76**, 011123.

11 S. Delong, F. Balboa Usabiaga and A. Donev, *The Journal of chemical physics*, 2015, **143**, 144107.

12 A. Gubbiotti, M. Chinappi and C. M. Casciola, *Physical review. E*, 2019, **100**, 053307.

13 E. Mahon, D. R. Hristov and K. A. Dawson, *Chemical Communications*, 2012, **48**, 7970–7972.

14 C. Turrina, A. Oppelt, M. Mitzkus, S. Berensmeier and S. P. Schwaminger, *MRS Communications*, 2022, **12**, 632–639.

15 S. Saravanan, R. S. Dubey, S. Saravanan and R. S. Dubey, *Romanian Journal of Information Science and Technology*, 2020, **23**, 105–112.

16 S. E. Favela-Camacho, E. J. Samaniego-Benítez, A. Godínez-García, L. M. Avilés-Arellano and J. F. Pérez-Robles, *Colloids and Surfaces A: Physicochemical and Engineering Aspects*, 2019, **574**, 29–35.

17 R. K. Singh, T. H. Kim, K. D. Patel, J. C. Knowles and H. W. Kim, *Journal of Biomedical Materials Research - Part A*, 2012, **100 A**, 1734–1742.

A.1.3 Studying the Impact of Cell Age on the Yeast Growth Behaviour of *Saccharomyces pastorianus var. carlsbergensis* by Magnetic Separation

RESEARCH ARTICLE

Studying the impact of cell age on the yeast growth behaviour of *Saccharomyces pastorianus* var. *carlsbergensis* by magnetic separation

Marco Eigenfeld[1] 🔘 | Leonie Wittmann[2] 🔘 | Roland Kerpes[1] 🔘 |
Sebastian P. Schwaminger[2,3,4] 🔘 | Thomas Becker[1] 🔘

[1]TUM School of Life Science, Technical Chair of Brewing and Beverage Technology, University of Munich, Freising, Germany

[2]TUM School of Engineering and Design, Technical University of Munich, Chair of Bioseparation Engineering, Garching, Germany

[3]Otto-Loewi Research Center, Medical Division of Medicinal Chemistry, University of Graz, Graz, Austria

[4]BioTechMed-Graz, Graz, Austria

Correspondence
Roland Kerpes, TUM School of Life Science, Technical Chair of Brewing and Beverage Technology, University of Munich, Weihenstephaner Steig 20, 85354 Freising, Germany.
Email: roland.kerpes@tum.de

Sebastian P. Schwaminger, TUM School of Engineering and Design, Technical University of Munich, Chair of Bioseparation Engineering, Boltzmannstr. 15, 85748 Garching, Germany.
Email: sebastian.schwaminger@medunigraz.at

Abstract

Despite the fact that yeast is a widely used microorganism in the food, beverage, and pharmaceutical industries, the impact of viability and age distribution on cultivation performance has yet to be fully understood. For a detailed analysis of fermentation performance and physiological state, we introduced a method of magnetic batch separation to isolate daughter and mother cells from a heterogeneous culture. By binding functionalised iron oxide nanoparticles, it is possible to separate the chitin-enriched bud scars by way of a linker protein. This reveals that low viability cultures with a high daughter cell content perform similarly to a high viability culture with a low daughter cell content. Magnetic separation results in the daughter cell fraction (>95%) showing a 21% higher growth rate in aerobic conditions than mother cells and a 52% higher rate under anaerobic conditions. These findings emphasise the importance of viability and age during cultivation and are the first step towards improving the efficiency of yeast-based processes.

KEYWORDS
bioseparation, fermentation, magnetic separation, physiological state, yeast

1 | INTRODUCTION

Saccharomyces yeast is an essential microorganism for food production, and is used in food supplements,[1] biofuels, and chemicals – especially bioethanol – to replace high-energy-density fuels with biobased resources.[2] They are the ones most widely used in pure cultures, especially in the beverage and baking industries, as well as in cocul-tures in mixed fermentation processes.[3] In particular, *Saccharomyces* species are a key factor in biotechnical applications, due to their high fermentative capacity.[4]

There is a growing interest in increasing the product yields of current fermentation procedures. This can be achieved by optimising fermentation performance either by metabolic/genetic engineering[5,6] or by focussing on the production quantity in dependence on singular cell age.

Marco Eigenfeld and Leonie Wittmann contributed equally to this study.

These applications, both biotechnological and food and beverages, are highly dependent on the physiological state of the cultures used. The physiological state of yeast cells is described by their viability, vitality, and cellular age. Viability represents the ratio of living to dead cells, whereas vitality describes the metabolic activity of living cells in dependence on the aging process.[7,8] Vitality is a key parameter for evaluating yeast cell quality in the brewing industry. Yeast cells with a high vitality enable the production of high-quality beer, as indicated in the study conducted by Krieger-Weber.[9] However, biochemical activity and yeast cell age also have a significant impact on beer quality.[10]

In previous studies, for instance, the utilisation of available sugar was shown to commence more slowly in a culture consisting exclusively of daughter cells than in a mixed culture,[11] due to the adaptation of daughter cells to a changing environment. The sole presence of daughter cells, indicating successful separation, was verified only by microscopy of the visible cell surface. In contrast, other studies have shown that the glucose uptake rate in aged cells (at the end of their life span) decreases to approximately 10% compared to young cells.[12] This reduction correlates with the simultaneous decrease in fructose-1,6-bisphosphate.[13]

Generally, aging is defined as a decline in physiological function[14] accompanied by metabolic changes[15] with a replication-specific increase in mortality, implying that old cells are more likely to die than young cells. When measured across a population, this property results in a sigmoidal survival curve,[12–14] which has been reported for haploid, and diploid yeast strains from all genetic backgrounds investigated to date.[16,17]

Two models are generally applied for the definition of yeast cell age: replicative lifespan (RLS) and chronological aging. RLS is defined as "the number of daughter cells produced by the mother cell before senescence occurs."[18] This parameter is determined by counting the number of bud scars resulting from each division process.[19] Senescence is the non-replicative state that leads to cell death and autolysis. The number of possible divisions of a yeast cell until it reaches senescence[20] is generally 10–30.[21] Depending on the cultivation medium, lower cell cycle numbers have also been observed, however. In contrast, chronological lifespan is related to the length of time a non-dividing cell can maintain its viability and re-enter proliferation under favourable conditions.[22] Metabolism might be of key importance to the molecular causes of chronological aging. Studies have confirmed that ethanol plays a vital role in aging, since ethanol influences the respiratory chain and, in turn, the chronological aging process,[23] whereas acidification due to acetic acid has been put forward as the determinant cause of aging.[24,25]

In contrast, during the RLS of yeast, changes in the metabolic level result in reduced substrate uptake and a decrease in growth rates, and anaerobic fermentation switches to respiration with the production of acetate and glycerol.[12] RLS is an established model for examining aging processes and describing the cell age distribution in yeast populations.[18] In contrast to chronological aging, in RLS cell damage (oxidised proteins, damaged mitochondria) and defects (extrachromosomal ribosomal rDNA circles, mutations) can be

eliminated, which results in a tool that can be used for rejuvenating a yeast culture.

The distribution of cell age in a yeast population as well as the viability and vitality of the cells are essential factors when it comes to ensuring their precise fermentation performance in industry.[26,27]

These relationships indicate how important it is to better understand yeast cell aging in cultivation processes, for instance, in the context of stress reactions[18] and age distributions in a culture.[12,28] It is essential to gain information on the interplay between yeast vitality and single-cell age to attain the desired effective control of (industrial) fermentation processes.

Beyond the industrial strains of *Saccharomyces* used in food and beverage fermentation, there is minimal knowledge regarding the impact of aging on food production and process performance, since it is not possible to perform non-invasive separation of differently aged fractions in cell numbers enabling fermentation on a 1-mL scale (inoculation cell concentration: 10^7 cells mL^{-1}). Fluorescence-activated cell sorting is a commonly used approach for sorting cells according to their fluorescence properties.[29,30] Here, flow cytometry detects yeast cells and determines their fluorescence intensity. The detected cells are then sorted according to their fluorescence intensities.[31] This approach cannot be used in our case, since the fluorescence intensities determined have to be processed by autofluorescence calculation and subtraction.[32] As flow cytometry cannot perform this offline data processing, another method of cell sorting needs to be developed.

Magnetic separation presents itself as a suitable method of yeast cell separation. In contrast to centrifugation, which focusses on cell differentiation by cell size, rather than directly on age, the advantage of magnetic separation is that no shear forces act on the yeast cells, and separation is directly correlated to age.[33] This method uses iron oxide nanoparticles, which can adsorb to the diamagnetic yeast cells due to electrostatic interaction with the cell surface. As many studies have already shown,[34–36] it is a non-invasive process that does not influence a yeast's metabolism. Using this method, Berovic et al. succeeded in significantly lowering the separation time of yeast cells in wine production without influencing the yeast's metabolism.[34]

Moreover, using magnetic nanoparticles increased the separation performance in terms of both time and efficiency in the course of bioethanol production with *S. cerevisiae*.[37] However, the aim of both applications was to concentrate an entire heterogeneous yeast population from the cultivation broth due to the unspecific binding of the magnetic nanoparticles. Magnetic separation is also applicable to age-related separation, as it is achieved by the biotinylation of mother cells adsorbing to magnetic streptavidin-coated beads. This technique has enabled the execution of gene expression studies; however, these could only be performed on an analytical scale and without selecting older cells, as they are coated with biotin.[38]

To enable age-based separation in these studies, we introduce a magnetic separation method to analyse the cultivation performance of *Saccharomyces pastorianus* var. *carlsbergensis* yeast cells (10^7 cells mL^{-1}) with higher RLS (mother cells) compared to low RLS (Figure 1). An advantage of our method is that it is non-invasive and
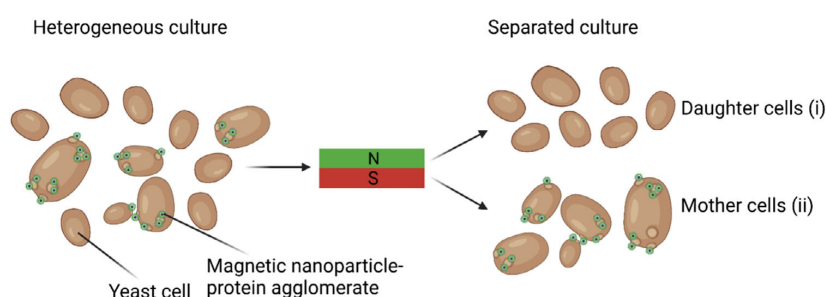
FIGURE 1 Diagram showing the magnetic separation process. A heterogeneous yeast culture is labelled with ethylenediaminetetraacetic acid (EDTA)-functionalised iron oxide nanoparticles, stabilised by a silica shell, which adsorbs to the linker-protein-labelled bud scars of the yeast cells. The supernatant, composed of the non-labelled daughter cells (i), is collected and magnetically separated from the old mother cells (ii), in a batch process.

does not influence cell viability, due to the use of functionalised, super-paramagnetic iron oxide nanoparticles (IONs).[39] Moreover, compared with FACS magnetic separation is both age-specific and fast, since we used the chitin-enriched bud scars for age differentiation.[40] Here, the signals of fluorescent bud scars and yeast cell autofluorescence overlap for differently aged yeasts, so data post-processing is needed to obtain the cell age distribution. In contrast, magnetic labelling of second-generation and older cells allows first-generation daughter cells to be isolated and their growth behaviour analysed. This non-invasive and fast-acting magnetic batch separation method provides scope for further investigation of the impact of young and old yeast cells in terms of the age and synthesis of bioproducts like ergosterol or fatty acid production in future studies. Additionally, the use of bud scars containing chitin means that this approach can be transferred to all other similar yeast strains for studying protein or chemical synthesis.

2 | MATERIAL AND METHODS

2.1 | Synthesis of EDTA-functionalised silica-coated iron oxide nanoparticles

Bare iron oxide nanoparticles were synthesised by co-precipitation, as previously published.[41,42] The bare iron oxide nanoparticles were then coated with silica to increase their colloidal stability, and amine groups were introduced for later functionalisation with ethylene-diaminetetraacetic acid (EDTA), as performed in ref.[43] It should be pointed out that the protocol used was modified to obtain the nanoparticle characteristics (Supplementary information [SI]). To do this, 179 mg of bare iron oxide nanoparticles were resuspended in 100 mL of Millipore water and dispersed by ultrasonication on ice (3 min, 20%, 10 s on, 15 s off, 20 kHz, Branson Ultrasonics). 100 mL of 5.5 g L^{-1} citric acid were prepared and ultrasonicated (3 min, 20%, 10 s on, 15 s off). Both solutions were mixed and again ultrasonicated (5 min, 20%, 10 s on, 15 s off). After 15 min of incubation, the pH was

adjusted to 11 with 25% tetramethylammonium hydroxide (Sigma–Aldrich). A nitrogen-evacuated 4 L flask was then filled with 2.72 L of ethanol abs. (99%, VWR), 0.72 L of Millipore water, 0.18 L of ammonia solution (25%, Carl Roth), and 0.18 mL of the bare iron oxide nanoparticles solution. The quantity of ethanol is necessary to disperse the bare iron oxide nanoparticles and minimise the agglomerate size of the nanoparticles, which are surrounded by the silica shell. The reaction was triggered by adding 6.94 mL of tetraethylorthosilicate (TEOS, Sigma–Aldrich) with a syringe via the septum. After a reaction time of 1 h at 4°C under continuous ultrasonication (45 kHz, VWR), 1.984 mL of (3-aminopropyl)triethxysilane (APTES, Sigma–Aldrich) were added by syringe, introducing amine groups to the silica shell. The reaction continued for another hour maintaining the aforementioned conditions. The particles were washed first by centrifugation (4600 × g, 30 min), and then seven times magnetically with ethanol absolute until a pH of 9.5–9.7 was attained. Finally, the particles were washed magnetically with degassed Millipore water until a conductivity of <150 μS cm^{-1} was reached. Prior to storage under a nitrogen atmosphere at 4°C, the particles were dispersed by ultrasonication on ice (5 min, 20%, 10 s on, 15 s off). The concentration was determined gravimetrically by drying 300 μL of the particle suspension overnight at 60°C.

In a second synthesis, the silica shell particles were functionalised with EDTA by amide bonding. Here, 100 mg of the particles obtained were mixed with 100 mL of 0.075 mol L^{-1} EDTA (EDTA disodium salt dihydrate, Carl Roth) in a 0.5 L flask at 60°C for 2 h in an ultrasonication bath (132 kHz, Sonorex). The EDTA-functionalised nanoparticles were then washed with degassed Millipore water ($\sigma < 150$ μS cm^{-1}) and stored as described above.

For characterisation of the EDTA nanoparticles, the hydrodynamic diameter was determined by dynamic light scattering (DLS), transmission electron microscopy (TEM) images taken, and the magnetic susceptibility analysed with a superconducting quantum interference device (SQUID), according to the method described in Wittmann et al.[42] The Fourier-transform infrared spectra (FT-IR) were measured as described by Turrina et al.[41]

2.2 | Strain and strain maintenance

We used the bottom-fermenting yeast strain *S. pastorianus* var. *carlsbergensis* TUM 34/70 from our in-house collection. This strain was grown on yeast extract peptone dextrose (YPD) agar plates (10 g L^{-1} Bacto yeast extract, 20 g L^{-1} bacto peptone, 20 g L^{-1} glucose, and 10 g L^{-1} agarose). The YPD medium was prepared and sterilised for viability determination as described in the SI. All media components were supplied by Merck Life Sciences (Darmstadt). Pure yeast cells were grown to the mid-log phase (optical density at 600 nm [OD$_{600}$] = 0.2–0.5) before the start of each experiment, except where noted. Inoculation was made to a concentration of 10^7 cells mL^{-1}.

2.3 | Bud scar staining

Budding yeast has been widely used as a model organism to examine the effects of age. Bud scar staining was performed according to Eigenfeld et al.[40] using a recombinant protein, *His6-Sumo-sfGFP-ChBD*, which selectively binds to yeast cell surface chitin due to the chitin binding domain (ChBD), as previously shown.[40] Briefly, a yeast cell suspension was washed three times at 1000 × g for 1 min in 20 mM MOPS buffer (Carl Roth, pH adjusted using 1 M NaOH) (pH 7.3) and diluted to an OD$_{600}$ of 1.0 using 20 mM MOPS buffer. A mixture was then made of 150 μL of yeast suspension, corresponding to 1.8×10^6 yeast cells, and 300 μL of 4000 nM protein solution (*His6-Sumo-sfGFP-ChBD*). The cells were stirred gently in darkness for 30 min at room temperature, harvested by centrifugation at 1000 × g for 1 min, and washed three times with 20 mM of MOPS (pH 7.3). Finally, the stained cell culture was resuspended in 1 mL of MOPS and used for cytometric measurements.

2.4 | Magnetic labelling and separation of heterogeneous yeast culture

For adsorption of the linker-protein-stained bud scars to the EDTA-functionalised nanoparticles, they were first loaded with 10 mM NiCl$_2$ (Nickel(II) chloride hexahydrate, Sigma–Aldrich) in a 1 g L^{-1} demineralised water (DI-water) solution for 15 min at 1000 rpm at 22°C. The particles were then washed twice with 20 mM MOPS, pH 7.3 for 10 min at 12,000 × g and resuspended in an ultrasonication bath for 15 min (45 Hz, VWR). The particles were concentrated to a 2 g L^{-1} solution in the final wash step.

Meanwhile, the bud scars were stained with the linker protein as described above using 20 mM of MOPS pH 7.3. The stained yeast cells were concentrated to an OD$_{600}$ of 2 and then mixed in a 1:1 ratio with a 0.16 g L^{-1} solution of nickel-loaded nanoparticles. Next, the mixture was incubated for 1.5 h at 1000 rpm and 22°C to ensure the specific binding of the particle agglomerates to the yeasts' bud scars.

After incubation, the magnetically labelled yeast cells were placed near a magnet to separate the non-labelled daughter cells from the magnetically labelled mother cells. After 30 min, the supernatant, containing the daughter cells, was collected by slow and careful pipetting (9.5 mL of 10 mL). The OD$_{600}$ was then determined for both fractions (for the blank measurement, either a buffer or a suspension with the corresponding particle concentration was used). The specificity of the binding was verified in triplicates by flow cytometry (Cytoflex, Beckman Coulter) and light microscopy (Zeiss Axio Observer 7). A minimum of 150 cells per sample (*n* = 3) were analysed for light microscopic analysis. As only 50% of the yeast cell surface was visible, the absolute bud scar number was determined as described in ref.[40] The absorption behaviour of the linker protein to the nanoparticles was determined by mixing 1 g L^{-1} of nickel-loaded nanoparticles with different concentrations of linker protein for 1 h at 1000 rpm, 22°C. The nanoparticles were magnetically separated for 10 min, and the supernatant was centrifuged for 5 min at 17,000 × g to remove all particles. The supernatant was then analysed using a Bicinchoninic acid assay (Tecan Infinite M200 PRO Series). For the scanning electron microscopy images, the yeast cells were first loaded with protein and particles as described and then fixed with 2.5% glutardialdehyde for 1 h, 1000 rpm, 22°C. The cells were then washed with 20 mM MOPS buffer, pH 7.3, and pipetted onto a microscopic slide. After 15 min of incubation, the sample was washed with 30%, 50%, 70%, 80%, 96%, and 100% ethanol. The final wash step was performed three times. The sample was dried in a desiccator overnight before being used for the scanning electron microscopy.

2.5 | Mother and daughter cell cultivation of the magnetically separated yeast cell culture

The mother and daughter cells from the magnetic separation and a non-separated yeast cell culture were inoculated at OD$_{600}$ = 1 in a 1 mL cultivation volume, which is equivalent to industrial conditions of 10^7 cells mL^{-1} for inoculation. Cultivation was performed in a sterile 48-well plate in triplicates using wort (composition found in SI) with double orbital shaking at 365 cpm (3 mm) in a plate reader (Cytation 5 plate reader, Agilent). Aerobic conditions were created at 25°C in Breathe-Easy Sealing Membrane sealed plates, and anaerobic conditions at 14°C, by covering the well plates with nitrogen and sealing with a non-permeable SealPlate covering. The OD$_{600}$ was measured every 3 min. When the stationary phase was reached, the wells were harvested to determine viability, age distribution, and sugar content (SI).

The growth rate was determined by natural logarithmisation of the OD$_{600}$ and linear fitting to the exponential growth phase.

2.6 | Data analysis

Data of intracellular pH-value (ICP) measurements were analysed in R studio.[44] To do this, yeast samples were eliminated from outliers using the mvoutlier package[45] according to front scatter and side scatter behaviour at 488 nm. Outliers in calibration curves were eliminated by applying Cook's distance, as described by Dennis Cook,[46]
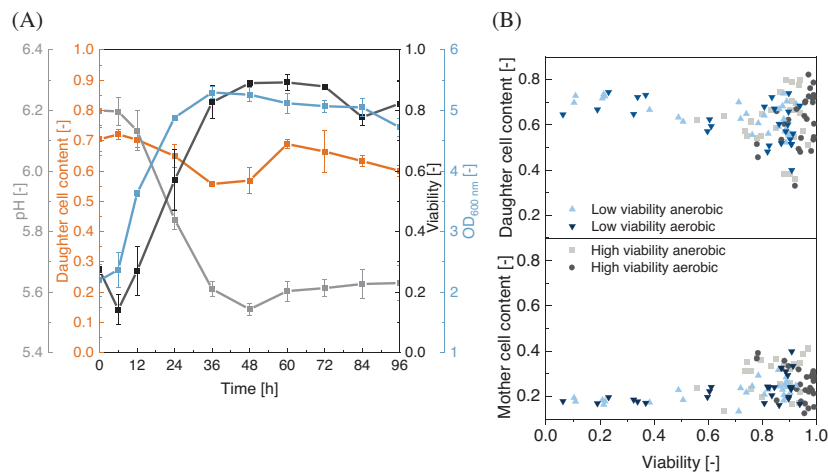
FIGURE 2 (A) Optimised age-distribution of inoculated culture (daughter–mother quotient of 2.97); $n = 3$; error bars represent the standard deviation of the triplicate measurement. (B) Comparison of the yeast population's viability and daughter/mother cell content; each point represents one distinct measurement.

using R studio software. The cut-off criterion for Cook's distance was chosen as 4 n^{-1}, as recommended by Hardin & Hilbe, where n represents the total number of data points.[47]

The yeast cell age distribution was determined as described by Eigenfeld et al.[32] Briefly, the replicative cell age distribution was determined by measuring the fluorescence intensity of yeast cells using stained bud scars, followed by autofluorescence prediction using the random forest model. Subsequent autofluorescence subtraction resulted in a fluorescence intensity distribution, allowing the determination of age fraction content by Gaussian mixture analysis.

The viable and non-viable cells were classified using a random forest model,[39] as published previously.

3 | RESULTS AND DISCUSSION

3.1 | Assessment of daughter cell content variation of heterogeneous culture over time

Yeast cells were cultivated aerobically and anaerobically in a YPD medium to determine the connection between replicative cell age, viability, vitality, growth (optical density at 600 nm; OD_{600}), and pH value. The results are shown in detail in the SI section (Figure S4). In addition, cultivations were conducted with yeast cells of good (93.5% $\pm$ 0.4%; daughter cell content: 0.41; first mother cell generation content: 0.28) or low (20.1% $\pm$ 3.1%; daughter cell content: 0.41; first mother cell generation content: 0.30) viability, keeping daughter and mother cell content constant (Figure S5A,B) (detailed age distribution is shown in Table S1, SI section). This experiment demonstrated that low-viability yeast with the same mother/daughter cell quotient performed worse, with 30% lower optical densities after 96 h

of fermentation ($p < 0.05$) and, therefore, does not work according to biomass formation in the fermentation process when compared to the good viability yeast population. However, in both cultivation processes (high and low viability), the daughter cell content increases on initiation of the exponential growth phase. According to the data we obtained, the yeast cells are conventionally harvested at the end of exponential growth and have a high daughter cell content. Therefore, in the next step, we used yeast cells taken from the second half of the exponential growth phase (daughter cell content: 0.71, first-generation mother cells: 0.24).

Additionally, to check whether this distribution affects fermentation, the viability of the culture was lowered to 0.27 (Figure 2A) with a mixture of one part yeast population and three parts thermally deactivated cells. Interestingly, there was no decrease in the daughter cell content after inoculation. Rather, the exponential growth phase was initiated rapidly, while a decrease in the daughter cell content increased the yeast viability from 0.14 to 0.83. Comparing the pH progression and the optical density, the fermentation process of the high-viability yeast process is similar to this optimised age-distribution (daughter cell content: 0.71, first-generation mother cells: 0.24) one. The pH decreases from 6.2 to 5.6 within 96 h, and the optical density follows the sigmoidal growth curve. The findings were obtained during the transient states of growth (i.e., in a nutritional shift-up, in a nutritional shift-down, and after the addition of cyclic AMP [cAMP]), indicating that the overall population requires several hours to reach the new balanced growth condition.[48]

These contrast with the traditional assumption that age fractions are constant in yeast cell populations but support the results of variations in cell age compositions, especially regarding daughter cell content, as previously demonstrated by the authors.[32] It is assumed that under optimal conditions, the daughter cell content is 50%, the mother cell content is 25%, the second-generation content

141

(A)

(B)
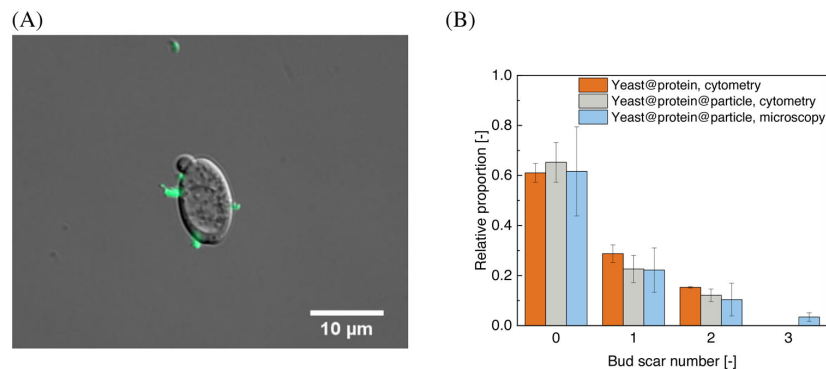
FIGURE 3 (A) Microscopic image of the specific binding of ethylenediaminetetraacetic acid (EDTA)-functionalised iron oxide nanoparticles, agglomerated with the linker protein, to the yeasts' bud scar. (B) Age distribution of a heterogeneous yeast culture, labelled only with the linker protein and with adsorbed EDTA-functionalised iron oxide nanoparticles derived from cytometric analysis ($n_{min} = 20,000$ counts, $n = 3$, error bars representing the standard deviation of the triplicate measurement). The age distribution is confirmed via microscopic image analysis ($n_{min} = 150$ cells, $n = 3$, error bars representing the standard deviation of the triplicate measurement) as an orthogonal method.

is 12.5%, and so on.[49] The deviation from this assumption can be explained by the difference in the G1 phase, which depends on cell age. Wang et al.[50] demonstrated by simulation that daughter cells have the same G1 phase duration as second-generation mother cells. A previous simulation performed by the authors confirmed a major proportion of daughter cells in an exponential growth phase.[32]

3.2 | Age cell fractions in cultivations with high- and low-viability yeast populations

Due to the similarities in the fermentation behaviour of the high-viability and optimised, age-distribution-inoculated, anaerobic fermentations described in the previous section, we compared the viability values with the daughter cell content (Figure 2B, top) and the mother cell content (yeast cells with one bud scar; first-generation mother cells) (Figure 2B, bottom) for each fermentation sample. This comparison indicated that yeast cell populations with low viability had a daughter cell content of >60%. In contrast, in a yeast population with high viability, the maximum RLS was higher. These results indicate that the age distribution within a yeast population varies in dependence on the physiological state of the whole population. A yeast population itself can adjust viability in the process, indicated by a high daughter cell content in populations with a low viability. In this case, the premature death of older cells can be assumed to rescue the survival of the whole population. Changes in RLS can furthermore be explained by variations in the preferred sugar composition, as cells of different ages consume specific sugars.[51–54] Another cause of the shift in yeast populations towards a higher daughter cell content due to a viability decrease can be a difference in stress resistance, since cells with a higher RLS have imbalances in their energy metabolism,[12,55,56] especially in an anaerobic environment.

3.3 | Influencing cultivation performance by shift of the cell age fraction

Based on these results, which indicate that daughter cell content impacts fermentation performance, the effect of cell age, especially that of mother cells and daughter cells that exhibit good viability, should be analysed under industrial cultivation conditions. To do this, a magnetic separation process is implemented to isolate two fractions taken from a heterogeneous yeast culture: (i) a daughter cell fraction and (ii) an enriched mother cell fraction (Figure 1) for subsequent growth studies in wort. IONs are very suitable for such processes, as they are inexpensive and easy to functionalise, and they exhibit superparamagnetic behaviour.[43,57,58] The EDTA-functionalised IONs, stabilised by a silica-shell, have a primary diameter of 142 ± 28 nm and show a maximum binding capacity of 0.0877 ± 0.0062 $g_{Linker-protein}/g_{Nanoparticle}$ to the His-tag of the linker protein (Figure S6A,C,F). Additional characterisation data of the EDTA-functionalised iron oxide nanoparticles, such as TEM, FT-IR, DLS, and SQUID, is given in the SI. Age-dependent magnetic labelling is ensured by the C-terminal ChBD that binds to the chitin-enriched bud scar of the yeast cell. GFP as a fluorescence marker is in between the His-tag and the ChBD. An advantage of this method is that it is non-invasive and does not influence cell viability, as it uses functionalised, superparamagnetic iron oxide nanoparticles.[39]

Figure 3A is a qualitative depiction of the specific binding of the linker protein particle agglomerates to the bud scars of a yeast cell. First, the recombinant protein linker was bound to the yeast cells. A correlation between the amount of fluorescence and the RLS of yeasts has been published previously by Eigenfeld et al.,[32] so this approach was applied as an orthogonal method. The specificity of the particle binding is verified, as the bud scar distribution with linker-protein-labelled yeast cells is comparable with the one obtained with the linker-protein-particle agglomerates. The two distributions

were measured by cytometry (Figure 3B) and compared. The microscopic analysis corresponds with the cytometry data. The standard deviation might be slightly higher; however, fewer yeast cells were analysed (n_{min} = 150 cells, n = 3) compared to the cytometric measurement. Differences might occur, as the latter analyses single cells (n_{min} = 20,000 counts, n = 3) in a laminar flow, whereas the former visualises cells that are fixed to a microscopic slide. Nevertheless, both methods suggest a non-labelled daughter cell content of 60%, with a magnetically labelled mother cell content of 40%, in a heterogeneous yeast culture. The binding of the EDTA-functionalised iron oxide nanoparticles proves to be specific, as the microscopy analysis suggests an unspecific binding proportion of only 9.53% ± 0.03%.

The data furthermore reveals that in this experiment, the number of yeast cells with four bud scars is negligibly small. In an earlier study, the proportion of mother cells with four bud scars or more was ≤ 5%.[32] A qualitative image of the binding system is shown in Figure 3A; additionally, a scanning electron image is presented in Figure S7 in the SI.

Next, a heterogeneous yeast culture was separated in a magnetic batch process to isolate the daughter cells from the mother cells. The adsorption of the EDTA-functionalised iron oxide nanoparticles to the bud scars via the linker protein was successful, as the daughter cell content was increased from 67.70% ± 0.17% in the heterogeneous culture to 94.33% ± 6.25% in the supernatant fraction, in the separation for aerobic cultivation. In the anaerobic case, it was increased from 70.87% ± 1.26% to 98.83% ± 0.83% (Figure 4A). It is this supernatant fraction that is later referred to as daughter cells. For the magnetically separated fraction (later referred to as mother cells), the daughter content is less than in the heterogeneous culture; however, some daughter cells are also captured. Even if the unspecific binding proportion is under 10%, daughter cells could have been separated accidently, being encapsulated in a crosslinked agglomerate.

On the other hand, a budding mother cell always contains a bound daughter cell, both being separated together. All three yeast cell fractions show high viability after cell separation; however, the daughter cell fraction is the highest, at 98.13% ± 0.11%, whereas the mother cell fraction is decreased to 92.65% ± 0.45% (Table S2). On completion of the cultivation, the viabilities indicate no significant difference between the three sets (viabilities: aerobic: 99.1% ± 0.2%; anaerobic: 96.9% ± 0.6%) These data suggest an interconnection between yeast cell age and yeast viability. In terms of yeast vitality, which defines cells' metabolic power, a good value was determined in all three samples, after separation as well as after aerobic cultivation or anaerobic fermentation (Table S3). ICP values above 6.2 are associated with excellent vitality, whereas values below 5.2 indicate stressed yeast cells with lower vitality.[59]

It is evident from the microscopic analysis that the daughter cells are smaller than the mother cells, while the heterogeneous culture lies somewhere in between (Figure S8A,B). The cytometric analysis confirms this trend. Furthermore, the surface roughness indicates that the older cells differ in morphology, which has been reported previously.[60] The size difference is not so pronounced because the cell growth occurs in the G1-phase before budding starts.[61,62] There-

fore, there might also be first-generation yeast cells in the daughter cell fraction, which have increased in size but have not yet started budding. Additionally, the age distribution of the cell fractions reveals that some daughter cells still remain in the magnetically separated fraction (bud scar number = 0) (Figure 4A upper images). This contamination of the mother cell fraction with daughter cells would result from magnetic forces and the experimental setup. By separating the mother cells using a magnet, the cells with magnetic particles become aligned towards the field and separated due to the magnetic field on the vessel wall. Daughter cells are also transported to the vessel wall. After conducting aerobic cultivation for 24 h, the age distributions of all three samples are comparable, with no significant differences (daughter–heterogeneous: p = 0.401; daughter–mother: p = 0.444; mother–heterogeneous: p = 0.241). This lack of difference can be explained by the cultivation conditions, because the yeast cells are in an aerobic environment and temperature, in which the generation time is 90 min or above.[63] The doubling time is reduced in an anaerobic environment with a cold fermentation temperature,[64] resulting in significant differences in the age distribution after 84 h (daughter–heterogeneous: p = 0.225; daughter–mother: p < 0.005; mother–heterogeneous: p < 0.005).

Magnetic separation processes for yeast cells have been developed since 1990, when Dauer and Dunlop presented a method of high gradient magnetic separation (HGMS) of $S.$ $cerevisiae$ based on the adhesion of γ-Fe_2O_3 particles. They used unfunctionalised iron oxide nanoparticles, which bind unspecifically to the yeast cell surface, targeting the separation of the whole heterogeneous population.[65] The same principle of separation was applied to bioethanol production with $S.$ $cerevisiae$. Magnetic separation is enabled by L-lysine-coated iron oxide nanoparticles bound to the cells.[37] However, the binding is unspecific for both processes and does not allow age-dependent separation, unlike the present study. The binding specificity of the magnetic nanoparticles to the yeast cells' bud scars relies on EDTA functionalisation and the His-tag of the linker protein on the one hand and the specific binding of the ChBD to the chitin-enriched bud scars on the other.[40] Therefore, it is now possible to conduct a non-invasive investigation of the growth not only of a heterogeneous population, but also of a separated one, consisting of a daughter-cell-enriched and a mother-cell-enriched fraction.

After successful separation, aerobic and anaerobic cultivation (inoculation of 10^7 cells mL^{-1}) of the three fractions under brewing process conditions is compared to determine their growth behaviour. The aerobic process curve in Figure 4B suggests that the daughter cells enter the exponential growth phase earlier than the mother cells and the heterogeneous culture. The fluctuations in the lag phase indicate that all fractions have to adapt to the new growth conditions after the magnetic separation in buffer without nutrients; however, comparing the growth rates, shown in Table S4 in the SI, it is clear that under aerobic conditions, the young daughter cells have a 22% higher growth rate (μ_{max} = 0.03740 ± 0.00497 h^{-1}) than the old mother cells (μ_{max} = 0.02927 ± 0.00154 h^{-1}). The maximum growth rate of the initial cell population (heterogeneous) is 0.03099 ± 0.00215 h^{-1}, that is, between that of the daughter and mother cell population. Entering
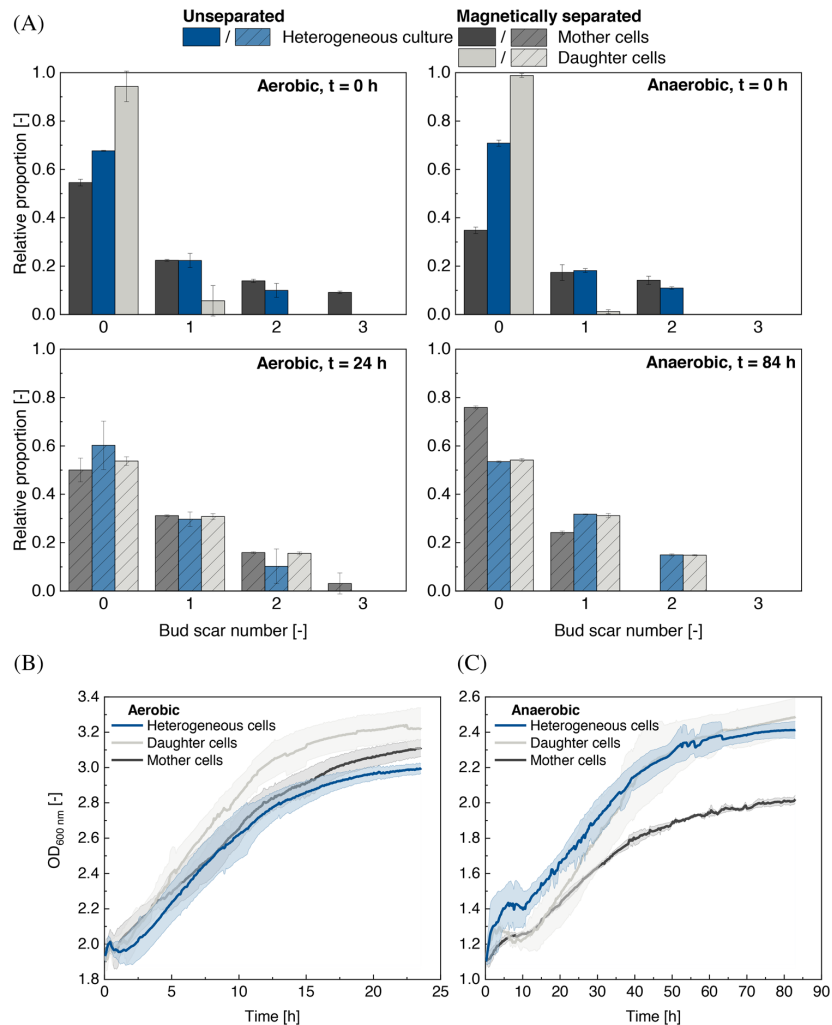
FIGURE 4 (A) Bud scar distribution of the heterogeneous culture, the magnetically separated fraction (mother cells), and the supernatant fraction (daughter cells) for aerobic and anaerobic cultivation at inoculation $t = 0$ h and in stationary phase at $t = 24$ h for aerobic and $t = 84$ h for anaerobic conditions; $n = 3$, error bars representing the standard deviation of the triplicate measurement. (B, C) Growth curves of heterogeneous, daughter-, and mother-cell-inoculated cultivation in an aerobic and anaerobic environment under industrial conditions (wort, inoculum: 1.4×10^7 cells mL^{-1} aerobic, 10^7 cells mL^{-1} anaerobic); $n = 3$. The shaded regions show the standard deviation of the triplicate measurement.

the stationary phase, the age distributions of all three fractions align. Moreover, the daughter cells result in a higher OD$_{600}$, which could be attributed to the more efficient use of nutrients in the metabolism of young cells.[12] The OD$_{600}$ of the heterogeneous population is lower than that of the mother cells, which might be attributed to the long adaptation process that can be seen between 1 and 3 h. In this frame, the separated and daughter cell sample is already growing. Focussing on the maximum growth rate, as shown in Table S4, the heterogeneous yeast culture is between the daughter and mother cell cultures. Nevertheless, the OD$_{600}$ of all three fractions is similar when taking into account the standard deviation. This observation is confirmed to

an even higher extent in anaerobic cultivation. Here, the mother cells attain an OD$_{600}$ of ∼2, whereas the daughter cells and the heterogeneous culture are at about ∼2.4, which is 17% lower after 80 h of cultivation time (Figure 4C). Again, the cells have to adapt to the new growing conditions during the lag phase, but the growth rate of the daughter cells ($\mu_{max} = 0.01853 \pm 0.00017$ h^{-1}) is 51% higher compared to the mother cells ($\mu_{max} = 0.00907 \pm 0.00045$ h^{-1}), indicating a huge influence of cell age on fermentation performance. Again, the initial yeast population is between the two other cell fractions in terms of growth rate. The difference in growth rates during aerobic cultivation is less pronounced, as the ATP production due to the respiratory

chain is faster and easier and, therefore, more difficult to analyse. Here, 34 ATP molecules are produced for one glucose molecule, whereas in anaerobic conditions, energy production is more complex, and only two ATP molecules are produced per molecule of glucose.[66] The older a cell is, the more energy-consuming cell waste accumulates, for example, defective proteins, mitochondria, or extrachromosomal ribosomal tRNA.[67]

Young cells, on the other hand, save this energy, which enables them to grow faster.[68,69] The difference in daughter cell content after 84 h of cultivation time might be due to the lag-behind of the mother cell cultivation, being in transition from exponential to stationary growth (Figure 4A). These results indicate that besides high viability, age also plays a crucial role in cultivation performance, as daughter cells grow faster and more efficiently under aerobic and anaerobic conditions, mainly due to their energy management and stress resistance. In future studies, this fast, non-invasive magnetic batch separation method will enable investigation of the impact of young and old yeast cells in terms of age and the synthesis of bioproducts like ergosterol or fatty acid production. Due to the method of yeast separation based on their chitin-containing bud scars, this approach can be transferred to all other yeast strains to study protein or chemical synthesis. By using an inoculum with more daughter cells, it will be possible to increase the efficiency of yeast-based processes in the brewing or pharmaceutical industry.

4 | CONCLUSION

In a controlled fermentation process, a defined relationship between the quantity of daughter and mother cells is of equal importance to good viability. It was shown that yeast cultivation with low viability but high daughter cell content (0.71% ± 0.04%) results in the same cultivation behaviour as yeast with good viability and low daughter cell content (0.41% ± 0.05%). A low quotient of both cell types with low viability has a negative impact. To obtain a good quotient for cultivation, aerobic cultivation of low-viability yeast is necessary, as previously used in practical processes.[70] Thus, good viability and a good quotient between daughter and mother cells can be determined after 60–72 h of aerobic cultivation. This paper presents a method of magnetic batch separation that enables fast and simple isolation of daughter and mother cells in a non-invasive process. Age-dependent labelling of the yeast cell with EDTA-functionalised iron oxide nanoparticles via the linker protein is specific, as the agglomerates bind directly to the bud scars. This approach enabled growth studies with increased and decreased daughter cell fractions to be performed. It is shown that the growth rate of an aerobic daughter-cell-inoculated culture is 22% higher than a mother-cell-inoculated one. Under anaerobic conditions, where the energy production is more complex, the difference in growth rates is 51%, showing that daughter cells are able to grow perceptibly faster. These findings form the basis on which to improve the process efficiency of the yeast-cultivating industries by increasing daughter cell content.

AUTHOR CONTRIBUTIONS

Marco Eigenfeld, Leonie Wittmann, Roland Kerpes, Sebastian P. Schwaminger, and Thomas Becker conceptualised the research; Marco Eigenfeld and Leonie Wittmann performed the experiments. Marco Eigenfeld and Leonie Wittmann conducted the data analysis and interpretation. Marco Eigenfeld and Leonie Wittmann wrote the manuscript. Roland Kerpes and Sebastian P. Schwaminger coordinated the research. Marco Eigenfeld, Leonie Wittmann, Roland Kerpes, Sebastian P. Schwaminger, and Thomas Becker revised and discussed the manuscript.

CONFLICT OF INTEREST STATEMENT
The authors declare that they have no competing interests.

DATA AVAILABILITY STATEMENT
The raw datasets generated during the current study are available on the flowrepository webpage as entry FR-FCM-Z6Y7.

ORCID
Marco Eigenfeld https://orcid.org/0000-0001-8026-4468
Leonie Wittmann https://orcid.org/0000-0002-3993-2089
Roland Kerpes https://orcid.org/0000-0002-1690-1917
Sebastian P. Schwaminger https://orcid.org/0000-0002-8627-0807
Thomas Becker https://orcid.org/0000-0001-6842-8300

REFERENCES

1. You, S. K., Joo, Y.-C., Kang, D. H., Shin, S. K., Hyeon, J. E., Woo, H. M., Um, Y., Park, C., & Han, S. O. (2017). Enhancing fatty acid production of *Saccharomyces cerevisiae* as an animal feed supplement. *Journal of Agricultural and Food Chemistry*, *65*, 11029–11035.
2. Hu, Y., Zhu, Z., Nielsen, J., & Siewers, V. (2019). Engineering *Saccharomyces cerevisiae* cells for production of fatty acid-derived biofuels and chemicals. *Open Biology*, *9*, 190049–190049.
3. Das, S., & Tamang, J. P. (2021). Changes in microbial communities and their predictive functionalities during fermentation of toddy, an alcoholic beverage of India. *Microbiological Research*, *248*, 126769.
4. Chisti, Y. (2020). Food, fermentation, and microorganisms. *Biotechnology Advances*, *43*, 107604.
5. Shi, S., Ji, H., Siewers, V., & Nielsen, J. (2015). Improved production of fatty acids by *Saccharomyces cerevisiae* through screening a cDNA library from the oleaginous yeast *Yarrowia lipolytica*. *FEMS Yeast Research*, *16*, https://doi.org/10.1093/femsyr/fov108
6. Yu, T., Zhou, Y. J., Wenning, L., Liu, Q., Krivoruchko, A., Siewers, V., Nielsen, J., & David, F. (2017). Metabolic engineering of *Saccharomyces cerevisiae* for production of very long chain fatty acid-derived chemicals. *Nature Communications*, *8*, 15587.

7. Serrano, R., Kielland-Brandt, M. C., & Fink, G. R. (1986). Yeast plasma membrane ATPase is essential for growth and has homology with (Na+ + K+), K+- and Ca2+-ATPases. *Nature*, *319*, 689.

8. Imai, T., & Ohno, T. (1995). The relationship between viability and intracellular pH in the yeast *Saccharomyces cerevisiae*. *Applied and Environmental Microbiology*, *61*, 3604–3608.

9. Krieger-Weber, S. (2009). Application of yeast and bacteria as starter cultures. In H. König, G. Unden, & J. Fröhlich (Eds.), *Biology of microorganisms on grapes, in must and in wine* (pp. 489–511). Springer Berlin Heidelberg.

10. Pires, E., & Brányik, T. (2015). By-products of beer fermentation. In *Biochemistry of beer fermentation* (pp. 51–80). Springer International Publishing.

11. Powell, C., Quain, D., & Smart, K. (2003). The impact of brewing yeast cell age on fermentation performance, attenuation and flocculation. *FEMS Yeast Research*, *3*, 149–157.

12. Leupold, S., Hubmann, G., Litsios, A., Meinema, A. C., Takhaveev, V., Papagiannakis, A., Niebel, B., Janssens, G., Siegel, D., & Heinemann, M. (2019). *Saccharomyces cerevisiae* goes through distinct metabolic phases during its replicative lifespan. *eLife*, *8*, e41046.

13. Litsios, A., Ortega, Á. D., Wit, E. C., & Heinemann, M. (2018). Metabolic-flux dependent regulation of microbial physiology. *Current Opinion in Microbiology*, *42*, 71–78.

14. Eigenfeld, M., Kerpes, R., & Becker, T. (2021). Understanding the impact of industrial stress conditions on replicative aging in *Saccharomyces cerevisiae*. *Frontiers in Fungal Biology*, *2*, https://doi.org/10.3389/ffunb.2021.665490

15. Kong, Y., Zhao, Y., Yu, Y., Su, W., Liu, Z., Fei, Y., Ma, J., & Mi, L. (2022). Single cell sorting of young yeast based on label-free fluorescence lifetime imaging microscopy. *Journal of Biophotonics*, 1–10.

16. Kaeberlein, M., Kirkland, K. T., Fields, S., & Kennedy, B. K. (2005). Genes determining yeast replicative life span in a long-lived genetic background. *Mechanisms of Ageing and Development*, *126*, 491–504.

17. Stumpferl, S. W., Brand, S. E., Jiang, J. C., Korona, B., Tiwari, A., Dai, J., Seo, J.-G., & Jazwinski, S. M. (2012). Natural genetic variation in yeast longevity. *Genome Research*, *22*, 1963–1973.

18. Chen, K., Shen, W., Zhang, Z., Xiong, F., Ouyang, Q., & Luo, C. (2020). Age-dependent decline in stress response capacity revealed by proteins dynamics analysis. *Scientific Reports*, *10*, 15211.

19. Mortimer, R. K., & Johnston, J. R. (1959). Life span of individual yeast cells. *Nature*, *183*, 1751–1752.

20. Fehrmann, S., Paoletti, C., Goulev, Y., Ungureanu, A., Aguilaniu, H., & Charvin, G. (2013). Aging yeast cells undergo a sharp entry into senescence unrelated to the loss of mitochondrial membrane potential. *Cell Reports*, *5*, 1589–1599.

21. Powell, C. D., Van Zandycke, S. M., Quain, D. E., & Smart, K. A. (2000). Replicative ageing and senescence in *Saccharomyces cerevisiae* and the impact on brewing fermentations. *Microbiology (Reading, England)*, *146*, 1023–1034.

22. Lee, J. W., Ong, T. G., Samian, M. R., Teh, A.-H., Watanabe, N., Osada, H., & Ong, E. B. B. (2021). Screening of selected ageing-related proteins that extend chronological life span in yeast Saccharomyces cerevisiae. *Scientific Reports*, *11*, 24148.

23. Kwon, Y.-Y., Kim, S.-S., Lee, H.-J., Sheen, S.-H., Kim, K. H., & Lee, C.-K. (2019). Long-living budding yeast cell subpopulation induced by ethanol/acetate and respiration. *The Journals of Gerontology: Series A*, *75*, 1448–1456.

24. Fabrizio, P., Gattazzo, C., Battistella, L., Wei, M., Cheng, C., Mcgrew, K., & Longo, V. D. (2005). Sir2 blocks extreme life-span extension. *Cell*, *123*, 655–667.

25. Burtner, C. R., Murakami, C. J., Kennedy, B. K., & Kaeberlein, M. (2009). A molecular mechanism of chronological aging in yeast. *Cell Cycle (Georgetown, Tex.)*, *8*, 1256–1270.

26. Kalayu, G. (2019). Serial re-pitching: Its effect on yeast physiology, fermentation performance, and product quality. *Annals of Microbiology*, *69*, 787–796.

27. Mochaba, F., O'Connor-Cox, E. S. C., & Axcell, B. C. (1998). Practical procedures to measure yeast viability and vitality prior to pitching. *Journal of the American Society of Brewing Chemists*, *56*, 1–6.

28. Aranda, A., Orozco, H., Picazo, C., & Matallana, E. (2019). Yeast life span and its impact on food fermentations. *Fermentation*, *5*, 37.

29. Angelini, A., Chen, T., de Picciotto, S., Yang, N. J., Tzeng, A., Santos, M. S., Van Deventer, J. A., Traxlmayr, M. W., & Wittrup, K. D. (2015). Protein engineering and selection using yeast surface display. *Methods in Molecular Biology*, *1319*, 3–36.

30. Yanakieva, D., Elter, A., Bratsch, J., Friedrich, K., Becker, S., & Kolmar, H. (2020). FACS-based functional protein screening via microfluidic co-encapsulation of yeast secretor and mammalian reporter cells. *Scientific Reports*, *10*, 10182.

31. Drescher, H., Weiskirchen, S., & Weiskirchen, R. (2021). Flow cytometry: A blessing and a curse. *Biomedicines*, *9*, 1613.

32. Eigenfeld, M., Kerpes, R., Whitehead, I., & Becker, T. (2022). Autofluorescence prediction model for fluorescence unmixing and age determination. *Biotechnology Journal*, *17*, 2200091.

33. Woldringh, C. L., Fluiter, K., & Huls, P. G. (1995). Production of senescent cells of *Saccharomyces cerevisiae* by centrifugal elutriation. *Yeast*, *11*, 361–369.

34. Berovic, M., Berlot, M., Kralj, S., & Makovec, D. (2014). A new method for the rapid separation of magnetized yeast in sparkling wine. *Biochemical Engineering Journal*, *88*, 77–84.

35. Tagizadeh, S.-M., Ebrahiminezhad, A., Ghoshoon, M. B., Dehshahri, A., Berenjian, A., & Ghasemi, Y. (2022). Impacts of magnetic immobilization on the growth and metabolic status of recombinant Pichia pastoris. *Molecular Biotechnology*, *64*, 320–329.

36. Safarik, I., Maderova, Z., Pospiskova, K., Baldikova, E., Horska, K., & Safarikova, M. (2015). Magnetically responsive yeast cells: Methods of preparation and applications. *Yeast*, *32*, 227–237.

37. Firoozi, F. R., Raee, M. J., Lal, N., Ebrahiminezhad, A., Teshnizi, S. H., Berenjian, A., & Ghasemi, Y. (2022). Application of magnetic immobilization for ethanol biosynthesis using Saccharomyces cerevisiae. *Separation Science and Technology*, *57*, 777–787.

38. Hendrickson, D. G., Soifer, I., Wranik, B. J., Kim, G., Robles, M., Gibney, P. A., & Mcisaac, R. S. (2018). A new experimental platform facilitates assessment of the transcriptional and chromatin landscapes of aging yeast. *eLife*, *7*, e39911.

39. Eigenfeld, M., Wittmann, L., Kerpes, R., Schwaminger, S., & Becker, T. (2023). Quantification methods of brewer's and pharmaceutical yeast cells' viability: Accuracy and impact of nanoparticles. *Analytical and Bioanalytical Chemistry*.

40. Eigenfeld, M., Kerpes, R., & Becker, T. (2021). Recombinant protein linker production as a basis for non-invasive determination of single-cell yeast age in heterogeneous yeast populations. *RSC Advances*, *11*, 31923–31932.

41. Turrina, C., Berensmeier, S., & Schwaminger, S. P. (2021). Bare iron oxide nanoparticles as drug delivery carrier for the short cationic peptide Lasioglossin. *Pharmaceuticals*, *14*, 405.

42. Wittmann, L., Turrina, C., & Schwaminger, S. P. (2021). The effect of pH and viscosity on magnetophoretic separation of iron oxide nanoparticles. *Magnetochemistry*, *7*, 80.

43. Salman, D., Juzsakova, T., Al-Mayyahi, M. A., Ákos, R., Mohsen, S., Ibrahim, R. I., Mohammed, H. D., Abdullah, T. A., Domokos, E., & Korim, T. (2021). Synthesis, surface modification and characterization of magnetic $Fe_3O_4@SiO_2$ core-shell nanoparticles. *Journal of Physics: Conference Series*, *1773*, 012039.

44. R Core Team. (2013). *R Foundation for Statistical Computing*.

45. Filzmoser, P., & Geschwandtner, M. (2018). mvoutlier: multivariate outlier detection.

46. Cook, R. D. (1977). Detection of influential observation in linear regression. *Technometrics*, *19*, 15–18.

47. Hardin, J. W., & Hilbe, J. M. (2007). *Generalized linear models and extensions*, Stata Press.

48. Dejean, L., Beauvoit, B., Alonso, A.-P., Bunoust, O., Guérin, B., & Rigoulet, M. (2002). cAMP-induced modulation of the growth yield of Saccharomyces cerevisiae during respiratory and respiro-fermentative metabolism. *Biochimica et Biophysica Acta (BBA) – Bioenergetics*, *1554*, 159–169.

49. Narziß, L. (2017). *Abriss der Bierbrauerei*. Wiley-VCH.

50. Wang, Y., Lo, W.-C., & Chou, C.-S. (2017). A modeling study of budding yeast colony formation and its relationship to budding pattern and aging. *PLoS Computational Biology*, *13*, e1005843.

51. Liu, P., Young, T. Z., & Acar, M. (2015). Yeast replicator: A high-throughput multiplexed microfluidics platform for automated measurements of single-cell aging. *Cell Reports*, *13*, 634–644.

52. Horkai, D., & Houseley, J. (2022). Dietary change without caloric restriction maintains a youthful profile in ageing yeast. *bioRxiv*, 2022.07.19.500645.

53. Frenk, S., Pizza, G., Walker, R. V., & Houseley, J. (2017). Aging yeast gain a competitive advantage on non-optimal carbon sources. *Aging Cell*, *16*, 602–604.

54. Soares Rodrigues, C. I., Den Ridder, M., Pabst, M., Gombert, A. K., & Wahl, S. A. (2023). Comparative proteome analysis of different Saccharomyces cerevisiae strains during growth on sucrose and glucose. *Scientific Reports*, *13*, 2126.

55. Fang, Y., Wang, X., Yang, D., Lu, Y., Wei, G., Yu, W., Liu, X., Zheng, Q., Ying, J., & Hua, F. (2021). Relieving cellular energy stress in aging, neurodegenerative, and metabolic diseases, SIRT1 as a therapeutic and promising node. *Frontiers in Aging Neuroscience*, *13*, https://doi.org/10.3389/fnagi.2021.738686

56. Houtkooper, R. H., Mouchiroud, L., Ryu, D., Moullan, N., Katsyuba, E., Knott, G., Williams, R. W., & Auwerx, J. (2013). Mitonuclear protein imbalance as a conserved longevity mechanism. *Nature*, *497*, 451–457.

57. Liu, S., Yu, B., Wang, S., Shen, Y., & Cong, H. (2020). Preparation, surface functionalization and application of Fe3O4 magnetic nanoparticles. *Advances in Colloid and Interface Science*, *281*, 102165.

58. Katz, E. (2020). Magnetic nanoparticles. *Magnetochemistry*, *6*, 6.

59. Weigert, C., Steffler, F., Kurz, T., Shellhammer, T. H., & Methner, F.-J. (2009). Application of a short intracellular pH method to flow cytometry for determining Saccharomyces cerevisiae vitality. *Applied and Environmental Microbiology*, *75*, 5615–5620.

60. Zakhartsev, M., & Reuss, M. (2018). Cell size and morphological properties of yeast Saccharomyces cerevisiae in relation to growth temperature. *FEMS Yeast Research*, *18*, https://doi.org/10.1093/femsyr/foy052

61. Turner, J. J., Ewald, J. C., & Skotheim, J. M. (2012). Cell size control in yeast. *Current Biology*, *22*, R350–R359.

62. Janssens, G. E., & Veenhoff, L. M. (2016). The natural variation in lifespans of single yeast cells is related to variation in cell size, ribosomal protein, and division time. *PLoS ONE*, *11*, e0167394.

63. Stahl, G., Salem, S. N. B, Chen, L., Zhao, B., & Farabaugh, P. J. (2004). Translational accuracy during exponential, postdiauxic, and stationary growth phases in Saccharomyces cerevisiae. *Eukaryotic Cell*, *3*, 331–338.

64. Cheng, Y., Du, Z., Zhu, H., Guo, X., & He, X. (2016). Protective effects of arginine on Saccharomyces cerevisiae against ethanol stress. *Scientific Reports*, *6*, 31311–31311.

65. Dauer, R. R., & Dunlop, E. H. (1991). High gradient magnetic separation of yeast. *Biotechnology and Bioengineering*, *37*, 1021–1028.

66. Stewart, G. G. (2017). The structure and function of the yeast cell wall, plasma membrane and periplasm. In *Brewing and distilling yeasts* (pp. 55—75). Springer International Publishing.

67. Sinclair, D. A., & Guarente, L. (1997). Extrachromosomal rDNA circles – A cause of aging in yeast. *Cell*, *91*, 1033–1042.

68. Jazwinski, S. M. (2005). Yeast longevity and aging – The mitochondrial connection. *Mechanisms of Ageing and Development*, *126*, 243–248.

69. Mcfaline-Figueroa, J. R., Vevea, J., Swayne, T. C., Zhou, C., Liu, C., Leung, G., Boldogh, I. R., & Pon, L. A. (2011). Mitochondrial quality control during inheritance is associated with lifespan and mother-daughter age asymmetry in budding yeast. *Aging Cell*, *10*, 885–895.

70. Nielsens, O. (2010). Status of the yeast propagation process and some aspects of propagation for re-fermentation. *Cerevisia*, *35*, 71–74.

SUPPORTING INFORMATION

Additional supporting information can be found online in the Supporting Information section at the end of this article.

Supplementary Information

1. Methods:

Media composition:

Yeast-peptone-dextrose medium (YPD): 10 g/L Bacto^{TM} yeast extract, 20 g/L bacto peptone, 20 g/L glucose

Sugar composition determination in wort:

Sugar composition in liquid samples was analyzed by high-performance anion-exchange liquid chromatography with pulsed amperometric detection (HPAEC-PAD) using Dionex ICS 5000 HPLC system (Thermo Fischer Scientific, USA) and an in-house method. Obtained retention times and peak areas were compared to an internal standard and quantified by Chromeleon 6.0 software (Thermo Fisher Scientific, USA).

Wort:

Sugar	Peak area count [-] 1st measurement	Peak area count [-] 2nd measurement	Mean value of sugar [mg/L]
Glucose	727.841	712.785	722.8±7.5
Fructose	184.146	131.910	166.7±26.1
Saccharose	277.210	282.314	278.9±2.5
Maltose	1919.966	1757.933	1865.9±81.0
Maltotriose	746.739	684.822	726.1±30.9
Sum	3855.902	3569.765	3760.5±143.0

Fluorescence-coupled flow cytometry

Flow cytometric determination of age fraction is a new possibility to understand the effect of single-cell age on fermentation behavior. We measured the fluorescence intensities of unstained yeast cells and bud scar-stained yeast cells (using His6-Sumo-sfGFP-ChBD) using a Cytoflex cytometer (Beckman Coulter) equipped with an argon–ion laser (15 mW laser power with an

1

excitation wavelength of 488 nm). The bud scar fluorescence was detected on the FL1 channel (525 nm) with at least 20000 cells in each analysis (sample flow: maximum 100 events/s; gain: 500). The other detectors (585, 660, and 780 nm) were measured as signals for autofluorescence calculation. Each bud scar distribution measurement of yeast suspension was analyzed in independent triplicate samples, each with a counting of 20000 cells.

Intracellular pH-value (ICP) calibration

For ICP measurement, a calibration curve of fluorescence emission and ICP is required. For ICP calibration, an ICP buffer was used. Figure S1 shows the resulting calibration curves. Using this ICP buffer, the second-degree polynomial regression was calculated to $-0.34925 \ x^2 + 2.59817 \ x + 1.71693$, with $R^2 = 0.9737$. Due to a lack of the presence of fluorescence quotients of >3.5, a second-degree polynomial is valid.

Determination of yeast cell viability and vitality

5-Carboxy-fluoresceindiacetate (CFDA) is a known fluorophore used for yeast vitality determination in flow cytometry [1]. It is a nonfluorescent compound that passes through the yeast cell membrane and gets hydrolyzed by esterase to the green fluorescent compound fluorescein. Thus, living cells exhibit green fluorescence [2], and nonviable cells and cells with compromised membrane lack fluorescence and exhibit only autofluorescence signals [3]. In this study, the viable and nonviable cells were classified using CFDA at different pH values and a random forest model, as published earlier [4], exemplarily shown in Figure S2. Yeast vitality was determined using the calibration curve for pH-dependent fluorescence behavior in Figure S1 for both whole and viable part of a population (Figure S3).

2

Determination of ICP

The ICP of the yeast population was determined based on experiments described by Imai& Ohno [5] and Weigert et al. [6]. Sample preparation was conducted on ice. Briefly, 2 mL of the yeast suspension (optical density at 600 nm (OD_{600}) = 1) was centrifuged at 7000 $\times g$ for 3 min, and the supernatant was discarded. The cells were washed three times in ICP buffer (McIlvaine buffer with pH 3 and containing additional 110 mM sodium chloride, 5 mM potassium chloride, and 1 mM magnesium chloride) and then resuspended in 2 mL of ICP buffer. Next, 50 μL of the suspension was made up to 2 mL with ICP buffer. In contrast to Weigert et al. [6], after adding 2 μL of CFDA solution (10 mM in Dimethylsulfoxide), the mixture was incubated at 30°C for 10 min instead of 30 min, protected from light. The subsequent measurement was conducted using a flow cytometer, as described earlier. Measurements for the calibration curve were conducted by incubating superdex beads at different pH values in a loading buffer, as described by Weigert et al. [6]. To each superdex particle-containing buffer, a constant concentration of Carboxyfluorescein was added.

Cultivation experiments with different cell viabilities

For the anaerobic cultivation test, 200 mL of YPD medium (pH 6.0) was inoculated into a sample of 10^7 cells/mL in a 300 mL flask with a removable fermentation tube and stored at 12°C. Additionally, a magnetic stirrer was used at 130 rpm to avoid cell sedimentation. The sample was monitored out every 12 h. First, yeast viability, vitality, and replicative cell age distribution were determined by flow cytometry, pH using a pH-meter, and OD_{600}.

For the aerobic cultivation test, 100 mL of YPD medium (pH 6.0) was inoculated into a sample of 1.5×10^7 cells/mL in a 300 mL flask with baffles and agitated with a frequency of 130 rpm at 12°C. Samples were collected every 12 h and subsequent yeast viability, vitality, replicative cell age distribution, pH, and optical density were measured. The following three yeast cultures

3

were compared: (I) high-viability yeast, resulting from a 1 day culture that was obtained from a freshly grown yeast colony and 1 day aerobic cultivation; (II) low-viability yeast that was grown from dry yeast of the strain TUM34/70; therefore, dry yeast was equilibrated in an isotonic solution (ringer solution) for 1 h and then used as inoculum; and (III) yeast sample with an optimal daughter/mother cell relationship grown by aerobic cultivation for 60 h, which was immediately used as inoculum.

After inoculation with yeast cells of good (93.5% ± 0.4%) or poor (20.1% ± 3.1%) viability, samples were collected after 6, 12, 24, 36, 48, 60, 72, 84, and 96 h. Replicative cell age, yeast viability, vitality, optical density, and pH value were analyzed. Replicative cell age distribution was determined by measuring the fluorescence intensity of yeast cells using stained bud scars, followed by autofluorescence prediction using the random forest model. Subsequent autofluorescence subtraction resulted in fluorescence intensity distribution, allowing the determination of age fraction content.

4

2. Results and Discussion:

Yeast vitality determination

First, we focused on yeast cell vitality, measured using ICP, as vitality is interconnected to viability (compare Figure S2 and S3). Correlation analysis between yeast viability and mean vitality of highly viable cells (93.5% $\pm$ 0.4% viability) resulted in an R^2 value of 0.921, and that between less viable cells (20.1% $\pm$ 3.1% viability) resulted in an R^2 value of 0.978. Hence, regarding vitality, highly viable cells have a mean value of 6.274 $\pm$ 0.055, and less viable ones have a mean value of 6.160 $\pm$ 0.139. In the case of low viability, the median vitality decreases due to the increased dead cell count. However, yeast populations' ICP results in a bimodal distribution (Figure S3). These results indicate that the ICP of yeast cells is constant until they die, decreasing to the extracellular pH value.

Particle characterization

The silica coating and the amine groups on the shell surface of the nanoparticles can be verified due to Fourier-transform infrared spectroscopy (FT-IR) (Figure S6 B). The peak positioned at 592 1/cm is caused by Fe-O-Si vibrations, thus confirming that silica has bound to the iron oxide core. The absorption band at 448 1/cm is characteristic for Si-O vibration, and the band at 794 1/cm is caused by Si-O bending. Furthermore, the peak at 1054 1/cm represents the Si-O-Si stretching vibrations [7, 8]. Bands at 1488 and 1638 1/cm correspond to N-H bending vibrations of amine groups, indicating the successful functionalization with amine groups due to the addition of (3-aminopropyl)triethxysilane (APTES) [7]. The successful formation of amide bonds due to the binding of ethylenediaminetetraacetic acid (EDTA) is visible by the disappearance of the N-H bending vibration at 1488 1/cm [9]. Additionally, the asymmetrical and symmetrical COO- stretching vibrations, located at 1570-1610 1/cm and 1350-1450 1/cm, respectively, verify the presence of the bound EDTA [10]. Both spectra are normalized in accordance with the Fe-O-Si stretching vibration for better comparability.

5

The EDTA-functionalized iron oxide nanoparticles exhibit a high colloidal stability due to the silica coating. Figure S6 A shows a transmission electron microscopy (TEM) image, where the homogeneous coating encapsulates several iron oxide particles. The primary diameter is 142.44 ± 28.16 nm, whereas the hydrodynamic diameter is 227.40 ± 5.57 nm, which implies a low agglomeration level in the liquid phase (Figure S6 A, C, and D). The polydispersity factor of 0.09986 ± 0.0178 confirms the monomodal behavior of the nanoparticle distribution as well. However, with the presence of the linker-protein in solution, uniform agglomerates up to 1000 nm are formed by having a maximum linker-protein adsorption capacity of 0.0877 ± 0.0062 $g_{Linker-protein}/g_{Particle}$ (compare Figure S6 D, and F). The same behavior was seen by Schwaminger et al. with a modified GFP protein [11]. The barrel shape of the protein includes mainly β-sheets and β-turns, which are orientated away from the surface, whereas the His-tag is binding to the nickel-loaded particles. The neutral charge, showing into solution, leads to favored agglomeration according to the DLVO-theory [12, 13]. These agglomerates, binding to the bud scars of the yeast cells, can be magnetically manipulated more efficiently, as the saturation magnetization with 10.07 emu/g is relatively low compared to the one of the bare iron oxide nanoparticles laying between 70 - 80 emu/g [14, 15]. It has to be emphasized that as long as uniform agglomerates are built, as seen in Figure S6 D, they are advantageous for the later magnetic separation process, as the Stoke's drag and Brownian motion are noticeably lower compared to the applied magnetic force.

6
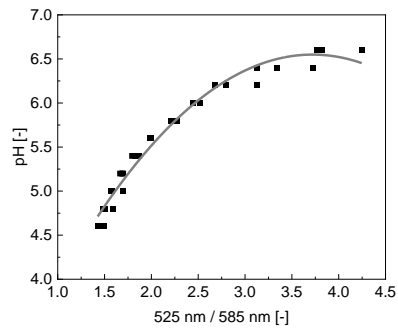
3. Figures:

Figure S1: Calibration curves for intracellular pH value determination. CFDA was transported in superdex particles by diffusion and measured at pH values between 4.6 and 6.6. An evaluation was made by dividing the fluorescence intensities at 525 and 585 nm.
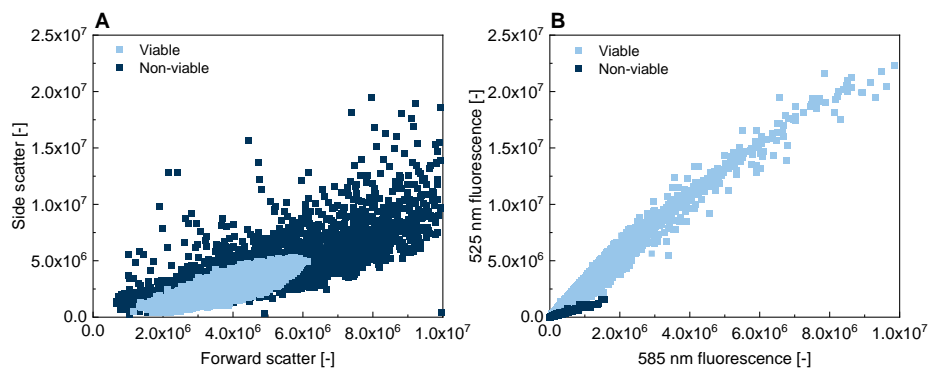

Figure S2: Differentiation between viable and nonviable yeast cells according to their fluorescence behaviour after incubation with CFDA; A: Scatter plot of front scatter and side scatter behaviours; B: Scatter plot of fluorescence signals at 585 and 525 nm; $n_{per\ sample}$ = 22000 particles.

7
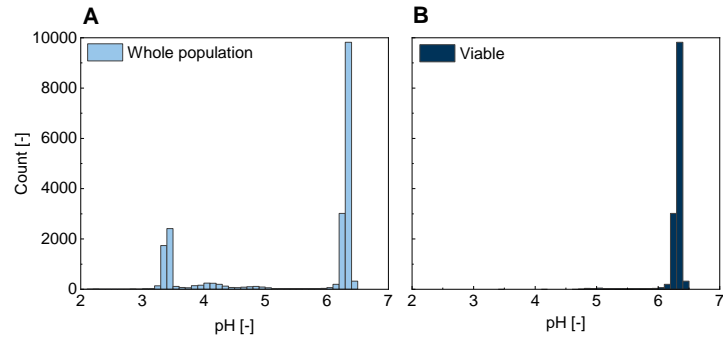
Figure S3: Vitality measurement via ICP for a whole yeast population including dead and viable cells. B: Vitality for only viable cells.
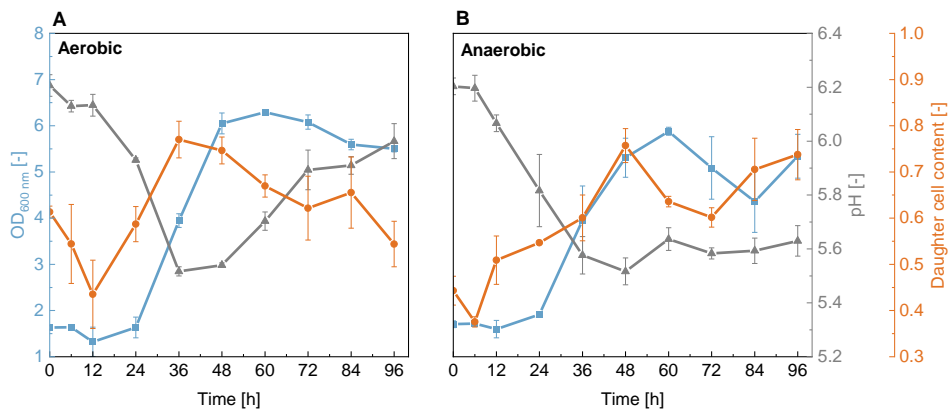
Figure S4: Variation in optical density, pH, and daughter cell content over time in different cultivations; A: Aerobic cultivation, B: Anaerobic fermentation; n = 3, error bars representing the standard deviation of the triplicate measurement.

8
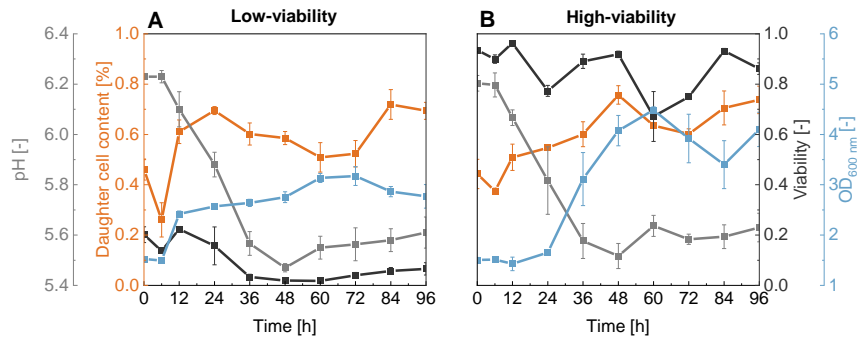
Figure S5: Anaerobic fermentation process. A: Fermentation process of yeast with low viability and a daughter–mother quotient of 1.70, B: High-viability inoculated culture (daughter–mother quotient of 1.47); n =3, error bars representing the standard deviation of the triplicate measurement.

9
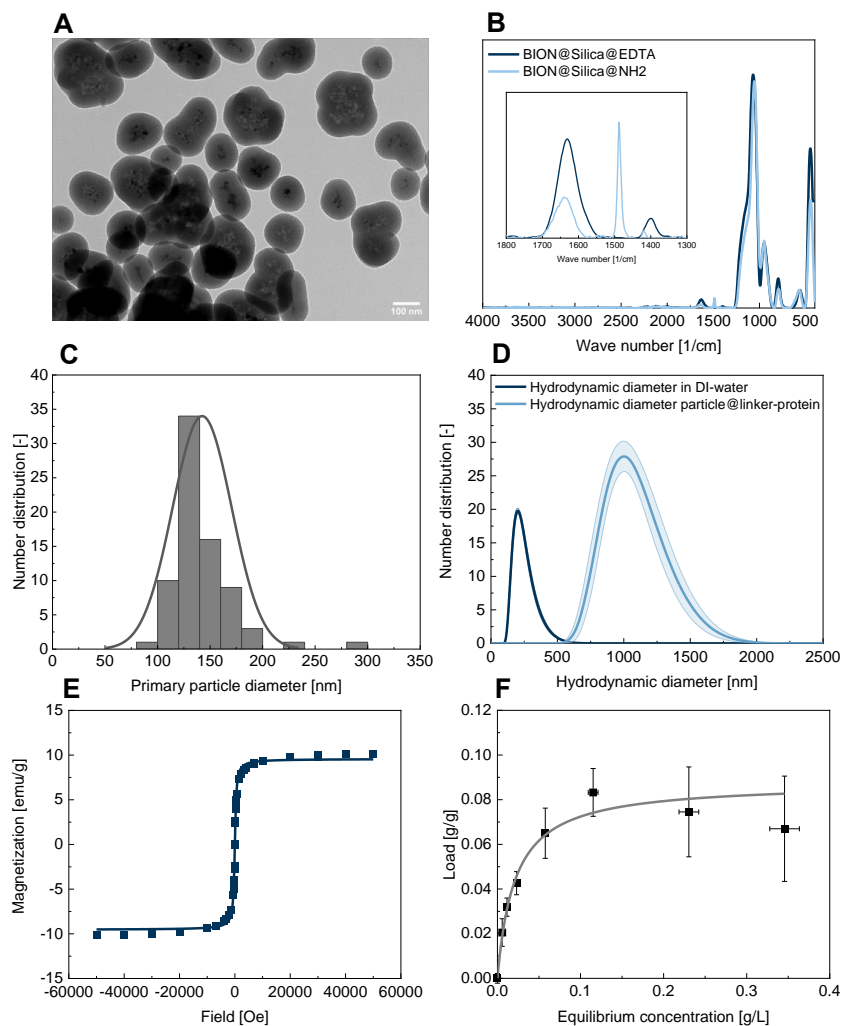
Figure S6: A: TEM image of the EDTA-functionalized iron oxide nanparticles. B: FT-IR spectrum of the first synthesis step, the coating with tetraethylorthosilicate (TEOS) and APTES, resulting in a silica coating with amine groups (light blue) and the second synthesis, forming the amide bonds to covalently bind EDTA on the surface (dark blue). C: Particle size distribution derived from the TEM images with ImageJ (n = 75). D: Number distribution of the hydrodynamic diameter of the EDTA-functionalized iron oxide nanoparticles in DI-water at pH 7 (dark blue) and the one with the adsorbed linker-protein ($c_{Linker-protein}$ = 0.08 g/L) in MOPS buffer at pH 7.3 (light blue). n = 3, $c_{Nanoparticle}$ = 1 g/L. E: Superconducting quantum interference device (SQUID) measurement of the nanoparticles. F: Adsoprtion isotherm of the linker-protein to the nanoparticles (n = 3, error bars representing the standard deviation of the triplicate measurement).

10
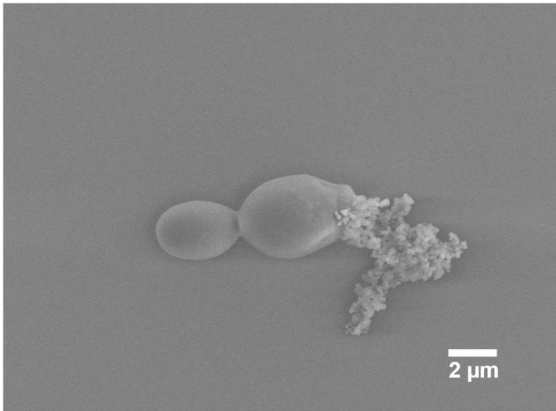
Figure S7: Scanning electron microscopy image of the labelled yeast cells. Magnification 3.4k X, high voltage 5 kV, aperture size 30 µm, distance 7.1 mm.
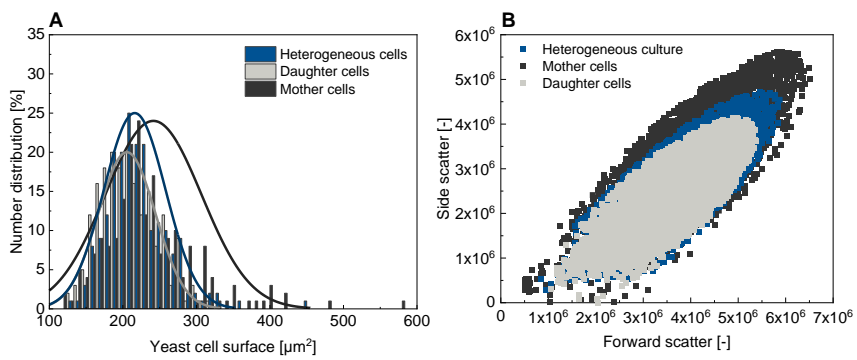
Figure S8: Analysis of the yeast cell surface by microscopy (n = 200) (A) and cytometric analysis (B) of a heterogeneous culture, the mother cell and daughter cell fraction.

11

4. Tables:

Table S1: Age distribution of yeast populations, used for assessing daughter cell variations over time. (n=3, error bars representing the standard deviation of the triplicate measurement)

	Daughter cell content [%]	1st generation mother cell content [-]	2nd generation mother cell content [-]	3rd generation mother cell content [-]	4th generation mother cell content [-]
93.5% viability culture	41.29 ± 4.60	27.96 ± 1.77	14.62 ± 3.36	11.13 ± 3.91	4.59 ± 4.35
20.1% viability culture	41.25 ± 4.04	30.16 ± 5.17	16.59 ± 2.40	9.09 ± 9.42	2.76 ± 1.48
Sample from second half of the exponential growth phase	71.63 ± 3.82	23.84 ± 6.94	5.34 ± 5.39	0	0

12

Table S2: Viability of the aerobic cultivation and the anaerobic fermentation at the start and the end of the process time for a heterogenous culture and the daughter and mother cells of the fractionated culture (n=3, error bars representing the standard deviation of the triplicate measurement)

	Aerobic		Anaerobic	
	Viability t_0 [-]	Viability t_{24} [-]	Viability t_0 [-]	Viability t_{84} [-]
Heterogeneous culture	0.9755 ± 0.0004	0.9906 ± 0.0024	0.9809 ± 0.0008	0.9701 ± 0.0053
Mother cells	0.9265 ± 0.0045	0.9928 ± 0.0005	0.9680 ± 0.0017	0.9630 ± 0.0036
Daughter cells	0.9813 ± 0.0011	0.9888 ± 0.0022	0.9899 ± 0.0007	0.9749 ± 0.0008

Table S3: Vitality of the aerobic cultivation and the anaerobic fermentation at the start and the end of the process time for a heterogenous culture and the daughter and mother cells of the fractionated culture (n=3, error bars representing the standard deviation of the triplicate measurement).

	Aerobic		Anaerobic	
	Vitality t_0 [-]	Vitality t_{24} [-]	Vitality t_0 [-]	Vitality t_{84} [-]
Heterogeneous culture	6.2533 ± 0.0015	6.4837 ± 0.0021	6.2597 ± 0.0005	6.4765 ± 0.0015
Mother cells	6.2740 ± 0.0026	6.4627 ± 0.0031	6.2657 ± 0.0055	6.4923 ± 0.0065
Daughter cells	6.2487 ± 0.0015	6.4760 ± 0.0017	6.2600 ± 0.0061	6.4837 ± 0.0025

13

Table S4: Maximum growth rates of the aerobic cultivation and the anaerobic fermentation at the start and the end of the process time for a heterogenous culture and the daughter and mother cells of the fractionated culture (n=3, error bars representing the standard deviation of the triplicate measurement).

Growth rate	Heterogeneous [1/h]	Daughter cells [1/h]	Mother cells [1/h]
Aerobic	0,03090 ± 0,00215	0,03740 ± 0,00497	0,02927 ± 0,00154
Anaerobic	0,01390 ± 0,00024	0,01853 ± 0,00017	0,00907 ± 0,00045

14

Table S5: Sugar composition of anaerobic cultivation after 84 h of cultivation

Heterogeneous population

Sugar	Peak area count [-] 1st measurement	Peak area count [-] 2nd measurement	Mean value of sugar [mg/L]
Glucose	0	0	0±0
Fructose	18.687	18.593	18.640±0.047
Saccharose	3.203	4.341	3.772±0.569
Maltose	1328.260	1408.352	1368.306±40.046
Maltotriose	480.478	556.608	518.543±38.065

Daughter cell population

Sugar	Peak area count [-] 1st measurement	Peak area count [-] 2nd measurement	Mean value of sugar [mg/L]
Glucose	0	0	0±0
Fructose	9.802	8.243	9.023±0.780
Saccharose	0	0	0±0
Maltose	1871	1130.566	566.219±564.348
Maltotriose	535.834	613.944	574.889±39.055

Mother cell population

Sugar	Peak area count [-] 1st measurement	Peak area count [-] 2nd measurement	Mean value of sugar [mg/L]
Glucose	19.205	29.863	24.534±5.329
Fructose	13.246	15.176	14.211±0.965
Saccharose	15.091	5.821	10.456±4.635
Maltose	1257.921	1190.380	1224.151±33.771
Maltotriose	479.327	516.583	497.955±18.628

15

Table S6: Sugar composition of aerobic cultivation after 24 h of fermentation

Heterogeneous population

Sugar	Peak area count [-] 1st measurement	Peak area count [-] 2nd measurement	Mean value of sugar [mg/L]
Glucose	0	0	0±0
Fructose	15.447	13.946	14.697±0.751
Saccharose	0	0	0±0
Maltose	506.232	558.354	532.293±26.061
Maltotriose	396.455	699.231	547.843±151.388

Daughter cell population

Sugar	Peak area count [-] 1st measurement	Peak area count [-] 2nd measurement	Mean value of sugar [mg/L]
Glucose	0	0	0±0
Fructose	9.541	14.824	12.183±2.642
Saccharose	0	0	0±0
Maltose	1287.945	1318.201	1303.073±15.128
Maltotriose	287.644	321.638	304.641±16.997

Mother cell population

Sugar	Peak area count [-] 1st measurement	Peak area count [-] 2nd measurement	Mean value of sugar [mg/L]
Glucose	0	0	0±0
Fructose	21.663	30.762	26.213±4.550
Saccharose	50.356	39.269	44.813±5.544
Maltose	914.66	842.65	878.655±36.005
Maltotriose	577.210	487.537	532.374±44.837

16

References:

1. Imai, T., I. Nakajima, and T. Ohno, *Development of a New Method for Evaluation of Yeast Vitality by Measuring Intracellular pH.* Journal of the American Society of Brewing Chemists, 1994. **52**(1): p. 5-8.
2. Breeuwer, P., et al., *Characterization of uptake and hydrolysis of fluorescein diacetate and carboxyfluorescein diacetate by intracellular esterases in Saccharomyces cerevisiae, which result in accumulation of fluorescent product.* Applied and environmental microbiology, 1995. **61**(4): p. 1614-1619.
3. Surre, J., et al., *Strong increase in the autofluorescence of cells signals struggle for survival.* Scientific Reports, 2018. **8**(1): p. 12088.
4. Eigenfeld, M., et al., *Quantification methods of brewer's and pharmaceutical yeast cells' viability: Accuracy and impact of nanoparticles.* Accepted.
5. Imai, T. and T. Ohno, *Measurement of yeast intracellular pH by image processing and the change it undergoes during growth phase.* Journal of Biotechnology, 1995. **38**(2): p. 165-172.
6. Weigert, C., et al., *Application of a short intracellular pH method to flow cytometry for determining Saccharomyces cerevisiae vitality.* Applied and Environmental Microbiology, 2009. **75**(17): p. 5615-5620.
7. Hamidon, T.S. and M.H. Hussin, *Susceptibility of hybrid sol-gel (TEOS-APTES) doped with caffeine as potent corrosion protective coatings for mild steel in 3.5 wt.% NaCl.* Progress in Organic Coatings, 2020. **140**: p. 105478.
8. Favela-Camacho, S.E., et al., *How to decrease the agglomeration of magnetite nanoparticles and increase their stability using surface properties.* Colloids and Surfaces A: Physicochemical and Engineering Aspects, 2019. **574**: p. 29-35.
9. Salman, D., et al., *Synthesis, Surface Modification and Characterization of Magnetic $Fe_3O_4@SiO_2$ Core-Shell Nanoparticles.* Journal of Physics: Conference Series, 2021. **1773**(1): p. 012039.
10. Dupont, D., et al., *Selective Uptake of Rare Earths from Aqueous Solutions by EDTA-Functionalized Magnetic and Nonmagnetic Nanoparticles.* ACS Applied Materials & Interfaces, 2014. **6**(7): p. 4980-4988.
11. Schwaminger, S.P., et al., *Design of Interactions Between Nanomaterials and Proteins: A Highly Affine Peptide Tag to Bare Iron Oxide Nanoparticles for Magnetic Protein Separation.* Biotechnology Journal, 2018. **0**(0): p. 1800055.
12. Schwaminger, S.P., et al., *Magnetic one-step purification of His-tagged protein by bare iron oxide nanoparticles.* ACS Omega, 2019. **4**(2): p. 3790-3799.
13. Derjaguin, B., *Untersuchungen über die Reibung und Adhäsion, IV.* Kolloid-Zeitschrift, 1934. **69**(2): p. 155-164.
14. Wittmann, L., C. Turrina, and S.P. Schwaminger, *The Effect of pH and Viscosity on Magnetophoretic Separation of Iron Oxide Nanoparticles.* Magnetochemistry, 2021. **7**(6): p. 80.
15. Turrina, C., S. Berensmeier, and S.P. Schwaminger, *Bare Iron Oxide Nanoparticles as Drug Delivery Carrier for the Short Cationic Peptide Lasioglossin.* Pharmaceuticals, 2021. **14**(5): p. 405.

17

CORRECTION

Studying the impact of cell age on the yeast growth behavior of *Saccharomyces pastorianus* var. *carlsbergensis* by magnetic separation

Eigenfeld Marco | **Wittmann Leonie** | **Kerpes Roland** | **Schwaminger Sebastian** |
Becker Thomas

In the original published article, calculation errors resulted from number transposition and cell reference mistakes, leading to incorrect values. The daughter cell fraction (<95%) showed a 27% higher growth rate in aerobic conditions than the mother cells and a 104% higher rate under anaerobic conditions. Therefore, the initially published values need correction. We apologize for this error.

In the Abstract:

Current: "Magnetic separation results in the daughter cell fraction (<95%) showing a 21% higher growth rate in aerobic conditions than mother cells and a 52% higher rate under anaerobic conditions."

Correction: "Magnetic separation results in the daughter cell fraction (<95%) showing a 27% higher growth rate in aerobic conditions than mother cells and a 104% higher rate under anaerobic conditions."

On page 7:

Current: "… however, comparing the growth rates, shown in Table S4 in the SI, it is clear that under aerobic conditions, the young daughter cells have a 22% higher growth rate …"

Correction: ".. however, comparing the growth rates, shown in Table S4 in the SI, it is clear that under aerobic conditions, the young daughter cells have a 27% higher growth rate …"

On page 8:

Current: "Again, the cells have to adapt to the new growing conditions during the lag phase, but the growth rate of the daughter cells (…) is 51% higher compared to the mother cells (…), …"

Correction: "Again, the cells have to adapt to the new growing conditions during the lag phase, but the growth rate of the daughter cells (…) is 104% higher compared to the mother cells (…), …"

Conclusion section:

Current: "It is shown that the growth rate of an aerobic daughter-cell-inoculated culture is 22% higher than a mother-cell-inoculated one. Under anaerobic conditions, where the energy production is more complex, the difference in growth rates is 51%, showing that daughter cells are able to grow perceptibly faster"

Correction: "It is shown that the growth rate of an aerobic daughter-cell-inoculated culture is 27% higher than a mother-cell-inoculated one. Under anaerobic conditions, where the energy production is more complex, the difference in growth rates is 104%, showing that daughter cells are able to grow perceptibly faster."

A.1.4 Millifluidic Magnetophoresis-based Chip for Age-specific Fractionation: Evaluating the Impact of Age on Metabolomics and Gene Expression in Yeast

Check for updates

Millifluidic magnetophoresis-based chip for age-specific fractionation: evaluating the impact of age on metabolomics and gene expression in yeast†

L. Wittmann, ‡[a] M. Eigenfeld, ‡[bc] K. Büchner, [b] J. Meiler,[a] H. Habisch, [c] T. Madl, [cd] R. Kerpes, *[b] T. Becker, [ce] S. Berensmeier [ae] and S. P. Schwaminger *[acd]

A novel millifluidic process introduces age-based fractionation of *S. pastorianus* var. *carlsbergensis* yeast culture through magnetophoresis. *Saccharomyces* yeast is a model organism for aging research used in various industries. Traditional age-based cell separation methods were labor-intensive, but techniques like magnetic labeling have eased the process by being non-invasive and scalable. Our approach introduces an age-specific fractionation using a 3D-printed millfluidic chip in a two-step process, ensuring efficient cell deflection in the magnetic field and counteracting magnetic induced convection. Among various channel designs, the pinch-shaped channel proved most effective for age differentiation based on magnetically labeled bud scar numbers. Metabolomic analyses revealed changes in certain amino acids and increased NAD$^+$ levels, suggesting metabolic shifts in aging cells. Gene expression studies further underlined these age-related metabolic changes. This innovative platform offers a high-throughput, non-invasive method for age-specific yeast cell fractionation, with potential applications in industries ranging from food and beverages to pharmaceuticals.

A Introduction

Saccharomyces yeast is a valuable model organism for aging research, offering insights into two distinct aging processes: chronological aging, which is defined by the survival time of the cell, and replicative aging, characterized by the number of division events a cell undergoes before reaching senescence. Senescence, a key aging marker, impedes cellular repair and is linked to age-related diseases.[1] The process of asymmetric cell division in yeast, wherein mother cells generate a finite number of daughter cells, presents a unique opportunity to gain a deeper understanding of these aging dynamics.[2]

Numerous studies have investigated cellular aging by analyzing heterogeneous cultures or relying on the variable correlation between cell size and age, often employing a sucrose gradient method.[3–8] However, the direct link between cell age, its metabolome, and gene expression remains a topic of debate, because of the lack of methodology, specifically sorting cells by their replicative age. Recent studies have shown that external factors, such as growth rate and stressors like formic acid, influence yeast metabolic reactions, impacting both oxidative stress response and protein biosynthesis.[6,7] Correia-Melo *et al.* highlighted the connection between metabolism and chronological aging, marked by shifts in intracellular metabolic processes and signaling pathways.[8] Thus, there is a need for a reliable, age-specific fractionation method of yeast cells to advance aging research concerning the replicative lifespan.

Historically, age-based cell separation was labor-intensive, relying on microdissection.[2] Modern microfluidic platforms, leveraging cell size differences or surface adhesion, have simplified this process.[9–11] However, these techniques can be invasive, potentially compromising age-analysis accuracy, and often lack scalability, making growth and omics studies difficult.[12,13] High-throughput technologies, like magnetic

[a] TUM School of Engineering and Design, Chair of Bioseparation Engineering, Technical University of Munich, Boltzmannstr. 15, 85748 Garching, Germany. E-mail: s.schwaminger@tum.de

[b] TUM School of Life Science, Chair of Brewing and Beverage Technology, Technical University of Munich, Weihenstephaner Steig 20, 85354 Freising, Germany. E-mail: roland.kerpes@tum.de

[c] Otto-Loewi Research Center, Division of Medicinal Chemistry, Medical University of Graz, Neue Stiftingtalstr. 6, 8010 Graz, Austria

[d] BioTechMed-Graz, Mozartgasse 12/II, 8010 Graz, Austria. E-mail: sebastian.schwaminger@medunigraz.at

[e] Munich Institute of Integrated Materials, Energy and Process Engineering, Technical University of Munich, Lichtenberstr. 4a, 85748 Garching, Germany

† Electronic supplementary information (ESI) available. See DOI: https://doi.org/10.1039/d4lc00185k

‡ All authors contributed equally.

Paper

labeling, facilitate collecting up to 106 cells per mL.[14–16] The method developed by Hendrickson *et al.* involves biotinylation of the yeast cell wall; however, this modification is not inherited by daughter cells. Consequently, mother cells can bind to streptavidin-coated magnetic beads and are retained by a magnet.[15] However, a fractionation based on distinct age remains absent.

Employing a laminar flow combined with an external magnetic field offers the advantages of being non-invasive and efficient compared to other methods.[17] The primary forces in this process are hydrodynamic drag and magnetophoretic force acting on the entities labeled with magnetic nanoparticles (MNP),[18,19] with the latter defined as,

$$\overrightarrow{F_{\mathrm{M}}} = \left| \overrightarrow{m}\left(\overrightarrow{B} \right) \right| \overrightarrow{\nabla} B = V_{\mathrm{m}} \rho_{\mathrm{m}} \left| \overrightarrow{M}\left(\overrightarrow{B} \right) \right| \overrightarrow{\nabla} B \quad (1)$$

Where $\overrightarrow{\nabla} B$ is the magnetic field gradient within the magnetic field strength B, inducing a magnetic dipole moment $\overrightarrow{m}$. It depends on the volume (V_{m}) and density (ρ_{m}) of the magnetic entity, as well as the volumetric magnetization in solution $\overrightarrow{M}$. Beyond this classical model, two phenomena enhance

magnetophoretic velocity, substantially impacting a magneto-responsive fractionation. The first, cooperative magnetophoresis, arises from the combined motion of interacting magnetic dipoles (Eqn S1 and S2†).[18,20,21] The second is a fluid dynamics instability caused by the magnetic field gradient (Eqn S3†).[19,22,23] The hydrodynamic drag force originates from the Stokes equations, with particles in laminar flow aligning with fluid streamlines based on size due to the inertial force.[24]

Integrating size separation with magnetic bud scar labeling[25,26] offers a promising method for age-based yeast cell fractionation (Fig. 1). Yeast cell bud scars are magnetically labeled using a linker-protein, giving each cell an age-dependent susceptibility (Fig. 2a).[25,26] In designing this millifluidic magnetophoretic process, several critical factors must be considered:

1. The particle concentration has to be regulated to avoid crosslinkage and undesired magnetically induced convective motion of unlabeled cells while ensuring all bud scars are covered.

2. The agglomerates' susceptibility, meaning size, must be substantial enough for magnetic manipulation within the
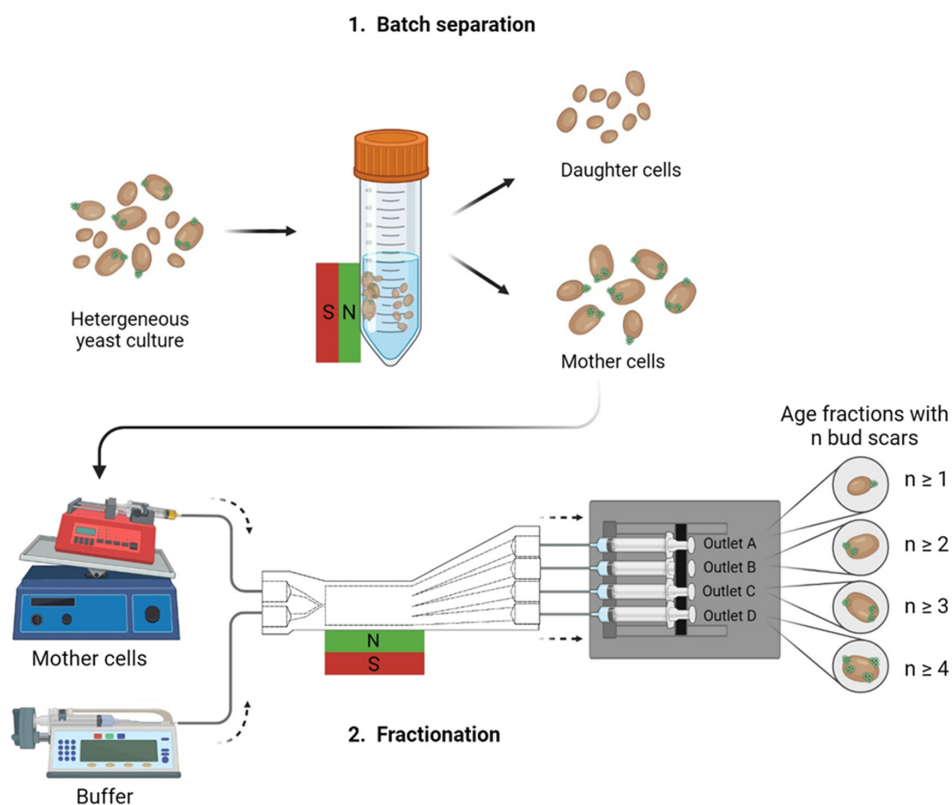

Fig. 1 Millifluidic yeast cell fractionation scheme. The age-dependent fractionation process consisted of a batch separation removing the young, unlabeled daughter cells. The magnetically labeled mother cells were introduced into the chip for further age-based fractionation. Three chip geometries were tested (compare Fig. 4a). Chip outlet A was the furthest away from the magnet; chip outlet D was the nearest one to magnet, consisting of the oldest cells with the highest bud scar number. Further details about the set-up are given in section B.
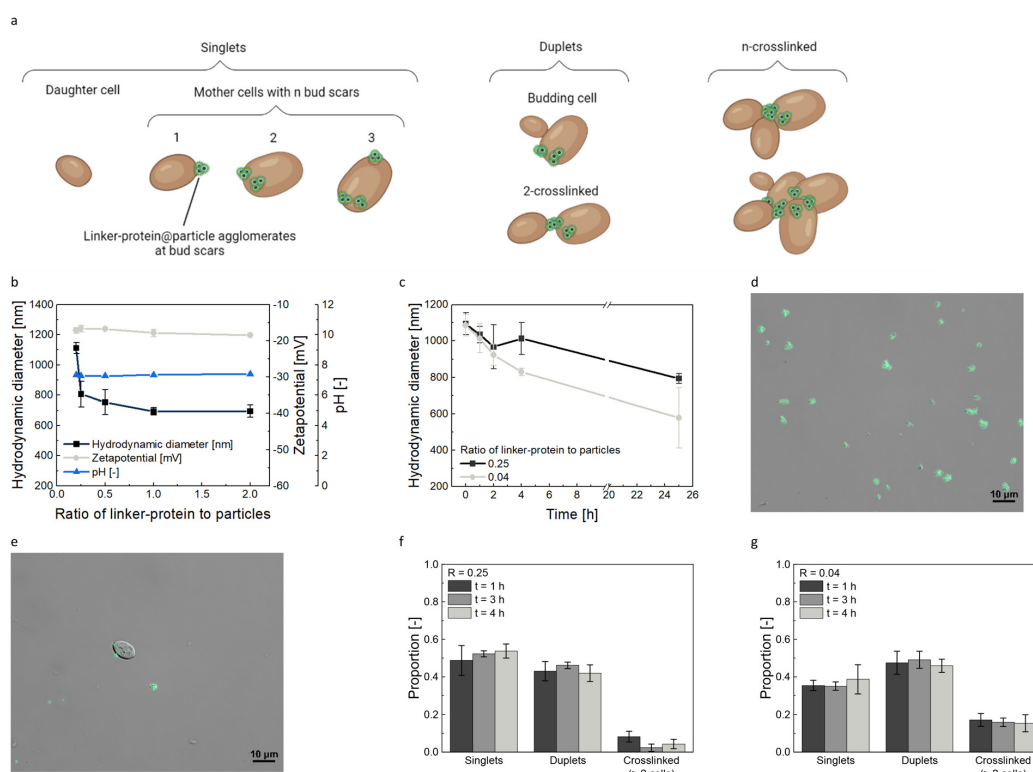
Fig. 2 Yeast cell-nanoparticle binding analysis. Schematic illustration of the magnetic labeling of yeast cell bud scars. Cells possessing n bud scars could bind n agglomerates. Unlike single cells, duplets are composed of either budding cells or a pair of cells crosslinked through the agglomerates. 'n-crosslinked cells' denotes an assembly of more than two cells (a). Hydrodynamic diameter, zeta potential, and pH measurements for different linker-protein to particle ratios in a pH 7.3 buffer after 24 h. While the linker-protein concentration was constant at $c_{\text{Linker-protein}}$ = 0.02 g L^{-1}, the particle concentration varied between c_{Particle} = 0.1 and 0.01 g L^{-1} (b). Hydrodynamic diameter over time for particles combined with linker-protein post-incubation in buffer was evaluated for two linker-protein-particle ratios. The particle concentrations were c_{Particle} = 0.5 and 0.08 g L^{-1} with a consistent linker-protein concentration of $c_{\text{Linker-protein}}$ = 0.02 g L^{-1} (c). Light microscopy image of agglomerates formed by a ratio of linker-protein to particles of R = 0.25 (d). Light microscopy visualization displays the specific binding of the particles labeled yeast cell bud scars (3.17×10^6 cells per mL) via the linker-protein at a R = 0.25 ratio (e). Crosslinkage analysis of magnetically labeled yeast cells (3.17×10^6 cells per mL). The relative distribution of singlets (single cells), duplets (two cells), and crosslinked cells (agglomerates of more than two cells) is presented, corresponding to the ratios as in (b) and observed at 1, 3, and 4 hours after incubation (based on n = 450 cells) (f) and (g). All data plots include the standard deviation from a triplicate measurement.

chip. From eqn (1), the magnetic response is contingent upon the magnetic dipole moment of the magnetic entities, influenced by the agglomerates' size and concentration.[18]

3. The agglomerate size must be consistent throughout the process.

Our study introduces a 3D-printed chip that separates yeast cells by bud scar count, advancing the microfluidic single-cell method to a high-throughput millifluidic platform, giving insights into metabolomics and gene expression.

B Methods

A Synthesis of ethylenediaminetetraacetic acid-functionalized silica coated iron oxide nanoparticles

Iron oxide nanoparticles were synthesized via co-precipitation[27,28] and subsequently coated with silica to increase the colloidal stability. As previously described, the MNPs were further functionalized with EDTA by an amide bonding.[25] Briefly, 179 mg of iron oxide nanoparticles were suspended in 100 mL of Millipore water, ultrasonicated on ice (3 min, 20%, 10 sec on, 15 sec off, 20 kHz, Branson Ultrasonics), mixed with citric acid (Carl Roth, c = 0.029 mol L^{-1}, V = 100 mL, ultrasonicated), and ultrasonicated as before. After 15 min incubation, the pH was adjusted to 11 using tetramethylammonium hydroxide (Sigma Aldrich). The mixture was transferred into a nitrogen-evacuated flask, combined with ethanol (V = 2.72 L, 99%, VWR), Millipore water (V = 0.72 L), ammonia (V = 0.18 L, 25%, Carl Roth), and the prepared MNP solution (V = 0.18 L), with the ethanol being critical to dispense the MNPs and minimize agglomerate size. The synthesis was started by adding 6.94 mL of tetraethyl orthosilicate (TEOS, Sigma Aldrich), forming the silica shell around the MNPs. The reaction was conducted at 4 °C and was

Paper

Lab on a Chip

continuously dispersed *via* ultrasonication (45 kHz, VWR). 1.984 mL (3-Aminopropyl)triethoxysilane (APTES, VWR) was added an hour later to introduce amine groups for the later EDTA functionalization. After another hour, particles were washed by centrifugation (1×, 4600 × g, 30 min) and magnetically (min. 7×) with ethanol until pH = 9.5–9.7 was reached. The washing was continued with degassed Millipore water (minimum 3×) to reach conductivity <150 μS cm^{-1}. Ultrasonication (5 min, 20%, 10 sec on, 15 sec off, Branson Ultrasonics) dispersed the MNPs before under nitrogen storage at 4 °C. The concentration was analyzed *via* gravimetry by drying 300 μL of MNP suspension overnight. The MNPs were functionalized with EDTA *via* amide bonding in a subsequent synthesis. Therefore, 100 mg particles were mixed with EDTA (c = 0.075 mol L^{-1}, V = 100 mL, Carl Roth) and ultrasonicated (132 kHz, Sonorex) at 60 °C for 2 hours. Subsequently, the EDTA-functionalized MNPs were washed with degassed Millipore water below a conductivity of 150 μS cm^{-1} and stored under nitrogen at 4 °C. 'MNP' refers to the EDTA-functionalized silica shell iron oxide nanoparticles in the following.

The magnetization was analyzed with a superconducting quantum interference device (SQUID) (Quantum Design MPMS XL-7) at 300 K (−50–50 kOe) using a minimum of 10 mg freeze-dried MNPs. The data was fitted by the LangevinMod fit in Origin2020. XRD (STOE Sadi-P) of freeze-dried MNPs was performed using a molybdenum source (0.7093 Å, 1 = 0). For transmission electron microscopy (TEM) measurement (JEOL 1400 plus), 10 μL of 0.1 g L^{-1} MNP solution was dried on a discharged carbon-coated copper grid. The images were analyzed *via* the Software ImageJ, and at least 100 particles were analyzed to obtain the primary particle diameter. Thermogravimetric analysis (TGA) (STA 449C Jupiter) was performed between T = 25–700 °C, holding 700 °C for 10 min, using freeze-dried MNPs in a 50 μL aluminum oxide jar. The MNPs were further characterized by Fourier-transform infrared spectroscopy (FT-IR) (Alpha II, Bruker) with a platinum attenuated total reflection module using 24 scans per sample between the wave number range 4000–400 cm^{-1}, subtracting the background by the concave rubber band method. The spectra were normalized to the vibration of the magnetite peak at ~570 cm^{-1}. Dynamic light scattering (DLS) and zeta potential measurements (Zetasizer Ultra, Malvern Panalytical) were conducted at a concentration of 1 g L^{-1} (if not stated otherwise) in water or the corresponding buffer at 25 °C. To determine the isoelectric point, the pH was adjusted by HCl or NaOH 24 h and 1 h before the measurement so that the particles could equilibrate. The data was fitted by using the Boltzmann fit in Origin2020. The magnetophoretic sedimentation velocity was measured by the LUMiReader (4532–123, LUM GmbH) at 630 nm (angle = 0°, light factor 1.00, T = 25 °C, 300 profiles: interval = 10 s, then 100 profiles: interval = 20 sec). Nickel was analyzed *via* induced coupled plasma optical emission spectroscopy (ICP-OES) (Agilent Technologies 700 series ICP-OES). For the adsorption isotherm to nickel, 1 g L^{-1} of MNPs (ultrasonicated, 3 min, 20%, 10 sec on, 15 sec off) were

incubated with nickel chloride hexahydrate (Sigma Aldrich, c = 0.05, 0.03, 0.01, 0.005, 0.001, 0.0005 and 0 mol L^{-1}) for 2 h at 1000 rpm at T = 22 °C. The samples were washed by centrifugation for 10 min at 12 000 × g twice with Millipore water and dispersed *via* ultrasonication (15 min) and pipetting. For investigating the kinetic and leaching behavior, samples were taken after 5, 15, 30, 60, and 120 min and 0, 1, 2, and 5 days, respectively, following the washing procedure as described. The samples were prepared for ICP-OES by dissolving 0.48 mL of labeled MNPs in 20% nitric acid for 2 h at 40 °C. After incubation overnight, the final volume was set to 7 mL, always using Millipore water. The calibration curve was generated using a multi-element standard solution (Sigma Aldrich).

B Yeast cell labeling

The yeast cells were magnetically loaded, as described in Eigenfeld and Wittmann *et al.*[25] Therefore, yeast cells (*Saccharomyces pastorianus* var. *carlsbergensis* TUM34/70) were grown in 15 mL yeast extract peptone dextrose medium, consisting of 10 g L^{-1} yeast extract (VWR), 20 g L^{-1} peptone (Carl Roth), 20 g L^{-1} D-glucose (Merck) at 120 rpm at 22 °C overnight until end-log phase. For labeling, the cells were rebuffered in 20 mM MOPS (pH = 7.3), and 3.17 × 10^7 cells per mL were incubated with 0.4 g L^{-1} linker-protein (*His6-Sumo-sfGFP-ChBD*),[26] enabling the specific labeling of the chitin-enriched yeast cell bud scars. After 30 min at 22 °C at 1000 rpm, the samples were washed twice with buffer at 1000 × g for 2 min. In the meantime, the MNPs were loaded with 0.01 mol L^{-1} nickel chloride hexahydrate for 15 min to form a chelat complex with EDTA. This allows the nanoparticles to form a coordinative bond to the His-tag of the linker-protein. The washing procedure was performed in buffer, and during the last washing step, the MNPs were concentrated to 2 g L^{-1}. Then, the linker-protein labeled yeast cells (c = 1.58 × 10^7 cells per mL) were incubated with the Nickel-loaded MNPs, which have been dispersed by ultrasonication (45 kHz) for 5 min shortly before the mixing (c = 0.4 g L^{-1}) for 1.5 h at 1000 rpm at 22 °C. That ratio was always kept constant, except stated otherwise (see Fig. 2b and c). The specificity of the nanoparticle binding has been verified before.[25] Microscopic images are taken by a Zeiss Axio Observer 7, 100× objective using bright field and fluorescent channels. The extinction wavelength was 480 nm and the emission wavelength was 505 nm. The exposure time for the fluorescent image was set to 1000 ms, for the bright field it was automatic.

C Device design and fabrication

The chip geometries were designed in Autodesk Inventor Professional 2023 and exported as a high-resolution STL file. Subsequently, support structures were added to the printing parts *via* the software Preform Version 3.27.1. The support structure density was 1.0, and the contact point size was set to 0.4 mm, manually removing structures inside the in- and outlets. The parts were printed with a layer of 0.025 mm with

Lab on a Chip

clear resin (Formlabs, RS-F2-GPCL-04) using a Form 3B+ stereolithographic (SLA) 3D printer (Formlabs). The flow channels were placed horizontally and twisted in every direction, and the tubing adapters were printed separately and glued into the chips afterward to facilitate the washing process. The printed parts were rinsed manually with 100%-isopropanol (VWR) using syringes or cannulas to remove the residual uncured resin inside the channels. Afterward, they were placed into an isopropanol bath for 2 hours before curing the structures for 30 min at 60 °C in UV light (Form Cure, Formlabs). The channel height was kept constant at 750 μm for all channels (Fig. S5†). First, we designed the rectangular channel, which was on a centimeter scale in length; however, too many convective and diffusive effects occurred. That is why the trapezoidal and pinch-shaped channels were designed with smaller lengths. Existing literature with similar separation processes was used to design the channels.[29–31] Then, solely yeast cells and only MNPs separately were fractionated to get an indication of the necessary magnetic field strength.

D Process development

The set-up consisted of a sample syringe pump (Legato 110, kdScientific), a buffer syringe pump (Alaris plus GH, Juaramed), and an outlet pump (A-51133, Havard Apparatus) with a manually constructed multi-syringe adapter. The syringes were connected to the chip *via* printed and commercial (Luer female, Reichelt Chemietechnik) adapters and silicone tubings (d_{inside} = 1.3 mm, VWR) to the chip. The chip was first flushed with buffer to start a fractionation process, avoiding bubble formation. Then, the sample pump was started, the pipe was connected to the chip, and the magnet was placed at the defined position. After the equilibration time, the outlet pipes were connected to the running outlet pump. Fraction A refers to the outlet being furthest away from the magnet; fraction D was the one nearest to the magnet. Before each run, the flow channel was flushed and cleaned with buffer to remove bubbles and residual MNPs. For storage, the flow channels were washed with ethanol and water; lastly, the chips were dried with compressed air.

The sedimentation behavior was analyzed by introducing 1.58×10^7 cells per mL of yeast suspension into a syringe, and yeast cell samples were collected *via* the connected sample pipe after t = 0, 5, 10, 15, and 20 min for 70 sec at $\dot{V}$ = 100 μL min⁻¹. The different dispersion methods included no dispersion, a shaker (Eppendorf) at 300 rpm, and a rocker (witeg) at 30 rpm with and without inserting a 5 mm silver sphere into the sample syringe. The yeast cell concentration was analyzed *via* UV-vis at 600 nm (Tecan Infinite M200). Analyzing the sedimentation behavior dependent on the yeast cells' (agglomerate) diameter and time further, the LUMiReader was used at 410 nm (angle = 0°, light factor 1.00, T = 22 °C, 350 profiles: interval = 20 s). For yeast, a refraction index (RI) of RI = 1.4 with a density of δ = 1.03 kg m⁻³, and for water, a refraction index of RI = 1.327 with a

density of δ = 997.8 kg m⁻³ and a viscosity of μ = 0.95 mPa s was used. To verify that the specificity of the binding and the viability were maintained during dispersion, a magnetically labeled yeast cell culture with and without dispersion *via* the rocker, including the silver sphere, were compared regarding their viability and binding specificity, as described in Eigenfeld and Wittmann *et al.*[25] The magnetically induced convective motion was investigated using the same particles and yeast cell concentrations under fractionation conditions and a $9 \times 9 \times 3$ cm neodymium-iron-boron magnet. A single experiment refers to the fractionation of only yeast cells or MNPs; for the mixture experiments, yeast cells and MNPs were mixed but without the linker-protein, investigating the independent hydrodynamic motion of each component. The yeast cell number was investigated microscopically by haemacytometry using a Neubauer counting chamber (Marienfeld), and the particle concentration was derived by UV-vis absorbance measurement at 400 nm. The yeast cell absorbance was subtracted *via* a linear equation system, necessitating a measurement and calibration curve for both components at 400 nm and 800 nm. The cell size was determined using microscopic images (Zeiss Axio Observer 7, 20× objective) and the particle analysis function in ImageJ. Single cells were selected by adjusting the circularity to 0.8–1.00.

E Age-dependent fractionation

The magnetically labeled yeast cells were magnetically separated for 15 min using a $7 \times 7 \times 3$ cm neodymium-iron-boron magnet for the prior batch separation. The daughter cell containing supernatant was removed carefully by pipetting with an adequate small pipette for the small volumes (for 1 mL suspension 30 μL residual volume was left). The magnetically separated mother cells were resuspended in the equivalent buffer volume and incubated for 15 min at 1000 rpm. The sample was drawn into a syringe with the 5 mm silver sphere and placed on the rocker at 30 rpm. The process started as described above with the conditions presented in Table 1. After the experiment, the samples were concentrated (3000 rpm, 10 min), and imidazole was used for MNP elution ($c_{Imidazole}$ = 0.26 mol L⁻¹ for 3.17×10^6 cells per mL). The samples were vortexed for 1 min and incubated for 10 min at 1000 rpm. Another batch separation followed, removing the eluted MNPs. After 15 min, the supernatant, containing the fractionated cells, was removed and washed twice with buffer (1 min, 17 000 × g). If used for cytometric analysis, the cells were loaded again with linker-protein, following the protocol described above. The remaining magnetically separated sample was resuspended in the buffer for subsequent UV-vis analysis at 400 nm to determine the particle concentration. The yeast cell number was determined microscopically (Zeiss Axio Observer 7) by haemacytometry using a Neubauer counting chamber. As described in ref. 25 and 26, a cytometric approach was used to evaluate the bud scar number, applying Gauss fits (detailed information in ESI,† Fig. S7).

Table 1 Optimum fractionation conditions to the corresponding chip geometries are presented. The magnet was placed upright with the corresponding distance at the edge of the sample inlet. The exact channel dimensions are detailed in the ESI† (Fig. S5)

Channel geometry	Magnet dimensions [cm]	Magnet distance [cm]	$\dot{V}_{Sample}$ [μL min^{-1}]	$\dot{V}_{Buffer}$ [μL min^{-1}]	Equilibration time [s]
Rectangular	9 × 9 × 3	1.4	220	920	23
Trapeze	5 × 1.5 × 1.5	0.5	220	920	0
Pinch-shaped	9 × 9 × 3	0.0	220	1100	0

F Nuclear magnetic resonance spectroscopy for metabolomics

Yeast cell pellets (cell numbers between 10^6 and 10^8 cells per mL) were frozen in liquid nitrogen directly after fractionation and kept at −80 °C until further processing, as previously described in more detail.[32,33] Pellets were mixed with 600 μL methanol/water (2 : 1) for protein precipitation and stopping of enzymatic reactions. Following homogenization in Precellys tubes filled with 1.4 mm diameter zirconium oxide beads on a Precellys24 tissue homogenizer with 2 cycles of 20 s at 25 °C (Bertin Technologies), transferred in empty 1.5 ml tubes, storage at −20 °C for 1 h, samples were centrifuged at 10 000 rpm for 30 min at 4 °C. Supernatants were transferred into new tubes, lyophilized for 10 h on a Savant SpeedVac SPD210 vacuum concentrator with cooling trap (Thermo Scientific) and finally resuspended in nuclear magnetic resonance (NMR) sample buffer containing 0.08 M Na_2HPO_4, 5 mM 3-trimethylsilyl propionic acid-2,2,3,3,-d4 sodium salt (TSP) and 0.04 (w/v)% NaN_3 in D_2O, adjusted to 7.4 pH with 8 M HCl and 5 M NaOH.

NMR experiments were performed at 310 K (600 MHz Bruker Avance Neo NMR spectrometer equipped with a TXI 600S3 probe head), applying the one-dimensional Carr–Purcell–Meiboom–Gill (CPMG) pulse sequence (cpmgpr1d, 512 scans, 73 728 points in F1, 12 019.230-Hz spectral width, recycle delay 4 s), with water suppression using presaturation. The ^1H 1D NMR experiments were recorded and automatically processed (exponential line broadening of 0.3 Hz, phased, and referenced to TSP at 0.0 ppm) by Bruker Topspin software version 4.1.3 (Bruker GmbH). To quantify metabolites of interest by targeted analysis, spectra were imported into Matlab 2014b (Mathworks), aligned, and normalized (by probabilistic quotient normalization[34]) using a state-of-the-art script developed by the group of Prof. Jeremy Nicholson at the Imperial College, London, UK. Processed raw spectra were further processed using an R script for integrating experimentally known chemical shift ranges of metabolites in yeast, cross-checked with commercially available standards, the human and yeast metabolome database, and Chenomx NMR Evaluation Suite 8.2 (Chenomx Inc.). Integrals (in arbitrary units, A.U., proportional to metabolite concentration) were statistically analyzed using MetaboAnalyst 5.0.[35] Besides univariate ANOVA, multivariate sparse partial least squares discriminant analysis (sPLS-DA) was used to identify metabolites that highly contribute to differences between sample groups. The integrals were normed according to yeast cell concentration.

G Quantitative polymerase chain reaction (qPCR) for gene expression

For gene expression analysis, we examined yeast cell fractions, including the initial yeast population and fractions from outlets A to D.

To ensure accurate analysis, the samples were centrifugated and treated with trizol reagent for metabolic quenching, effectively stopping metabolic activity and RNA degradation. The treated cells were stored at −80 °C until ribonucleic acid (RNA) isolation was carried out using the Roboclon Universal RNA Purification Kit. We used spectrophotometry to assess RNA concentrations and purity (NanoDrop, Thermo Scientific).

For complementary deoxyribonucleic acid (cDNA) synthesis, we utilized the Maxima H Reverse transcriptase and Ribolock RNAse inhibitor (ThermoFisher), known for its reliability and efficiency. Per preparation, 4 μL RT buffer, 0.5 μL Ribolock, 0.5 μL reverse transcriptase, 0.5 μL RNAse free water, 1 μL Primer oligo DT, and 1 μL DNTPs were used. The primers needed for the real-time reverse transcriptome quantitative polymerase chain reaction (RT-qPCR) were designed using the Clone Manager 9 software from Sci Ed Software. These primers were then synthesized by TIB Molbiol Syntheselabor GmbH (Berlin), and their sequences are available in Tables S2 and S3.† As housekeeping genes, KRE11, UBC6, and TAF10 were used for their stability and consistent expression, making them suitable as references for normalizing the target gene expression levels, as reported by Beugholt et al.[36]

During qPCR measurements, a 10 μL final volume was used containing 0.7 μL of DNA template, 0.4 μL of each respective primer, 5 μL of SybrGreen (Biozym), and 3.5 μL of RNase-free water.

To analyze gene expression, we performed real-time RT-qPCR and evaluated the expression stabilities using the geNorm algorithm based on M and V values. For this analysis, we employed the qBase+ software (Biogazelle), as proposed by Vandesompele et al. in 2002.[37] The C_q values from RT-qPCR were then imported into qBase+ software for further examination and comprehensive evaluation of gene expression patterns. The Minimum information for publication of quantitative real-time polymerase chain reaction experiments (MIQE) guidelines are detailed in Table S4.†

C Results

A Process-relevant characterization of binding and agglomeration behavior of the yeast@linker-protein@particle complex

Achieving continuous high separation selectivities necessitates the understanding of concentration and time dependence of

the linker-protein@particle agglomerate formation (particle characterization in the ESI† (Fig. S1), the term MNP/particle refers to the final ethylenediaminetetraacetic acid (EDTA)-functionalized silica shell iron oxide nanoparticles). Fig. 2b illustrates the hydrodynamic diameter, zeta potential, and pH values for varying particle concentrations, maintaining a consistent linker-protein concentration during labeling.[25,38] As the ratio R of linker-protein to particle increases from 0.2 to 2, the hydrodynamic diameter of the linker-protein@particle agglomerates diminishes from 1112.0 ± 36.2 nm to 695.6 ± 40.0 nm. Schwaminger *et al.* discussed the formation of large clusters composed of small-sized protein-particle agglomerates.[38] Hence, adding protein acts as 'glue', instigating agglomeration through hydrophobic interactions. However, upon reaching a specific linker-protein to MNP ratio, the MNP surface becomes saturated, and the bridging interaction is repressed by repulsive forces,[39,40] evidenced by the zetapotential decrease from -17.1 ± 0.8 mV ($R = 0.2$) to -18.4 ± 0.2 mV ($R = 2$). In addition to concentration, time significantly influences the agglomeration dynamics. For consistent magnetophoretic deflection in the chip, sustaining a stable hydrodynamic diameter of the linker-protein@particle agglomerate is crucial. At a ratio of $R = 0.04$, the hydrodynamic diameter steadily decreases from 1086.7 ± 58.6 nm post-incubation to 577.5 ± 165.1 nm over 25 h, as illustrated in Fig. 2c. Conversely, for a higher ratio of $R = 0.25$, uniform agglomerates of 793.3 ± 26.4 nm are formed after the same duration. While still debatable, protein corona formation is generally agreed to involve the rapid formation of an initial protein monolayer, with subsequent changes in particle agglomeration over time. Still, a higher ratio promotes stabilization.[40–43] Finding a balance between fractionation process duration and agglomerate uniformity, a ratio of $R = 0.25$ emerges as best because the agglomerates' size remains relatively constant, around 1000 nm for the initial five hours (microscopic visualization in Fig. 2d). The age-dependent magnetic yeast labeling is depicted in Fig. 2e, and Eigenfeld and Wittmann *et al.* previously confirmed its specificity through microscopic and cytometric analysis using the same ratio of $R = 0.25$.[25] As can be seen in Fig. 2d, the MNPs are covered completely with the linker-protein avoiding repulsive forces between the yeast cells and the MNPs. Nevertheless, the maintenance of the binding could not be verified with the existing analytical methods, which could negatively influence the subsequent selectivity of the fractionation. The dependence of crosslinkage among magnetically labeled yeast cells on used MNP concentration is emphasized in Fig. 2f and g. At a ratio $R = 0.04$, the single cells (singlets) account for approximately 0.35 of the total. In contrast, crosslinked cells (cell agglomerates of more than two cells) have a proportion of about 0.18, being time-independent. In contrast, for an increased ratio of $R = 0.25$, singlets comprise around a proportion of 0.5, and crosslinked cells are reduced to less than 0.10, again showing time-independence. For both concentrations, duplets, primarily budding cells (Fig. S2a†), represent 0.45–0.50 of the total since cells from the terminal exponential growth phase were used.

The subsequent process employs a consistent ratio of linker-protein to particle of $R = 0.25$, which ensures optimal MNP agglomerate size and reduced crosslinkage. Additionally, the agglomerates are microscopically visible, correspond to the bud scar size,[25,44] and the labeled yeast cells can be magnetically manipulated easily.

C Development of a magneto-responsive fractionation process

Upon entering the chip, the magnetically labeled cells are subjected to an inhomogeneous magnetic field. The resulting magnetophoretic motion is accelerated due to interparticle- and hydrodynamic interactions with the surrounding fluid, known as cooperative and convective magnetophoresis.[18,20–23] The propensity of these interparticle interactions is quantified by the aggregation parameter (Eqn S1 and S2†) with a determined value of $N^* = 0.01$, further specified in the ESI,† for $N^* > 1$, particles would agglomerate, leading to crosslinkage. However, the MNPs used in our study, encapsulated in a silica shell with a low saturation magnetization of 13.1 emu g^{-1}, are less prone to magnetic dipole coupling. This encapsulation enhances their performance in the application, although the induced convective motion by hydrodynamic interaction remains inevitable. It is characterized by the magnetic Grash of number $\mathbf{Gr_m}$ (Eqn S3†), calculated as $\mathbf{Gr_m} = 603.2$, indicating a strong regime of induced convective motion ($\mathbf{Gr_m} \gg 1$).

The fractionated heterogeneous yeast culture contains magnetically labeled mother cells and non-magnetically labeled daughter cells. Preliminary studies were conducted to understand the influence of this convective motion on separation efficiency. These experiments, which involved solely yeast cells or MNPs (Fig. 3a), were compared with trials using a mixture of both but without linker-protein (Fig. 3b). So, the direct influence of the MNPs on the non-magnetic unlabeled yeast or daughter cells is analyzed. Fig. 3a reveals that yeast cells are unaffected by the magnetic field without MNPs. In contrast, MNPs experience a magnetophoretic force, diverting them significantly to chip outlet C with a mean proportion of 0.51 ± 0.06. The main particle fraction does not accumulate in chip outlet D because an increased magnetic field gradient would cause the particles to adhere to the chip wall, preventing flow into the outlet channels. In mixed solution, the deflection pattern of the MNPs remains constant as in solely conditions, but the non-magnetic yeast cells are carried along the MNP motion (Fig. 3b). This magnetic-induced convective motion would compromise the separation efficiency of the fractionation process with a heterogeneous, labeled culture, suggesting that daughter cells might co-migrate with mother cells. Additionally, it can be assumed that not all nanoparticle agglomerates bind to the yeast cells, which increases the effect of magnetically induced convection. Increasing the hydrodynamic force by an increased buffer flow was not purposeful, as the magnetophoretic force reached a threshold beyond which it could not surmount the hydrodynamic drag force (Fig. S3b and e†). Elevating the magnetic field further intensifies the

Paper
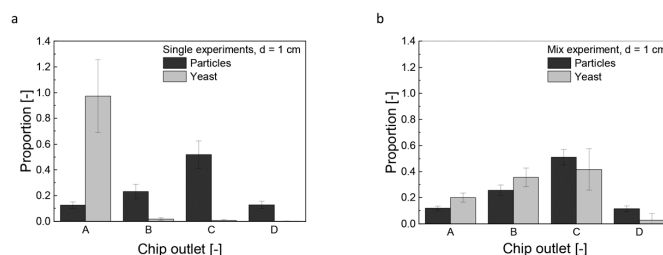
Fig. 3 Single fractionation experiments for solely yeast and particles in the rectangular geometry (a). Fractionation experiment for yeast-particle mixture without linker-protein in the rectangular channel (b). Chip outlet A was the furthest away from the magnet; chip outlet D was the nearest one to magnet, and the magnet distance was d = 1 cm. The relation between the magnetic field strength and magnet distance is given in Fig. S3 d. $\dot{V}_{Sample}$ = 220 μL min^{-1}, $\dot{V}_{Buffer}$ = 920 μL min^{-1}, $c_{Particle}$ = 0.4 g L^{-1}, cell number = 1.58 × 10^7 cells per mL. All data plots include the standard deviation from a triplicate measurement.

magnetically induced hydrodynamic force (Fig. S3c and f, Eqn S2†). Microfluidic techniques using magnetic labeling are widely used for separation processes. Robert *et al.* separated magnetic macrophages from non-magnetic monocytes, having an iron content of 0.02 g L^{-1}, a concentration consistent with our study. They minimized monocyte drag by increasing buffer velocity and counteracting the magnetophoretic force.[45] Notably, their study employed a lower magnetic field strength of 0.26 T, in contrast to our 0.41 T (compare Fig. S3f†). The characteristic length of the system profoundly affects the induced convective motion (Eqn S3†). This is crucial because they used a microfluidic channel, while this study used centimeter-scale millifluidic channels. However, a high-throughput fractionation necessitates a millifluidic flow channel geometry, high concentrations, flow rates, and a stronger applied magnetic field. Yet, the convective motion of non-magnetic entities remains an inherent challenge in these settings. Although working with a microfluidic chip, Lin *et al.* presented a process-oriented solution, proposing a two-stage method for separating magnetically labeled white from red blood cells, effectively separating the co-migrating red blood cells.[46]

Consequently, this study adopts a two-step process for the age-based fractionation. A batch separation was performed outside the chip, separating non-magnetic daughter cells from magnetically labeled mother cells.[15,25] Subsequently, the mother cells were subjected to age-based fractionation within the chip (Fig. 1).

D Channel design for the age-based fractionation of a yeast cell culture

Three different millifluidic flow channels were evaluated to differentiate age based on bud scar numbers, as presented in Fig. 4a. The first channel employed a traditional rectangular design, commonly utilized in numerous microfluidic applications.[31,47–50]

The second channel featured a trapezoidal design, enhancing the exposure to the magnetic field gradient due to its widened shape.[30,51] A pinch-shaped geometry, the third

channel, combined magnetic with intertial sorting,[19,29,52,53] providing an additional separation criterion since yeast cells increase in size during their replicative lifespan.[4,25] As can be seen in the average bud scar number in Fig. 4b, the batch-separated fraction (pre-fractionation, see Fig. 1 step 1) only consists of young cells having a bud scar number of almost zero, a result consistent across all channel geometries.

After the batch separation, the mother cells exhibit an average bud scar number of approximately 1.7 across all three chip geometries. For the subsequent fractionation in the rectangular chip (Fig. 4c), the average bud scar count increases from 2.08 ± 0.41 at chip outlet A (furthest from the magnet) to 3.67 ± 1.55 at chip outlet D (closest to the magnet). This high variation in the oldest fraction is attributed to the low cell concentration of 8.73 × 10^3 ± 8.00 × 10^3 cells per mL at that outlet, making age analysis difficult. The chip's extended length in the millifluidic design results in prolonged residence time for labeled cells, promoting increased convective mixing motion and diffusion.[18,23,54] These effects reduce the separation selectivities shown in Table S1.† Only in fraction C cells with two or more bud scars are enriched. Most cells reach outlet A, minimally influenced by the magnetophoretic force due to buffer flow dilution, which reduces cell concentration and magnetic responsiveness (eqn (1)). In the trapezoidal channel, the average bud scar count remains consistent at approximately two across all outlets (Fig. 4d). Analysis of cell fractions in Fig. 4e indicates a lack of age fractionation, with bud scars ranging from one to five at every outlet. Notably, almost no cells are collected in fraction C. For the pinch-shaped channel, the average bud scar number increases from 2.33 ± 0.82 in fraction A to 6.27 ± 0.45 in fraction D, suggesting enrichment of old cells. Fig. 4e confirms this, as fractions C and D contain cells with two or more bud scars at concentrations of 1.66 × 10^6 ± 4.81 × 10^5 cells per mL and 1.18 × 10^6 ± 1.54 × 10^5 cells per mL, respectively. Fraction D also shows a higher proportion of cells with four to six bud scars. However, a distinct bud scar number separation per outlet remains unfeasible. While the geometric adaption can reduce magnetically induced convective motion, complete elimination is unattainable. Additionally, cells continuously grow throughout their replicative life span, serving
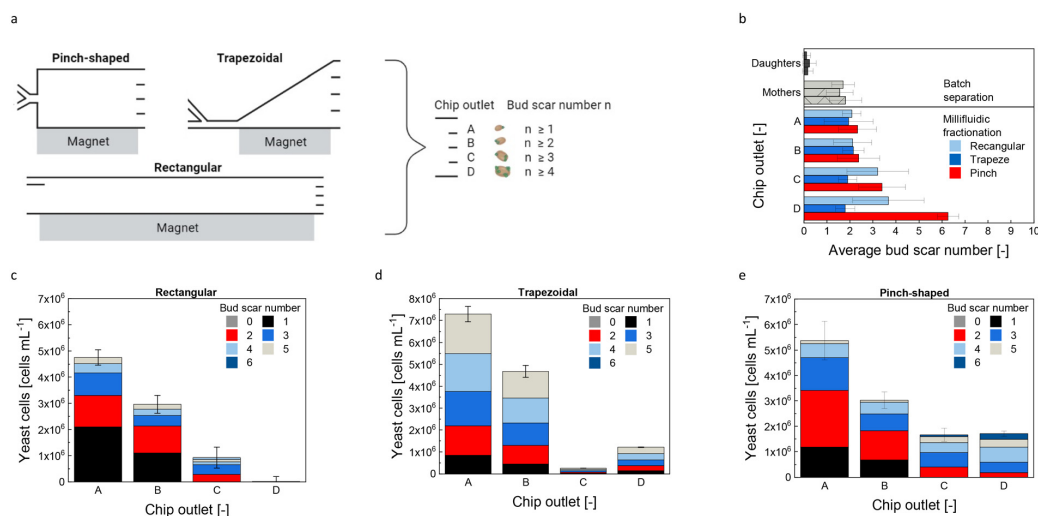
Fig. 4 Scheme of different chip designs for age-dependent fractionation (a). Average bud scar number for different fractions with different flow channels (b). Yeast cell concentration for the different fractions and corresponding bud scar numbers for the rectangular (c), the trapezoidal (d), and pinch-shaped channel (e) with $c_{Particle}$ = 0.4 g L^{-1}, cell number = 1.58×10^7 cells per mL. Error bars represent the standard deviation of the triplicate measurement. Outlet A was the furthest away from the magnet; outlet D was the nearest to the magnet. Daughter and mother cells refer to the prior batch separation.

as a size separation criterion, but also exhibit size variability during their cell cycle.[4] As illustrated in Fig. S2a,† budding and agglomerating cells have a larger diameter (14 μm) than single cells (10 μm), possibly leading to mixed age fractions. Previous studies have demonstrated the efficacy of intertial cell manipulation for microfluidic yeast cell separations.[52,55,56] Using a pinch-shaped channel to separate yeast cells only based on morphology, a throughput of only 3.75×10^4 cells per min was achieved.[52,56] However, both fractionation methods are unsuitable for higher-scaled yeast cell fractionation or differentiation by age, only by cell groupings like singlets, duplets, and clusters.

Integrating intertial fractionation with magnetophoresis, based on age-related magnetic load, in a millifluidic pinch-shaped chip proved the most effective approach for achieving bud scar differentiation. This method has a high throughput of $1.90 \times 10^6 \pm 5.71 \times 10^5$ cells per min, with reproducible separation efficiencies across three independent processes: The mean and standard deviation of three independent fractionation processes is 1.00 ± 0.00 for fraction A, 0.95 ± 0.02 for fraction B, and 0.97 ± 0.00 and 0.84 ± 0.08 for fractions C and D, respectively.

E Metabolite level changes over cell age

Leupold *et al.* noted a decline in metabolite concentrations and growth rates with chronological aging.[16] As shown in Fig. 5a and S8,† older cells, successfully fractionated with the pinch-shaped geometry, showed significant increases in nicotinamide adenine dinucleotide (NAD^+) (*p*-value: 0.008), lactic acid (*p*-value: 0.015), and formic acid (*p*-value: 0.027)

levels. Our study further revealed a five-fold adenosine diphosphate (ADP) accumulation between outlets D and A, reinforcing the NAD^+ impact. The rise in lactic acid aligns with energy cofactor concepts, correlating with yeast cells' intracellular pH and adenosine triphosphatase (ATPase) activity.[57] This suggests decreased adenosine triphosphate (ATP) cofactor levels, reduced ATPase activity, and subsequent intracellular acidification.

Cell membrane transporters internalize amino acids and are subsequently processed into alpha-keto acids by the Ehrlich pathway.[58] These acids are either decarboxylated into aldehydes reduced to higher alcohols or oxidized to its corresponding acids before yeast cells excrete them. Among the essential amino acids, levels of leucine, methionine, phenylalanine, tryptophan, and tyrosine are lower in younger cells with an average bud scar number of 2.33 ± 0.82 in fraction A, but rise in older ones having an average bud scar number of 6.27 ± 0.45 in fraction D (*p*-value: 0.050 (leucine), 0.024 (methionine), 0.064 (phenylalanine), 0.098 (tryptophan), 0.036 (tyrosine)). Conversely, isoleucine (*p*-value: 0.298) and valine levels remain consistent throughout replicative aging (*p*-value: 0.271).

These observations can be explained by various hypotheses: (i) Rapid growth and division: Younger cells are often engaged in rapid growth and division. The lower amino acid levels might indicate increased use for protein synthesis and other cellular activities associated with growth.[25,59] (ii) Metabolic shift: the decrease in amino acid levels within younger cells might signal a shift in their metabolism, prioritizing different pathways. These pathways might encompass energy production, nucleotide synthesis, or alcohol formation, reducing the
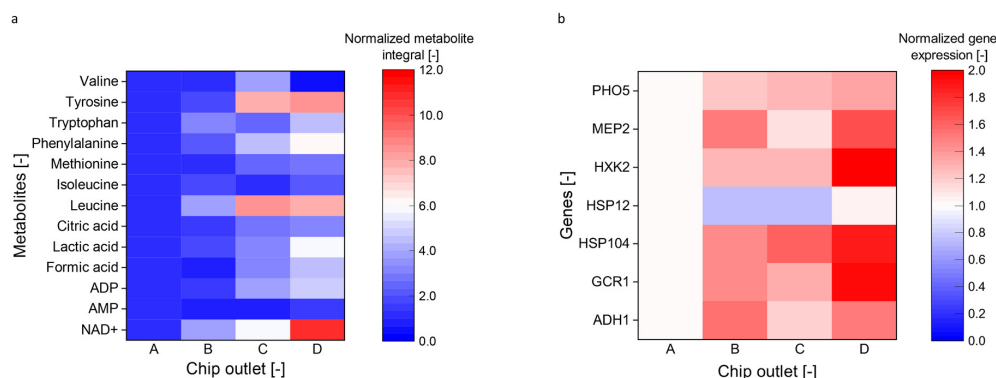
Fig. 5 Heat map depicting the normalized integral area of selected metabolites against the cell fraction (a). Comparative analysis of gene expression across cell fractions (b). Both normalized to the cells from chip outlet A. Data included from a triplicate measurement.

accumulation of specific amino acids. Notably, the synthesis of esters, an energy-intensive process demanding cofactors,[60] could be linked to this hypothesis. Consequently, the decreased amino acid levels might be due to the prevalence of ester synthesis, which often occurs during later fermentation phases. Many studies have been analyzing the metabolic pathways associated with the volatilome formation by yeast mediated fermentation, encompassing both genetic and environmental influences.[61,62] However, an age-related perspective determined in a representative cell number remains absent. Using the proposed millifluidic chip makes it feasible to explore the interplay between age and metabolites on a scale beyond single-cell analysis.

F Variation of cellular age on gene expression

Our study found that gene expression increases with the median cell age of yeast cells. As shown in Fig. 5b, the genes ADH1 and MEP2 showed an upregulation of around 50%. Other genes, including GCR1, HSP104, HXK2, and PHO5, were upregulated by a factor of 2 for cells having a bud scar number of 6.27 ± 0.45 compared to younger cells having a bud scar number of 2.33 ± 0.82. However, the expression of gene HSP12 did not significantly vary with the median cell age. All reference genes indicate no significant change in all four outlet samples.

These findings suggest that aging cells may experience changes in genes related to metabolism and energy regulation. For instance, genes involved in glucose metabolism and mitochondrial function may also show altered expression in other organisms. In our study, we observed an upregulation of the gene HXK2, which codes for the metabolic enzyme hexokinase,[63] indicating a potential need for increased glycolytic activities and stress response in aging cells.[64]

The genes ADH1 (ref. 65 and 66) and GCR1 (ref. 67 snd 68) served as markers for the glycolytic pathway and ethanol formation capacity, reflecting the overall metabolic state of

the cell. The expression of GCR1 increased with cell age about factor 2, with cells having an average bud scar number of 2.33 ± 0.82 showing the lowest expression. Accompanying heightened GCR1 expression, the HSP104 gene, which is involved in protein re-folding and reflects the cells' replication stress status, showed doubled expression with age. Different expression behavior of HSP104 and HSP12, of which the latter is not upregulated with cell age, is due to lack of a common activator, *i.e.* heat stress.[69] The role of ADH1 in the formation of higher alcohols *via* the Ehrlich pathway also is consistent with the metabolite changes of the cell.

The observed changes reflect the cell's adaptive strategies to counteract the aging effects and maintain cellular functionality under stress conditions. They show upregulated genes linked to metabolism and stress response, indicating metabolic shifts and a need for heightened defenses. This upregulation, especially in genes related to glucose metabolism and mitochondrial function, underscores the impact of aging on cellular energy processes.[66,68] Aging cells might face greater energy needs, necessitating adaptive measures for energy balance. Chen *et al.* found that glycolytic flux rises with increased growth rates,[70] suggesting older cells may amplify glycolytic activity to meet energy requirements. Similarly, older cells might have reduced energy efficiency, compensating through heightened glycolytic activity and gene expression. Stress conditions, especially during anaerobic fermentations, can reduce growth and biomass due to energy shortages,[25] affecting processes like aroma or protein production. Using separated young cells could offset aging effects on both genomic and metabolite levels. This approach offers potential improvements for yeast processes in the beverages and pharmaceutical industries.

D Conclusions

We present a novel millifluidic process using magnetophoresis for age-based fractionation of *S. pastorianus* var. *carlsbergensis*

culture. An optimal linker-protein to MNP ratio of $R = 0.25$ ensures homogeneous agglomerate size, enabling cell deflection in the magnetic field while reducing crosslinkage. Magnetic-induced convective motion, inherent in the process, reduces separation selectivity, necessitating a prior batch separation of daughter and mother cells. Among tested geometries, the pinch-shaped design achieved best age fractionation, increasing the average bud scar number from 2.33 ± 0.82 in fraction A to 6.27 ± 0.45 in fraction D, processing $1.90 \times 10^6 \pm 5.71 \times 10^5$ cells per min. This design combines magnetophoretic and inertial fractionation, with older cells having more bud scars and thus larger volumes, showing increased deflection towards the magnet. This chip, fabricated using 3D printing technology, offers an economical, high-throughput platform with high and reproducible separation selectivity, replacing single-cell microfluidic methods. Metabolomic data indicates age-related declines in specific amino acids and a rise in NAD^+ production, possibly due to younger cells' metabolic activities. Gene expression studies highlight age-related changes, especially in metabolism and stress response genes. Aging cells seem to adjust their metabolic pathways, suggesting potential energy inefficiencies. Young cells can mitigate aging effects, benefiting the beverages and pharmaceutical industries. Our millifluidic platform introduces a non-invasive method for age-based fractionation, revolutionizing in-line age analysis in yeast processes.

Author contributions

L. W., J. M., H. H. and M. E. – methodology, investigation, data curation. L. W., H. H. and M. E. – formal analysis. K. B. data curation. L. W. and M. E. – writing – original draft, visualization, validation, methodology. R. K. and S. S. – conceptualization, project administration, supervision. S. S., T. M., T. B. and S. B. – Resources. L. W., M. E., J. M., B. K., H. H., T. M., R. K., S. S., S. B., and T. B. – writing – review & editing.

Conflicts of interest

There are no conflicts to declare.

Acknowledgements

References

1 S. Fehrmann, C. Paoletti, Y. Goulev, A. Ungureanu, H. Aguilaniu and G. Charvin, *Cell Rep.*, 2013, **5**, 1589–1599.

2 R. K. Mortimer and J. R. Johnston, *Nature*, 1959, **183**, 1751–1752.

3 C. D. Powell, D. E. Quain and K. A. Smart, *FEMS Yeast Res.*, 2003, **3**, 149–157.

4 F. Ferrezuelo, N. Colomina, A. Palmisano, E. Garí, C. Gallego, A. Csikász-Nagy and M. Aldea, *Nat. Commun.*, 2012, **3**, 1012.

5 F. Bühligen, P. Lindner, I. Fetzer, F. Stahl, T. Scheper, H. Harms and S. Müller, *J. Biotechnol.*, 2014, **187**, 60–70.

6 K. Kumar, V. Venkatraman and P. Bruheim, *Microb. Cell Fact.*, 2021, **20**, 64.

7 L. Zeng, Z. Si, X. Zhao, P. Feng, J. Huang, X. Long and Y. Yi, *Int. J. Biochem. Cell Biol.*, 2022, **148**, 106236.

8 C. Correia-Melo, S. Kamrad, R. Tengölics, C. B. Messner, P. Trebulle, S. J. Townsend, S. Jayasree Varma, A. Freiwald, B. M. Heineike, K. Campbell, L. Herrera-Dominguez, S. Kaur Aulakh, L. Szyrwiel, J. S. L. Yu, A. Zelezniak, V. Demichev, M. Mülleder, B. Papp, M. T. Alam and M. Ralser, *Cell*, 2023, **186**, 63–79.e21.

9 R. O'Laughlin, M. Jin, Y. Li, L. Pillus, L. S. Tsimring, J. Hasty and N. Hao, *Transl. Med. Aging*, 2020, **4**, 151–160.

10 S. S. Lee, I. A. Vizcarra, D. H. E. W. Huberts, L. P. Lee and M. Heinemann, *Proc. Natl. Acad. Sci. U. S. A.*, 2012, **109**, 4916–4920.

11 K. L. Chen, M. M. Crane and M. Kaeberlein, *Mech. Ageing Dev.*, 2017, **161**, 262–269.

12 K. Reinmets, A. Dehkharghani, J. S. Guasto and S. M. Fuchs, *Lab Chip*, 2019, **19**, 3481–3489.

13 N. H. Thayer, M. Robles, J. Xu, E. L. Schinski, M. Hotz, R. Keyser, A. Millett-Sikking, V. Okreglak, J. V. Rogers, A. J. Waite, B. J. Wranik, A. G. York, R. Scott Mcisaac and D. E. Gottschling, *bioRxiv*, preprint, DOI: **10.1101/2022.02.14.480146**.

14 G. E. Janssens, A. C. Meinema, J. González, J. C. Wolters, A. Schmidt, V. Guryev, R. Bischoff, E. C. Wit, L. M. Veenhoff and M. Heinemann, *Elife*, 2015, **4**, e08527.

15 D. G. Hendrickson, I. Soifer, B. J. Wranik, G. Kim, M. Robles, P. A. Gibney and R. S. McIsaac, *Elife*, 2018, **7**, 1–31.

16 S. Leupold, G. Hubmann, A. Litsios, A. C. Meinema, V. Takhaveev, A. Papagiannakis, B. Niebel, G. Janssens, D. Siegel and M. Heinemann, *Elife*, 2019, **8**, e41046.

17 T. Salafi, K. K. Zeming and Y. Zhang, *Lab Chip*, 2017, **17**, 11–33.

18 S. S. Leong, Z. Ahmad, S. C. Low, J. Camacho, J. Faraudo and J. K. Lim, *Langmuir*, 2020, **36**, 8033–8055.

19 F. Alnaimat, S. Karam, B. Mathew and B. Mathew, *IEEE Nanotechnol. Mag.*, 2020, **14**, 24–41.

20 J. Faraudo, J. S. Andreu and J. Camacho, *Soft Matter*, 2013, **9**, 6654–6664.

21 G. De Las Cuevas, J. Faraudo and J. Camacho, *J. Phys. Chem. C*, 2008, **112**, 945–950.

22 J. G. Lee, V. Porter, W. A. Shelton and B. Bharti, *Langmuir*, 2018, **34**, 15416–15424.

23 G. Kitenbergs and A. Cēbers, *J. Magn. Magn. Mater.*, 2020, **498**, 166247.

24 C. Ruffert, in *Mikrofluidische Separationsverfahren und -systeme*, Springer-Verlag GmbH Deutschland, Groß-Umstadt, 2018, pp. 109–126.

25 M. Eigenfeld, L. Wittmann, R. Kerpes, S. P. Schwaminger and T. Becker, *Biotechnol. J.*, 2023, **18**, e2200610.

26 M. Eigenfeld, R. Kerpes and T. Becker, *RSC Adv.*, 2021, **11**, 31923–31932.

27 L. Wittmann, C. Turrina and S. P. Schwaminger, *Magnetochemistry*, 2021, **7**, 80.

28 C. Turrina, S. Berensmeier and S. P. Schwaminger, *Pharmaceuticals*, 2021, **14**(5), 405.

29 M. Yamada, M. Nakashima and M. Seki, *Anal. Chem.*, 2004, **76**, 5465–5471.

30 F. Shen and J. K. Park, *Anal. Chem.*, 2018, **90**, 920–927.

31 J. Wu, Q. Yan, S. Xuan and X. Gong, *Microfluid. Nanofluid.*, 2017, **21**, 1–12.

32 A. S. Gross, A. Zimmermann, T. Pendl, S. Schroeder, H. Schoenlechner, O. Knittelfelder, L. Lamplmayr, A. Santiso, A. Aufschnaiter, D. Waltenstorfer, S. O. Lara, S. Stryeck, C. Kast, C. Ruckenstuhl, S. J. Hofer, B. Michelitsch, M. Woelflingseder, R. Müller, D. Carmona-Gutierrez, T. Madl, S. Büttner, K. U. Fröhlich, A. Shevchenko and X. Tobias Eisenberg, *J. Biol. Chem.*, 2019, **294**, 12020–12039.

33 D. Bresilla, H. Habisch, I. Pritišanac, K. Zarse, W. Parichatikanond, M. Ristow, T. Madl and C. T. Madreiter-Sokolowski, *Sci. Rep.*, 2022, **12**(1), 21050.

34 S. M. Kohl, M. S. Klein, J. Hochrein, P. J. Oefner, R. Spang and W. Gronwald, *Metabolomics*, 2012, **8**, 146–160.

35 Z. Pang, J. Chong, G. Zhou, D. A. De Lima Morais, L. Chang, M. Barrette, C. Gauthier, P. É. Jacques, S. Li and J. Xia, *Nucleic Acids Res.*, 2021, **49**, W388–W396.

36 A. Beugholt, K. Büchner, D. U. Geier and T. Becker, *Front. Chem. Eng.*, 2022, **4**, 1035348.

37 J. Vandesompele, K. De Preter, F. Pattyn, B. Poppe, N. Van Roy, A. De Paepe and F. Speleman, *Genome Biol.*, 2002, **3**(7), research0034.

38 S. Schwaminger, S. Blank-Shim, I. Scheifele, V. Pipich, P. Fraga-García and S. Berensmeier, *Biotechnol. J.*, 2018, 1–22.

39 H. Wang, R. Ma, K. Nienhaus and G. U. Nienhaus, *Small*, 2019, **15**, 1900974.

40 K. Nienhaus and G. U. Nienhaus, *Small*, 2023, 19.

41 D. Baimanov, R. Cai and C. Chen, *Bioconjugate Chem.*, 2019, **30**, 1923–1937.

42 S. Milani, F. Baldelli Bombelli, A. S. Pitek, K. A. Dawson and J. Rädler, *ACS Nano*, 2012, **6**, 2532–2541.

43 E. Casals, T. Pfaller, A. Duschl, G. J. Oostingh and V. Puntes, *ACS Nano*, 2010, **4**, 3623–3632.

44 M. Eigenfeld, R. Kerpes and T. Becker, *RSC Adv.*, 2021, **11**, 31923–31932.

45 D. Robert, N. Pamme, H. Conjeaud, F. Gazeau, A. Iles and C. Wilhelm, *Lab Chip*, 2011, **11**, 1902–1910.

46 S. Lin, X. Zhi, D. Chen, F. Xia, Y. Shen, J. Niu, S. Huang, J. Song, J. Miao, D. Cui and X. Ding, *Biosens. Bioelectron.*, 2019, **129**, 175–181.

47 N. Pamme and C. Wilhelm, *Lab Chip*, 2006, **6**, 974–980.

48 M. D. Tarn and N. Pamme, *Methods Mol. Biol.*, 2017, **1547**, 69–83.

49 B. Ngamsom, M. M. N. Esfahani, C. Phurimsak, M. J. Lopez-martinez, J. Raymond, P. Broyer, P. Patel and N. Pamme, *Anal. Chim. Acta*, 2016, **918**, 69–76.

50 F. Alnaimat, S. Dagher, B. Mathew, A. Hilal-Alnqbi and S. Khashan, *Chem. Rec.*, 2018, **18**, 1596–1612.

51 W. Zhao, T. Zhu, R. Cheng, Y. Liu, J. He, H. Qiu, L. Wang, T. Nagy, T. D. Querec, E. R. Unger and L. Mao, *Adv. Funct. Mater.*, 2016, **26**, 3990–3998.

52 Q. Chen, D. Li, J. Zielinski, L. Kozubowski, J. Lin, M. Wang and X. Xuan, *Biomicrofluidics*, 2017, **11**(6), 064102.

53 V. Kumar and P. Rezai, *Microfluid. Nanofluid.*, 2017, **21**, 83.

54 P. Agnihotri, *Microfluid. Nanofluid.*, 2023, **27**, 12.

55 D. Jiang, S. Liu and W. Tang, *Micromachines*, 2022, **13**(10), 1659.

56 P. Liu, H. Liu, D. Yuan, D. Jang, S. Yan and M. Li, *Anal. Chem.*, 2021, **93**, 1586–1595.

57 K. Kasamo, *J. Plant Res.*, 2003, **116**, 517–523.

58 F. Bianchi, J. S. Van't Klooster, S. J. Ruiz and B. Poolman, *Microbiol. Mol. Biol. Rev.*, 2019, **83**(4), e00024-19.

59 A. Papagiannakis, B. Niebel, E. C. Wit and M. Heinemann, *Mol. Cell*, 2017, **65**, 285–295.

60 S. M. G. Saerens, F. R. Delvaux, K. J. Verstrepen and J. M. Thevelein, *J. Microb. Biotechnol.*, 2010, **3**, 165–177.

61 A. G. Cordente, S. Schmidt, G. Beltran, M. J. Torija and C. D. Curtin, *Appl. Microbiol. Biotechnol.*, 2019, **103**, 4325–4336.

62 Y. Kamei, Y. Tamada, Y. Nakayama, E. Fukusaki and Y. Mukai, *J. Biol. Chem.*, 2014, **289**, 32081–32093.

63 P. Herrero, J. Galíndez, N. Ruiz, C. Martínez-Campa and F. Moreno, *Yeast*, 1995, **11**, 137–144.

64 K. A. Morano, C. M. Grant and W. S. Moye-Rowley, *Genetics*, 2012, **190**, 1157–1195.

65 S. B. Raj, S. Ramaswamy and B. V. Plapp, *Biochemistry*, 2014, **53**, 5791–5803.

66 J. R. Dickinson, L. E. J. Salgado and M. J. E. Hewlins, *J. Biol. Chem.*, 2003, **278**, 8028–8034.

67 H. Uemura and D. P. Fraenkel, *Mol. Cell. Biol.*, 1990, **10**, 6389–6396.

68 D. Clifton, S. B. Weinstock and D. G. Fraenkel, *Genetics*, 1978, **88**, 1–11.

69 S. Chowdhary, A. S. Kainth and D. S. Gross, *Mol. Cell Biol.*, 2017, **37**(24), e00292-17.

70 M. Chen, T. Xie, H. Li, Y. Zhuang, J. Xia and J. Nielsen, *Proc. Natl. Acad. Sci. U. S. A.*, 2023, **120**(25), e2302779120.

178

1 Electronic Supplementary information to

2 **Millifluidic magnetophoresis-based chip for age-specific fractionation:**
3 **Evaluating the impact of age on metabolomics and gene expression in**
4 **yeast**

5 Wittmann, L. [a]†, Eigenfeld, M. [b,c]†, Büchner, K.[b], Meiler, J.[a], Habisch, H.[c], Madl, T.[c,d], Kerpes, R.[b,*], Becker, T.[c],
6 Berensmeier, S.[a,e], Schwaminger, S. P.[a,c,d,*]

[a]Technical University of Munich, TUM School of Engineering and Design, Chair of Bioseparation Engineering, Boltzmannstr. 15, 85748 Garching, Germany

[b]Technical University of Munich, TUM School of Life Science, Chair of Brewing and Beverage Technology, Weihenstephaner Steig 20, 85354 Freising, Germany

[c]Medical University of Graz, Otto-Loewi Research Center, Division of Medicinal Chemistry, Neue Stiftingtalstr. 6, 8010 Graz, Austria

[d]BioTechMed-Graz, Mozartgasse 12/II, 8010 Graz, Austria

[e]Technical University of Munich, Munich Institute of Integrated Materials, Energy and Process Engineering, Lichtenberstr. 4a,

85748 Garching

† All authors contributed equally

*Corresponding authors:

Sebastian P. Schwaminger, E-mail: s.schwaminger@tum.de; sebastian.schwaminger@medunigraz.at

Roland Kerpes, E-mail: roland.kerpes@tum.de

7

8 **A Results and Discussion**

9 **A Magnetic nanoparticle characterization.**

10 Achieving continuous high separation selectivities necessitates the understanding of concentration and time
11 dependence of the linker-protein@particle agglomerate formation (see Section Results A). Therefore, the
12 nanoparticles are characterized in the following. The magnetic nanoparticles (MNP) (ethylenediaminetetraacetic
13 acid (EDTA)- functionalized silica shell iron oxide nanoparticles) utilized for labeling the yeast cell's bud scars, as
14 previously described [1], exhibit an iron oxide core, enabling magneto-responsive behavior. Superconducting quantum
15 interference device (SQUID) measurements, presented in Fig. S1 a, reveal no remanence and superparamagnetic
16 behavior, having a saturation magnetization of 13.13 emu g^{-1}. X-ray diffraction (XRD) measurements reveal that the
17 iron oxide nanoparticles (IONs) exhibit a diameter of 13.11 ± 2.07 nm (Fig. S1 b). Further, the XRD analysis confirms
18 the typical reflections ((220), (311), (400), (511), and (440)) for magnetite with its cubic crystal structure [2]. These
19 iron oxide cores, evident in transmission electron microscopy (TEM) images in Fig. S1 c, are encapsulated by a silica
20 shell that precludes the IONs from agglomerating, as previously shown [3,4]. For these particles to bind with the
21 histidine tag of the linker-protein, an EDTA surface was introduced via an amide bond [1,5]. Although this surface is
22 not discernible in the TEM images, it is detectable in the thermogravimetric analysis (TGA). TGA results corroborate
23 the presence of different coatings. Fig. S1 d illustrates the weight loss across temperatures for the different coating
24 steps. The initial weight loss step, associated with the desorption of surface-bound water, is evident at temperatures
25 below 100°C. The iron oxide core is stable up to 700°C, with negligible weight loss. For the coatings, the weight loss
26 between 100 and 700°C is attributed to the decomposition of functional groups, such as the carboxyl groups in the
27 EDTA-functionalized particles. However, the thermal stability for the ION@Si and ION@Si@NH_2 particles is higher
28 and leaves more residual [6,7]. The overall EDTA content is calculated to be 15.33 wt%. The Fourier-transform infrared
29 spectroscopy (FT-IR) data in Fig. S1 e confirms the different particle functionalization steps. The Fe-O-Si vibration, at

1

30   592 cm^{-1}, verifies the binding of the silica to the ION core, besides the Si-O-Si stretching vibration at 1080 cm^{-1} and

31   the Si-O vibration at 794 cm^{-1}. The successful functionalization with amine groups is confirmed by the 1488 and 1638

32   cm^{-1} bands, which are associated with the N-H bending vibrations. This is indicative of the effective incorporation of

33   (3-aminopropyl)triethoxysilane (APTES) [8]. EDTA was coated on the particles in an additional synthesis step, proved

34   by the asymmetrical and symmetrical COO$^-$ stretching vibrations, located at 1570 – 1610 cm^{-1} and 1350 – 1450 cm$^-$

35   ^{1}, respectively. Furthermore, the disappearance of the N-H bending vibration at 1488 cm^{-1} signifies the successful

36   establishment of an amide bond between APTES and EDTA [5]. The primary particle size from TEM analysis is 120.62

37   ± 16.86 nm (compare Fig. S1 c and f). After synthesis, dynamic light scattering (DLS) measurements yielded a

38   hydrodynamic diameter of 2297.67 ± 850.78 nm (ζ = -8.22 ± 0.39 mV, pH = 9.1) for the ION@Si@NH$_2$ precursor and

39   179.01 ± 11.99 nm (ζ = 21.10 ± 0.62 mV, pH = 4.89) for the EDTA-functionalized MNPs with a polydispersity index of

40   0.17 ± 0.02 (Fig. S1 g). These results confirm the colloidal stability and monomodal distribution of the built

41   ION@Si@EDTA particles (the term 'Si' refers to the silica shell). Moreover, the hydrodynamic diameter can be

42   preserved for up to 28 days, as confirmed by an agglomeration study in Fig. S1 h. After this period, the hydrodynamic

43   diameter measures 176.60 ± 32.55 nm, with a zeta potential of -29.26 ± 1.53 mV. The EDTA-functionalized surface

44   enables the binding of the linker-protein via the His-tag. Therefore, this surface is saturated with nickel (Ni) ions,

45   achieving maximum binding capacities of 4 mg$_{Ni}$ g$_{Particle}^{-1}$ (Fig. S1 i), corresponding to 0.40 nickel ions per nm$_{Particle}^2$,

46   comparable to Fraga García et al. [9]. The binding kinetics occurs within minutes (Fig. S1 j), a finding that aligns with

47   previous studies [10], and the built EDTA@Ni chelate complex remains sTab. for several days, as no leaching was

48   observed over five days, presented in Fig. S1 k. The differences in surface charges for the precursor particles, the

49   EDTA-functionalized ones, and those saturated with nickel ions were investigated across a range of pH values in

50   water. The study reveals that the isoelectric point (IEP) of the ION@Si@NH$_2$ is at pH 8.8 and decreases to pH 6.8 for

51   the ION@Si@EDTA (Fig. S1 l). The presence of loaded nickel ions slightly reduces the IEP to 7.6. The particles are

52   colloidally sTab. (ζ > I 20 mV I) or unsTab. (-20 mV < ζ > 20 mV), dependent on the surface charge. This pH-dependent

53   agglomeration directly influence the sedimentation velocity under a magnetic field gradient, as Fig. S1 m shows.

54   After the synthesis, the ION@Si@NH$_2$ particles exhibit a pH of 9.1, close to the IEP, leading to rapid sedimentation

55   in a magnetic field. Contrarily, the ION@Si@EDTA exhibit a pH of 4.89 after the synthesis, further away from their

56   IEP. Thus, they tend to sediment slower in the magnetic field due to the formation of smaller agglomerates. These

57   findings emphasize the importance of carefully controlling the agglomeration behavior for the subsequent

58   magnetophoretic fractionation process (Fig. S1 m).

59   Consequently, adhering to the established particle dispersion protocol for each iteration of fractionation

60   experimentation became important. The MNPs, stored at a temperature of 4°C under a nitrogen atmosphere,

61   exhibit an average hydrodynamic diameter of 306.73 ± 7.96 nm, accompanied by a polydispersity index of 0.32 ±

62   0.1. The MNP solution underwent ultrasonication to disperse larger agglomerates, which diminishes the

63   polydispersity index to 0.13 ± 0.01 (d$_{hyd}$ = 226.57 ± 0.85 nm). Consequently, this ensures the use of relatively

64   homogeneous agglomerates for the nickel loading procedure. Post-loading, the hydrodynamic diameter increases

65   to approximately 1000 nm, as the nickel-loaded MNPs arre resuspended in the buffer utilized for incubation with

66   the linker-protein labeled yeast cells (Fig. S1 n).

67   The process of nickel loading is notably time-intensive, requiring approximately two hours. Improving the efficiency

68   of the overall labeling process, we assessed whether nickel-loaded particles could be stored for several days and

69   subsequently reused. This involved monitoring the hydrodynamic diameter over a three-day storage period, as

70   presented in Fig. S1 o. The findings suggest that a consistent hydrodynamic diameter cannot be maintained, as the

71   distribution indicates a reduction in the hydrodynamic diameter throughout the storage. This reduction implies that,

72   even during storage, the agglomerates persist in achieving equilibrium within the buffer. Consequently, the MNPs

73   were freshly loaded with nickel ions before each fractionation iteration to ensure reproducible agglomerate sizes.

74   **B Homogenization of magnetically labeled yeast cells during the fractionation process**

75   Maintaining a consistent sample concentration flowing into the chip was essential in optimizing the magneto-

76   responsive fractionation process since the magnetic dipole moment modulates the magnetophoretic force acting

77   upon the labeled yeast cells. This moment is a function of both concentration and agglomerate size, as described in

78   Equation 1.

79   The brewing industry uses top-fermenting *S. cerevisiae* and bottom-fermenting *S. pastorianus* var. *carlsbergensis*

80   for ale and lager production. Both encompass strains that flocculate or remain single cells, influencing the aroma

81   formation and reuse after fermentation [11,12]. The sedimentation rate is primarily influenced primarily by the strain's

82   flocculation characteristics within minutes [13,14]. Although the strain employed in this study was non-flocculating,

83   consisting mainly of single cells or budding cells (Fig. 2 f and S2 a), they tend to sediment due to buoyancy depending

84   on the cell (agglomerate) size (Fig. S2 c). Fig. S3 a illustrates the sedimentation behavior of yeast cells within the

85   sample syringe before their introduction into the millifluidic chip. Notably, the yeast cells exhibited significant

86   sedimentation without any dispersion method (when stationary). Within 20 min, they settled to a proportion 0.27

87   ± 0.4 of their initial count, leading to an inhomogeneous yeast concentration during fractionation. Consequently, a

88 dispersion method ensures homogeneity throughout the fractionation process. Previous studies used conventional
89 magnetic stirring for mixing inside the syringe [15], but these were incompatible due to their interference with the
90 MNPs. Therefore, alternative dispersion strategies were explored. This sphere facilitates direct mechanical mixing
91 inside the syringe when positioned on the rocker. As presented in Fig. S3 a, the shaker does not significantly mitigate
92 sedimentation, especially at higher mixing rates, which induce turbulences within the chip. The rocker results in
93 better dispersion but with variability, maintaining between a proportion of 0.77 ± 0.12 and 0.93 ± 0.15 of the initial
94 yeast cell number. Introducing a sphere within the syringe emerges as the most efficient approach. With the sphere's
95 motion enabled by the teetering rocker, yeast cells are uniformly dispersed, preserving nearly 100 % of the initial
96 yeast cell number. Importantly, this method does not comprise yeast cell viability: 75 ± 14 % of cells are viable pre-
97 insertion and 79 ± 13 % post-process without affecting the magnetic labeling of the yeast cells (Fig. S2 b).

98 **C Magnetic aggregation and magnetically induced convection**

99 The cooperative motion is quantified by the dimensionless aggregation parameter N^*, influenced by the volume
100 fraction Φ_0 in the solution, and the magnetic coupling parameter Γ are expressed as,

$$N^* = \sqrt{\Phi_0\, e^{(\Gamma - 1)}} \tag{S1}$$

$$\Gamma = \frac{\mu_0 m^2}{2\pi d^3 k_B T} \tag{S2}$$

101 Where $\mu_0 = 4\pi \times 10^{-7}$ N A^{-2} is the magnetic permeability of free space, $\vec{m}$ the induced magnetic dipole moment, k_B
102 $= 1.38 \times 10^{-23}$ J K^{-1} is Boltzmann's constant and T is the absolute temperature. In line with the observations made by
103 Leong et al., field-induced self-assembly of particles is not anticipated to occur when the dimensionless aggregation
104 parameter is $N^* < 1$.
105 The second dimensionless number, characterizing the motion of MNPs when exposed to a magnetic field, is the
106 magnetic Grashof number Gr_m, accounting for the induced convective motion, given by

$$Gr_m = \frac{\rho \nabla B \left(\frac{\partial M}{\partial c}\right)_H (c_s - c_\infty) L_c^3}{\eta^2} \tag{S3}$$

107 Where ρ is the density, $\vec{\nabla}B$ is the magnetic field gradient within the magnetic field strength B, M is the volumetric
108 magnetization in solution. c_s is the particle concentration at the collection plane, c_∞ is the one in the sample
109 solution, and L_c is the characteristic length of the system subjected to magnetophoresis, which is the chip width in
110 our case.
111 The following values are used for calculating the magnetic Grashof number and the aggregation parameter:
112

Magnetization at 0.38 T [A m^{-1}]	28450.88
Particle diameter d [m]	9.68x10^8
Particle volume [m^{-3}]	4.75x10^{22}
Volume all particles in system [m^3]	3.89x10^6
Density particles, 22°C [g L^{-1}]	2800.80
Density water, 22°C [g L^{-1}]	997.77
Density system ρ [g L^{-1}]	998.03
Particle volume fraction φ	0.00015
Coupling parameter Γ	1.36x10^{28}
Magnetic field gradient at collection surface ∇B [T m^{-1}]	4.82
Volumetric magnetization of solution M [(A m^{-1}) (g L^{-1})$^{-1}$]	10.16
Particle concentration at collection plane c_s [g L^{-1}]	0
Particle concentration of bulk solution c_∞ [g L^{-1}]	0.4
Characteristic length of system L_c [m]	0.00313
Viscosity η [kg ms^{-1}]	0.00010
Chip volume [m^3]	0.02721

113

114

3

B Figures and Tables

124 (k). Zeta potential for the precursor APTES-coated and final EDTA-functionalized IONs and those saturated with nickel ions for different pH values ($c_{Particles}$ = 1 g
125 L^{-1}) (l). Cumulative velocity distribution over the magnetophoretic sedimentation velocity for the precursor APTES-coated (pH = 9.1) and final EDTA-functionalized
126 (pH = 4.89) IONs in water after synthesis ($c_{Particles}$ = 1 g L^{-1}) (m). DLS measurement of the MNP solution in water after storage (black), after dispersion (blue) before
127 the nickel loading, and before labeling, but after nickel loading (red) in the necessary concentrations of the protocol (n). Number distribution of the DLS
128 measurement for a storage study of the nickel-loaded MNPs in buffer over three days (o). Error bars or shaded areas represent the standard deviation of a
129 triplicate measurement.

130

131
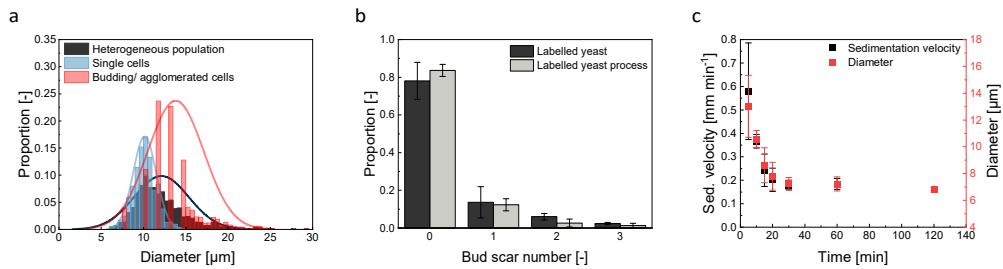
132 Fig. S2 Yeast cell diameter of a heterogeneous population derived from ImageJ analysis of n = 1168 cells containing 45 % single cells and 55 % buddying/
133 agglomerated cells (a). Age distribution of a magnetically labeled heterogeneous yeast culture derived from cytometric analysis (n_{min} = 20000 counts, n = 3, error
134 bars representing the standard deviation of the triplicate measurement) before the process (black) and in during the process with the dispersion via the rocker
135 and the sphere (b). Sedimentation velocity and corresponding yeast cell (agglomerate) diameter over time at 410 nm (c). Error bars represent the standard
136 deviation of a triplicate measurement.

137

138
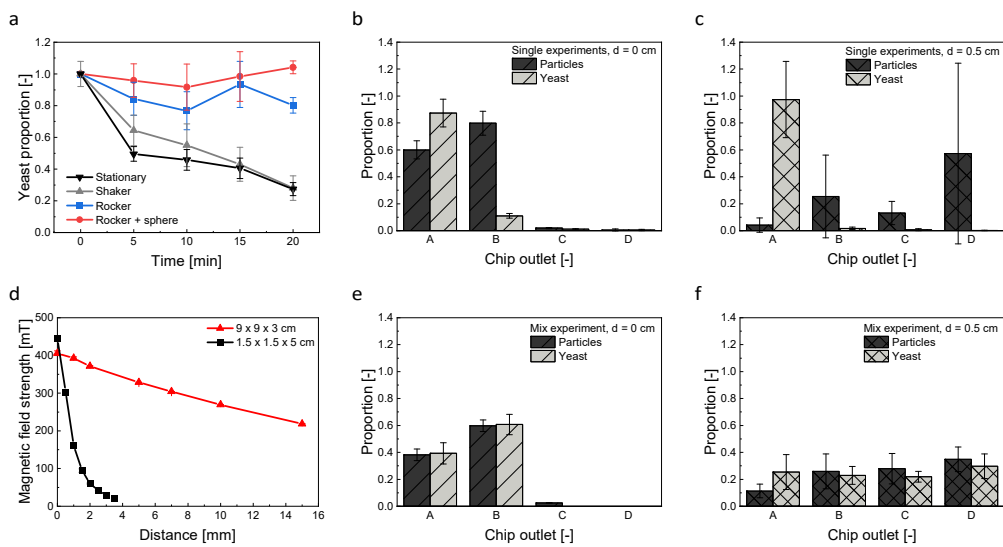
139 Fig. S3 Yeast proportion of the initial cell number of 1.58x10^7 cells mL^{-1} in sample syringes over time for different dispersion methods using no dispersion method
140 (stationary), a shaker, a rocker, and an inserted sphere in the sample syringe positioned on the rocker to avoid sedimentation (a). Single fractionation experiments
141 for solely yeast and particles (b) and (c) and for yeast-particle mixture without linker-protein (e) and (f) in the rectangular geometry. Chip outlet A was the furthest
142 away from the magnet; chip outlet D was nearest to the magnet. V_{Sample} = 220 µL min^{-1}, V_{Buffer} = 1840 µL min^{-1}, the magnet distance was 0 cm (a) and (d). V_{Sample}
143 = 220 µL min^{-1}, V_{Buffer} = 920 µL min^{-1}, the magnet distance was 0.5 cm, $c_{Particle}$ = 0.4 g L^{-1}, cell number = 1.59x10^7 cells mL^{-1} (b) and (e). Measured magnetic field
144 strength using an AC/DC magnetometer (PCE Instruments) over the distance from the magnet surface at the middle for the used magnets (9 x 9 x 3 cm for the
145 rectangular and 1.5 x 1.5 x 5 cm for the trapezoidal geometry) (d). All data plots include the standard deviation from a triplicate measurement.

146

147

148

5
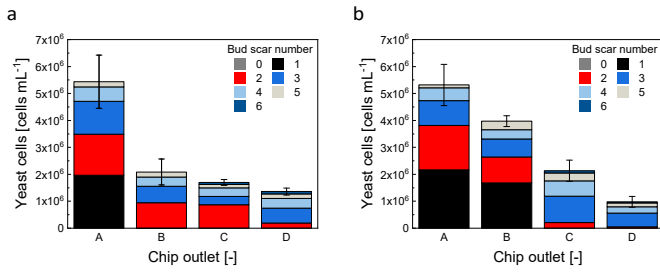
149 Fig. S4: Reproduction of the yeast cell fractionation with the pinch-shaped geometry. Yeast cell concentrations for the different fractions and corresponding bud
150 scar numbers are shown. $c_{Particle}$ = 0.4 g L^{-1}, cell number = 1.59x10^7 cells mL^{-1}. Error bars represent the standard deviation of the triplicate measurement. Outlet A
151 was the furthest away from the magnet; outlet D was the nearest to the magnet. Daughter and mother cells refer to the prior batch separation.
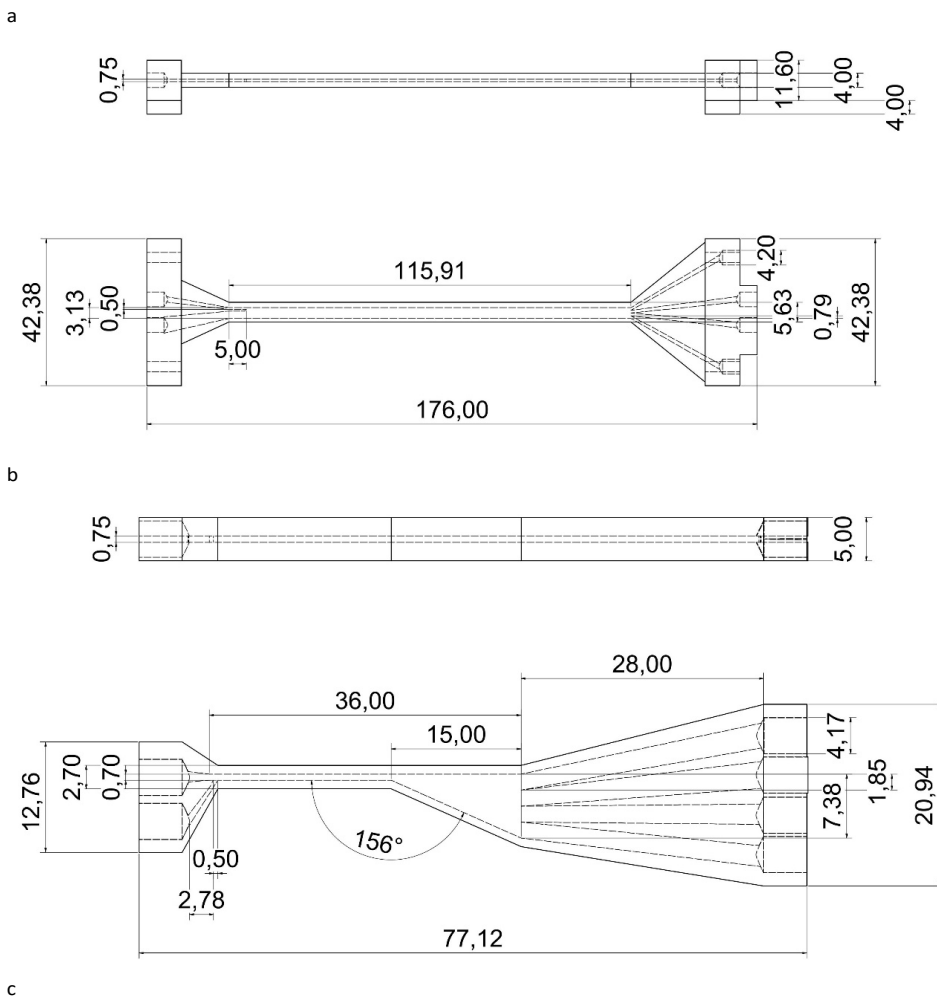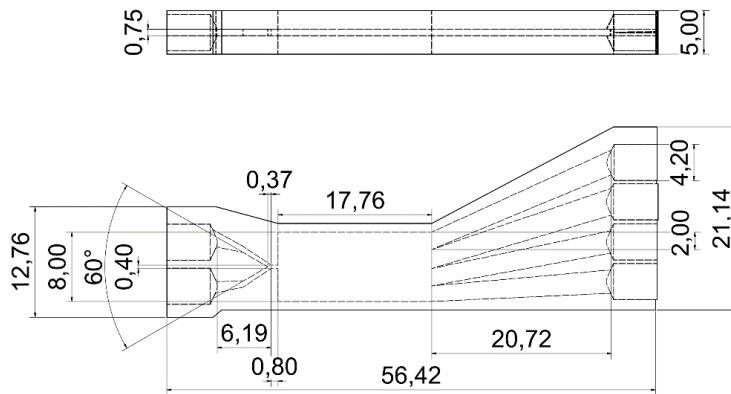
152   Fig. S5 Technical drawings in [mm] of the rectangular (a), trapezoidal (b), and pinch-shaped (c) chip.
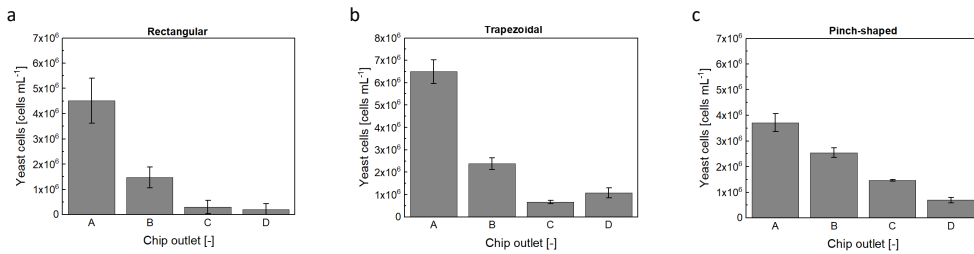
Fig. S6: Yeast cell concentration for different fractionations with different flow channels (rectangular (a), trapezoidal (b), pinch-shaped (c)). The yeast cells were not labeled with linker-protein or MNPs. Error bars represent the standard deviation of the triplicate measurement. Outlet A was the furthest away from the magnet; outlet D was the nearest to the magnet.

153

154

155   Tab. S1: Separation selectivities for the different chip geometries derived from the cumulative bud scar number distribution related to the cell number in each
156   chip outlet. The rectangular and trapezoidal geometry fractionation was performed once, and the pinch geometry process was conducted three times.

Chip outlet	Bud scar number n	Rectangular	Trapezoidal	Pinch
A	≥ 1	0.48	0.48	1.00 ± 0.00
B	≥ 2	0.94	0.95	0.95 ± 0.02
C	≥ 3	0.96	0.40	0.97 ± 0.00
D	≥ 4	0.66	0.34	0.84 0.08

157

C Methods

159   **A Comparison between microscopic determined bud scar distribution and flow cytometric analysis.**

160 To ensure the reliability of flow cytometric results on bud scar distribution in heterogeneous yeast populations and
161 associated outlet distributions, we proposed two distinct measurement methodologies, described earlier in detail
162 [1,16,17]:

163

164   1.   Microscopy-based approach:
165 This involved manual counting of bud scars via confocal and light microscopy and subsequent predictions using the
166 Bayes theorem. The method followed the protocol by Eigenfeld et al. [17], which postulates that only 40% of the yeast
167 cell surface was observable through microscopy. Consequently, predictions had to be made for the remaining 60%
168 of the cell surface where bud scars were unobservable.
169   1.   Flow cytometric approach [16]:
170   a.   Outlier elimination using the R package 'mvoutlier'.

7

171   b.   Autofluorescence predictions via the Random Forest algorithm.

172   c.   Single-cell autofluorescence subtraction from each yeast cell.

173   d.   Analysis of the resultant fluorescence signals via Gaussian histogram curve fitting (Fig. S6).

174   Notably, each Gaussian curve corresponds to an age cluster, symbolizing cells with an identical

175   count of bud scars.

176 This comparative study aids in validating the flow cytometric determinations against a microscopy-based reference.

177 The results showed no noTab. differences between the two measurement methods in terms of heterogeneous

178 populations (p-value = 0.9375), mother cells (p-value = 0.8125), and daughter cells (p-value = 0.5781) when a

179 Wilcoxon paired test was employed. Furthermore, through the automated Gaussian mixture analysis provided by

180 the R package 'GaussianMixture', we found p-values of 1 for both heterogeneous populations and mother cells and

181 a p-value of 0.4609 for daughter cells.
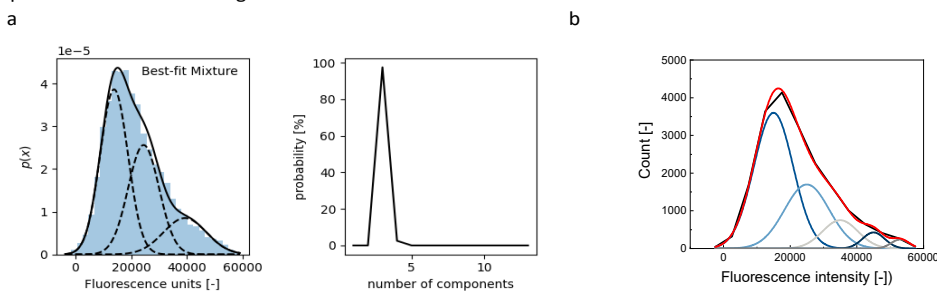
182 Fig. S7 Gaussian mixture analysis using R package 'GaussianMixture' (a) and using OriginLabs 2021 (R1 = 0.9995) (b) for a heterogeneous population.

183 **B Primer sequences for quantitative polymerase chain reaction experiments**

184 Tab. S2: Primer sequences of ones used to amplify the housekeeping genes.

TAF10	forward primer	TAACAACAGTCAGGCGAGAG
	reverse primer	CACCGTCAGAACAACTTTGC
KRE11	forward primer	ATTCGCCCTTGACACTGG
	reverse primer	CTCTCGGAGGTACAACTG
UBC6	forward primer	ATGCGGCAAATACAGGTGATG
	reverse primer	TTGTTCAGCGCGTATTCTGTC

185

186 Tab. S3: Primer sequences of the tested genes.

Gene		Primer sequence
MEP2	forward primer	ACGAGGAATCCACTGCTTAC
	reverse primer	CGTCTGTGTTACCCACAATC
HSP104	forward primer	TAACTCAAGAGGCCAAGGAC
	reverse primer	TCCTTAGTGCCAGTTTGTTC
HXK2	forward primer	GGCTGCCAATGCTTTGAAGG
	reverse primer	ACCGGAACCATCTTCAGCAG
HSP12	forward primer	CTCTGCCGAAAAAGGCAAGG
	reverse primer	GACGGCATCGTTCAACTTGG
PHO5	forward primer	TTCAACATCACCTTGCAGAC
	reverse primer	ATTGGCATCGTAGTCCCAAG
ADH1	forward primer	GTGCTCACGGTGTCATCAAC
	reverse primer	GCATACCGACCAAAACGGTG
GCR1	forward primer	CCAAACAACGACTCCACTAC
	reverse primer	ATCATTGGGCTCCGACTTAC

187

188 **C Minimum information for publication of quantitative real-time polymerase chain reaction experiments guidelines**

189 Tab. S4: Minimum information for publication of quantitative real-time polymerase chain reaction experiments (MIQE) checklist for authors, reviewers, and editors. All essential information (E) must be submitted with the manuscript. Desirable information
190 (D) should be submitted if available. If using primers obtained from RTPrimerDB, information on quantitative polymerase chain reaction (qPCR) target, oligonucleotides, protocols, and validation was available from that source.

9

ITEM TO CHECK	IMPORTANCE	CHECKLIST
EXPERIMENTAL DESIGN		
Definition of experimental and control groups	E	control group: Sample A, youngest fraction
Number within each group	E	3 Biological replicates
Assay carried out by core lab or investigator's lab?	D	
Acknowledgement of authors' contributions	D	
SAMPLE		
Description	E	Yeast cells, separated for cell age
Volume/mass of sample processed	D	
Microdissection or macrodissection	E	not applicable
Processing procedure	E	After separation, cells were submerged in 1/3 vol. 5% phenol in abs. ethanol and frozen
If frozen - how and how quickly?	E	
If fixed - with what, how quickly?	E	5 % Phenol in absolute Ethanol, 1:3 with liquid sample, directly after cell fractionation
Sample storage conditions and duration (especially for FFPE samples)	E	Samples were stored at -80°C in 2/3 separation buffer and 1/3 vol. 5% phenol in abs. ethanol
NUCLEIC ACID EXTRACTION		
Procedure and/or instrumentation	E	Enzymatic cell lysis with subsequent spin column extraction
Name of kit and details of any modifications	E	Roboklon Universal RNA Kit, Roboklon GmbH, Berlin, Germany
Source of additional reagents used	D	
Details of DNase or RNAse treatment	E	None, as per protocol
Contamination assessment (DNA or RNA)	E	Denaturing RNA gel electrophoresis for degradation, no-reverse-transcription control in the qPCR
Nucleic acid quantification	E	Sheet_3
Instrument and method	E	Nanodrop 2000c spectrophotometer
Purity (A260/A280)	D	
Yield	D	
RNA integrity method/instrument	E	MOPS-Gel electrophoresis
RIN/RQI or Cq of 3' and 5' transcripts	E	not applicable
Electrophoresis traces	D	
Inhibition testing (Cq dilutions, spike or other)	E	not applicable due to small sample volume

REVERSE TRANSCRIPTION		
Complete reaction conditions	E	Thermo Scientific™ Maxima H Minus Reverse Transcriptase, according to manufacturer protocol, with 200 U of enzyme per reaction
Amount of RNA and reaction volume	E	1849.5 ng/µL, Samples 6: 810 ng/µL, Samples 7: 483.3 ng/µL; rection volume 20 µL
Priming oligonucleotide (if using GSP) and concentration	E	NEB Oligo dT VN
Reverse transcriptase and concentration	E	Thermo Scientific™ Maxima H Minus Reverse Transcriptase, 200 U of enzyme per reaction
Temperature and time	E	30 min at 50°C
Manufacturer of reagents and catalog numbers	D	
Cqs with and without RT	D*	
Storage conditions of cDNA	D	
qPCR TARGET INFORMATION		
If multiplex, efficiency and LOD of each assay.	E	not applicable
Sequence accession number	E	Sheet_2
Location of amplicon	D	
Amplicon length	E	Sheet_2
In silico specificity screen (BLAST, etc.)	E	Primer BLAST, https://www.ncbi.nlm.nih.gov/tools/primer-blast/
Pseudogenes, retropseudogenes, or other homologs?	D	
Sequence alignment	D	
Secondary structure analysis of amplicon	D	
Location of each primer by exon or intron (if applicable)	E	only exons targeted
What splice variants were targeted?	E	not applicable
qPCR OLIGONUCLEOTIDES		
Primer sequences	E	Sheet_2
RTPrimerDB Identification Number	D	
Probe sequences	D**	
Location and identity of any modifications	E	not applicable
Manufacturer of oligonucleotides	D	
Purification method	D	
qPCR PROTOCOL		

11

Complete reaction conditions	E	Biozym Blue S'Green qPCR Mix Separate ROX
Reaction volume and amount of cDNA/DNA	E	10 µL
Primer (probe), Mg++ and dNTP concentrations	E	Primer conc. 400 nM each
Polymerase identity and concentration	E	Manufacturer Master Mix
Buffer/kit identity and manufacturer	E	Biozym Blue S'Green qPCR Mix Separate ROX, Biozym Scientific GmbH
Exact chemical constitution of the buffer	D	
Additives (SYBR Green I, DMSO, etc.)	E	SYBR Green
Manufacturer of plates/tubes and catalog number	D	
Complete thermocycling parameters	E	Initial denaturation: 2 min, 95°C; 45x 5 sec, 95°C, 30 sec, 60°C
Reaction setup (manual/robotic)	D	
Manufacturer of qPCR instrument	E	Roche LightCycler 480 II
qPCR VALIDATION		
Evidence of optimization (from gradients)	D	
Specificity (gel, sequence, melt, or digest)	E	Melting curve, single peaks for all reactions
For SYBR Green I, Cq of the NTC	E	37.11
Standard curves with slope and y-intercept	E	
PCR efficiency calculated from slope	E	
Confidence interval for PCR efficiency or standard error	D	
r2 of standard curve	E	
Linear dynamic range	E	
Cq variation at lower limit	E	
Confidence intervals throughout range	D	
Evidence for limit of detection	E	
If multiplex, efficiency and LOD of each assay.	E	not applicable
DATA ANALYSIS		
qPCR analysis program (source, version)	E	LightCycler 480 Software release 1.5.0; qbase+, V3.4
Cq method determination	E	Proprietary Roche LighCycler
Outlier identification and disposition	E	according to qbase+
Results of NTCs	E	

Justification of number and choice of reference genes	E	according to geNorm V and geNorm M
Description of normalization method	E	Modified Pfaffl Method, according to Hellemans et al., implemented in qbase+
Number and concordance of biological replicates	D	
Number and stage (RT or qPCR) of technical replicates	E	technical duplicates in the qPCR
Repeatability (intra-assay variation)	E	not applicable
Reproducibility (inter-assay variation, %CV)	D	
Power analysis	D	
Statistical methods for result significance	E	One-way ANOVA
Software (source, version)	E	Biogazelle qbase+, V3.4
Cq or raw data submission using RDML	D	

191
192 *: Assessing the absence of DNA using a no RT assay was essential when first extracting RNA. Once the sample had been validated as RDNA-free, the inclusion of a no-RT control was
193 desirable but no longer essential.
194 **: Disclosure of the probe sequence was highly desirable and strongly encouraged. However, since not all commercial pre-designed assay vendors provide this information, it cannot
195 be an essential requirement. Use of such assays was advised against.
196

197

198

199

200

201

202

203

D Data analysis of the metabolome and gene expression

In Fig. 5, the metabolome and gene expression data are normalized to outlet A of the pinch shaped fractionation, and not to the daughter cells. This distinction is essential, as the daughter cells were separated prior to the millifluidic fractionation to avoid the magnetically induced co-migration. Consequently, direct comparisons between the separated daughter cells and the older fractionated cells are not feasible for two reasons. First, the daughter cells were not fractionated in the chip and, therefore, did not undergo 'sorting stress.' Second, they were fixed at varying time points due to the multi-step experimental process.
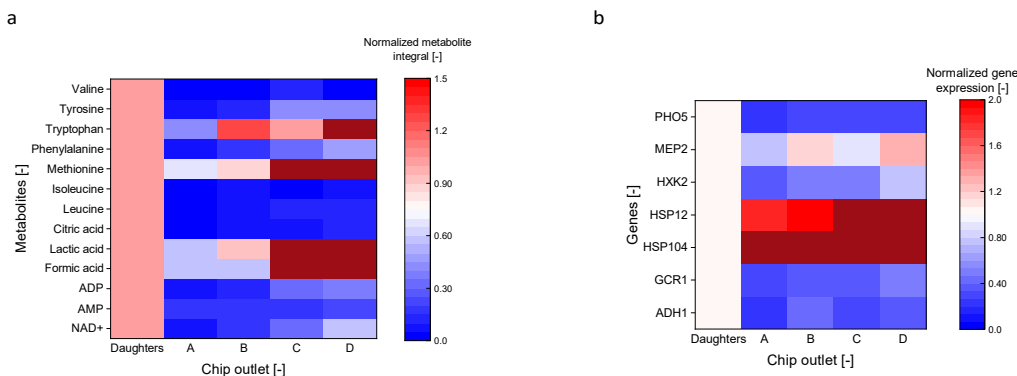
Fig. S8 Heat map depicting the normalized integral area of selected metabolites (a) and gene expression (b) against the cell fraction. Normalized to the daughter cells. Data included from a triplicate measurement.

References

1   M. Eigenfeld, L. Wittmann, R. Kerpes, S. P. Schwaminger and T. Becker, *Biotechnol. J.*, , DOI:10.1002/biot.202200610.

2   C. Turrina, S. Berensmeier and S. P. Schwaminger, *Pharmaceuticals*, , DOI:10.3390/ ph14050405.

3   S. E. Favela-Camacho, E. J. Samaniego-Benítez, A. Godínez-García, L. M. Avilés-Arellano and J. F. Pérez-Robles, *Colloids Surfaces A Physicochem. Eng. Asp.*, 2019, **574**, 29–35.

4   L. Wittmann, C. Turrina and S. P. Schwaminger, *Magnetochemistry*, 2021, **7**, 80.

5   D. Salman, T. Juzsakova, M. A. Al-Mayyahi, R. Akos, S. Mohsen, R. I. Ibrahim, H. D. Mohammed, T. A. Abdullah, E. Domokos and T. Korim, *J. Phys. Conf. Ser.*, 2021, **1773**, 0–12.

6   Y. Liu, R. Fu, Y. Sun, X. Zhou, S. A. Baig and X. Xu, *Appl. Surf. Sci.*, 2016, **369**, 267–276.

7   I. Dindarloo Inaloo, S. Majnooni, H. Eslahi and M. Esmaeilpour, *Appl. Organomet. Chem.*, 2020, **34**, 1–17.

8   T. S. Hamidon and M. H. Hussin, *Prog. Org. Coatings*, 2020, **140**, 105478.

9   P. Fraga García, M. Freiherr Von Roman, S. Reinlein, M. Wolf and S. Berensmeier, *ACS Appl. Mater. Interfaces*, 2014, **6**, 13607–13616.

10 J. Chen, Y. Hao and M. Chen, *Environ. Sci. Pollut. Res.*, 2014, **21**, 1671–1679.

11 G. G. Stewart, *Fermentation*, , DOI:10.3390/fermentation4020028.

12 K. J. Verstrepen, G. Derdelinckx, H. Verachtert and F. R. Delvaux, *Appl. Microbiol. Biotechnol.*, 2003, **61**, 197–205.

13 E. V. Soares and M. Mota, *J. Inst. Brew.*, 1997, **103**, 93–98.

14 M. Stratford, *Adv. Microb. Physiol.*

15 R. Sánchez, B. Horstkotte, K. Fikarová, H. Sklenářová, S. Maestre, M. Miró and J. L. Todolí, *Anal. Chem.*, 2017, **89**, 3787–3794.

16 M. Eigenfeld, R. Kerpes, I. Whitehead and T. Becker, *Biotechnol. J.*, , DOI:10.1002/biot.202200091.

17 M. Eigenfeld, R. Kerpes and T. Becker, *RSC Adv.*, 2021, **11**, 31923–31932.

A.2 Permissions

A.2.1 The Effect of pH and Viscosity on Magnetophoretic Separation of Iron Oxide Nanoparticles

All articles published by MDPI are made immediately available worldwide under an open access license. This means:

- Everyone has free and unlimited access to the full-text of all articles published in MDPI journals;

- Everyone is free to re-use the published material if proper accreditation/citation of the original publication is given;

- Open access publication is supported by the authors' institutes or research funding agencies by payment of a comparatively low Article Processing Charge (APC) for accepted articles.

No special permission is required to reuse all or part of article published by MDPI, including figures and tables. For articles published under an open access Creative Common CC BY license, any part of the article may be reused without permission provided that the original article is clearly cited. Reuse of an article does not imply endorsement by the authors or MDPI.

A.2.2 Magnetophoresis in Microfluidic Applications: Influence of Magnetic Convection in Hydrodynamic Fields

Nanoscale is a hybrid (transformative) journal and gives authors the choice of publishing their research either via the traditional subscription-based model or instead by choosing our gold open access option. For authors who want to publish their article gold open access, Nanoscale charges an article processing charge (APC) of £3,000 (+ any applicable tax). Our APC is all-inclusive and makes your article freely available online immediately, permanently, and includes your choice of Creative Commons licence (CC BY or CC BY-NC) at no extra cost. It is not a submission charge, so you only pay if your article is accepted for publication.

A.2.3 Studying the Impact of Cell Age on the Yeast Growth Behaviour of *Saccharomyces pastorianus var. carlsbergensis* by Magnetic Separation

### A.2.4 Millifluidic Magnetophoresis-based Chip for Age-specific Fractionation: Evaluating the Impact of Age on Metabolomics and Gene Expression in Yeast

A.3 Figures
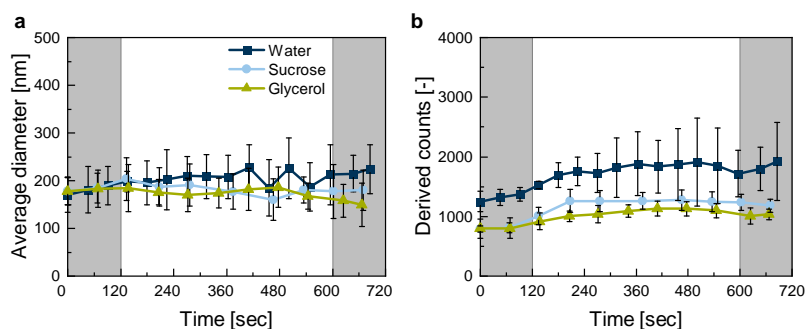
Figure A.1: DLS kinetic measurement of silica-coated MNPs (c = 1 g L^{-1}) at pH = 7 in water (η = 0.888 mPas), glycerol, or sucrose (both η = 2.774 mPas). The sample was measured without the magnetic field for 120 sec (grey area), then it was moved into the homogeneous magnetic field (B = 180 mT) for 480 sec, and finally, the field was removed again for 120 sec. The average diameter corresponds to the intensity-weighted mean hydrodynamic diameter. The standard deviation represents the width of the distribution of a triplicate measurement.
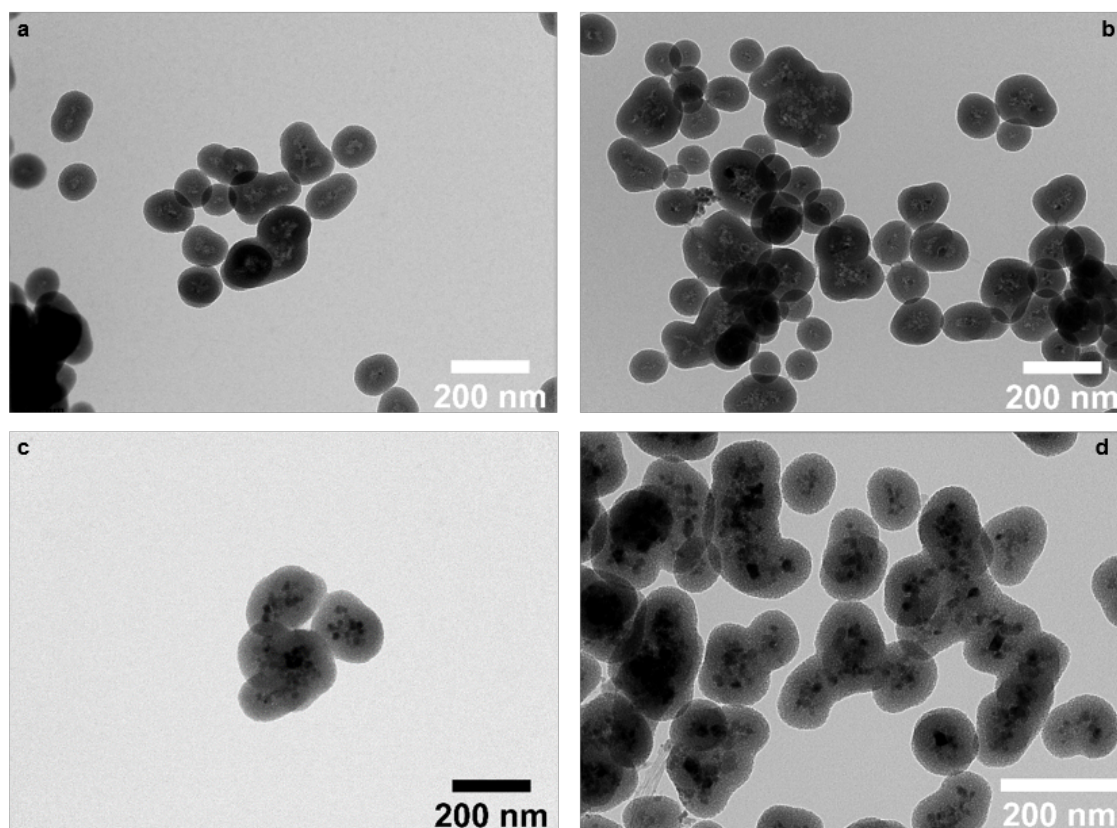
Figure A.2: TEM images for normal ION@Si@EDTA (m$_{BION}$ = 178 mg) synthesized in the 132 kHz (a) and 45 kHz (b) ultrasonic bath at 60k magnification. ION@Si@EDTAs with a thin silic coating (m$_{BION}$ = 235 mg) are shown in (c) and (d), in the 132 kHz and 45 kHz ultrasonic bath, respectively, at 40 k magnification.

195
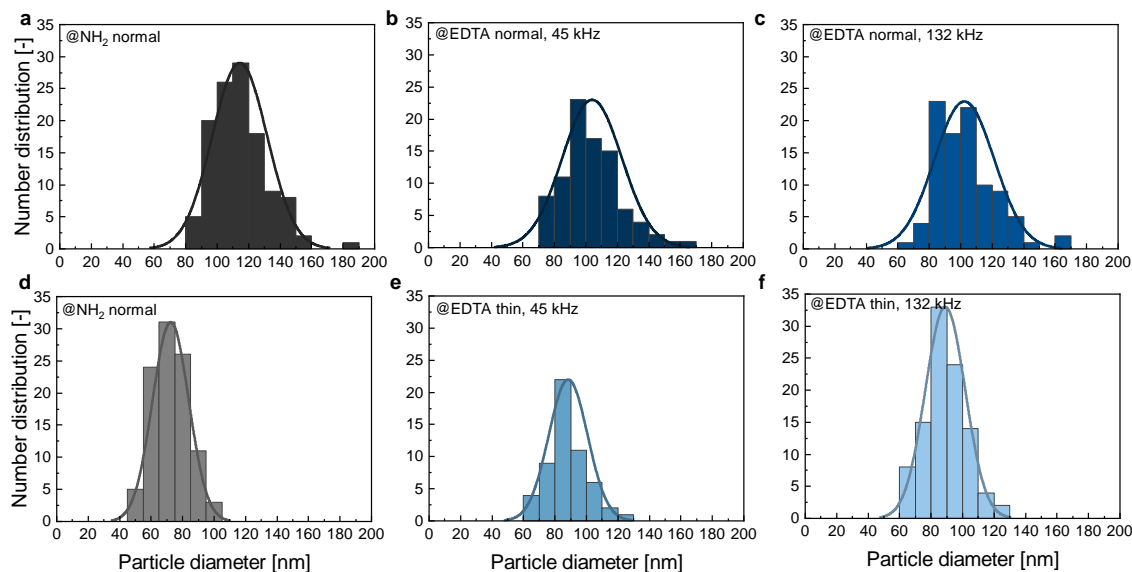
Figure A.3: Number distribution (n = 100) for the primary particle diameter derived from TEM images for the MNP@Si@NH$_2$ (a, d) and ION@Si@EDTA having a normal (m$_{BION}$ = 178 mg) (b, c) and thin (m$_{BION}$ = 235 mg) (e, f) silica shell in the 132 kHz and 45 kHz ultrasonic bath.
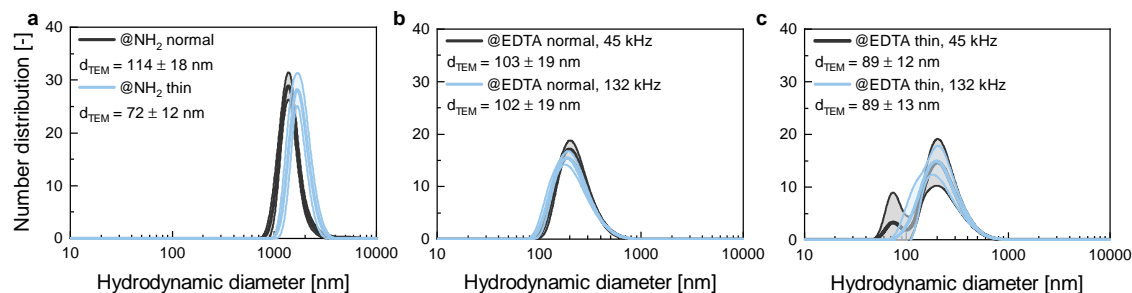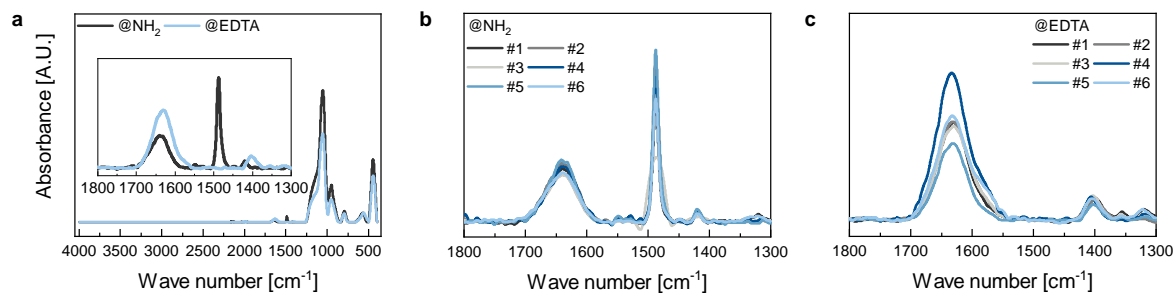

Figure A.4: DLS measurement for the MNP@Si@NH$_2$ (a) and ION@Si@EDTA having a normal (m$_{BION}$ = 178 mg) (b) and thin (m$_{BION}$ = 235 mg) (c) silica shell in the 132 kHz and 45 kHz ultrasonic bath with primary particle diameter derived from TEM analysis (n = 100). The shaded area represents the standard deviation of an analytical triplicate measurement.
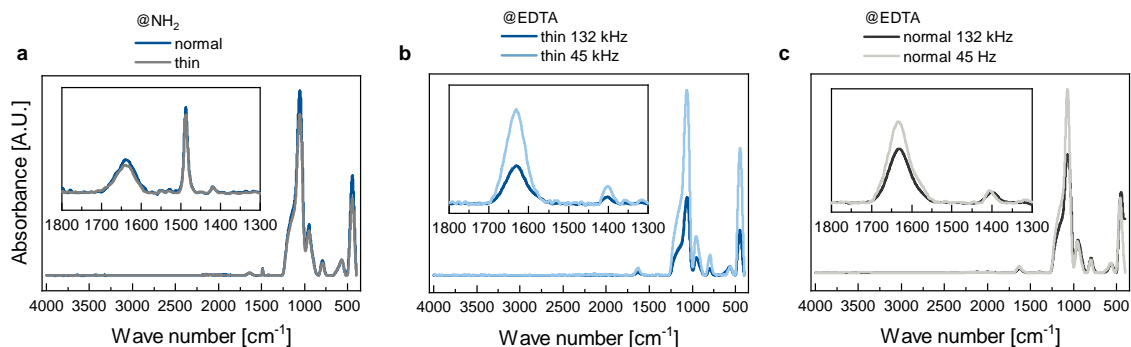
Figure A.5: FT-IR spectra for the MNP@Si@NH$_2$ (a) and ION@Si@EDTA having a thin (m$_{BION}$ = 235 mg) (b) and normal (m$_{BION}$ = 178 mg) (c) silica shell in the 132 kHz and 45 kHz ultrasonic bath.
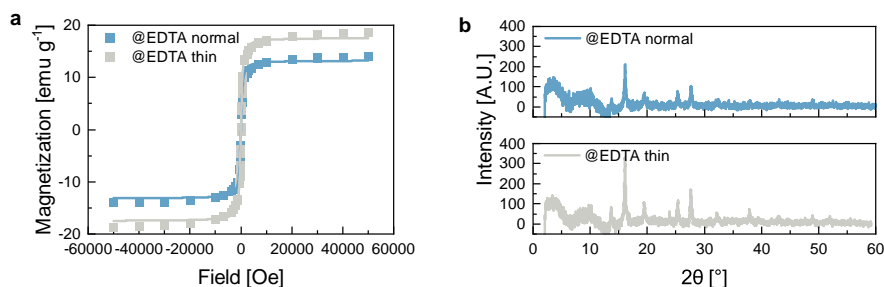
Figure A.6: (a) SQUID measurement ION@Si@EDTA having a normal (m$_{BION}$ = 178 mg) and thin (m$_{BION}$ = 235 mg) silica shell. (b) XRD measurement ION@Si@EDTA having a normal (m$_{BION}$ = 178 mg) and thin (m$_{BION}$ = 235 mg) silica shell.
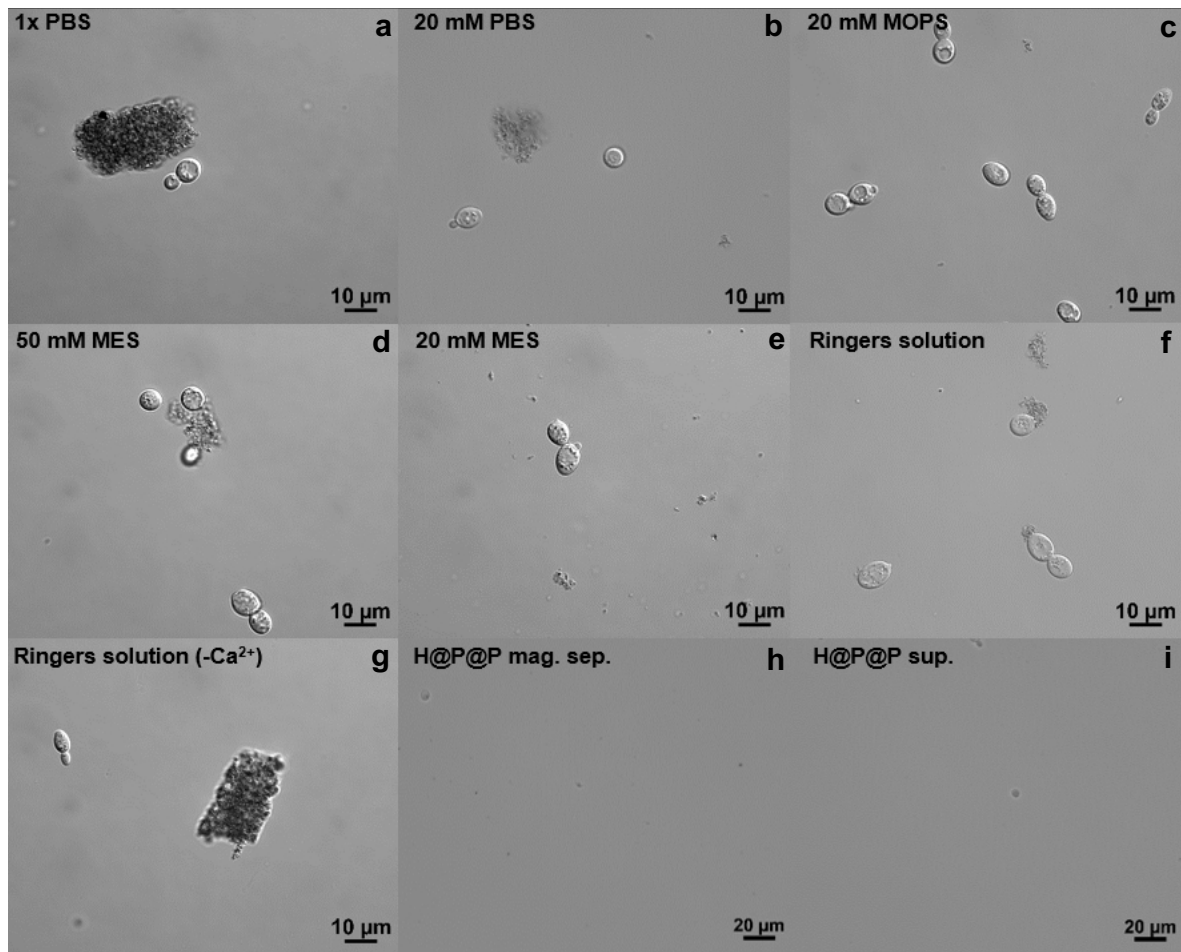

**Figure A.7:** FT-IR spectra for the MNP@Si@NH$_2$ (a, b) and ION@Si@EDTA (a, c) for batch #1 – #6.

197
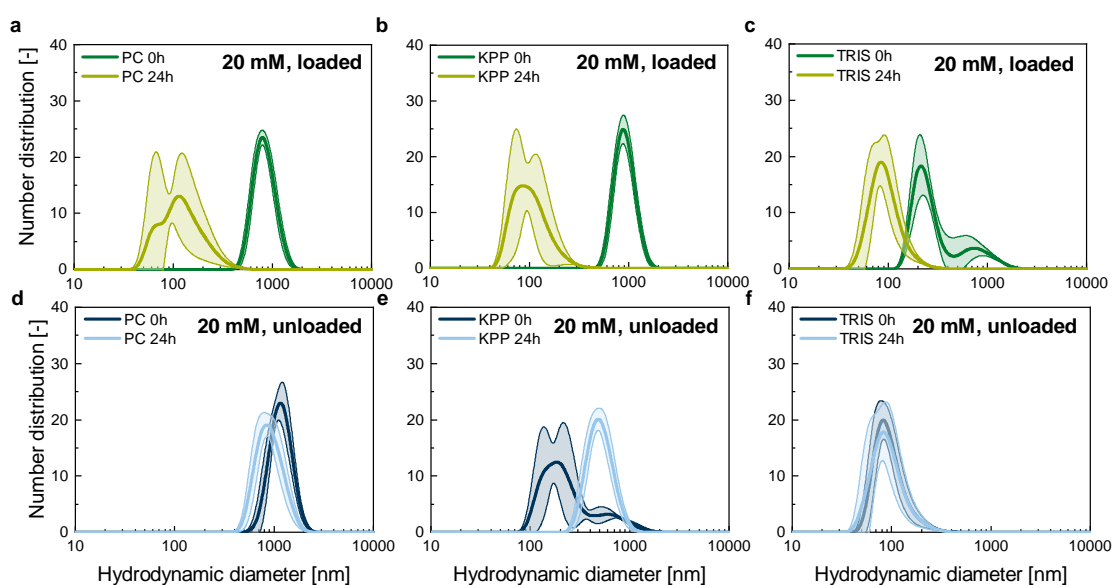
Figure A.8: DLS measurement of ION@Si@EDTAs (c = 1 g L^{-1}) in PC pH = 8, KPP pH = 8, and TRIS pH = 8 at a concentration of c = 20 mM loaded with nickel ions or unloaded measured directly and 24 h after incubation. The shaded area represents the standard deviation of a technical triplicate measurement.

Figure A.9: Light microscopy images of yeast cells incubated with nickel loaded nanoparticles, but without the linker-protein for 1x (a) and 20 mM PBS (b), 20 mM MOPS (c), 50 (d) and 20 mM MES (e) and RS (f, g) with and without linker-protein following the ratios displayed in [211]. (h) and (i) show microscopic images of the magnetically labeled yeast cells after imidazole elution for the magnetically separated fraction containing only nanoparticles and the supernatant fractions containing the unlabeled yeast cells.
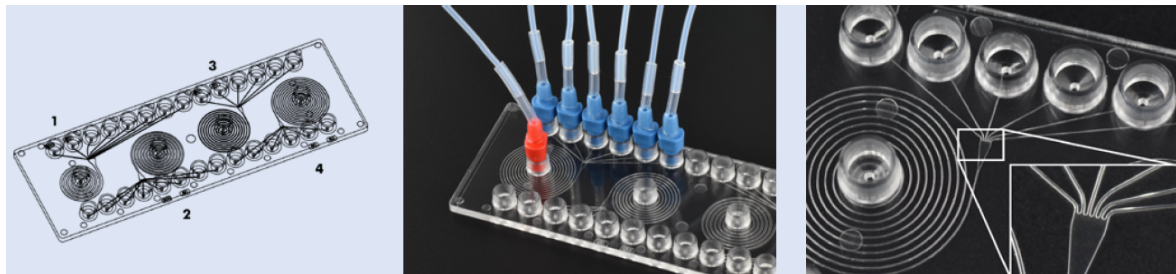

Figure A.10: Spiral sorter *chip Fluidic 382* with different sorting units used for sized-based sorting. Purchased from microfluidic ChipShop GmbH [220].
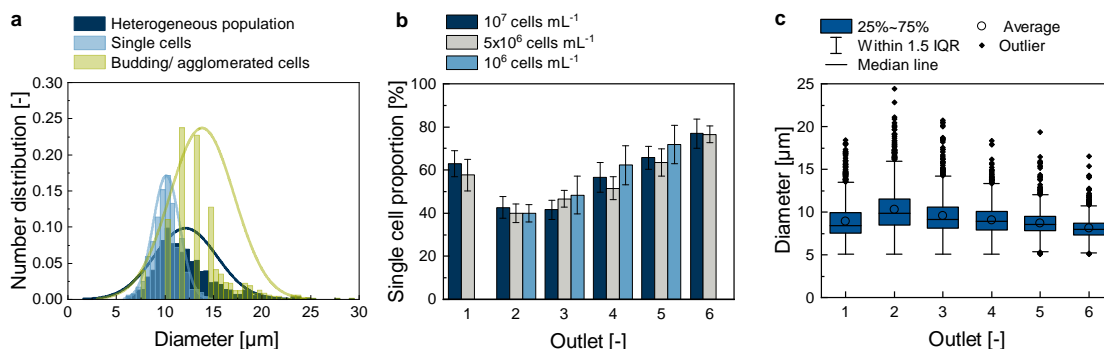
Figure A.11: Yeast cell fractionation using the 500 x 120 µm spiral chip at 1.5 mL min^{-1}. Cell proportion of cells < and > 9 µm are shown for the different outlets for process time t = 5 min. (a) Cell concentration was 10^6 cells, 1051 cells were analyzed per outlet 2 – 5. (b) Cell concentration was 5×10^6 cells, 1374 cells were analyzed per outlet 1 – 6 (c) Cell concentration was 10^7 cells, 1444 cells were analyzed per outlet 2 – 5. Error bar represent standard deviation of a triplicate measurement.
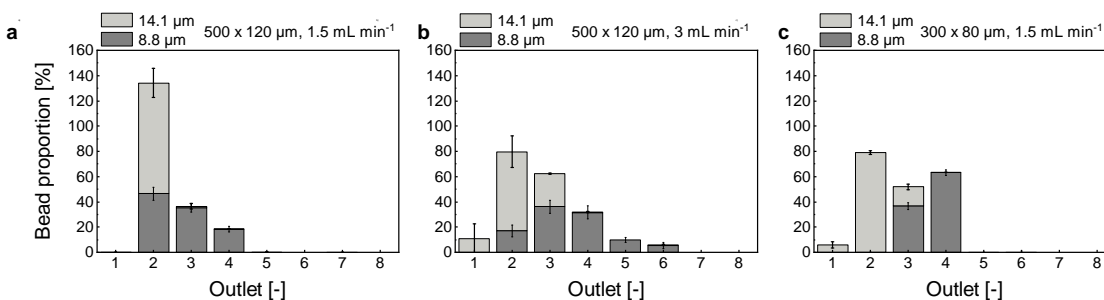
Figure A.12: Theoretical PMMA bead fractionation merged from single bead fractionation úsing 10^6 particles mL^{-1} for each fractionation. Bead proportion for 8.8 and 14.1 µm are shown for the different outlets for process time t = 5 min. (a) Fractionation using the 500 x 120 µm spiral chip at 1.5 mL min^{-1}, (b) the 500 x 120 µm spiral chip at 3 mL min^{-1}, and (c) the 300 x 80 µm spiral chip at 1.5 mL min^{-1}. Error bar represent standard deviation of a triplicate measurement.
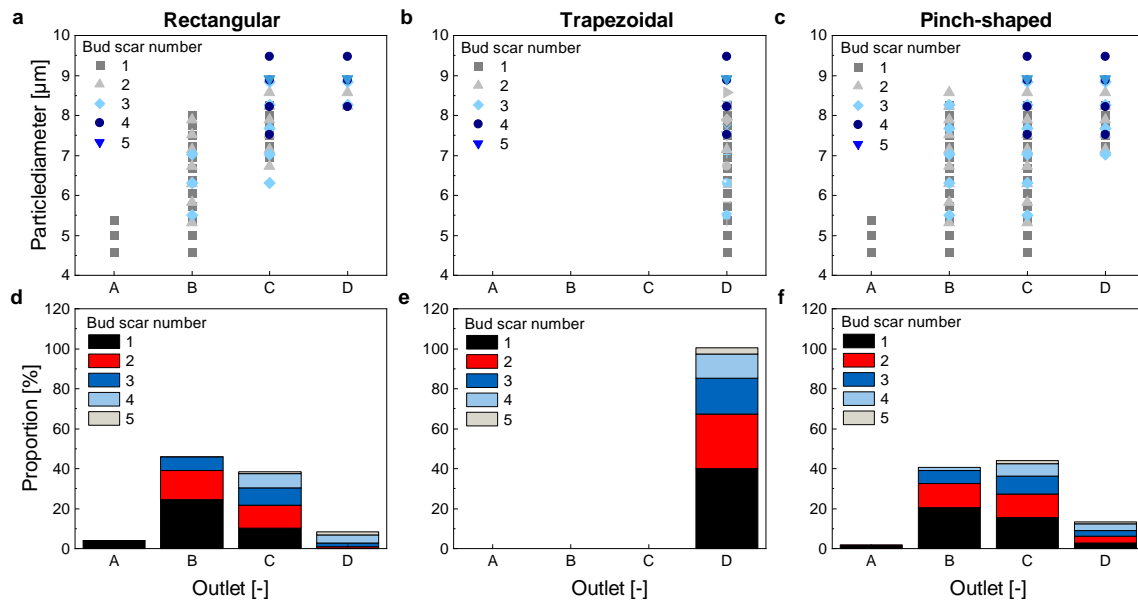
Figure A.13: Simulation of yeast fractionation in a rectangular channel (a) and (d), a trapezoidal channel (b) and (e), and a pinch-shaped channel (c) and (f), using a model of 1000 yeast cells. The simulation follows a grid release approach, with additional details provided in Section A.5. In (a), (b), and (c), the simulated particle diameter of the yeast cell is shown for the different bud scar numbers over the outlets. In (d), (e), and (f), the simulative results of the proportion of the differently aged yeast cells are presented.
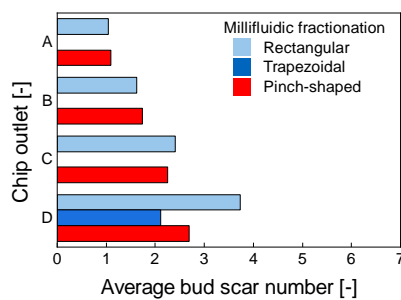
Figure A.14: Average bud scar number for different fractions with different flow channels. The simulation follows the same conditions as described in Figure caption A.13.

A.4 Tables

Table A.1: Separation efficiencies for separating single yeast cells < 9 µm using different process durations, chip dimensions for different outlets. Standard deviation is derived from a triplicate measurement (at least 300 cells per outlet).

Duration [min]	Chip dimensions [µm]	Outlet				
		2	**3**	**4**	**5**	**6**
5	500x120	0.8539 ± 0.0132	0.8695 ± 0.0044	0.8653 ± 0.0041	0.8714 ± 0.0060	0.8699 ± 0.0052
5	300x80	0.8419 ± 0.0139	0.8343 ± 0.0129	0.8370 ± 0.0122	0.8519 ± 0.0178	0.8410 ± 0.0016
10	300x80	0.8346 ± 0.0124	0.8390 ± 0.0134	0.8467 ± 0.0169	0.8460 ± 0.0042	0.8394 ± 0.0098

A.5 Materials and Methods

Agglomeration studies

For the agglomeration studies, a 1 g L^{-1} MNP – buffer suspension was used. The MNP stock solution was always ultrasonicated before usage [109]. After 1 h or 24 h of incubation time, the sample was measured via DLS.

Synthesis balance

For balancing the synthesis, the corresponding volumes were measured with a cylinder, and the iron concentration was measured with the phenanthroline assay, as described in [82].

Spiral sorting

The microfluidic spiral chip employed in these experiments was the "Spiral Chip Fluidic 382" from Microfluidic ChipShop, based in Jena, Germany. This chip features four rectangular channels of varying dimensions, constructed from PMMA. For the purposes of this study, two channels were utilized, specifically those measuring 500 x 120 µm and 300 x 80 µm (width x height). Each spiral is designed with a single inlet and eight outlet channels. The necessary tubing and adapters for operating the chip were provided by the supplier (Figure A.15). It was essential to securely attach the inlet tube and adapter using superglue and duct tape to ensure they could withstand the fluid pressure during the experiments. These

adapters were then carefully connected to the chip. For each experimental run, a new 20 mL syringe was employed. The sample pump, set to 100% force to prevent motor stalling due to back pressure, was consistently used across all experiments involving this chip. To maintain sample homogeneity and prevent sedimentation, the syringe pump was placed on a rocker shaker set at 50 rpm, and a metal sphere (8 mm diameter, silver) was placed inside each syringe. Each of the chip's outlet tubes was positioned to dispense into a separate 5 mL Eppendorf tube. The samples were allowed to drip freely from these tubes, with no additional extraction methods applied at the outlets. The volume of output was determined gravimetrically. Throughout the experimental process, nitrile gloves were worn to minimize the risk of contaminating the microfluidic chip and the Eppendorf tubes. The chip itself was affixed to a platform to ensure stability. Prior to each use, the chip underwent a thorough cleaning process to remove any impurities. This process involved suspending the outlet tubes in a container filled with filtered buffer and drawing the liquid through the chip using an empty 20 mL syringe. Post-cleaning, the condition of the chip's outlets was meticulously checked under a microscope (10x objective) to confirm the absence of contamination. All buffers used in these experiments were sterile-filtered. The yeast cell experiement duration was 5 min, if not stated otherwise.

Yeast cells were prepared as described in Eigenfeld and Wittmann et al. [109]. Following the sorting experiments, the volume of each sample was determined using gravimetry. The samples were then concentrated by centrifuging at 1000 x g for 1 min. Depending on the concentration of the output samples, the excess buffer was carefully removed with a pipette, ensuring that the remaining cell concentration fell within the optimal range of the standard curve, specifically between OD 6 and OD 0.05. To resuspend the cell pellets, each sample was gently agitated until the cells were evenly distributed. Subsequently, 100 µL of each resuspended sample was transferred onto a microplate. The optical density of these samples was measured at 600 nm using a microplate reader, with readings taken in analytical triplicate to ensure accuracy. For cell diameter analysis, a volume of 10 µL from the samples collected from outlets two to six was placed onto microscope slides. Each sample was then covered with a coverslip to prepare for imaging. Photographs of these samples were captured using a 20x objective lens on the microscope. These images were exported in PNG format for further analysis. Image analysis was conducted using ImageJ, a widely recognized image processing software. This step involved careful examination and measurement of cell diameters from the captured images, providing morphological data related to the sorting experiments.

For the PMMA particles, a concentration of 10^6 particles mL^{-1} was chosen because of limited particle availability. The experiment was run for 2 min 50 sec. The absorption was measured at 300 nm in an analytical triplicate using 100 µL. The samples on the microplate were
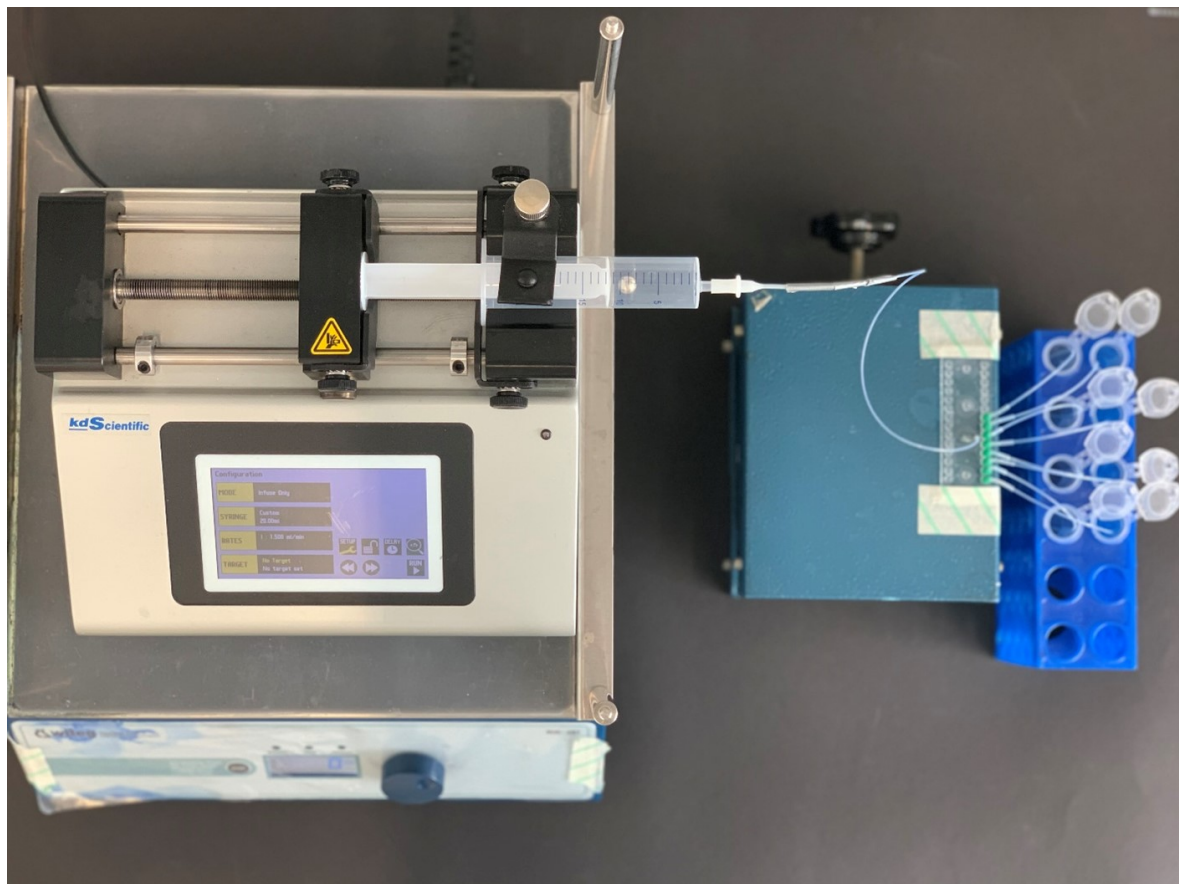
Figure A.15: Experimental setup using the Spiral Chip Fluidic 382 including the sample pump with a 20 mL syringe with an inserted silver sphere (8 mm diameter), placed onto a rocker shaker. Sample were collected in 5 mL Eppendorf tubes.

resuspended with a pipette between each measurement due to the high sedimentation of the particles.

Yeast cell model for finite element simulation simulation

For numerical simulations, COMSOL Multiphysics version 5.6 was used. These simulations were rendered in a three-dimensional format, encompassing three geometric elements: The flow cell, the magnet, and an air sphere. First, the chip geometries were created in 2D format. These sketches were then linked to form curves and subsequently converted into solids. The solids were unified and ultimately extruded to develop the full 3D geometry. The dimensions of the magnets used in the simulations were 90 x 90 x 30 mm (rectangular, pinch-shaped) and 50 x 15 x 15 mm (trapezoidal), while the air sphere had a diameter of 240 mm. To mirror the experimental setup, the magnet was positioned beneath the flow cell at the same distance as in the fractionation experiments [211]. The simulated 20 mM

MOPS buffer solution was assigned properties consistent with those in literature: A relative permeability of $\mu = 1$, a density of $\rho = 997$ kg m^3, and a viscosity of η 0.000891 Pas. The simulation environment was set to a temperature of T $= 298.15$ K, and an "Extremely Fine" mesh was selected. Magnetic fields (mfnc) were defined, and the magnetic field strength was H $= 907500$ A m^{-1} for Q-90-90-30-N and H $= 927500$ A m^{-1} for Q-50-15-15-N. The first study involved a steady-state solution solving for mfnc (magnetic fields no currents) and spf (laminar flow). The second study focused on solving particle tracking in fluid flow (fpt) over time. Inlet velocities for the buffer and sample were defined individually for each geometry, while the outlet pressure was set dependent for all but the rectangular channel (Table A.2). The velocities used in the simulations were derived from experimental flow rates and the cross-sectional area of the inlet, as outlined in Table A.2. In the fpt study, magnetic (F$_{mag}$) and drag (F$_{drag}$) forces acting on the particles were defined. For calculating particle permeability, yeast density values ($\rho = 1102.9$ kg m^{-3}) and a relative permeability of $\mu = 1$ were employed. Particle agglomerates were assumed to have a density of $\rho = 2800.8$ kg m^{-1} and a relative permeability of $\mu = 1.41073$ according. These values were based on the proportions of the SQUID measurement results. The release time for all particles was set at 0 seconds, with simulation times ranging from 20 to 300 seconds and time steps of 0.1, 0.01, and 0.001 seconds. The simulation results included data on magnetic flux density, longitudinal and transverse velocities, particle trajectories, Reynolds number, and evaluation groups to export the final particle positions for subsequent analysis.

Table A.2: Sample inlet, buffer, and outlet settings used in the simulation for the different chip geometries.

	$\mathbf{v}_{Sample}$ [m s^{-1}]	$\mathbf{v}_{Buffer}$ [m s^{-1}]	$\mathbf{v}_{Outlet}$ [m s^{-1}]
Rectangular	0.000977777778	$P_0 = 0$	0.001062654765
Trapezoidal	0.0006349206	0.003725777778	$P_0 = 0$
Pinch-shaped	0.003888888889	0.0116666667	$P_0 = 0$

For the yeast cell model, a microscopic analysis was conducted on a sample of 150 yeast cells, each exhibiting labeled bud scars. Using a microscope with a 100x magnification, the bud scars were counted and further analyzed [109]. To estimate the surface area of these yeast cells, a simplified elliptical approximation was utilized.

$$S = a \cdot b \cdot \pi \tag{A.1}$$

The yeast cells' surface area was calculated by measuring their longest and shortest dimensions, orthogonal to each other. The diameter was calculated by the following equation

$$d = \sqrt{S/\pi} \tag{A.2}$$

An analysis of a typical heterogeneous yeast culture revealed an average distribution of 61% daughter cells, 28% first generation mother cells, 7% second generation mother cells, and 3% third generation mother cells. For a magnetically separated culture, a separate microscopic analysis was performed. All measured cell surfaces in Origin were sorted into 33 groups of a histogram, all with a similar group mean value. The cell surfaces sorted by size were counted down to diameter and assigned to a yeast group, starting with a daughter cell proportion. Permeabilities and densities were adjusted according to the number of bound ION@Si@EDTA agglomerates and yeast cell diameter (Equation A.3). In the end, a spherical particle was modeled, comprising of a magnetically labeled yeast cell.

$$\mu_P = \mu_Y \cdot \frac{V_{Y,K}}{V_{Y,K} + n \cdot V_{MNP}} + n \cdot \mu_{MNP} \cdot \frac{V_{MNP}}{V_{Y,K} + n \cdot V_{MNP}} \tag{A.3}$$

Here, n is the number of bud scars, $V_{Y,K}$ is the class sphere volume, V_{MNP} is the particle agglomerates' volume of $V = 0.155798087 \ m^{-3}$ and μ_{MNP} is the agglomerates permeability of 1.41073. The densities were calculated following the same equation. In the simulation,

Table A.3: Settings used for a release from a grid. The following criteria were defined: Radius (R_c), number of radial positions (N_c), initial velocity (v_{Sample}), direction of release (r_x, r_y, r_z), and the initial particle position ($q_{x,0}$, $q_{y,0}$ and $q_{z,0}$).

	($q_{x,0}$, $q_{y,0}$ and $q_{z,0}$)	(r_x, r_y, r_z)	R_c [mm]	N_c	v_{Sample} [m s^{-1}]
Rectangular	5, 2.88, 0.375	(1,0,0)	0.23	2	0.000977777778
Trapezoidal	-21, -0.35, 0.375	(1,0,0)	0.28	2	0.0006349206
Pinch-shaped	0.4, 0.3, 0.375	(1,0,0)	0.09	2	0.003888888889

particle release was modeled to replicate the experimental conditions. This involved the simultaneous release of a predefined number of particles from a grid, with their positions precisely determined. The initial coordinates for the particle positions were specified based on spatial dimensions ($q_{x,0}$, $q_{y,0}$ and $q_{z,0}$), as detailed in Table A.3. Along with these coordinates, the initial velocity of the particles (v_{sample}) and the exact time of their release (0 sec) were also defined. For simulations involving a hexapolar release pattern, additional parameters were set. This included specifying the coordinates for the central point (q_c), determining the radius (R_c), and setting the number of radial positions (N_c), all of which were outlined in Table A.3. Each particle defined in the simulation was assigned a separate inlet to ensure precise control over its release.

The simulation encompassed a total of 628 particles, which were derived from the defined set of 33 particles. These were simultaneously released at 19 distinct points, allowing for controlled simulation of particle behavior and dynamics under conditions mirroring those of the laboratory experiments. This approach provided a robust framework for analyzing particle movement and interactions within the simulated environment.

Cells deflected into the outlet's A to D were detected to compare the generated experimental data. A precise definition for reaching one of the outlets was established for each flow cell. Initially, all yeast cell models were simulated without adjusting the permeability, which did not represent the real deflection behavior, as intra- and interparticle effects were neglected. Therefore, the yeast cell with the highest magnetic deflection (scaling factor = volume $\times$ permeability) in exit D was increased by a scaling factor in a black box model. The scaling factor was set according to 1.004 for the rectangular, 1.00525 for the trapezoidal, and 1.006 for the pinch-shaped channel.

The scaling factor of the cell with the largest magnetic deflection ($\mu_{x,scaled}$) was divided by the actual permeability of this cell ($\mu_{x,not-scaled}$). The multiplication of this with the original permeability of the other cells resulted in the new permeability.

Millifluidic process setup for magnetophoretic fractionation
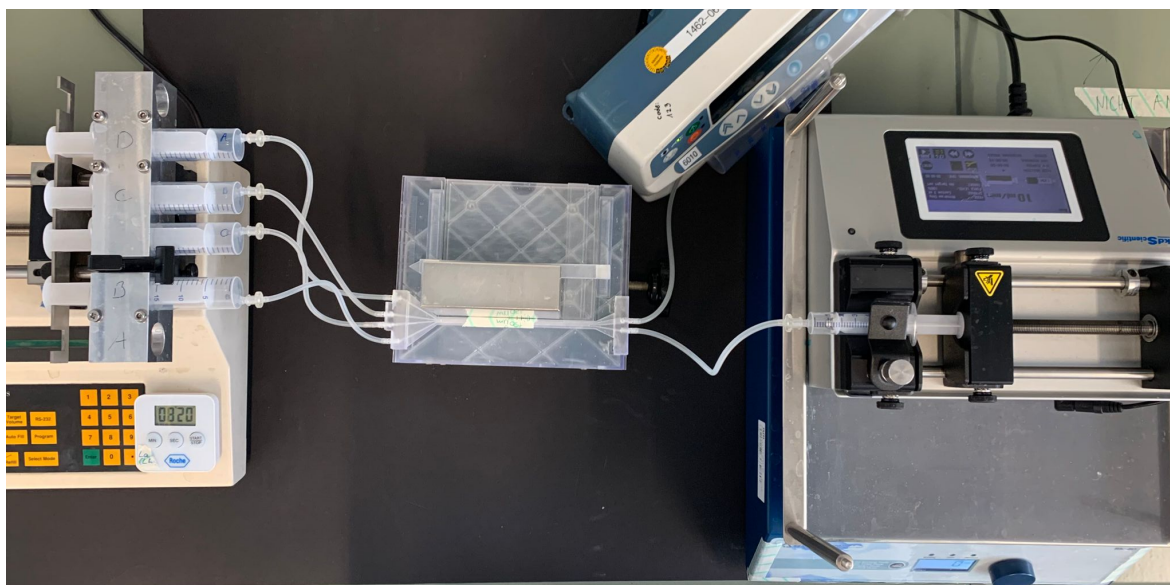
Figure A.16: General setup of the magnetophoretic fractionation experiments, here displayed with the rectangular chip. The buffer syringe pump is used with a 60 mL buffer syringe. Four 20 mL outlet syringes are run with the outlet syringe pump and a 6 mL sample syringe with an inserted 5 mm silver sphere is used with the sample syringe pump, placed onto the rocker shaker.